Geochemical and Isotopic Studies of Sarnu-Dandali-Kamthai Carbonatite-Alkaline Complex, India

Thesis submitted to

Indian Institute of Technology Gandhinagar, India

For the degree of
Doctor of Philosophy

in
Earth Sciences

by
Milan Kumar Mahala
(17330018)

Under the Supervision

of
Prof. Jyotiranjan S. Ray

Geosciences Division
Physical Research Laboratory Ahmedabad, India

February 2023

Dedicated to

my family

and

the scientific communities of the world

Declaration

I, Milan Kumar Mahala, declare that this written submission represents my ideas in my own words, and where others' ideas or words have been included, I have adequately cited and referenced the original sources. I also declare that I have adhered to all principles of academic honesty and integrity and have not misrepresented or fabricated, or falsified any idea/data/fact/source in my submission. I understand that any violation of the above can cause disciplinary action by the Institute and can also evoke penal action from the sources which have thus not been appropriately cited or from whom proper permission has not been taken when needed.

14/02/2023

Milan Kumar Mahala
(Roll no. 17330018)

Date: 14 Feb 2023

Certificate

It is certified that the work contained in the thesis entitled **“*Geochemical and Isotopic Studies of Sarnu-Dandali-Kamthai Carbonatite-Alkaline Complex, India*”** by Mr. Milan Kumar Mahala (Roll no. 17330018) has been carried out under my supervision and this work has not been submitted elsewhere for a degree.

Jyotiranjan S. Ray

Prof. Jyotiranjan S. Ray
(Thesis Supervisor)
Geosciences Division
Physical Research Laboratory
Unit of Department of Space, Government of India
Date: 14 Feb 2023 Ahmedabad-380009, Gujarat, India

Acknowledgements

I started my Ph.D. journey in PRL in 2017 to get a glimpse of research in isotope geochemistry that only a few institutes in the country were offering at that time. The research culture and facilities of this renowned institute motivated me to continue my research career. So far, I have come across many faculty members, support staff, colleagues, seniors, and juniors who have played a vital role in this journey. It is now time to express my heartfelt gratitude towards them, to whom I owe a lot.

I am sincerely grateful to my supervisor, Prof. J.S. Ray, for his guidance, support, and motivation. From coursework, field and lab training to thesis writing, his involvement in every aspect of my Ph.D. has been the foundation of my research career. His expertise in Igneous Petrology helped me visualize complex geological processes associated with my Ph.D. problem. I am incredibly thankful for his continued support, even during the time he was away on deputation.

I am extremely thankful to my PRL Co-supervisor, Dr. Arvind Singh, for his guidance and support during the analyses. His statistics lectures during my coursework helped me immensely later during the data interpretation. I learned a lot during my discussions with him in the group seminars.

I am also incredibly thankful for the support and encouragement of the Director, Dean, and academic committee members of PRL, and Heads, Geosciences Division. I am grateful to the Director of IITGN and Prof. Nithin V. George, Dean of IITGN, for giving me extended time to submit my thesis.

I express my heartfelt gratitude to Prof. A.D. Shukla, one of my DSC members, for his assistance during my sample analysis in his lab, and I am also thankful for his motivational words. I am sincerely thankful to Dr. A.B. Sarbadhikari, another DSC member, for his valuable comments during reviews. I am grateful to Prof. Kanchan Pandey, IIT Bombay, for Ar-Ar dating. I am immensely grateful to Profs. R.D. Deshpande, M.G. Yadava, Ravi Bhushan, Sanjeev Kumar, Neeraj Rastogi, Dr. A.K. Sudheer, and other faculty members for teaching me foundational aspects of various fields in geosciences and other disciplines during my coursework. I thank Dr. Vineet Goswami for his help during TIMS analyses and Dr. Amzad Laskar for sparing his valuable time for discussions with me.

I am indebted to Dr. Bivin Geo George, my lab senior, for training me in various analytical methods in PRL. I am also incredibly thankful for his continued support and mentorship. I am also thankful to Dr. Ikshu Gautam for teaching me column chemistry and TIMS measurements. I am grateful to Dr. Niharika Sharma for helping me during my stable isotope measurements. I had excellent discussions with Dr. Iftikhar Ahmad, Dr. Anirban Chatterjee, Dr. Oinam Kingson, and Dr. Alok Kumar during various stages of my Ph.D., and I am grateful to them for teaching me a lot of new things. The assistance provided by Jitender Kumar, Sangeeta Verma, Nazir Ahmed, and Mahesh Gaddam during various analyses in PRL has been extremely helpful. I also thank Drs. Nilanjana Sorcar and Sneha Mukherjee of NCESS for the EPMA analyses. I express my gratitude to Prof. Himanshu Shekhar and Karla, IITGN, for the coursework on scientific writing.

Staff members of PRL Library, Computer Centre, Administration, Accounts, Workshop, CMD, Purchase, and Stores helped me at various junctures of my Ph.D. life, and I am grateful *to them. I am thankful to my GSDN batchmates, Himanshu, Atif, Amit, and Partha, for making my time in PRL wonderful. Ankit had always kept me in high spirits. I enjoyed the company of Sovan, Pravin, Madhu, Shivani, Abhay, Kamlesh, Sharika, Anshika, Tanu, Tanmay, Ramanuj, Sudipta, Hrushi, Sushant, and Suraj. I am thankful to Dr. Deepika for her help on various occasions. I also thank Nisha, Abdur, Subir, Dipak, Dipti, Anil, and Kiran for their suggestions and advice on various matters. I would thank Siddhartha for his help during stable isotopic analysis. I am fortunate to have juniors - Deva, Deepak, Sidhartha, Tatsat, Bhuvan, Sanjit, Swagatika, Ajheta, Shreya, Debashis, Kamran, and Guru with whom I had great moments.*

I would like to express my gratitude to my family for their unconditional love, support, and motivation to continue research. Finally, I thank Almighty God for bestowing his love on me. Although I tried, it is almost impossible to mention everyone who has contributed to this journey of research in some or the other way. I thank every one of them who has helped me complete this thesis work.

Milan Kumar Mahala

Abstract

Carbonatites, rich in carbonate minerals, are unique magmatic rocks because they are derived from a silicate-rich mantle. Being the largest extractor of mantle carbon, they play a vital role in Earth's deep carbon cycle. Although they represent less than 1% of all mantle-derived magmas, their presence throughout the geologic time, overwhelming presence in continental settings, close association with alkaline silicate rocks, special affinity towards deep mantle plumes, and extremely high contents of rare earth elements make them one of the most interesting rocks for studying the fluids in the Earth's mantle and many unusual magmatic processes.

The carbonatite research has come a long way since its first identification as magmatic rocks in 1950. We now understand many aspects of its origin and evolution; however, many other characteristic features and responsible processes remain undecipherable. To contribute to the global effort of unraveling the mysteries of carbonatite magmatism, I took up the study of one of several carbonatite complexes of the Deccan Traps magmatic province that came into existence during the late Cretaceous Period. This carbonatite complex is located in the Sarnu-Dandali and Kamthai localities of Rajasthan. It exposes diverse alkaline silicate rocks along with minor carbonatite and is believed to represent one of the earliest magmatic manifestations of the Deccan-Reunion plume activity in the Indian subcontinent. In my Ph.D. work, I studied all different rock types of the complex for their field relations, mineralogy, geochemical, and C-O-Sr-Nd-Pb isotopic compositions and determined the timings of various magmatic phases using ^{40}Ar-^{39}Ar dating method with the following major objectives: (1) Ages of emplacement of various magmatic bodies; (2) Nature of differentiation and evolution of carbonatites and their relationship with the associated alkaline silicate rocks; (3) Role of crustal assimilation (if any) in the origin and diversification of carbonatites; (4) Nature of the mantle source(s) for different magmatic activities in the complex and role of the Reunion-Deccan plume in their origin; (5) Nature (source) of carbon in carbonatites.

Our age data reaffirm the recurrence of magmatic activities in the Sarnu-Dandali and Kamthai during two main phases; one during 89-79 Ma and the other during 69-66 Ma, with the older phase likely related to the continental breakup of India and Madagascar, and the latter clearly linked to the Deccan Traps activities. Based on field-age-geochemical-isotopic data and models, we clearly establish that liquid immiscibility is the main magmatic process responsible for the generation of carbonatite-alkaline silicate rock association in the complex and that crustal assimilation likely played a key role in the immiscibility process as well as subsequent differentiation leading to diversification of rocks. Isotopic data suggest plume origin for carbonatites; however, the metasomatized continental lithosphere appears to have played a significant role, particularly in enriching the parental magma with rare earth elements. Primordial carbon appears to have remained a major source for carbonatites in the Deccan Province.

Contents

Chapter 1

Introduction

Carbonatites are unique among magmatic rocks as they contain the highest volume of magmatic carbonates. They are also unique because they are one of the largest extractors of carbon from the Earth's mantle, and therefore, they provide information about the significant role of carbon plays in Earth's deep interior. Carbonatite occurrences are rare, and they, along with alkaline silicate igneous rocks, constitute <1% of the igneous rock record on Earth. Carbonatite occurrences have been reported from all continents, and their age range from Archean to Present (e.g., Woolley and Kempe, 1989; Yaxley et al., 2022); thus, they are very useful messengers of mantle evolution through time. Carbonatites are also known to be excellent tracers of their mantle source compositions as their magmas are little affected by crustal contamination during their rapid ascent through the crust and tendency to buffer contamination because of high contents of the trace elements whose isotopes are used for studying such processes. They are of economic interest for being rich in rare earths, fluorine, phosphorus, niobium, etc.

Although initially thought to be a result of the melting of sedimentary carbonates and/or hydrothermal origin, carbonatites have now been recognized as one the most important igneous rocks, with the eruption of carbonate lavas by Oldoinyo Lengai volcano, Tanzania clearing all doubts about their magmatic origin. In spite of several decades of intensive research, petrogenetic aspects of these rocks remain elusive. We are yet to understand why most carbonatites in the world are calcitic (Ca-rich), whereas the primary near-solidus carbonatite melt under upper mantle conditions is dolomitic (Ca-Mg rich), and the lone active carbonatite volcano erupts Na-K rich carbonates. Similarly, it remains to be understood the reason for their overwhelming presence on the continents and whether they originate from the lithospheric mantle or the asthenospheric mantle. One of the two most intriguing aspects of these rocks has been their presence in many Large Igneous Provinces (LIPs) and their close association with alkaline silicate rocks. Therefore, apart from experimental petrologic studies, detailed geochemical and isotopic studies are needed in every known carbonatite to fully understand their origin, evolution, and the role they play in the evolution of the planetary interior.

1.1. Carbonatite Basics

Carbonatites are defined according to the IUGS definition as igneous rocks that contain more than 50% modal magmatic carbonates (Le Maitre 2002, Streckeison 1980). Apart from carbonate minerals (calcite, dolomite, ankerite, etc.), they contain minor silicate (olivine, pyroxene, amphibole, mica, etc.), phosphate (apatite, monazite, etc.) and oxide minerals (magnetite, ilmenite, etc.) as well. Carbonatites are also known to contain numerous exotic minerals such as pyrochlore, perovskite, bastnaesite, strontianite, etc. Carbonatites are generally named calcite carbonatite, dolomite carbonatite, ankerite carbonatite, etc., based on the dominant carbonate mineral present. However, the more popular nomenclature scheme has been the chemical classification. Chemically the carbonatites having < 20% SiO_2 are classified into calciocarbonatites, magnesiocarbonatites, and ferrocarbonatites according to their CaO, MgO, MnO, FeO, and Fe_2O_3 contents, and those with >20% SiO_2 are classified as silicocarbonatites (Wolley and Kempe, 1989). There exists another variety of carbonatites that is called the natrocarbonatite, which are richer in the Na_2CO_3 and K_2CO_3 relative to $CaCO_3$, known only from the active carbonatite volcano of Oldinyo Lengai. This nomenclature is neither mineralogical nor chemical. A modification to mineralogical classification of carbonatites by lowering the modal percentage of carbonates (>30%) was proposed by Mitchell (2005). According to Mitchell (2005), a purely descriptive definition of carbonatites, based on the modal mineralogy, is inadequate to describe the lithological complexities associated with carbonatite complexes. Recently, Yaxley et al. (2022) proposed a new classification based on primary mineral assemblage and not on those developed during subsolidus conditions. According to these authors, calcite in a carbonatite that develops exsolved dolomite lamellae should be considered as calcite carbonatite, and the abundant primary non-carbonate mineral such as apatite, clinopyroxene, olivine, or magnetite should be added as prefixes. The carbonate-rich rocks formed in the crust (e.g., antiskarns, anatectic carbonate-rich rocks) should not be considered carbonatites as per their scheme. However, in this work, the chemical classification scheme has been used as the primary nomenclature system to describe the carbonatites of the studied complex.

About 76% of carbonatite complexes in the world are spatially associated with diverse ultrabasic and alkaline silicate rocks, out of which the alkaline silicate rock association is the most dominant (~72%; Woolley and Kjarsgaad, 2008). The alkaline silicate rocks associated with the carbonatites comprise both intrusive and extrusive varieties and include melteigite, ijolite, urtite, melilitite, nephelinite, nepheline syenite, phonolite, basanite, tephrite, trachyte, syenite, quartz syenite, and melilitolite. Carbonatites and alkaline silicate rocks commonly occur in the uplifted regions of the continents that are associated with regional rifts (e.g., Foley and Fisher, 2017). However, minor occurrences of these associations have been reported in collisional settings (e.g., Hou et al., 2006; Xu et al., 2014). Most carbonatites associated with these rocks are interpreted to have a magmatic origin and have genetic relationships with the associated alkaline silicate rocks, although other carbonatites are thought to be precipitated from residual carbo(hydro)thermal solutions derived at the end stage of the fractional crystallization of diverse and unspecified magmas commonly at low temperature and pressure conditions. These carbonatites do not necessarily have any affinity with alkaline silicate rocks (e.g., Mitchell 2005; Woolley and Kjarsgaard, 2008). However, any detailed geochemical and isotopic investigation for this type of rock appears to be lacking.

1.2. Origin of Carbonatites

According to the current understanding of the origin of carbonatites based on experimental petrology on model systems and rock systems, as well as the geochemical and isotopic studies on the carbonatites, the parental melts of the carbonatites are believed to get generated primarily in three ways. These are as follows:

a) *Generation of primary carbonate magma by near-solidus melting of carbonate or CO_2-bearing mantle peridotite*: Primary carbonatite melts of alkali-bearing calcic magnesian composition can get generated by melting of the carbonate-bearing mantle at the solidus of an oxidized peridotite (< 9 GPa; e.g., Dasgupta and Hirschman, 2006; Pinter et al., 2021). They can also get generated in the cooler lithospheric mantle near peridotite+CO_2±H_2O solidus. The emplacement of primary Ca-Mg melts directly into the crust is limited below pressure <2.0 GPa due to carbonate limiting reaction (dolomite + orthopyroxene = clinopyroxene + olivine + CO_2 (fluid)). However, if emplaced rapidly or emplaced along the wehrlitized melt conduits, they can be directly emplaced in the crust (e.g., Wyllie and Lee, 1998; Dalton and Wood, 1993; Yaxley et al., 2022; and references therein). Newania carbonatite in India is a good example of the emplacement of primary magnesian carbonatite melt (e.g., Ray et al., 2013).

b) *Derivation of residual carbonatite melt by fractional crystallization of a carbonated silicate magma*: Parental carbonated silicate magma derived from carbonate or CO_2-bearing mantle can undergo crystal fractionation of early minerals, subsequently giving rise to a CO_2±H_2O-rich residual carbonatite melt (e.g., Watkinson & Wyllie, 1971; Lee & Wyllie, 1994). The evidence for this mode of origin has been presented by Doroshkevich et al. (2017) for the carbonatites of the Belaya Zima complex in Russia. However, there is not enough evidence for this mode of origin.

c) *Derivation of carbonatite melt by liquid immiscibility from a parental carbonated silicate magma*: At crustal pressure (0.1-1.0 GPa), carbonate-rich and silicate-rich liquids are immiscible (Lee and Wyllie, 1997; Wyllie and Lee, 1998) and the fractionation of carbonated silicate (nephelinite and melilitite) magmas, at crustal pressure, can modify the composition of residual carbonated silicate magmas that can lead to the formation of immiscible silicate and carbonatite melts (Brooker and Kjarsgaard, 2011; Chandra et al., 2019; Lee and Wyllie, 1998; Schmidt and Weidendorfer, 2018; and references therein). Studies of Melt inclusion records in various silicate minerals in alkaline silicate rocks associated with carbonatite complex have reported the coexisting immiscible silicate + carbonate ± sulfide melts, supporting the liquid immiscibility origin of the carbonatites (e.g., Guzmics et al., 2012; Panina and Motorina, 2008; Ryabchikov and Kogarko, 2016). Geochronological, geochemical, and isotopic data from coexisting carbonatites alkaline silicate rocks in numerous complexes worldwide tend to support this mode of origin (e.g., Feng et al., 2021; Halama et al., 2005; Ray, 2009; Solovova et al., 2005; Stoppa et al., 2005).

1.3. Carbonatites as messengers from the mantle

Carbonatites occur in continental and oceanic settings and, therefore, define the nature and characteristics of their mantle source regions under different tectonic settings. Owing to their high volatile contents (e.g., CO_2, H_2O, etc.) and low viscosity, the parental magmas of these rocks are emplaced rapidly in the crust without getting much contaminated during their ascent, thus preserving their mantle source signature efficiently. Extracting carbon from the mantle for a long time, carbonatites spanning across geologic ages are important tracers of the deep carbon cycle of the planet. Isotopic studies of oceanic carbonatites suggest an asthenospheric origin (e.g., Hoernle et al., 2002; Doucelance et al., 2010), whereas the carbonatites in the continental settings have been interpreted to have either lithospheric or a mixture of lithospheric and asthenospheric components in their source (e.g., Bell and Simonetti, 2010; Ray et al., 2013; Bizimis et al., 2003; Ackerman et al., 2017). A compilation of initial $^{143}Nd/^{144}Nd$ data for global carbonatites is shown in *Fig. 1.1*, where only the highest radiogenic Nd isotopic compositions for a given complex were taken, assuming they are the best estimate of the mantle. The Nd isotopic compositions vs. age, constrained from the global carbonatites, depict a time-integrated mantle evolution from ~3.0 Ga to the Present. From the data, it appears that most of the carbonatite mantle sources have evolved, similar to what would be expected for a chondritic or primitive mantle source. However, there are sources that do not follow this trend and show either superchondritic or subchondritic $^{143}Nd/^{144}Nd$, which are likely due to the involvement of light rare earth element (LREE) depleted mantle sources or incorporation of ancient recycled continental crustal material in carbonatite sources, respectively (Yaxley et al., 2022).

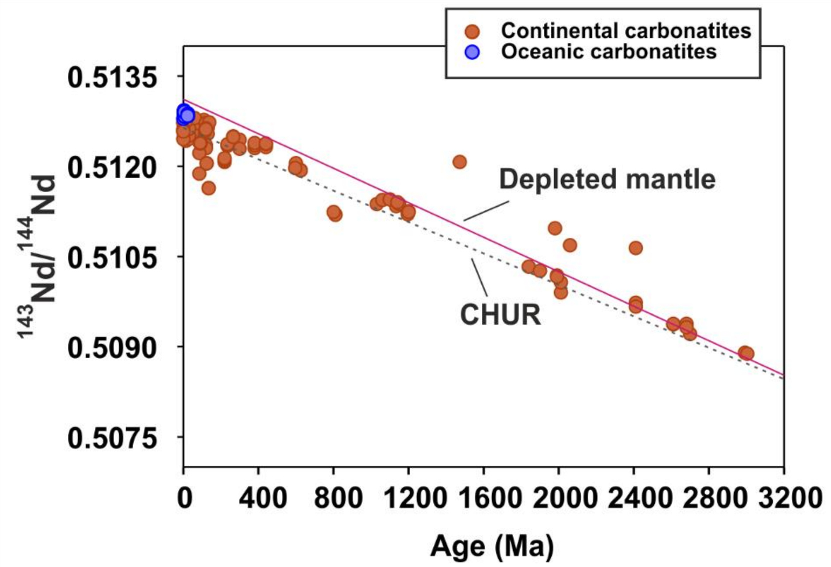

Fig.1.1. Initial $^{143}Nd/^{144}Nd$ of global carbonatites versus time showing the secular evaluation of mantle. CHUR = Chondritic Uniform Reservoir. CHUR data: Present day $^{43}Nd/^{144}Nd$ = 0.512638 (Goldstein et al., 1984) and $^{147}Sm/^{144}Nd$ = 0.1967 (Jacobsen and Wasserburg, 1980). Depleted mantle evolution trend was plotted using present day $^{143}Nd/^{144}Nd$ = 0.513114 (Michard et al., 1985), and Sm/Nd = 0.3596 (Salters and Stracke, 2004).

Despite the fact that much progress has been made in the field of carbonatite research aimed at deciphering the information they carry about the nature of mantle and its evolution, many aspects of carbonatite generation and emplacement remain provisional. Some of these questions that are important for the continuation of carbonatite research using innovative methods are listed below.

1. What is the nature of parental carbonatite magma, and how does it evolve during its crustal emplacement?
2. What is the primary mode of origin of carbonatites? Does crustal assimilation play any role in the generation of carbonatites?

3. Are the enriched mantle components observed in carbonatites in continents derived from the lithospheric mantle or from crustal components recycled into the mantle?
4. Why are so many carbonatites associated with continental flood basalt provinces, and do they have direct genetic links with the deep mantle plume sources which are responsible for flood volcanism?
5. Has the source of carbon in the carbonatites varied with time? If so, how?

1.4. Indian Carbonatites

Studies on Indian carbonatite complexes have been reviewed by Ray and Ramesh (2006), Krishnamurthy (2019), and Randive and Meshram (2020). The updated distribution of the Indian carbonatites is shown in Fig. 1.2, and a summary of their vital data, such as locality, age, types, associations, and mantle sources, is presented in Table 1.1. Currently, 27 carbonatite complexes are known in India, out of which one is a putative carbonatite occurrence (Munnar carbonatite of Kerala) because of suspected sedimentary signatures (Hegner et al., 2020). Whereas the magmatic nature of many of these carbonatite complexes has been well established, the origins of many others, such as Chaktalo, Hingoria, Chitrangi, Kunavaram, Udaiyapatti-Chhinagoundan Palyam, Ariyalur, and Murud-Janjira, remain unknown. Although some carbonatite complexes have no reported ages, on the basis of available ages, Indian carbonatites can be classified into Proterozoic and Mesozoic carbonatites. Except for two carbonatite occurrences in northern India (Newania, Kutni-Beldih), all Proterozoic carbonatites are known from peninsular India, south of the Deccan Traps. The mode of occurrences of the Indian carbonatite complexes varies from sub-volcanic to plutonic types, although a few lava flows and tephra deposits have also been reported (Randive and Meshram, 2020). One confirmed carbonatite complex, Newania of Rajasthan, is not associated with any alkaline silicate rock, whereas most others have associations with a wide variety of alkaline silicate rocks (e.g., Ray et al., 2013).

The Indian carbonatite complexes are associated with regional rifts, faults, and tectonic lineaments (e.g., Krishnamurthy, 2019). They are mostly confined to six major structural domains, such as the Eastern Ghats Mobile Belt - Southern Granulite Terrane, Western Ghats, Narmada-Son Rift Zone, Cambay - Aravalli Rift zones, Assam-Meghalaya plateau, and Central Indian Suture - North Singhbhum Mobile Belt (Krishnamurthy 2019). Some carbonatite-alkaline complexes such as Amba Dongar and Siriwasan, Mundwara, and Sarnu-Dandali-

Kamthai are associated with the Deccan continental flood basalts (CFB) (Basu et al., 1993; Ray et al., 2006) and a few others with the Rajmahal-Sylhet Traps (e.g., Sung valley, Samchampi, Samteran, Swangkre, and Jasra; Ray and Pande, 2001; Srivastava et al., 2019), whose origin may have been linked to deep mantle plumes. In contrast, all other Indian carbonatites are found in non-plume settings. Table 1.1. summarizes all such information known for Indian carbonatites.

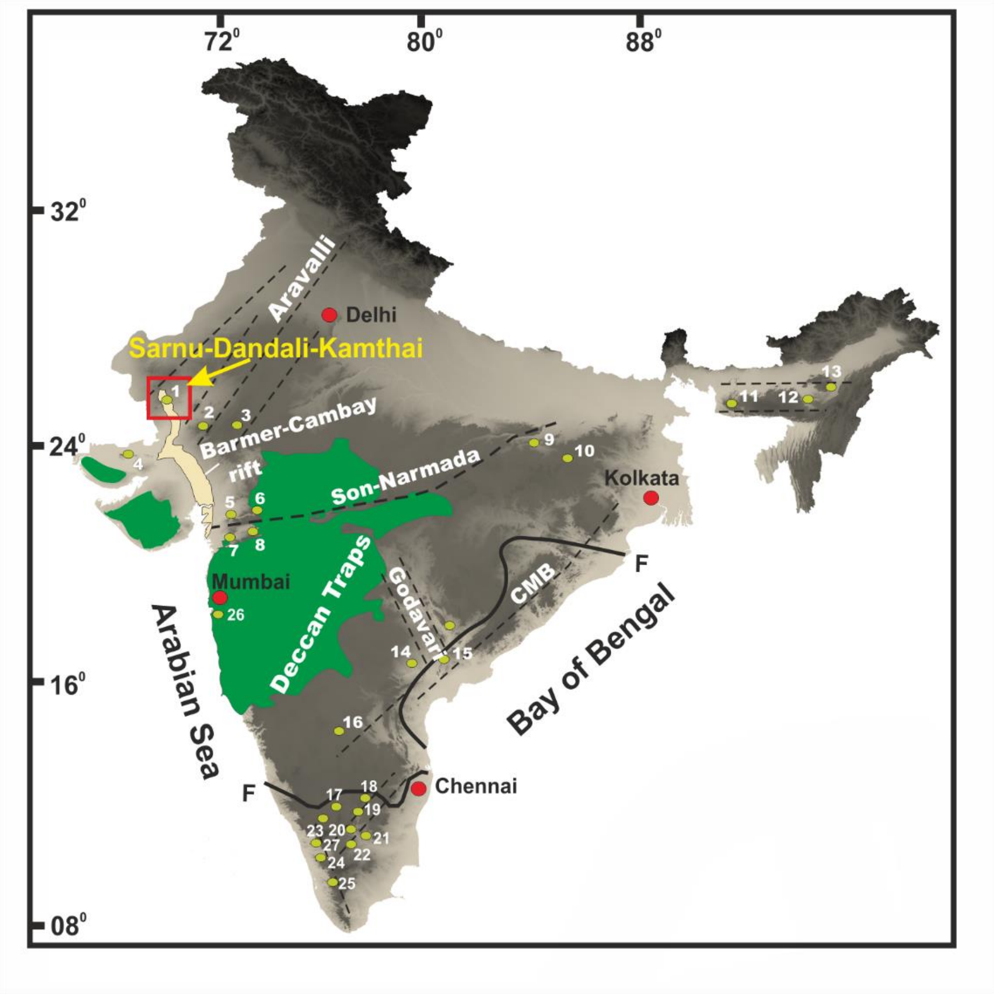

Fig. 1.2. Schematic map showing the distribution of Indian carbonatite complexes (numbered) along with associated major structural features (modified after Krishnamurthy 2019; Ray and Ramesh, 2006). Complexes: 1. Sarnu-Dandali-Kamthai (Barmer); 2. Mer-Mundwara; 3. Newania; 4. Pachham; 5. AmbaDongar and Siriwasan; 6. Chhaktalo; 7. Hingoria; 8. Mahdawa; 9. Chitrangi; 10. Kutni-Beldih; 11.Swangkre-Rongjeng-Jasra; 12. Sung valley; 13. Samchampi-Samteran; 14. Eluchuru; 15. Kunavaram; 16. Khaderpet-Anumpalle; 17. Hogenakal; 18. Sevattur; 19. Samalpatti; 20. Pakkanadu; 21. Udaiyapatti-Chhinnagoundan Palayam; 22. Ariyalur; 23. Ajjipura-Kollegal; 24. Munnar; 25. Khambamettu; 26. Murud-Janjira; 27. Gundlupet. CMB - Charnockite Mobile Belt, F—F – Charnackite - non-charnockite boundary of Fermor (1936)

The available Sr-Nd isotopic data for the Indian carbonatites are shown in a plot of ε_{Nd} (t) vs. ε_{Sr} (t) and are compared with various mantle reservoirs (Fig.1.3). As can be seen, barring three carbonatites, Sung Valley, Samchampi and Sarnu-Dandali-Kamthai (SDK), all Indian carbonatites plot in the fourth quadrant suggesting derivation from LREE-enriched mantles sources. Although they show derivation from LREE-enriched sources, Newania carbonatites show unusual Sr isotopic composition, which has been attributed to metamorphism (Ray et al., 2013). The enriched source signatures observed in all these carbonatites have been inferred to be a result of the derivation of these carbonatites from the Indian subcontinental lithospheric mantle sources, which were metasomatized during different tectonic events throughout their evolutionary histories (Kumar et al., 1998; Schleicher et al., 1998; Pandit et al., 2002; Ray et al., 2013; Renjith et al., 2016; Ackerman et al., 2017). The Sung valley and Samchampi carbonatites show LREE-depleted mantle signatures (ε_{Nd} (t) > 0), and they have been inferred to have been generated by low-degree melting of the Kergulen plume (e.g., Ghatak and Basu, 2013). Based on Sr-Nd-Pb isotopic data for only three carbonatite samples from the SDK complex, (ε_{Nd} (t) > 0 and ε_{Sr} (t) < 0; Fig. 1.3), which possesses signatures of an LREE-depleted mantle source, Simonetti et al. (1998) had proposed derivation of these carbonatites from a mixed source of the Reunion plume and the Indian sub-continental lithospheric mantle. On the contrary, the other prominent carbonatite complex of the Deccan CFB province, Amba Dongar carbonatites, show signatures of derivation from an LREE-enriched mantle (ε_{Nd} (t) > 0, ε_{Sr} (t) < 0) (e.g., Banerjee et al., 2019; Chandra et al., 2019; Ray et al., 2000; Simonetti et al., 1998). In addition, the involvement of continental lithosphere and lower crust has also been suggested in the modification of the isotopic signals of the associated alkaline silicate rocks in this complex (Ray et al., 2000; Chandra et al., 2019; Simonetti et al., 1998).

As summarized above, detailed geochemical and isotopic studies on Indian carbonatites are too few to address the most important questions regarding their petrogenesis. Questions pertaining to the reason behind the association of carbonatites and alkaline silicate rocks, the nature of the mantle sources and their evolution through time, the role of lithosphere and crust in the generation and diversification of carbonatites, and the nature of carbon in carbonatites through time are some of the interesting aspects of the Indian carbonatites those inspired me to take up this research project. In an attempt to answer some of these questions, I focused on the Sarnu-Dandali-Kamthai (SDK) carbonatite-alkaline complex, which is considered unique in many aspects because of its polychronous magmatic history and temporal and spatial association with the Deccan CFB.

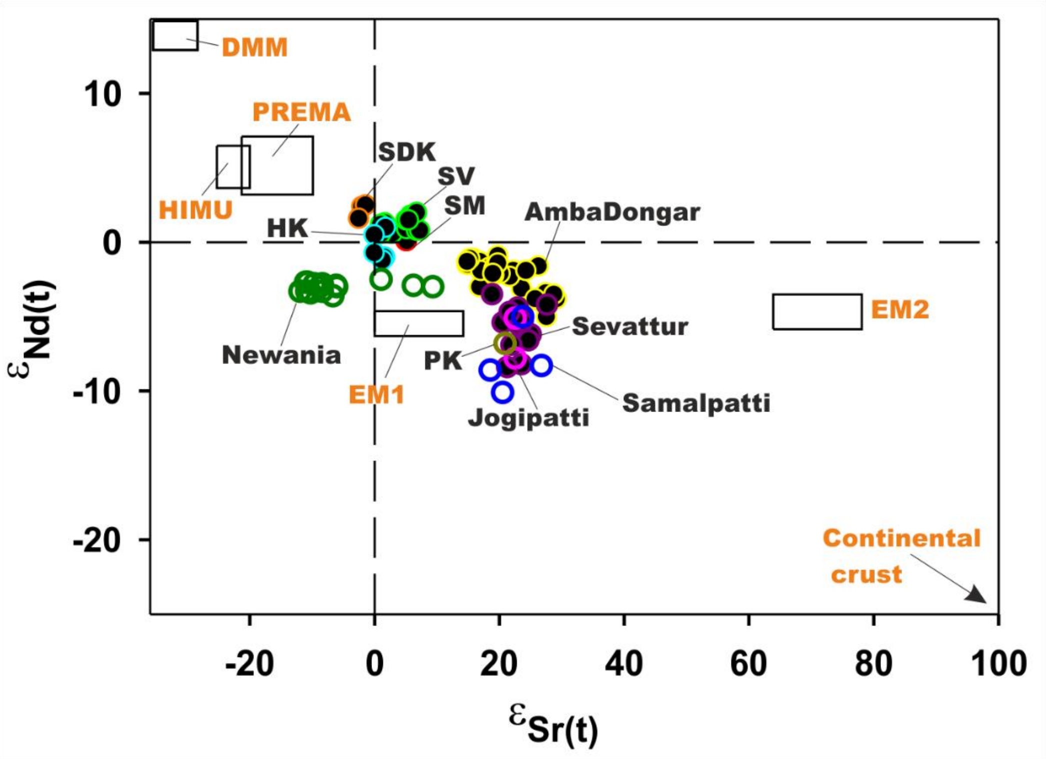

Fig.1.3. ε_{Nd} (t) vs. ε_{Sr} (t) diagram for the Indian carbonatites. Also shown are different mantle reservoirs (DMM, HIMU, PREMA, EM1, and EM2. Abbreviations: DMM = Depleted MORB Mantle; HIMU = Hi μ, where μ = $^{238}U/^{204}Pb$; EM1 = Enriched Mantle 1; EM2 = Enriched Mantle 2; PREMA = Prevalent Mantle; The values for DMM, HIMU, EM1, and EM2 are taken from Zindler and Hart, 1986. PREMA values are from Wornet et al. (1986). SV – Sung Valley, SM – Samchampi, HK – Hogenakal, PK – Pakkanadu.

1.5. Rationale and Objectives of this study

The SDK carbonatite-alkaline complex in north-west India is believed to be a late Cretaceous alkaline complex associated with the emplacement of the Deccan large igneous province (LIP), which, in addition to the CFB eruptions, was responsible for numerous alkaline and felsic magmatic activities in northwestern India. The characteristics that set the SDK complex apart from other similar complexes were that: (1) the complex was initially dated to be ~68.5 Ma, which was considered to be the earliest phase of Deccan Traps activity and a rock from the complex showed high $^{3}He/^{4}He$ signal (12.8 times the current atmospheric ratio) suggesting a deep mantle (plume) origin (Basu et al., 1993); (2) the complex apparently had multiple episodes of alkaline magmatism spanning in age from 89 to 66 Ma (Sheth et al., 2017); (3) the first Indian carbonatite hosted REE deposit was discovered in this complex (Bhushan and Kumar, 2013). Therefore, the complex provided a unique opportunity to address certain unanswered questions related to carbonatite origin and evolutions, such as (1) Are carbonatites owe their origin to deep mantle plumes? (2) If indeed the SDK carbonatite magmatism is caused by the plume, then how are they related to the flood basalt volcanism? (3) Do recurring alkaline (and carbonatite) activity in one complex suggest lithospheric origin? (4) What is the exact reason for the coexistence of carbonatites and alkaline silicate rocks? (5) How does the REE mineralization take place in carbonatites?

With the above motivation, I took up a detailed field, petrographic, geochronological (^{40}Ar/^{39}Ar), geochemical (major-trace), and isotopic (C-O-Sr-Nd-Pb) study of the rocks of the SDK carbonatite-alkaline complex to not only understand the origin and evolution of the complex but also shed some light on the origin of carbonatites in general. The objectives of my Ph.D. work were to:

1. Determine the timings (ages) of emplacements of various magmatic bodies within the SDK complex.
2. Understand the differentiation processes and the evolution of carbonatites of SDK complex and their relationship with the associated alkaline silicate rocks.
3. Understand the role of crustal assimilation (if any) in the origin and diversification of carbonatites and associated silicate rocks.
4. Understand the nature of the mantle source(s) for different magmatic activities in the complex and the relationship to regional/global tectonic activities such as India-Madagascar separation and Reunion-Deccan Plume activity etc.
5. Establish the nature (source) of carbon in the SDK carbonatites.

Table 1.1. Summary of Indian carbonatite complexes

Locality	Age	Type of carbonatites	Associated alkaline silicate rocks	mantle source(s)	References
1. Sarnu-Dandali-Kamthai (Barmer), Rajasthan	~66.1±1.4 Ma$_a$[1] ~68.57±0.08 Ma$_b$[2] 89.4-86.3 Ma and 66.3 Ma$_b$[3]	calciocarbonatite, ferrocarbonatite	nephelinite, melanephelinite, ijolite, melteigite, phonolite, lamprophyre, alkali pyroxenite, foidal syenite, alkali syenite	Asthenosphere (plume source)	Bhushan and Kumar (2013); Bhushan, 2015; Chandrasekaran et al. (1990); [1]Bhunia et al. (2022); Dongre et al. (2021); [2]Basu et al. (1993), [3]Sheth et al. (2017)
2. Mer-Mundwara, Rajasthan	~68.5 Ma[2]$_a$ ~70-64 Ma[4]$_a$ ~80.0-90.0 Ma[5]$_a$ and ~102-110 Ma[5]$_a$	calciocarbonatite	theralite, melteigite, pyroxenite, syenite, lamprophyre	Asthenosphere (plume source)	[2]Basu et al. (1993); [4]Rathore et al. (1996); [5]Pande et al. (2017); Subramaniam and Rao (1972,1977); Chakravorty and Bose (1978); Subramanyam and Leelanandam (1989, 1991); Sharma et al. (2022)
3. Newania, Rajasthan	2273±13 Ma (Dol. carbonatite) and 1551±46 Ma[5]$_c$ (ankerite carbonatite), 1473±63 Ma[6]$_c$ 2414±420 Ma[6]$_c$ 2120±22 Ma[18]	dolomitic carbonatite with ankerite carbonatite	No associated alkaline silicate rocks	metasomatized subcontinental lithospheric mantle	Viladkar 1998; Viladkar and Wimmenauer (1986); Viladkar et al. (2017); Doroshkevich et al. (2010); [5]Schleicher et al. (1997); [6]Ray et al. (2013); [18]Sorokhtina et al. (2022)
4. Pachham Island, Gujarat	----	calciocarbonatite	lamprophyre	----	Ray et al. (2014)
5. Amba Dongar and Siriwasan	65.0±0.3 Ma[7]$_b$ 65.4±2.5 Ma[8]$_a$	calciocarbonatite ferrocarbonatite	nephelinite, tinguaite, phonolite/phononephelinite, basanite, tephrite, syenite/nepheline syenite	metasomatized subcontinental lithospheric mantle	Sukheswala and Udas (1967); Viladkar (1986,2012,2018); Srivastava (1994,1997); Simmoneti et al. (1995); Doroshkevich et al. (2009)

					Gwalani et al. (1993); Chandra et al. (2018,2019); Banerjee and Chakrabarti (2019); [7]Ray and Pande (1999); Ray et al. (2000); Ray and Shukla (2004); [8]Fosu et al. (2019)
6. Chhaktalo, Madhya Pradesh	----	calcite rich	----	----	Hari et al. (1998); Khandelwal et al. (1997);
7. Hingoria, Gujarat	----	----	Trachybasalt, trachyte, Mugearite	----	Udas and Krishnamurthy (1968); Krishnamurthy and Cox (1980)
8. Mahdawa, Maharashtra	----	calciocarbonatite	nephelinite	----	Sant et al. (1991)
9. Chitrangi, Uttar Pradesh	----	carbonate ocelli	aillikite	----	Srivastava, 2013
10. Kutni-Beldih, West Bengal	748±24 Ma[8]$_{d}$	calciocarbonatite	nepheline syenite, phoscorite, alkali pyroxenite, glimmerite	----	Chakrabarty and Sen (2010) Basu and Bhattacharya (2014)
11. Swangkre-Rongjeng-Jasra, Meghalaya	107±4 Ma[9]$_{e}$ 106.8±0.8[10]$_{a}$ 105.2±0.5 Ma[11]$_{a}$	calciocarbonatite	potassic lamprophyre-ijolite-syenite (Swangkre-Rongjeng), alkali clinopyroxenite-syenite-ijolite (Jasra)	metasomatized subcontinental lithospheric mantle	[9]Sarkar et al. (1996); Nambiar and Golani (1985); Srivastava et al. (2016, [10]2019); [11]Heaman et al. (2002)
12. Sung Valley, Meghalaya	107.2±0.8 Ma[12]$_{b}$ 106.8±1.5 Ma[13]$_{a}$ 149±5 Ma[14]$_{e}$ 134±20 Ma[15]$_{c}$ 106±11 Ma[16]$_{f}$	calciocarbonatite	clinopyroxenite-melilitite-nepheline syenite-ijolite	Asthenosphere (plume source)	Krishnamurthy 1985; [12]Ray and Pande (2001); Srivastava et al. (2005,[13]2019); [14]Sarkar et al. (1996); [15]Veena et al. (1998); [16]Ray et al. (2000); Basu and Murty (2006); Melluso et al. (2010); Ghatak and Basu (2013); Choudhary et al. (2021)
13. Samchampi-Samteran, Assam	~105 Ma[17]	calciocarbonatite	syenite/nepheline syenite, ijolite-melteigite, alkali pyroxenite	metasomatized subcontinental lithosphere	Nag et al. (1999); Saha et al. (2017)
14. Eluchuru, Andhra Pradesh	----	calciocarbonatite	syenite	----	Ratnakar and Leelanandam (1989)

15. Kunavaram, Andhra Pradesh	----	----	nepheline syenite	----	Sharma et al. (1971)
16. Khaderpet-Anumpalle, Andhra Pradesh	----	calciocarbonatite	Kimberlite	----	Smith et al. (2013)
17. Hogenakal, Tamil Nadu	2401±25 Ma[19]$_{g}$ 2415±10 Ma[19]$_{f}$ 1994±0.076 Ma[23]$_{f}$	calciocarbonatite	syenite	subcontinental lithospheric mantle	Kumar et al. (1998); Natrajan et al. (1994)
18. Sevattur, Tamil Nadu	771±18 Ma[20]$_{f}$ 801±11 Ma[21]$_{c}$	calciocarbonatite, ferrocarbonatite	syenite	subcontinental lithospheric mantle	[20]Kumar and Gopalan (1991); Krishnamurthy, 1977; Kumar et al. (1998); [21]Schleicher et al. (1997); Viladkar and Subramanian (1995); Pandit et al. (2002, 2016); Vladykin et al. (2008); Ackerman et al. (2017)
19. Samalpatti, Tamil Nadu	700±30 Ma[22]$_{e}$	calciocarbonatite silicocarbonatite	syenite	subcontinental lithospheric mantle	Borodin et al. (1971); [22]Moralev et al. (1975); Pandit et al. (2002,2016); Ackerman et al. (2017)
20. Pakkanadu, Tamil Nadu	771±2 Ma[24]$_{e}$	ferrocarbonatite	syenite	subcontinental lithospheric mantle	Rao et al. (1978); Pandit et al. (2002, 2016); [24]Moralev et al. (1975)
21. Udaiyapatti-Chhinnagoundan Palayam	----	calcite rich veins	----	----	Kumar et al. (2001)
22. Ariyalur, Tamil Nadu	----	high Ba, Sr, F rich	----	----	Grady, 1971
23.Ajjipura-Kollegal, Karnataka	----	calciocarbonatite magnesiocarbonatite	No alkaline silicate rocks	----	Anantharamu et al. (1995)
24. Munnar, Kerala	1020±70 Ma[25]$_{a}$	metacarbonate	No alkaline silicate rocks	----	[25]Hegner et al. (2020)
25. Khambamettu, Kerala	2470±15 Ma[26]$_{a}$	calciocarbonatite	syenite	metasomatized mantle source	[26]Renjith et al. (2016)

26. Murud-Janjira, Maharashtra	----	calcite rich veins	lamprophyre, tephrite, nephelinite, nepheline syenite	----	Melluso et al. (2002); Desai and Viegas (2010)
27. Gundlupet, Karnataka	----	calciocarbonatite	syenite	----	Brahma et al., 2022

Note: a- U-Pb dating, b- ^{40}Ar-^{39}Ar dating (mineral/whole rock), c- Pb-Pb dating (whole rock), d- Chemical dating (pyrochlore), e- ^{40}K-^{40}Ar dating (whole rock), f- Rb-Sr dating, g- Sm-Nd dating

Chapter 2

Geology and Earlier Work

2.1. Regional geology, field relations, and tectonic framework

The late Cretaceous Sarnu-Dandali-Kamthai (SDK) carbonatite-alkaline complex is located on the central-eastern rift margin of the Barmer basin, the northward extension of the Cambay basin (e.g., Bladon et al., 2015a; Bladon et al., 2015b). The Barmer basin is known to have undergone extensional tectonics during the late Cretaceous-mid Eocene (e.g., Bladon et al., 2015a). The basin contains thick Mesozoic and Cenozoic sedimentary rocks, comprising sandstones and siltstones, deposited over the magmatic rocks of the Neoproterozoic Malani Igneous Suite (MIS; Bladon et al., 2015a; Dolson et al., 2015). The MIS activities took place during 770-750 Ma (Gregory et al., 2009), and subsequent episodes of basin evolution and fluvio-marine sedimentation resulted in formation of thick sedimentary sequences during Neoproterozoic and Mesozoic periods, though disjointed and discontinuous, in various sectors of the Cambay-Barmer rift valley. Raageshwari and Tavidar volcanics, temporally covalent to Deccan activity are present in the Barmer basin at shallow depth (*Fig.2.1a; Bladon* et al., *2015b*). The Meso-Neoproterozoic Delhi-Aravalli Fold Belts (DAFB) run NE-SW at the eastern margin of the Malani group of rocks. The Archean supracrustal rocks (Banded Gneissic Complex - BGC) are exposed at the Southeastern margin of the DAFB (*Fig,2,1a*).

The occurrence of alkaline rocks in the SDK complex was first reported by Udas et al. (1974) and later investigated by Das et al. (1978) and Chandrasekaran et al. (1990). Chandrasekaran et al. (1990) reported an older mildly alkaline series (e.g., alkali olivine basalt, hawaiite, trachyandesite, trachyte, alkali syenite) in the complex, those overly the Malani rhyolitic tuffs (*Fig.2.1b*) The other alkaline rocks reported from the complex are ijolite, melteigite, melanephelinite, foidal syenite, and phonolite, which occur as small plugs and dykes, and intrude into the basement and the overlying sediments (Chandrasekaran et al., 1990). Alkali pyroxenite is reported from within foidal syenite. Phonolite dykes intrude mela-nephelinites and mark the end stage of alkaline magmatism in the complex (Chandrasekaran et al., 1990; Bhushan, 2015). The carbonatites are a minor component of the complex and occur

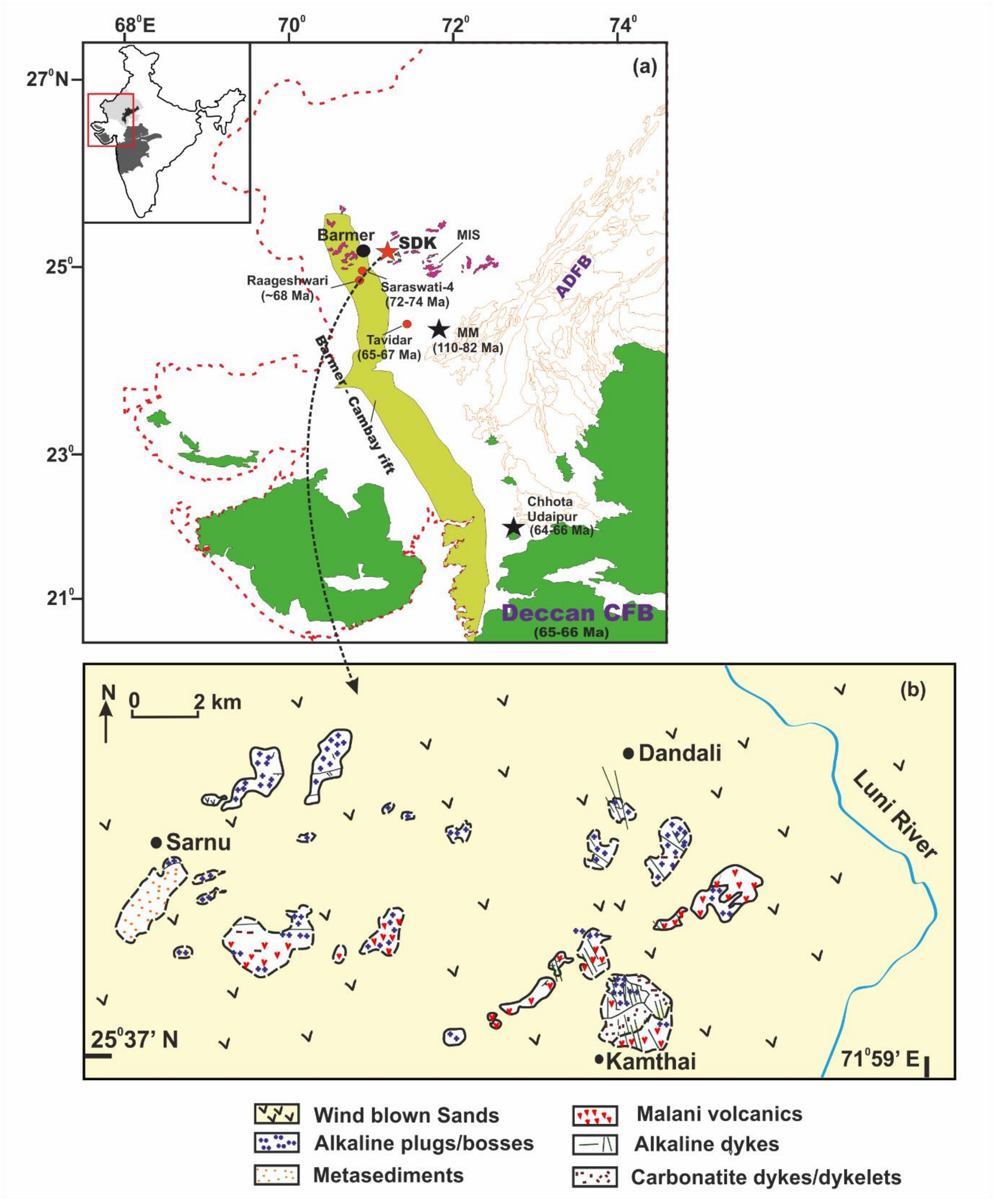

Fig. 2.1. (a) Part of western India showing the Deccan Traps (Green), the Barmer-Cambay rift, location of the Sarnu-Dandali-Kamthai carbonatite-alkaline complex (red star), and other Deccan equivalent volcanics (Tavidar, Raageshwari and Saraswati-4) in the Barmer-Cambay rift. Also shown are Mer-Mundwara (MM) and Chhota Udaipur sub-provinces, hosting several late Cretaceous carbonatite-alkaline complexes; the inset shows the map of India, the Deccan Traps (gray) and the Aravalli Craton (black) in the state of Rajasthan (washed gray); (b) A detailed geological map of the SDK complex showing the distributions of various alkaline and carbonatite bodies (modified after Chandrasekaran et al., 1990).

as dykes/dykelets, plugs, veins, and sills, and have been found as either isolated bodies or in association with melanephelinite and other basic alkaline members (Chandrasekaran et al., 1990; Bhushan and Kumar, 2013; Bhushan, 2015; Srivastava et al., 1993; Wall et al., 1993). Most dykes of the complex trend NW-SE, parallel to the pre-rift structural trend in the Barmer basin, though a few NE-SW, parallel to syn-rift tend, trending dykes have also been reported (Baldon et al., 2015). Late-stage carbonatite veins intrude some of the tephrite and phono-tephrite dikes.

2.2. Regional geophysical studies

According to Kilaru et al. (2013), the MIS basement of the Barmer region is overlain by ~3.5 km thick Mesozoic sediments and modern alluvium. As constrained by gravity data, the thickness of MIS varies between 3 to 7 km (Kilaru et al., 2013). The depth of Moho in the Gadra-Sarnu region is approximately 32 km, and it increases toward Aravalli-Delhi old belt in the NE (Kilaru et al., 2013). The presence of a high-density layer (2.9 g/cm^3) near Moho below the Barmer rift has been interpreted as underplating of mafic intrusions (Kilaru et al., 2013). A high-density and high-velocity layer at the base of the lower crust has also been reported under the Cambay rift (Kaila et al., 1990; Mishra et al., 1998), which has been linked to Deccan volcanism-related magmatic underplating. Bandalamudi et al. (2022) identified a zone of crustal thinning (32.5-35.4 km) centered beneath the sites of pre-Deccan alkaline magmatism in the Barmer rift, which lie above a lower velocity upper mantle anomaly, hypothesized to be the trace of a plume conduit.

2.3. Alkaline Silicate Rocks

^{40}Ar-^{39}Ar ages reported by several earlier workers for various silicate magmatic bodies of the SDK complex are summarized in Table 2.1. Chandrasekaran et al. (1990) reported concentration data for major oxides and selected trace elements (Cr, Ni, Co, Cu, Zn, Ba, Sr, Li, Rb) for mildly alkaline series and alkaline series rocks of the SDK complex. From their study, they suspected that the rocks of the mildly alkaline series, alkali olivine basalt-hawaiite-trachyandesite-trachyte-alkali syenite, possibly belonged to a separate cycle of igneous activity compared to the pure alkaline series. Based on ^{40}Ar-^{39}Ar ages on some of the mildly alkaline rocks (89-86 Ma), Sheth et al. (2017) suggested that these rocks belonged to an older alkaline magmatism and were likely related to the Indo-Madagascar separation. Earlier, Basu et al.

(1993) obtained an age of ~68.57 Ma for a biotite separate from an alkali pyroxenite from the complex, supporting the idea of multiple generations of alkaline magmatism in the complex. Recently, Dongre et al. (2022) reported ^{40}Ar-^{39}Ar ages that varied between 68.17 and 65.44 Ma for the phlogopite xenocrysts from an alkaline lamprophyre and suggested the ~68 Ma age represents the age of mantle metasomatism. Dhote et al. (2022) recently reported a phlogopite-spinel-white xenolith containing carbonates and phlogopite xenocrysts hosted by two lamprophyre dykes from the SDK complex. Based on petrography, he suggested that phlogopites are the result of mantle metasomatism caused by silica-undersaturated carbonated silicate and(or) carbonate magmas. He also suggested that silicate magmatism and carbonate magmatism occurred at different times, where carbonate magmatism preceded silicate magmatism.

The younger alkaline activity (66-69 Ma) of the SDK complex was thought to be related to the Deccan-Reunion plume that gave rise to the Deccan Traps (Basu et al., 1993; Simonetti et al., 1998; Dongre et al., 2022); however, these studies did not provide sufficient geochemical and isotopic evidence. Petrographic studies by Chandrasekaran et al. (1990) reported that the ijolites, which probably represent the younger alkaline phase (69-66 Ma), consisted essentially of titanaugite, nepheline and apatite. The alkali pyroxenites comprised titanaugite, biotite, iron-oxide, apatite, and interstitial nepheline. The foidal syenite contained abundant nephelinite and orthoclase with minor aegirine augite. Simonetti et al. (1998) reported major oxide, selected trace elements for four melilitites, one phonolitic nephelinite, four phonolite samples, and Sr - Nd-Pb isotopes for melilitites. Based on Sr-Nd-Pb isotopic studies, they argued for a Reunion plume-type component in the source of these alkaline silicate rocks and carbonatites. Viladkar reported high BaO (up to 7.43wt%) and SrO (up to 1.95 wt%) contents in sanidines in phonolites from the SDK complex. A melanephelinite flow (~66.3 Ma) reported by Sheth et al. (2017) was rich in clinopyroxene and nepheline.

Petrography and mineral chemistry for a few 89-86 Ma SDK rocks have been discussed by Sheth et al. (2017). Syenites are composed primarily of alkali feldspar with minor amphibole, mica, Fe-Ti oxides, titanite, and zircon minerals. The feldspars are albitic and micas are phlogopitic in composition. Abundant clinopyroxene, nepheline with minor perovskite, sodalite, and mica constitute the nephelinite. The clinopyroxenes are diopsides. Phonolites are rich in alkali feldspar (K-rich) and clinopyroxene (aegirine rich).

In spite of a number of earlier studies reporting emplacement ages for alkaline rocks in the SDK complex, the emplacement age of the carbonatite remained unknown, and hence, the relationship of carbonatites with the alkaline silicates. Similarly, not all varieties of alkaline rocks were dated, which created difficulty in establishing the timings of various intrusive and extrusive activities in the complex and their geodynamic implications. Given the location of the complex, regional structural association, spatiotemporal association with Deccan Traps, and complexity of rock associations within the complex, a detailed geochronological, geochemical, and Sr-Nd-Pb isotopic investigation was a necessity to understand the origin of the complex and nature of the mantle sources for different magmatic activities.

2.4. Carbonatites

The SDK carbonatite-alkaline complex is the first carbonatite-hosted REE deposit discovered in India (Bhushan and Kumar, 2013). The types of carbonatites in the SDK complex and their mineralogy, micro-textures, mineral chemistry, and REE content have been reported in Bhushan and Kumar (2013) and Bhushan (2015). The SDK carbonatites are dominantly calciocarbonatites, with minor ferrocarbonatites. Besides calcite as the most abundant mineral constituent, these carbonatites contain apatite, K-feldspar, biotite, Fe-Ti oxides, magnetite, strontianite, barite, and borates (Bhushan and Kumar, 2013; Bhushan 2015). The REE-rich carbonatites contain REE-rich minerals, such as Carbocernaite (Ce), bastnaesite (La), synchisite (Ce), parisite (Ce), ancylite (Ce), and cerianite (Ce), which are highly enriched in LREEs. Available C and O isotopic data from the carbonatites of the complex confirm the magmatic nature of these rocks and suggest differentiation through fractional crystallization (Chandrasekaran and Srivastava, 1992; Ray and Ramesh, 1999; Ray and Ramesh, 2006). It has been suggested that these carbonatites have fractionally crystallized from a H_2O-CO_2 rich carbonate melt at ~800^{o}C that gave rise to the correlated variation observed in the $\delta^{13}C$ versus $\delta^{18}O$ in primary carbonatites (Ray and Ramesh, 2006). Ray and Ramesh (2006) also suggested that the SDK carbonatites showing much $\delta^{18}O$ >15‰ are the result of secondary or low temperature (50-100^{o}C) alteration by CO_2-bearing meteoric/hydrothermal water.

Upadhyay et al. (2021) presented macrotextures of hematite, hosting REE phases, in the SDK carbonatites and showed that non-redox transformation of primary magnetite to hematite might have facilitated the precipitation of REE-bearing minerals (e.g., bastnaesite, parasite, synchisite) in hematites by hydrothermal fluids. Aranha et al. (2022) developed a GIS-based model for mineral exploration targeting REE deposits in the SDK region. Bhunia et al. (2022) reported a U-Pb age of 66.1±1.4 Ma (2σ) and a mean $^{206}Pb/^{238}U$ age of 68.4±1.8 Ma (2σ) for three zircon grains from single carbonatite from the SDK complex and suggested a Reunion plume origin for the carbonatites. A few Sr-Nd-Pb isotopic data from the SDK complex indicate that the isotopic variations in the carbonatites are the result of Reunion plume interaction with the Indian subcontinental lithospheric mantle (Simonetti et al., 1998).

In spite of the above studies, multiple aspects of the SDK carbonatites remain unknown, viz., age of carbonatites, nature/reason of their association with alkaline silicate rocks; mode of origin, nature of the mantle source, nature of their relationship with the Deccan flood basalts etc. Therefore, a detailed geochemical and C-O-Sr-Nd-Pb isotopic study of the SDK carbonatites was required.

2.5. Origin and evolution of the complex

Based on the ^{40}Ar-^{39}Ar age (68.57 Ma), $^{3}He/^{4}He$ ratio (12.6 R_A), and $(^{87}Sr/^{86}Sr)_i$ (0.70449) for an alkali pyroxenite from the SDK complex, Basu et al. (1993) had proposed a lower mantle (Reunion plume) source for the origin of the alkaline magmatism in the complex that pre-dated the Deccan flood basalt eruptions. Based on a few Sr-Nd-Pb isotopic data, Simonetti et al. (1998) invoked plume-lithosphere interaction for the origin of the Sarnu-Dandali-Kamthai (previously known as Barmer) carbonatite-alkaline complex. These authors, based on geochemical modeling, had suggested a garnet lherzolite source for the origin of the melilitites of the complex. Chatterjee (2021) suggested that the primary magma for the Sarnu-Dandali alkaline rocks probably originated by < 5% melting of a Ti-rich mantle. Except for these few studies, there have been no detailed investigations to understand the origin of the multiple episodes of alkaline activities in the complex, reasons for the coexistence of carbonatites and alkaline silicate rocks, nature of carbon in carbonatites (primordial/recycled) and the nature of sources lithospheric/plume for these activities, given that they appear to form part of the extended Deccan Igneous Province.

Table 2.1. Summary of reported ^{40}Ar-^{39}Ar ages for the Sarnu-Dandali-Kamthai complex

Sample	Description	Plateau/Isochron Age ±2σ Ma		Reference
Sarnu #C11	biotite from alkali pyroxenite	68.57	0.08	Basu et al. (1993)
SD 13	peralkaline syenite	88.9	0.5	Sheth et al. (2017)
SD 14	nephelinite	86.8	0.5	
SD 19	phonolite	88.1	0.5	
SD 20	syenite	88.2	0.5	
SD 01	rhyolite	87.3	0.5	
SD 11	melanephelinite	66.3	0.4	
Bt_3_1_SDL	phlogopite xenocryst from alkaline lamprophyre	68.2	1.0	Dongre et al. (2022)
Bt_3_3_SDL	phlogopite xenocryst from alkaline lamprophyre	65.4	1.5	
Bt_4_3_SDL	phlogopite xenocryst from alkaline lamprophyre	70.2	1.6	
Bt_4_4_SDL	phlogopite xenocryst from alkaline lamprophyre	67.5	0.9	

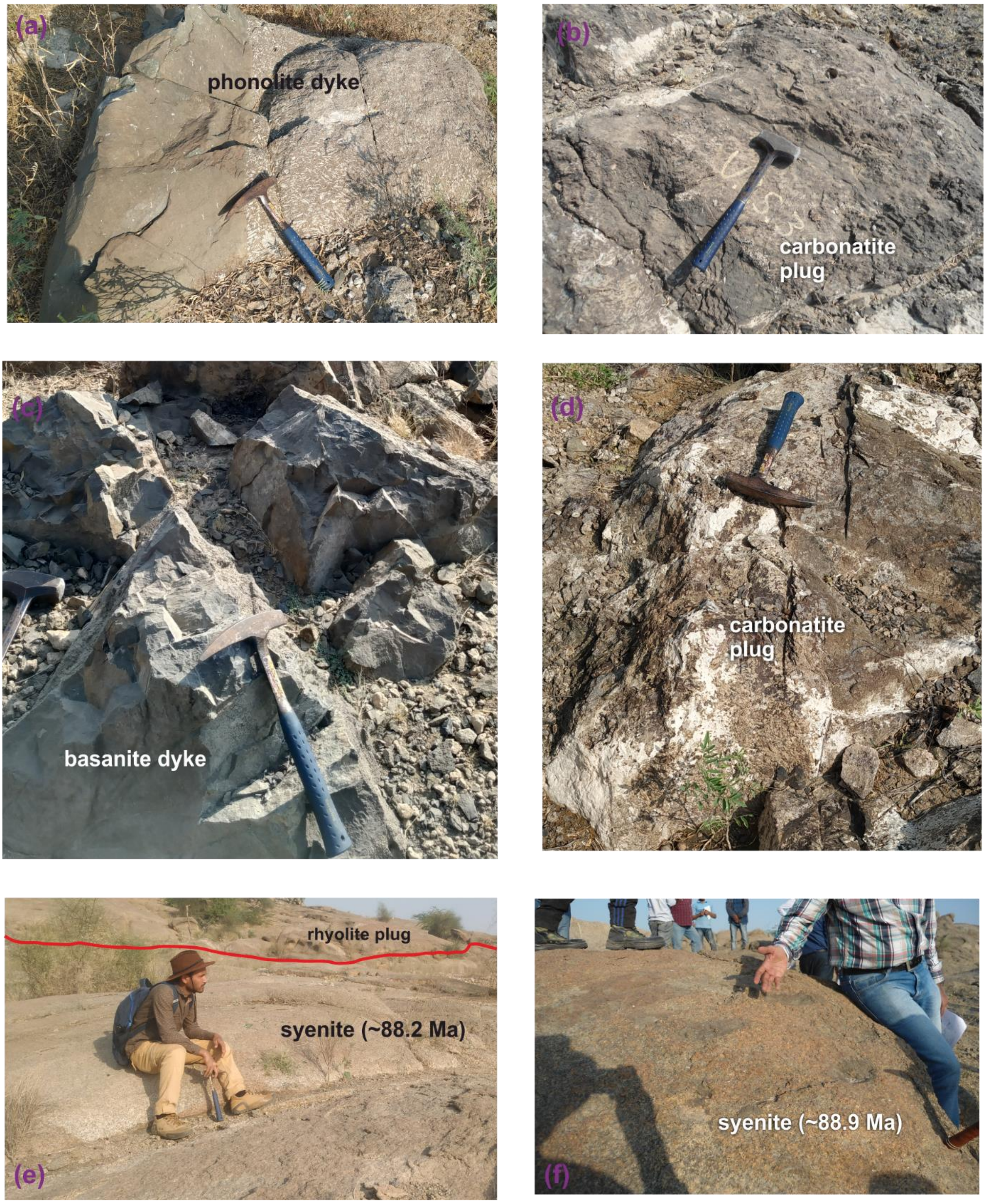

Fig. 2.2. Field Photographs: (a) Phonolite dyke containing coarse-grained alkali feldspar and exhibiting porphyritic (on the right side of the outcrop) and aphanitic textures; (b) Carbonatite plug with a dark-colored altered surface; (c) NW trending fine-grained basanite dyke exposed near Kamthai; (d) Brown colored carbonatite plug locally containing white alteration patches; (e) A plutonic syenite body, exposed near a rhyolite plug, contains coarse-grained alkali feldspar crystals and has been dated to be ~88.2 Ma (Sheth et al., 2017); (f) A syenite, dated to be ~88.9 Ma (Sheth et al., 2017), contains coarse-grained K-feldspar crystals.

Chapter 3

Samples and Methods

3.1. Field studies and Sampling

Samples for this thesis work were collected during three field visits to the Sarnu-Dandali-Kamthai alkaline-carbonatite complex, Rajasthan, in 2018, 2020, and 2021. A reconnaissance survey was carried out during our first field visit as part of a workshop organized by the Geological Survey of India (GSI) and Atomic Minerals Directorate (AMD). The study area is largely covered with wind-blown sediments with a limited number of good rock exposures. Figure 3.1a shows a map of the Sarnu-Dandali-Kamthai (SDK) complex, containing the field information. Alkaline silicate rocks, such as syenite, nephelinite, phonolite etc., constituting more than 90% by volume of the complex, occur as dykes/dykelets, plugs, and pluton, whereas carbonatites occur as minor dykes, veins, plugs, and sills. Most dykes of the complex trend

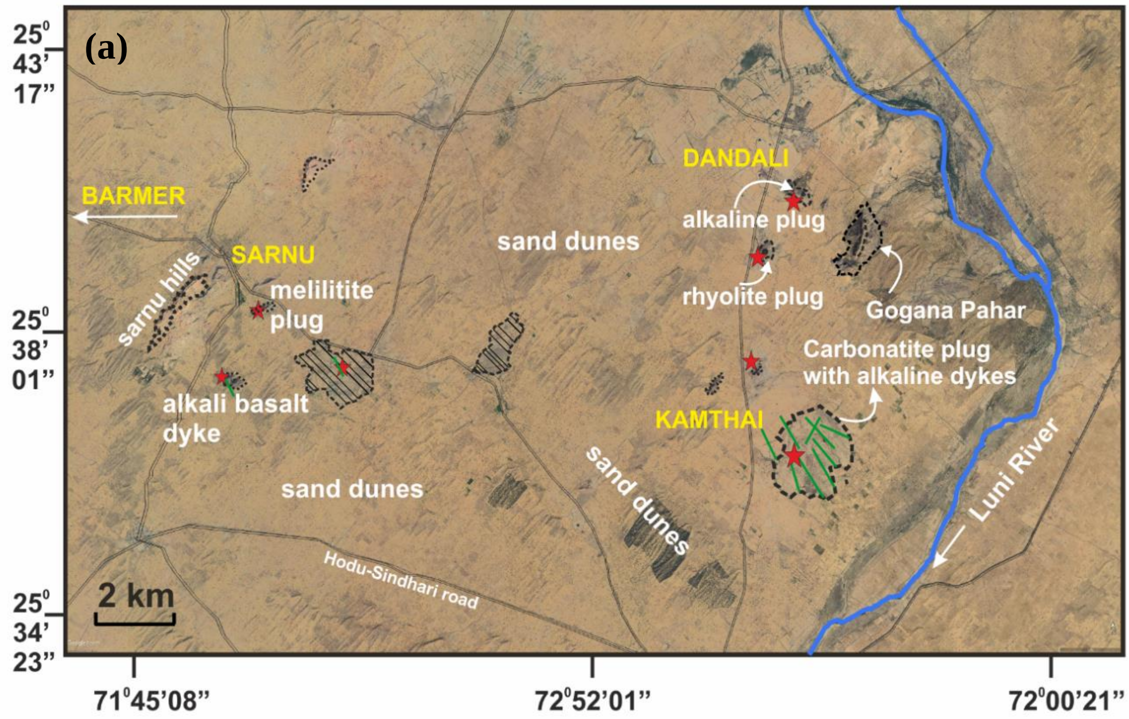

Fig. 3.1. (a) Google Earth image of the SDK complex, showing the distribution of carbonatites, alkaline plugs/dykes, and low hills exposed in a largely sand-covered terrain. Also shown are the locations of Sarnu, Dandali, and Kamthai villages, roads (thin lines), the Luni River, and the sampling locations (marked in red stars).

Fig. 3.2. Field photographs of carbonatite and alkaline silicate rock outcrops in the Sarnu-Dandali-Kamthai complex. (a) Biotite megacrysts within the carbonatite (C) and contact between carbonatite and melanephelinite (MN) dyke; (b) carbonatite plug, weathering gives it a leopard skin-like appearance; (c) a carbonatite dyke, intruding a melanephelinite dyke; (d) a phonolite (PH) dykelet, intruding a melanephelinite (MN) dyke; (e) xenolith of phonolite within a melanephelinite (MN) host dyke; (f) a phonolite (PH) dyke (>1 km), trending NE-SW near Kamthai.

NE-SW, though a few NE-SW trending dykes are also present. In outcrops where carbonatite and alkaline silicate rocks occur together, the former is often found intruding the latter. However, instances of alkaline silicate rock veins intruding the carbonatites of the complex have also been reported (e.g., Chandrasekaran et al., 1990), which suggests that the alkaline magmatism preceded and succeeded the carbonatite magmatism in the complex.

Samples for my work were collected from outcrops of both the alkaline silicate rocks and carbonatites of the complex as well as the country rocks. Care was taken to avoid Sampling from the (visibly) altered parts of the rocks. Similarly, Sampling was done from the distal parts of the alkaline silicate rocks that are intruded by carbonatite veins to avoid the influence of carbonatites. A total of 47 representative silicate rocks (e.g., phonolite, melanephelinite, nephelinite, tephrite, basanite, alkali basalt, syenite, phonotephrite, and rhyolite) and 35 carbonatite rock samples were collected. Sample details are presented in *Table 3.1*

3.2. Petrography

3.2.1. Thin sections and XRD

Petrographic studies of carbonatites and alkaline silicate rocks were done to identify minerals present, study textures, and establish paragenesis. Polished thin sections of rocks were prepared and studied under a camera-mounted Olympus BX53M petrological microscope. Different minerals were identified, and their sizes were measured. The photomicrographs of the samples with their petrographic descriptions have been provided in Chapter 4. X-Ray Diffraction (XRD) studies were carried out for selected carbonatites and alkaline silicate rocks to confirm minerals identified from thin sections and to classify the carbonate minerals. ~2g of fine rock powder (diameter ≤ 50 µm) for each sample was loaded on the metal holder of an XRD (D2 PHASER, Bruker®) installed in the Physical Research Laboratory. The XRD instrument with a Cu target (λ =1.54056 Å) and Ni filter was operated at 30 Kv voltage and 20 mA current. The diffraction patterns were compared with the ICDD databases for mineral phase identification. The results of XRD analyses are given in Chapter 4.

3.2.2. In situ Chemical Analyses

In-situ chemical analysis of the minerals of carbonatite and alkaline silicate rocks was carried out using a CAMECA SX-Five EMPA (Electron Micro-Probe Analyzer) at the National Centre for Earth Science Studies (NCESS), Trivandrum. The instrument was operated at a voltage of 20 kV and a current of 20 nA with a Lanthanum Hexaboride filament. The thin polished sections of rock samples were coated with 20 nm thin layer of gold for EPMA analysis. The concentration of major and minor elements, Si, Al, Na, K, Mg, Fe, Ti, Ca, Mn, P, F, and trace elements Rb, Sr, Ba, Nb, and REEs were determined in selected phenocryst phases (calcite, clinopyroxene, apatite, K-Na feldspar, Ca feldspar, apatite, magnetite, and biotite) as well as in the groundmass. The calibrations were carried out at an acceleration voltage of 20kV and beam current between 20nA and 200nA using element standards provided by CAMECA-AMETEK. The details of the calibration of the standards and X-ray lines for the respective elements can be found in Sorcar et al. (2021). Data acquisition, quantification, and processing were carried out using Sx-SAB version 6.1 and SX-Results software by CAMECA. BSE (Back Scattered Electron) images were also taken for microtextural study. The chemical composition of the analyzed phases, along with backscattered electron images, are given in Chapter 4.

3.3. Analytical Methods

This section describes the analytical methods followed to obtain geochemical and isotopic data for this work.

3.3.1. ^{40}Ar-^{39}Ar dating

For the determination of the age of emplacement of the younger phases of alkaline magmatism of the Sarnu-Dandali-Kamthai (SDK) complex, we choose the ^{40}Ar-^{39}Ar dating method. The older phase of alkaline magmatism had already been dated to 89-86 Ma by Sheth et al. (2017). The details of ^{40}Ar-^{39}Ar dating have been given by Dalrymple and Lanphere (1971), McDougall and Harrison (1988), and Dalrymple (1991). In this method, ^{39}K atoms in a sample to be dated are converted to ^{39}Ar by irradiating it with thermal and fast neutrons in a nuclear reactor. The age is calculated by the following equation:

$$t = (1/\lambda)^* \ln [(^{40}Ar^*/\ ^{39}Ar)^*J+1] \qquad (3.1)$$

Where λ refers to the total decay constant of ^{40}K and has a value of 5.543×10^{-10} y^{-1}. J is the irradiation parameter, defined as

$$J = (\lambda/\ \lambda_e)^* [(^{39}K/^{40}K)^* (\Delta T)^* \int\Phi(\varepsilon)\sigma(\varepsilon)\, d\varepsilon \qquad (3.2)$$

where λ_e refers to the decay constant for decay of ^{40}K to ^{40}Ar by electron capture, ΔT is the duration of irradiation, $\Phi(\varepsilon)$ is the neutron flux density at energy ε, and $\sigma(\varepsilon)$ is the capture cross-section of ^{39}K of neutrons at energy ε.

About 25g of fresh rock chips were cut out from rock samples. Care was taken to avoid weathered parts, domains having altered/secondary minerals/veinlets etc. Chips were ground and sieved to uniform grain sizes (~250µm). In addition, biotite separates from a tephrite and a carbonatite vein, and sanidine-separate from a phonolite were carefully picked powdered samples. The rock chips and mineral grains were ultrasonicated in milli-Q water followed by 10% acetic acid (to remove carbonates) for 10 minutes each and dried. About 200 mg of each sample were packed in aluminum capsules, kept inside a 0.5 mm thick cadmium cylinder, and sent for neutron irradiation. The Minnesota hornblende reference/standard material (MMhb-1) of age 523.1 ± 2.6 Ma (Renne et al., 1998) was used as a flux monitor, and high-purity CaF_2 and K_2SO_4 salts were used for interference corrections arising from production of Ar from isotopes of Ca and K, respectively. High-purity nickel wires were placed in the sample/standard capsules to monitor the neutron fluence variation. The neutron irradiation was performed in the heavy-water moderated DHRUVA nuclear reactor at the Bhabha Atomic Research Center (BARC), Mumbai, for ~120 hours.

The irradiated samples were heated incrementally from ~600^{o}C to 1400^{0}C, at steps of 50/100 °C, in an ultra-high vacuum furnace in a Thermo Fisher Scientific noble gas extraction system. Argon gas was extracted during each step and passed through Ti-Zr getters for purification. Isotopic ratios of $^{40}Ar/^{39}Ar$, $^{37}Ar/^{39}Ar$, and $^{36}Ar/^{39}Ar$ of the purified Argon gas were measured in a Thermo Fisher Argus mass spectrometer at the Department of Earth Sciences, Indian Institute of Technology Bombay in a Thermo Fisher ARGUSVI multi-collector mass spectrometer. System blanks were measured at regular intervals before and during the analysis of each sample. The measured $^{40}Ar/^{39}Ar$ was corrected for atmospheric ^{40}Ar using an atmospheric $^{40}Ar/^{36}Ar$ ratio of 295.5. The mean values for the interference correction factors $(^{36}Ar/^{37}Ar)_{Ca}$, $(^{39}Ar/^{37}Ar)_{Ca}$, and $(^{40}Ar/^{39}Ar)_{K}$ were 0.003169, 0.005355, and 0.002805, respectively, for our analyses. Fluence-corrected J values (based on ^{60}Co activity on irradiated Ni wires) for J values for each sample are given in *Table 4.1* (Chapter 4).

3.3.2. Geochemical Analyses

Whole rock samples were processed for geochemical and isotopic characterization. Fresh rock samples were broken into chips of size < 3-4 cm using a jaw crusher and homogenized. ~250-300g of fresh rock chips of each sample were cleaned ultrasonicated in milli-Q water for 10 minutes to remove any secondary particles adsorbed on the rock surfaces and dried overnight at 80^0C. These chips were powdered using a TEMA vibratory disk mill. The cup was cleaned and conditioned before powdering each sample to avoid contamination. Coning and quartering method was followed to select the representative fraction (~60g) of the powder for geochemical analyses.

A. Major element Analyses

Prior to the measurement of major element contents, Loss on Ignition (LOI) was determined. About 6g of powder of each sample was heated overnight at ~110^0C to remove moisture) and kept in a desiccator to avoid the re-absorption of moisture. LOI was determined by heating ~1g accurately weighed sample powder in a preheated muffle furnace (Thermo®) at 1050^0C for 2 hours and calculating the loss of weight in percentage. About 4g of sample powder was mixed well with ~1g of wax binder (Chemplex®) in an agate mortar. The mixture was transferred to a 37mm standard aluminum cup and pressed in a compressor at a pressure of 200KN/m^2 for 10 seconds to make a pressed pellet for XRF. Pellets of 16 international rock standards: BHVO-2, BCR-2, JB-2, STM-1, AGV-2, JGB-2, G-2, JG-2, JSY-1, MUH-1, JLS-1, JDO-1, COQ-1, were also prepared in the same manner to be used as calibration standards (*Table 3.2*). The concentrations of major and minor oxides, Na, K, Fe, Mg, Al, Ca, Si, Mn, and P (in wt%) and selected trace elements, Rb, Sr, Zr, and Ba (in ppm), were measured on XRF using a calibration protocol involving multiple international standards (Potts 1987).

Fig.3.3. Photograph of the X-Ray Fluorescence Spectrometer (Rigaku® Supermini 200) installed at the Physical Research Laboratory, Ahmedabad.

The measurements were carried out in an X-Ray Fluorescent (XRF) spectrometer (Rigaku®) *(Fig 3.3)* at Physical Research Laboratory, Ahmedabad. The instrument was operated at a potential of 50 kV, and the P10 gas flow rate was 24.7mL/min. During the measurements, international standards BHVO-2, BCR-2, and COQ-1 were also analyzed as unknowns to check for the accuracy and precision of measurements. The precision of measurements determined by repeated analyses of the standards was better than 2% at the 2σ level. The measured and reported concentrations show excellent agreement (*Table 3.3*). Alkaline silicate rocks were analyzed using a calibration method that reproduced BHVO-2 and BCR-2, whereas carbonatites were analyzed using a calibration method that reproduced COQ-1.

B. Trace element Analyses

Contents of trace elements (< 0.1 wt%) in the alkaline silicate rocks and carbonatites were measured in dissolved sample solutions using a Thermo^{TM} Q-ICPMS at PRL Ahmedabad *(Fig. 3.4)*. The instrumental parameters and operating conditions of the analysis are provided in *Table 3.4*. Sample solutions were in 2% HNO_3 (v/v). Two separate digestion procedures were followed for alkaline silicate rocks and carbonatites; those are outlined in *Tables 3.6* and *3.7*, respectively**.** The powdered samples were digested in precleaned (by acid) vials (Savillex, US) in a Clean Chemistry Lab at PRL, Ahmedabad. All acids used during the digestion of the samples were ultrapure trace-grade acids (from Fluka, US; Seastar®, Canada). After digestion, the diluted sample solutions were prepared in 2% HNO_3 with dilution factors (DF) ranging between ~5,000 and ~20,000 for alkaline silicate rocks and 4,000 and 4,00,000 for carbonatites.

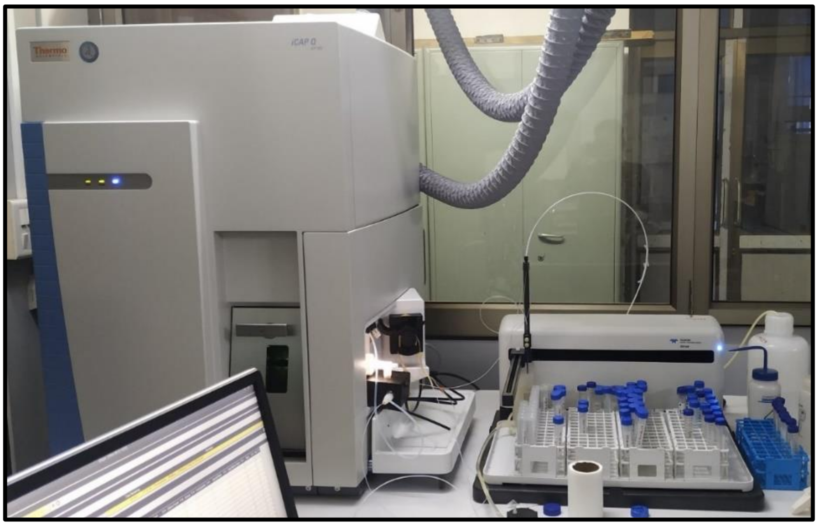

Fig. 3.4. Photograph of the Quadrupole ICPMS (Thermo® iCAP) at Physical Research Laboratory, Ahmedabad

The standard solutions of AGV-2 with DF between 4000 and 20000 were used for the calibration, and BHVO-2 and COQ-1 were analyzed as unknowns for accuracy and precision checks of our measurements. Typical calibration curves for a few elements are given in *Fig. 3.5*. The reproducibility of our measurements, determined from repeated analyses of BHVO-2 and COQ-1, was better than 2% for REEs and 5% for other elements at the 2σ level. The detection limit for REEs was 0.0003 ppb, and for other trace elements was 0.006 ppb.

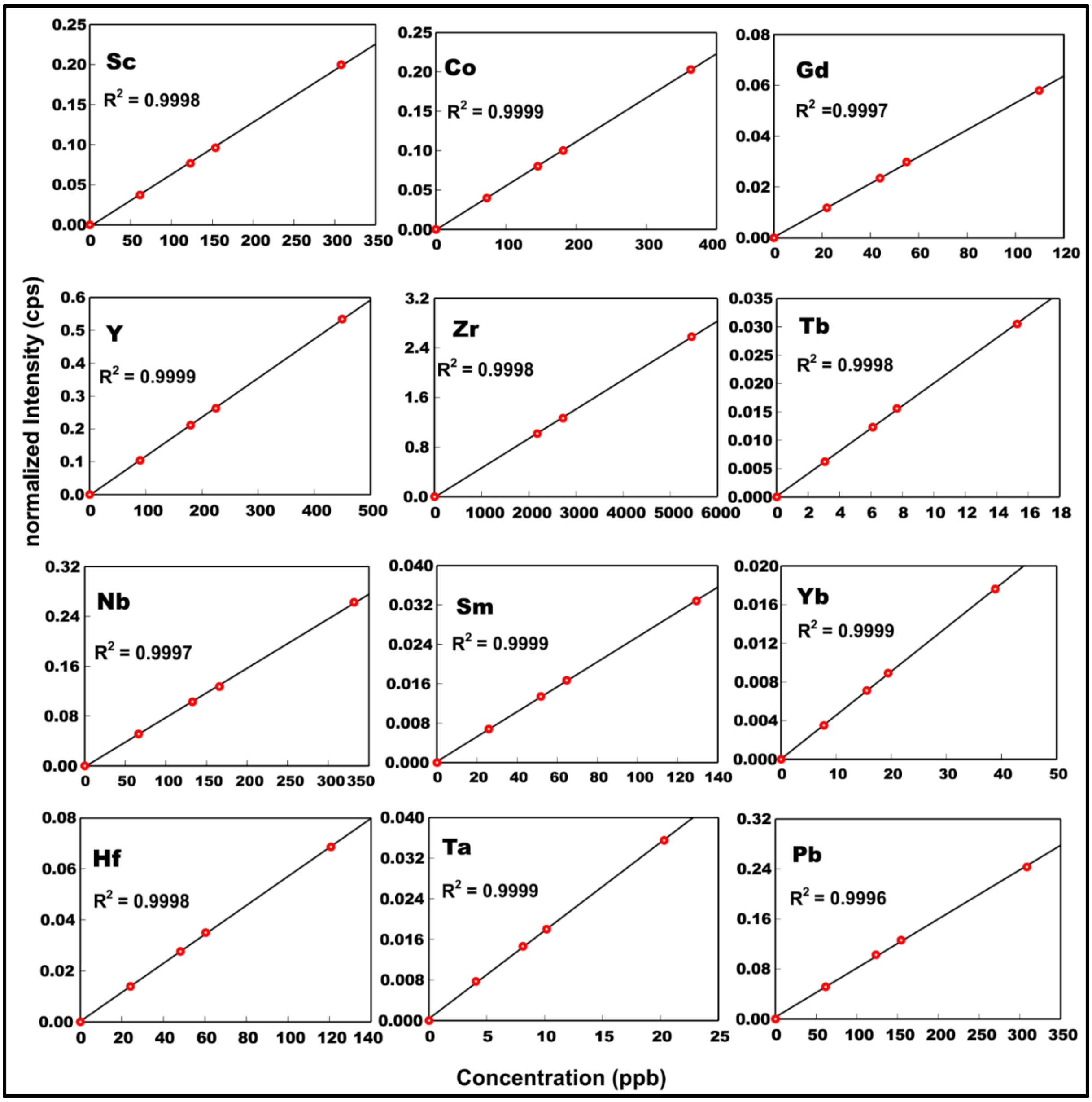

Fig. 3.5. Typical calibration curves for selected trace elements obtained using various dilutions of an international rock standard, AGV-2, during the measurement of trace element concentrations in Q-ICPMS.

The measured concentrations of BHVO-2 and COQ-1, compared with their reported concentrations in *Table 3.5*, are in excellent agreement with the reported values.

3.3.3. Isotope Geochemistry

A. Stable C-O Isotopic compositions

Stable C and O isotopic compositions of carbonates in carbonatites/ alkaline silicate rocks were measured at PRL using an Isotope Ratio Mass Spectrometer (IRMS). Samples used for this purpose were either fine-grained whole rock powders or powders of carbonate phases collected by means of micro-drilling from hand specimens. The measured C and O isotopic compositions are expressed in δ notation relative to a standard in permille (‰). By definition

$$\delta^{13}C_{V\text{-}PDB} = [(^{13}C/^{12}C)_{sample} / (^{13}C/^{12}C)_{V\text{-}PDB} - 1] \times 10^3$$

$$\delta^{18}O_{V\text{-}SMOW} = [(^{18}O/^{16}O)_{sample} / (^{18}O/^{16}O)_{V\text{-}SMOW} - 1] \times 10^3$$

where V-PDB (Vienna Pee Dee Belemnite) and V-SMOW (Vienna Standard Mean Ocean Water) are the standards used for C and O, respectively.

Since the carbonates of carbonatites and alkaline silicate rocks of SDK complex were composed primarily of calcites (>90%), as revealed by the powdered XRD (X-ray Diffraction) method, the samples were treated as pure calcites for the dissolution protocol, before mass spectrometry. About 10-20 mg of sample powder was taken in a tube and flushed with N_2 gas in a Kiel IV carbonate device to remove atmospheric gases from the tube. Anhydrous ortho-phosphoric acid (100% H_3PO_4) was then added to the sample and reacted at 71^0C for 45 minutes to allow the completion of the decarbonation reaction and release of CO_2 for isotopic measurements. The abundance ratios of CO_2 isotopologues (44,45 &46) were measured in the samples with respect to those for a laboratory reference CO_2 in dual inlet mode in a Thermo MAT 253 isotope ratio mass spectrometer. An in-house carbonate standard of known isotopic composition, MMB (Makrana Marble), was also analyzed after every 8 samples to calibrate the reference CO_2. $\delta^{13}C$ and $\delta^{18}O$ were calculated from $\delta^{45}$and δ^{46} using the Craig correction equation (e.g., Craig, 1957). International standard NBS-19 and internal standard MMB were analyzed repeatedly to check the accuracy and precision of the analytical data *(Table 3.8).*

B. Sr-Nd-Pb isotopic compositions

For Sr-Nd-Pb isotopic analyses, the samples were first dissolved and made into solutions before being processed for column chemistry to separate the elements of interest for mass spectrometry. The dissolution protocols followed for alkaline silicate rocks and carbonatites are given in *Tables 3.9* and *3.10*, respectively.

For Pb isotopic analyses, the silicate samples were dissolved following the procedures in *Table 3.9*. The dissolved silicate sample in 6N HCl (after step 9; *Table 3.9*) was dried down at 100^0C and added with 100µl HBr (9N) and kept overnight on a hotplate at 80^0C. The solution was dried at 100^0C, and step 10 was repeated two more times to ensure the complete conversion of the sample into bromide form. The dried sample was taken back into solution in 1.5ml of

0.7N HBr acid and processed for Pb column chemistry (*Table 3.14*). A similar procedure was followed for carbonatites after step 9 in *Table 3.10*.

Fig. 3.6. Photograph of the Thermal Ionization Mass Spectrometer (Thermo® Triton Plus) used for analytical work.

Sr and REE cuts were collected through a primary cation exchange column chemistry procedure *(Table 3.11)*. The Sr cuts of carbonatites were dried down and taken in 1 ml of 3N HNO_3 to proceed for further Sr purification by Sr-specific column chemistry *(Table 3.12)*. The REE cuts collected through the primary column were dried and taken in ~100µl of 0.18N HCl to process for Nd separation by anion exchange column chemistry *(Table 3.13)*. For Pb column chemistry, the silicate and carbonatite samples, after digestion in respective methods *(Tables 3.8, 3.9)*, were further treated with ~100µl of 9N HBr and dried at 80^0C. This step was repeated two times more to ensure the complete conversion of the sample into bromide form. Finally, the dried sample was taken in 0.7N HBr (1.5 ml) before processing for Pb column chemistry *(Table 3.13)*.

Sr, Nd, and Pb isotopic ratio measurements were performed on a Thermo Scientific^{TM} Triton Plus Thermal Ionization Mass Spectrometer (TIMS) *(Fig. 3.6)* at PRL, Ahmedabad. Chemically separated Sr from the samples were loaded on top of the preloaded 0.1M ultrapure H_3PO_4 on single-degassed and oxidized Ta filaments in dilute HNO_3 (2N). Similarly, the preconcentrated Nd was loaded on top of the double-degassed Re filaments (99.90% Re) in dilute HCl (2N), and Pb was loaded on the bed of the preloaded ultrapure silica gel – H_3PO_4 mixture on the degassed single-zone refined Re (99.99% Re) filaments. Sr, Nd, and Pb isotopic ratio measurements were performed in static multicollection mode with an idle time of 3s and an integration time of 8.389s. For Sr, Isobaric interference of ^{87}Rb on ^{87}Sr was corrected using ^{87}Rb /^{85}Rb = 0.386. All the measured Sr isotopic ratios were corrected for instrumental mass fractionation using an exponential fractionation (internal) correction (Thirlwall 1991a), assuming the true value of ^{88}Sr/^{86}Sr = 8.375209. Accuracy and precision of Sr isotopic measurements were checked through multiple measurements of the international Sr standard SRM-987 (NIST), which yielded a value of ^{87}Sr/^{86}Sr = 0.710249 ± 0.000009 (2σ; n=14), which is in good agreement with the NIST certified value (^{87}Sr/^{86}Sr = 0.710236 ± 0.00052 (2σ)). The USGS Rock standard BHVO-2 was also analyzed to check the accuracy of our measurements, which yielded a value of ^{87}Sr/^{86}Sr = 0.703479 ± 0.000002 (2σ; n=7), which is well within its reported value of ^{87}Sr/^{86}Sr = 0.703478 ± 0.000068).

For Nd, an exponential fractionation (internal) correction assuming the true value of ^{146}Nd/^{144}Nd = 0.7219 was performed to correct the instrumental mass fractionation (Thirlwall 1991a). The measurements of international Nd standard, JNdi-1, in our lab yielded ^{143}Nd/^{144}Nd = 0.512102 ± 0.000010 (2σ; n=17). Six measurements of BHVO-2 gave an average of ^{143}Nd/^{144}Nd = 0.512972 ± 0.000003 (2σ), which is well within its reported values of 0.512981 ± 0.000010 (2σ; Weis et al., 2006). Measured Pb isotope data were corrected for Instrumental mass fractionation using a linear fractionation factor of 0.101% per amu (Wasserburg et al., 1981) and assuming the true Pb isotopic ratios (^{206}Pb/^{204}Pb, ^{207}Pb/^{204}Pb, and ^{208}Pb/^{204}Pb) for NBS-981 (NIST) standard from Todt et al. (1996). Repeated (n=10) measurements of an international Pb standard, NBS-981, yielded external reproducibility (2σ) of 0.012, 0.013, and 0.027 for ^{206}Pb/^{204}Pb, ^{207}Pb/^{204}Pb, and ^{208}Pb/^{204}Pb, respectively, with 2SE (Standard Error) reproducibility of 0.004, 0.004, and 0.009, respectively. The total procedural blank obtained during our measurements for Sr was < 400 pg, Nd was < 150 pg and Pb was < 100 pg.

Table 3.1. Field descriptions of samples collected from the Sarnu-Dandali-Kamthai complex, Rajasthan

Sample#	Location	Description
KT-18-1C	N25.632, E71.927	coarse-grained, banded, and coarse-grained calcite carbonatite plug, alternately white and dark-colored bands.

KT-18-2C	N25.632, E71.927	dark brown colored, fine-grained calcite carbonatite dyke
KT-18-3	N25.633, E71.862	leucocratic, porphyritic phonolitic dyke containing K-feldpsar megaphenocrysts
KT-18-4C	N25.633, E71.862	dark brown colored carbonatite plug shows patches of dissolved and reprecipitated carbonate (earthy brown colored), appears like a panther's skin
KT-18-5C	N25.634, E71.930	dark brown colored carbonatite plug shows patches of dissolved and reprecipitated carbonate (earthy brown colored), appears like a panther's skin
KT-18-6	N25.636, E71.930	fine-grained, melanocratic melanephelinite dyke; groundmass contains carbonate
KT-18-7C	N25.636, E71.930	carbonatite dyke containing coarse biotite megacrysts; Intrudes a melanephelinite dyke (KT-18-6).
KT-18-8C	N25.636, E71.930	carbonatite dyke containing abundant coarse white calcite minerals with partly brown-colored minerals
KT-18-9	N25.636, E71.929	leucocratic, porphyritic rock containing megaphenocrysts of K-feldpsar(sanidine), the largest dyke in the region (> 1 km)
KT-18-10C	N25.638, E71.932	fine-grained, brown-colored carbonatite veins; intrudes melanephelinite dyke
KT-18-11	N25.638, E71.932	fine-grained, melanocratic melanephelinite dyke; intruded by carbonatite veins (KT-18-10C)
KT-18-12	N25.648, 71.912	leucocratic, aphanitic phonolite dyke; intrudes the Malani rhyolites (country rock), exposed 1 km north of Kamthai village
KT-18-13	N25.648, E71.912	leucocratic, aphanitic phonolitic dyke; intrudes syenite pluton (KT-18-14), exposed north of Kamthai village, exposed near Evadi Bhimji
KT-18-14	N25.648, E71.912	Syenite pluton containing coarse-grained feldspars
KT-18-15	N25.664, E71.788	fine-grained, melanocratic melilitite lava; contain phenocrysts of melilite, clinopyroxene; groundmass doesn't contain carbonate; collected near Sarnu.
KT-20-1	N25.634, E71.921	leucocratic, porphyritic phonolite dyke; contains K-feldpsar phenocrysts; exposed near Kamthai
KT-20-2	N25.634, E71.921	aphanitic, melanocratic melanephelinite dyke; contains carbonate

KT-20-3C	N25.634, E71.922	fine-grained, light gray colored carbonatite dyke
KT-20-4	N25.634, E71.922	Porphyritic, melanocratic melanephelinite dyke containing phenocrysts of feldspathoids, top surface is vesiculated; contains carbonate
KT-20-5	N25.634, E71.922	melanocratic, porphyritic phonolite dyke; contains K-feldpsar phenocrysts; exposed near Kamthai
KT-20-6C	N25.632, E71.927	Coarse-grained calcite carbonatite plug, contains white and dark calcite bands
KT-20-7C	N25.634, E71.929	brown colored carbonatite dyke with earthy white alteration patches; intrudes alkaline silicate rocks
KT-20-9C	N25.634, E71.929	Coarse-grained calcite carbonatite dykelet, consists of alternate white and dark brown bands; intrudes melanephelinite dyke, trend- 450^0
KT-20-10	N25.634, E71.929	aphanitic, melanocratic melanephelinite dyke; groundmass contains carbonate; intruded by KT-20-9C.
KT-20-11C	N25.634, E71.929	buff-colored, coarse-grained carbonatite vein intruding a melanephelinite dyke
KT-20-12	N25.634, E71.932	melanocratic, aphanitic phonolite dyke; trends in N20^0E
KT-20-13	N25.634, E71.932	melanocratic, aphanitic phonolite dyke
KT-20-14C	N25.633, E71.928	fine-grained, brown-colored carbonatite dyke with alteration patches
KT-20-15C	N25.632, E71.927	fine-grained, dark brown-colored carbonatite dyke
KT-20-16C	N25.631, E71.924	fine-grained, brown-colored carbonatite dyke
KT-20-17	N25.638, E71.926	phonolite porphyry dyke; contains megaphenocrysts of feldspar crystals
KT-20-18	N25.638, E71.926	aphanitic, felsic phonolite dyke; conjugate of the phonolite dyke (KT-20-17)
KT-20-19	N25.636, E71.931	aphanitic, melanocratic melanephelinite lava flow; top surface shows chilled and pitted texture; contains carbonate

KT-20-20	N25.636, E71.931	aphanitic, melanocratic melanephelinite lava flow; top surface shows chilled and pitted texture; contains carbonate
KT-20-21	N25.636, E71.931	aphyric and felsic phonolite dyke/dykelet
KT-20-22C	N25.637, E71.935	fine-grained, brown colored carbonatite vein; intrudes a basanite dyke
KT-20-23	N25.637, E71.934	a basanite dyke intruded by a carbonatite vein (KT-20-22C)
KT-20-24C	N25.637, E71.933	fine-grained, mesocratic carbonatite sill, intrudes a phonotephrite dyke
KT-20-25C	N25.637, E71.933	fine-grained, light-medium colored carbonatite, intrudes a phonotephrite dyke
KT-20-26	N25.637, E71.933	fine-grained phonotephrite dyke, not well exposed
KT-20-27	N25.637, E71.933	fine-grained phonotephrite dyke, not well exposed
KT-20-28C	N25.637, E71.931	fine-grained, brown colored carbonatite veins intruding a fractured melanephelinite dyke
KT-20-29	N25.637, E71.932	aphanitic, melanocratic tephrite dyke; highly fractured and intruded by carbonatite veins (KT-20-28C)
KT-20-30C	N25.637, E71.932	fine-grained, brown-colored carbonatite veins intruding a fractured melanephelinite dyke, trend- 315^0
KT-20-31	N25.637, E71.932	aphanitic, fractured tephrite dyke containing phlogopite minerals.
KT-20-33C	N25.637, E71.932	fine-grained, brown-colored late-stage carbonatite veins intruding fractured alkaline silicate rocks, contains silica veins
KT-20-34	N25.638, E71.932	fenitized phonolite dyke containing abundant K-feldspar crystals concentrated along fluid migrating channels.
KT-20-35	N25.638, E71.931	fenitized phonolite dyke containing abundant K-feldpsar crystals concentrated along fluid migrating channels.
KT-20-36	N25.638, E71.931	melanocratic, aphanitic nephelinite dyke; contains carbonate

KT-20-37C	N25.639, E71.930	fine-grained, brown colored carbonatite veins intruding fractured alkaline silicate rocks, trend- 2570
KT-20-38C	N25.639, E71.930	fine grained, brown colored carbonatite vein.
KT-20-39	N25.639, E71.930	green colour, aphanitic phonolitic nephelinite; intrudes KT-20-41; does not contain carbonate
KT-20-41	N25.639, E71.930	aphanitic, melanocratic rock, contains carbonate; intruded by Phonolitic nephelinite (KT-20-39)
KT-20-42	N25.648, E71.912	rhyolite plug containing K-feldpsar phenocrysts
KT-20-43	N25.648, E71.912	rhyolite plug containing K-feldpsar phenocrysts
KT-20-44	N25.648, E71.912	felsic, aphanitic phonolite dyke; intrudes rhyolite plug (KT-20-43,44)
KT-20-45	N25.675, E71.912	syenite pluton; contains coarse-grained feldspar crystals
SAR-20-2	N25.649, E71.813	aphanitic alkali basalt dyke, develops joints
SAR-20-3	N25.648, E71.777	porphyritic alkali basalt dyke, contains megaphenocrysts of clinopyroxene
SAR-20-4	N25.648, E71.777	alkali basalt dyke, porphyritic, contains megaphenocrysts of clinopyroxene
SAR-20-5	N25.648, E71.777	porphyritic tephriphonolite dyke, contains megaphenocrysts of clinopyroxene
KT-21-1C	N25.633, E71.931	fine-grained, brown-coloured alvikite
KT-21-2	N25.629, E71.930	medium-grained phonolite dyke; contains euhedral phenocrysts of K-feldpsar
KT-21-4	N25.631, E71.933	fine-grained, melanocratic rock. It contains calcite macrocrysts.
KT-21-5C	N25.631, E71.933	coarse euhedral calcite-bearing dyke

KT-21-6	N25.631, E71.933	melanocratic melanpehelinite lava, contains phenitized veins.
KT-21-7C	N25.631, E71.933	fine-grained, mesocratic carbonatite dyke
KT-21-8C	N25.631, E71.933	fine-grained carbonatite dyke, contains phlogopite crystals
KT-21-9C	N25.631, E71.933	dark brown coloured, medium-grained carbonatite plug with weathered top
KT-21-10C	N25.631, E71.933	porphyritic, Calcite phenocrysts rich carbonatite plug
KT-21-11C	N25.631, E71.933	Coarse grained calcite carbonatite (white coloured) dyke
KT-21-12C	N25.631, E71.933	dark brown coloured carbonatite plug with alteration patches, contains calcite crystals
KT-21-13	N25.631, E71.929	jointed and fractured tephrite plug, phenitized by carbonatite veins; contains phlogopite veins
KT-21-14C	N25.631, E71.929	banded calcite carbonatite dyke with alternating coarse and fine bands
KT-21-15C	N25.631, E71.929	fine-grained, dark brown ferrocarbonatite dyke
KT-21-16	N25.631, E71.929	fine-grained, melanocratic, vesiculated melanephelinite dyke. Intruded by a phonolite dykelet (KT-21-17)
KT-21-17	N25.631, E71.929	felsic phonolite dykelet/vein intruding melanephelinite dyke (KT-21-16)
KT-21-18C	N25.633, E71.926	coarse grained, white coloured calcite carbonatite plug
KT-21-19C	N25.633, E71.926	coarse-grained calcite carbonatite plug.
KT-21-21	N25.631, E71.933	phonolite xenolith within melanephelinite lava (KT-21-6); porphyritic; contains euhedral crystals of feldspar
KT-21-22	N25.631, E71.933	phonolite xenolith hosted by melanephelinite lava (KT-21-6); contains euhedral feldspar crystals

Table 3.2: International rock standards used for XRF calibration

Rock Standards	Description	Supplier
BHVO-2	Hawaiian basalt	USGS
BCR-2	Columbia river basalt	USGS
JB-2a	Basalt from Oshima Volcano	GSJ
G-2	Granite	USGS
JG-2	Naegi Granite	GSJ
JG-3	Mitoya Granodiorite	GSJ
JSY-1	Japanese Syenite	GSJ
STM-1	Nepheline Syenite from Table Mountain, Oregon	USGS
AGV-2	Andesite from Guano Valley	USGS
MUH-1	Harzburgite	IAG
JDO-1	Kuzuu Dolomite	GSJ
JGB-2	Tsukuba-san leucogabbro	GSJ
JLS-1	Garo Limestone	GSJ
CGL-001	serpentinite	IAG
COQ-1	Oka Carbonatite	USGS
JR-1	Japanese Rhyolite	GSJ

Note: USGS: United States Geological Survey; GSJ: Geological Survey of Japan; IAG: International Association of Geoanalyst

Table 3.3: Measured and reported major oxide concentrations of BHVO-2, BCR-2, COQ-1

Major Oxide (in wt%)	BHVO-2 (measured) mean ± 1σ (n = 4)	BHVO-2 (reported) mean ±1σ	BCR-2 (measured) mean ± 1σ (n = 7)	BCR-2 (reported) mean± 1σ	COQ-1 (measured) mean ± 1σ (n = 7)	COQ-1* (reported) mean± 1σ
SiO_2	49.6 ± 0.3	49.9 ± 0.6	53.95 ± 0.10	54.0 ± 0.20	3.46 ± 0.05	3.47 ± 0.11
TiO_2	2.68 ± 0.04	2.73 ± 0.04	2.254 ± 0.002	2.265 ± 0.024	0.141± 0.008	0.150 ± 0.002
Al_2O_3	13.3 ± 0.1	13.5 ± 0.2	13.35 ± 0.10	13.48 ± 0.12	0.37 ± 0.02	0.37 ± 0.04
Fe_2O_3(t)	12.3 ± 0.2	12.3 ± 0.2	13.74 ± 0.10	13.77 ± 0.19	2.89 ± 0.07	2.94 ± 0.09
MnO	0.177 ± 0.045	0.169±0.002	0.181± 0.001	0.197 ± 0.003	0.428± 0.007	0.430 ± 0.002
MgO	7.30 ± 0.27	7.23 ± 0.12	3.58 ± 0.03	3.60 ± 0.04	1.24 ± 0.01	1.25 ± 0.03

CaO	11.4 ± 0.1	11.4 ± 0.2	6.975 ± 0.149	7.114 ± 0.075	48.3 ± 0.2	48.30 ± 0.38
Na_2O	2.29 ± 0.14	2.22 ± 0.08	3.13 ± 0.06	3.12 ± 0.04	0.04 ± 0.01	0.04
K_2O	0.47 ± 0.08	0.52 ± 0.01	1.756 ± 1.767	1.774 ± 0.019	0.15 ± 0.01	0.16 ± 0.02
P_2O_5	0.25 ± 0.01	0.27 ± 0.02	0.352 ± 0.005	0.359 ± 0.009	2.54 ± 0.09	2.6 ± 0.12

Note: * USGS

Table 3.4: Instrumental parameters and operating conditions for trace element analysis

ICPMS	
Brand and Model	Thermo™ Scientific™ iCAP ICPMS
Forward Power	1550 w
Cooling gas (Ar) flow rate	14 L/min
Auxiliary gas (Ar) flow rate	0.8 L/min
Nebulizer gas (Ar) flow rate	1.14 L/min
Interface temperature	31.49 ^{0}C
Peristatic pump speed	40 rpm
Plasma cooling water flow rate	0.5 L/min
Data Acquisition parameters	
Resolution mode	Normal
Measurement mode	STDS
Channels	1
Dwell time	0.01s
Number of sweeps	90
Detector dead time	25 ns
Sampling uptake time	90s
Wash time	90s
Scanned masses	^{45}Sc, ^{51}V, ^{52}Cr, ^{59}Co, ^{60}Ni, ^{63}Cu, ^{66}Zn, ^{71}Ga, ^{85}Rb, ^{88}Sr, ^{89}Y, ^{90}Zr, ^{93}Nb, ^{115}In, ^{137}Ba, ^{139}La, ^{140}Ce, ^{141}Pr, ^{146}Nd, ^{147}Sm, ^{153}Eu, ^{158}Gd, ^{159}Tb, ^{163}Dy, ^{165}Ho, ^{167}Er, ^{169}Tm, ^{172}Yb, ^{175}Lu, ^{178}Hf, ^{181}Ta, ^{208}Pb, ^{209}Bi, ^{232}Th, ^{238}U
Main runs	4
Calibration	External

Table 3.5: Measured and reported concentrations of the international standards BHVO-2 and COQ-1.

Analytes	BHVO-2 (measured) mean ±2σ (n = 2) (ppm)	BHVO-2 (certified*) Mean ±2σ (ppm)	COQ-1 (measured) Mean ±2σ (n=3) (ppm)	COQ-1(certified**) Mean (2σ) (ppm)
Sc	31.95 ±0.15	31.83 ±0.68	1.01 ±0.22	3 ±0.2
V	318.7 ±1.4	318.2 ±4.6	123 ±11	110 ±12
Cr	289.49 ±1.33	287.2 ±6.2	1.02 ±0.18	<10 ±NA
Co	45.23 ±0.17	45 ±0.6	2.35 ±0.20	<5 ±NA
Ni	120.92 ±1.03	119.8 ±2.4	3.71 ±0.70	13 ±2

Cu	131.53 ±0.78	129.3 ±2.8	2.05 ±0.08	<10 ±NA
Rb	9.34 ±0.08	9.261 ±0.192	13.35 ±0.02	NA
Cs	0.0994 ±0.0020	0.0996 ±0.0044	NA	NA
Ba	130.423 ±0.906	130.9 ±2	1054 ±41	1000 ±(<200)
Th	1.24 ±0.03	1.22 ±0.04	12 ±1	10 ±2
U	0.407 ±0.001	0.412 ±0.07	10 ±0.6	11 ±1.2
Nb	18.26 ±0.46	18.10 ±0.40	3882 ±59	3900 ±120
Ta	1.17 ±0.06	1.15 ±0.04	37.05 ±2.03	NA
La	15.379 ±0.264	15.20 ±0.16	714 ±15	750 ±20
Ce	37.731 ±0.254	37.53 ±0.38	1456 ±11	1700 ±NA
Pb	1.658 ±0.021	1.65 ±0.08	4.3 ±0.4	NA
Pr	5.377 ±0.050	5.34 ±0.06	150 ±5	150 ±12
Sr	399.220 ±4.887	394.1 ±3.4	11509 ±78	12000±<200
Nd	24.346 ±0.178	24.27 ±0.5	448 ±13	480 ±30
Zr	177.812 ±0.766	171.2 ±2.6	71 ±1	65 ±6
Hf	4.404 ±0.045	4.47 ±0.06	0.30 ±0.01	NA
Sm	6.051 ±0.073	6.023 ±0.114	51 ±1	56 ±4
Eu	2.021 ±0.017	2.043 ±0.024	12 ±0.4	15 ±1.2
Gd	6.186 ±0.047	6.207 ±0.076	44 ±1	50 ±2
Tb	0.925 ±0.003	0.94 ±0.02	4 ±0.1	4 ±0.2
Dy	5.305 ±0.009	5.280 ±0.056	17 ±0.6	18 ±NA
Ho	0.987 ±0.004	0.9887 ±0.0106	3 ±0.1	3 ±0.2
Y	25.900 ±0.004	25.91 ±0.56	59 ±0.4	81 ±10
Er	2.496 ±0.005	2.511 ±0.028	7.00 ±0.22	7.00 ±0.12
Tm	0.314 ±0.003	0.3349 ±0.0062	1.01 ±0.03	NA
Yb	1.994 ±0.001	1.994 ±0.054	6 ±0.2	6 ±1
Lu	0.260 ±0.002	0.275 ±0.004	0.79 ±0.04	NA

Note: * after Jochum et al., 2016; ** values reported by IUGS, Uncertainties (2σ) are given in brackets
NA: Not Available (Reported)

Table 3.6: Sample dissolution protocol followed for trace element analysis of silicate rocks

Step 1:	About 60 mg of homogenized sample powder was taken in a 17 ml PFA Savillex Teflon vial and capped.
Step 2:	~1 ml of HF + HNO_3 (2:1) acid mixture was added to the sample in the vial, ultrasonicated for 45 minutes with the cap closed, and kept overnight on a hotplate at 120^{0}C.
Step 3:	The next day, the solution was dried at 100^{0}C till the sample solution dried to a cake-like appearance.
Step 4:	~ 0.5 ml of 8N HNO_3 was added to the vial and thoroughly mixed until the sample dissolved, then dried at 120^{0}C.

Step 5:	~0.5 ml of 8N HNO_3 was added again to the sample, mixed well to check the dissolution of the sample, then dried at 120^0C.
Step 6:	If the sample was dissolved entirely, dissolution procedures in steps 6,7 and 8 were skipped. Otherwise, the sample was treated with concentrated HCl and (or) HCl +HNO_3 (3:1) and kept overnight cap-closed on a hotplate at 80^0C.
Step 7:	The next day, the solution was dried at 100^0C, and step 6 was repeated once more to ensure the complete dissolution of the sample. Then, the sample was dried at 100^0C
Step 8:	~0.5 ml of 8N HNO_3 was added to the sample and dried at 100^0C. This was repeated once more.
Step 9:	The dried sample was taken in ~1 ml of 2% HNO_3 to prepare the stock solution for ICPMS measurements.

Table 3.7: Sample dissolution protocol for trace element analysis of carbonatites

Step 1:	About 60 mg of homogenized sample powder was taken in a 17 ml PFA Savillex Teflon vial (vial 1) and capped.
Step 2:	~1 ml of 6N HCl was added to the sample and kept overnight on a hot plate at 80^0C.
Step 3:	The dissolved fraction (carbonates+apatites) was transferred to another vial (vial 2) carefully through a pipette.
Step 4:	The insoluble fraction, primarily silicates (silicate fraction: SF), was added with ~200 ml of Milli-Q water, and the clear solution was transferred to vial 2. This step was repeated once to ensure the complete removal of the soluble carbonate+apatite fraction from the SF.
Step 5:	The dissolved fraction in vial 2 was dried at 100^0C and added with ~0.5 ml of 8N HNO_3 to the vial. Then, the vial was capped and kept overnight on a hotplate at 100^0C.
Step 6:	The solution in vial 2 was dried at 120^0C, and ~0.5 ml of 8N HNO_3 was added and dried at 120^0C.
Step 7:	The insoluble fraction in vial 1 was dissolved like the silicate rocks (see *Table 3.6*).
Step 8:	~0.5 ml of 8N HNO_3 was added to both vial 1 and vial 2, and the solution in vial 2 was transferred to vial 1 and mixed well. Then, the solution in vial 1 was dried on a hotplate at 110^0C.
Step 9:	The dried sample in vial 1 was added with 10 ml of 2% HNO3, capped, and heated gently (at 60^0C) for 30 minutes.
Step 10:	The diluted solution of the sample was taken to prepare a stock solution for ICPMS measurements.

Table 3.8: Measured and recommended $\delta^{13}C_{V\text{-}PDB}$ and $\delta^{18}O_{V\text{-}SMOW}$ values of carbonate standards

	$\delta^{13}C_{V\text{-}PDB}$ (‰)	$\delta^{18}O_{V\text{-}SMOW}$ (‰)

NBS-19(primary international standard)		
measured (n=5)	2.09±0.07	28.53±0.09
recommended (Brand et al., 2014)	1.95	28.65
MMB (Lab standard)		
measured (n=10)	3.94±0.08	-10.75±0.11
recommended (Ray 1997)	3.81±0.08	-10.69±0.12
COQ-1 (Carbonatite standard)		
measured (n=10)	-5.10±0.07	7.86±0.08
Reported (Ackerman et al., 2017)	-5.21±0.01	7.38±0.02

Note: Precisions/Errors are at 1 sigma.

Table 3.9: Sample dissolution procedure for isotopic analyses of alkaline silicate rocks

Step 1:	About 60 mg of homogenized sample powder was taken in a 17 ml PFA Savillex Teflon vial and capped.
Step 2:	~1 ml of HF+HNO_3 acid mixture was added to the sample in the vial, ultrasonicated for 45 minutes with the cap closed, and kept overnight on a hotplate at 120^{0}C.
Step 3:	The next day, the solution was dried at 100^{0}C till the sample solution dried to a cake-like appearance.
Step 4:	~ 0.5 ml of 8N HNO_3 was added to the vial and thoroughly mixed until the sample dissolved, then dried at 120^{0}C.
Step 5:	~0.5 ml of 8N HNO_3 was added again to the sample, mixed well to check the dissolution of the sample, and dried at 120^{0}C.
Step 6:	If the sample was dissolved entirely, dissolution procedures in steps 6,7 and 8 were skipped. Otherwise, the sample was treated with concentrated HCl and (or) HCl +HNO_3 (3:1) and kept overnight cap-closed on a hotplate at 80^{0}C.
Step 7:	The next day, the solution was dried at 100^{0}C, and step 6 was repeated once more to ensure the complete dissolution of the sample. Then, the sample was dried at 100^{0}C
Step 8:	~0.5 ml of 8N HNO_3 was added to the sample and dried at 100^{0}C. This was repeated once more.
Step 9:	The sample was added with 1ml of 6N HCl and Kept on a hotplate overnight at 80^{0}C. The next day, the solution was dried down at 100^{0}C. The step was repeated once more to convert the sample into chloride form.
Step 10:	The dried sample was taken in 1 ml of 1N HCl to process for primary column chemistry (Sr+REE separation).

Table 3.10: Sample dissolution protocol for Isotopic analyses of Carbonatites

Step 1	About 60 mg of homogenized sample powder was taken in a 17 ml PFA Savillex Teflon vial (vial 1) and capped.
Step 2	~1 ml of 6N HCl was added to the sample and kept for 4 hours on a hot plate at 80^0C.
Step 3	The dissolved fraction, primarily carbonates and apatites (Carbonate Fraction: CF), was transferred to another vial (vial 2) carefully through a pipette.
Step 4	The insoluble fraction, primarily silicates (Silicate Fraction: SF), was added with ~200 ml of Milli-Q water, and the clear solution was transferred to vial 2. This step was repeated once to ensure the complete removal of the soluble CF left (if any) from vial 1.
Step 5	The CF in vial 2 was dried at 100^0C before adding ~0.5 ml of 8N HNO_3 to the vial. Then, the vial was capped and kept overnight on a hotplate at 100^0C.
Step 6	The solution in vial 2 was dried at 120^0C, ~0.5 ml of 8N HNO_3 was added to the vial, and dried at 120^0C.
Step 7	The insoluble fraction, SF, in vial 1 was dissolved like the silicate rocks (see *Table 3.7*) and dried down.
Step 8	~0.5 ml of 8N HNO_3 was added to both vial 1 and vial 2, and the solution in vial 2 was transferred to vial 1 and mixed well. Then, the solution in vial 1 was dried on a hotplate at 110^0C.
Step 9	~0.5 ml of 6N HCl was added to the dried sample and kept cap closed on a hot plate overnight. The sample solution was then dried at 100^0C. The step was repeated once more to convert the sample into chloride form.
Step 10	The dried sample was further added with ~0.5 ml of 2N HCl and dried. The dried sample was taken in 1 ml of 1N HCl for primary column chemistry (Sr + REE separation).

Table 3.11: Column chemistry protocol followed for Sr and REE separation by cation exchange chromatography

Step 1:	The Biorad® AG 50W-X8 cation exchange resin (200-400 mesh) was cleaned with Milli-Q water to remove the loose floating particles.
Step 2:	Cleaned Quartz columns were filled with the AG 50W-X8 resin up to a height of ~16 cm.
Step 3:	The columns were cleaned with ~15 ml of 6N HCl and passed with ~16 ml of milli-Q water.
Step 4:	The columns were conditioned with ~6 ml of 2N HCl. Previously prepared sample solutions in 1 ml of 1 N HCl were centrifuged at 14.5 rpm for 5 minutes.

Step 5:	A clear sample solution (~1 ml) in 1N HCl was loaded gently onto the top of a resin bed and allowed to pass through the column. Subsequently, ~1ml of 1N HCl was passed.
Step 6:	~22 ml of 2N HCl was eluted and discarded for removal of Fe, K, Na, Rb, Ca, etc.
Step 7:	Sr was eluted with ~10 ml of 2N HCl in a separate clean vial. The Sr cuts for each sample were dried down.
Step 8:	REEs were eluted with ~18 ml of 6N HCl in a separate clean vial. The REE cuts for each sample were dried and taken in ~100 μl of 0.18N HCl.
Step 9:	The columns were cleaned two times with a full volume of 6N HCl and one time with a full volume of milli-Q water for regeneration.
Step 10:	The dried Sr elements for silicate samples are ready for isotopic measurements. The dried Sr for each carbonatite sample was taken in ~1ml of 3N HCl. This Sr was kept ready for further purification of Sr from Ca by Sr-specific column chemistry. See *(Table 3.12)* for the protocol for Sr-specific column chemistry.

Table 3.12: Protocol for Sr-specific column chemistry

Step 1:	The Sr-specific resin was taken in a clean centrifuge tube (~15 ml), added with Milli-Q water, and centrifuged for 8 minutes to remove the loose floating particles. This step was repeated once more.
Step 2:	Precleaned Biorad® ~2 ml columns were passed with ~200 μl of milli-Q water.
Step 3:	~300 μl of Sr-specific resin in the milli-Q medium was loaded onto the columns and conditioned with 1ml of 3N HNO_3.
Step 4:	Previously separated Sr from the carbonatite samples (refer to step 10, *Table 3.10*) in ~1ml of 3N HCl was loaded gently onto the top of a resin bed and allowed to pass through the column.
Step 5:	~500 μl of 3N HCl was eluted and discarded thrice for removal of Ca.
Step 6:	Sr was eluted in ~500 μl of milli-Q water in a separate clean vial. This step was repeated three times more to complete the collection of Sr. The purified Sr for each sample was dried down to make it ready for TIMS measurements.

Table 3.13: Column chemistry Protocol followed for Nd separation by anion exchange chromatography

Step 1:	The Eichrom® Ln-specific anion exchange resin (50-100 mesh) was cleaned with Milli-Q water to remove the loose floating particles.
Step 2:	Cleaned Quartz columns were filled with the Ln-specific resin up to a height of ~9 cm.

Step 3:	The columns were cleaned with ~5 ml of 6N HCl and subsequently passed with ~5 ml of milli-Q water.
Step 4:	The columns were conditioned with ~2 ml of 2N HCl.
Step 5:	A clear sample solution (~100 µl ml) in 0.18N HCl was loaded gently onto the top of a resin bed and allowed to pass through the column. Subsequently, ~100 µl of 0.18N HCl was passed.
Step 6:	~16 ml of 0.18N HCl was eluted and discarded.
Step 7:	Nd was eluted with ~8 ml of 0.3N HCl in a separate clean vial. The Nd cuts for each sample were dried down to make it ready for TIMS measurements.
Step 8:	The columns were cleaned with ~5 ml of 6N HCl, followed by a full volume of milli-Q water for regeneration.

Table 3.14: Protocol for Pb separation from a sample solution

Step 1:	A precleaned Pb column was rinsed with sub-boiled Milli-Q (SBMQ) (250µl) three times. Then, the Pb column was rinsed with one reservoir of double-distilled (D.D.) HCl 3times.
Step 2	The Pb column was rinsed with 250 µl SBMQ. Then, the column was loaded with 250 µl AG1 X8 resin (in SBMQ).
Step 3	One reservoir of 6N D.D. HCl was passed through the column, then 250 µl of SBMQ was passed two times.
Step 4	The column was conditioned with ~250 µl of 0.7N HBr.
Step 5	The sample solution (in 1.5ml 0.7N HBr) was loaded onto the resin, and the waste beakers were replaced with the sample vial to collect the Sr+REE cut.
Step 6	~250 µl of HBr (0.7N) was passed through the column. Then the vial was replaced by the waste beaker.
Step 7	~250 µl of 2N D.D. HCl was passed through the column.
Step 8	Pb was eluted in a newly cleaned vial by passing 0.5N D.D. HCl (6N) 2 times through the column. The vial was labeled with the sample name.
Step 9	~2.5 µl of ultrapure H_3PO_4 was added to the Pb cut and dried on a hotplate at 80^0C to make it ready for measurement.

Chapter 4

Results

4.1. Sample characterization

4.1.1. *Petrography*

The microphotographs of the representative carbonatites and alkaline silicate rocks from the Sarnu-Dandali-Kamthai (SDK) alkaline-carbonatite complex are given in *Fig. 4.1***,** and their petrographic details are discussed below.

A. Alkaline Silicate Rocks

Nephelinites of SDK complex consist of microphenocrysts (<300 µm) of clinopyroxene (~50%), nepheline, and calcite set in a groundmass of nepheline and carbonates *(Fig. 4.1a & Fig. 5.2a)*. Phonolites of the complex, being subvolcanic, show a bimodal distribution of grain sizes with the phenocrysts of feldspar, clinopyroxene, sphene, monazite, and biotite set in a groundmass of feldspar and clinopyroxene *(Fig. 4.1b)*. Sanidine is the most abundant phenocrystic feldspar (500 - 4000 µm), which often shows Carlsbad twinning. Some porphyritic phonolites contain much larger crystals of sanidine (>1 cm). Albite is the common microphenocryst, and it makes up a large part of the groundmass. Phenocrysts of clinopyroxene are euhedral to subhedral aegirine/aegirine-augite with a size ranging from 500 and 1000 µm and often show zoning. Some oikocrysts of aegirine envelope earlier formed sphene.

The tephriphonolites are made up of microphenocrysts/phenocrysts of clinopyroxene (aegirine-rich), melilite, and sphene *(Fig. 4.1c)*. Melanephelinites contain phenocrysts/microphenocrysts of clinopyroxene (aegirine rich), nepheline, calcite, and Na-feldspar set in a groundmass of nepheline, albite, and carbonate. Clinopyroxene accounts for ~45% of the microphenocryst population. One melanephelinite sample (KT-21-4) hosts a carbonate inclusion (xenolith), which contains a euhedral megacryst of calcite sharing boundary with a K-feldspar megacryst *(Fig. 4.1d)*. In addition, this K-feldspar also hosts carbonate inclusions *(Fig. 4.1e)*.

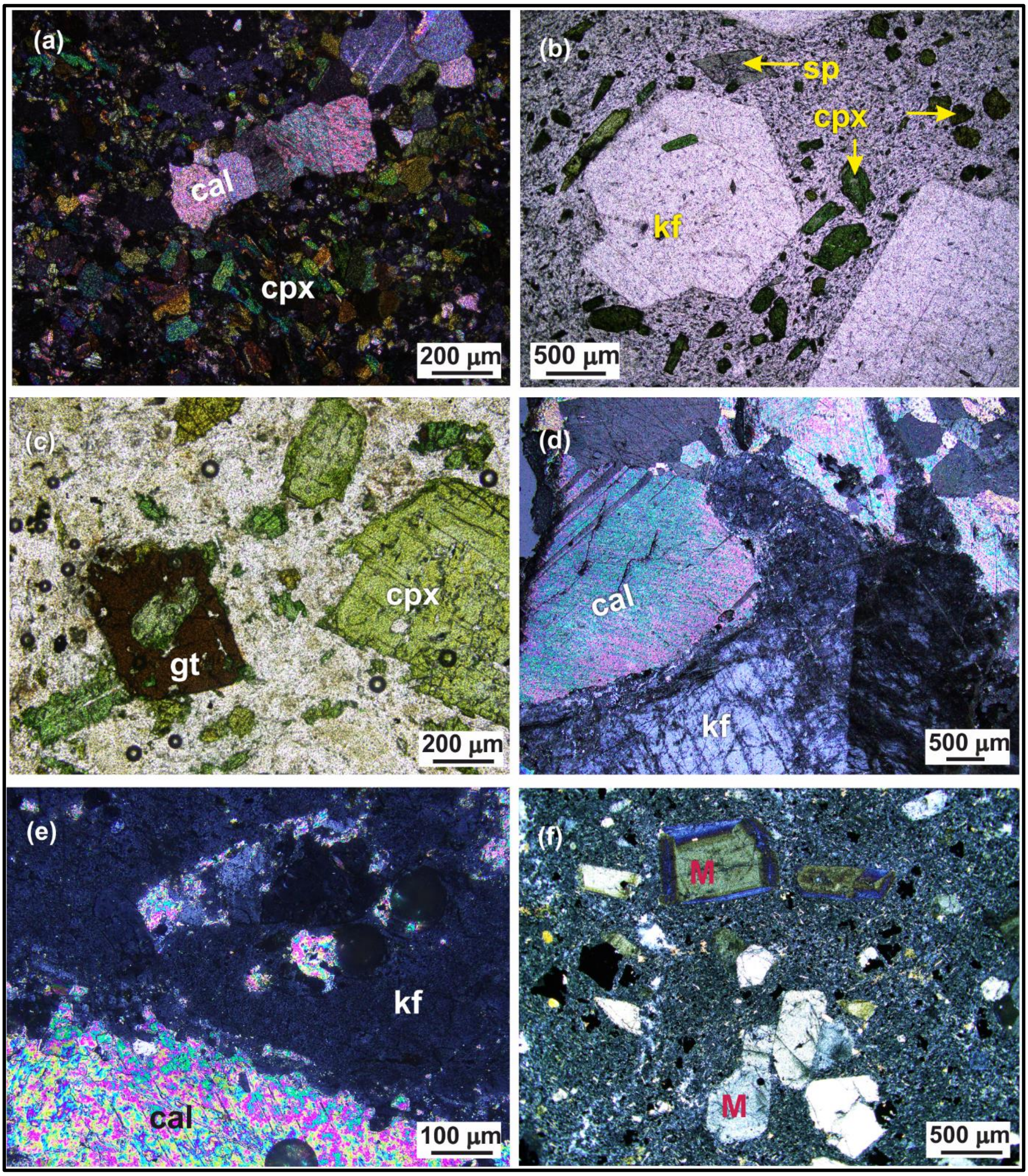

Fig. 4.1. Photomicrographs showing petrographic features of alkaline silicate rocks from the SDK complex: (a) Clinopyroxenes and primary calcites in a nephelinite (KT-20-36); (b) Phonolite consisting of phenocrysts of K-feldspar (sanidine) and clinopyroxene (aegirine); (c) Tephriphonolite (SAR-20-5) containing phenocrysts of clinopyroxene, garnet in a groundmass of melilite, feldspar, and clinopyroxene (aegirine); (d) Euhedral calcite megacryst in the carbonate xenolith hosted in a melanephelinite (KT-21-4); (e) Carbonate inclusions within a K-feldspar megaphenocryst of a melanephelinite (KT-21-4); (f) Melilitite containing phenocrysts of melilite. Abbreviations: cal: calcite, cpx: clinopyroxene, kf: K-feldspar, sp: sphene, gt: garnet, and m: melilite.

Phonotephrites and Tephrites of the complex are often porphyritic and contain clinopyroxene (diopside + aegirine), nepheline, feldspars, and minor sphene/monazite set in a groundmass of nephelinite, feldspar, and clinopyroxene. The clinopyroxene phenocrysts are often fractured and larger than nepheline phenocrysts. Their groundmass consists of plagioclase and clinopyroxene. Melilitites contain euhedral phenocrysts of melilite set in a groundmass of clinopyroxene and melilite *(Fig. 4.1f)*.

B. Carbonatites

The unaltered carbonatites mainly display primary cumulate textures where calcite grains, euhedral to subhedral with varying sizes (300 – 600 µm), are in mutual contact *(Fig. 4.2a)*. Calcite-carbonatites form the bulk (>90%) of the carbonatites of SDK complex. One of the carbonatites (KT-18-1C) contains euhedral to subhedral phenocrysts of K-feldspar (1000 – 2000 µm). Apatite is the second most abundant mineral in the carbonatites, and it mostly occurs as microphenocrysts (<300 µm) and often shows clusters between calcites. They also occur as inclusions within calcite grains. Clinopyroxene occurs as subhedral/anhedral/acicular microphenocrysts and is primarily found in thin bands between cumulates of calcite and apatite *(Fig. 4.2b)*. Mica, pyrochlore, magnetite, and ilmenite occur as accessory phases *(Fig. 4.2c)*. One carbonatite (KT-18-7C), associated with a melanephelinite, contains megacrysts of biotite *(Fig. 4.2d)*.

Some carbonatites show postmagmatic recrystallization and re-equilibration textures in whish recrystallized calcite grains have grown to large sizes, sometimes reaching >4000 µm *(Fig. 4.2e)*. Furthermore, these carbonatites also show postmagmatic alteration, as suggested by veins filled with secondary carbonate and oxide minerals. The recrystallized calcite grains are mostly anhedral and often have higher brightness than primary calcites in plane-polarized light (PPL) and exhibit lower-order interference colors in crossed-polarized light (XPL; *Fig. 4.2f)*.

4.1.2. *Mineralogy and Mineral Chemistry*

A. XRD Data

Powder X-ray diffraction (XRD) spectra (counts vs. 2θ) of representative alkaline silicate rocks and carbonatites were generated to identify major mineral phases present in our samples. We determine that the phonolites of SDK complex contain nepheline, sanidine (K-feldspar), and

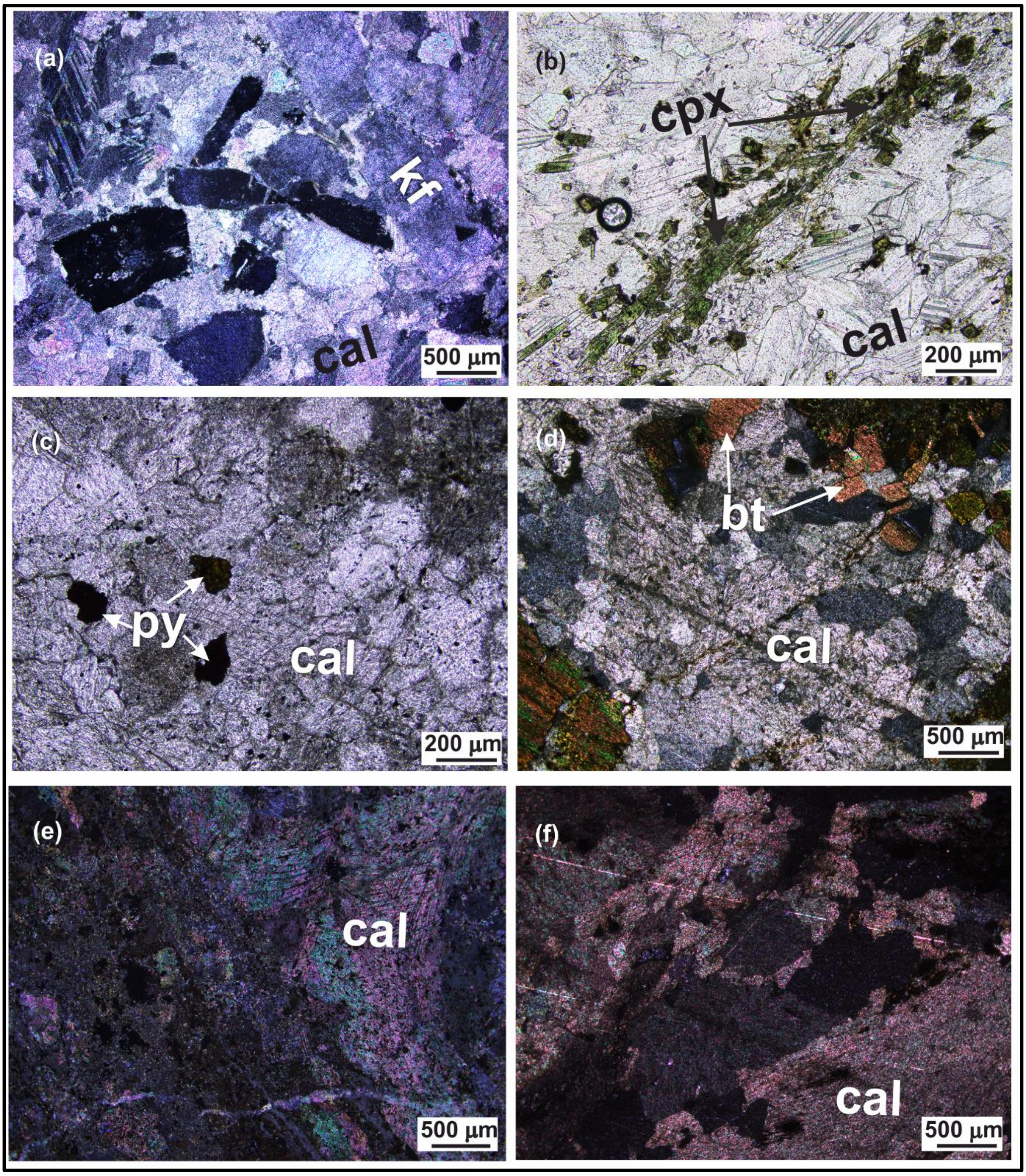

Fig. 4.2. Photomicrographs of carbonatites from the SDK complex showing different petrographic features: (a) A coarse-grained calcite carbonatite (KT-18-1C) showing the cumulates of calcite phenocrysts. K-feldspar phenocrysts are locally clustered; (b) A coarse-grained calcite carbonatite (KT-20-6C) showing calcite cumulates with aegirine (cpx) crystals; (c) A fine-grained calcite carbonatite (KT-20-28C) showing pyrochlore microphenocrysts surrounded by calcites; (d) Microphenocrysts/phenocrysts of biotite together with calcite phenocrysts; (e) A large recrystallized calcite (right) in a carbonatite with secondary calcite veins. Note that primary calcite grains on the left side are much smaller than the recrystallized calcite; (f) Recrystallized calcites (large crystals) in a partly altered carbonatite (KT-18-8C). Abbreviations used are: cal: calcite, kf: K-feldspar, cpx: clinopyroxene, py: pyrochlore, and bt: biotite.

aegirine (clinopyroxene) as major mineral phases *(Fig. 4.3a)*, whereas clinopyroxene, nepheline, and Na(K) feldspar are the dominant phases in melanephelinites. Calcite forms the dominant or the only carbonate mineral in the carbonatites *(Fig 4.3b)*. Calcite also occurs as an accessory phase in many alkaline silicate rocks.

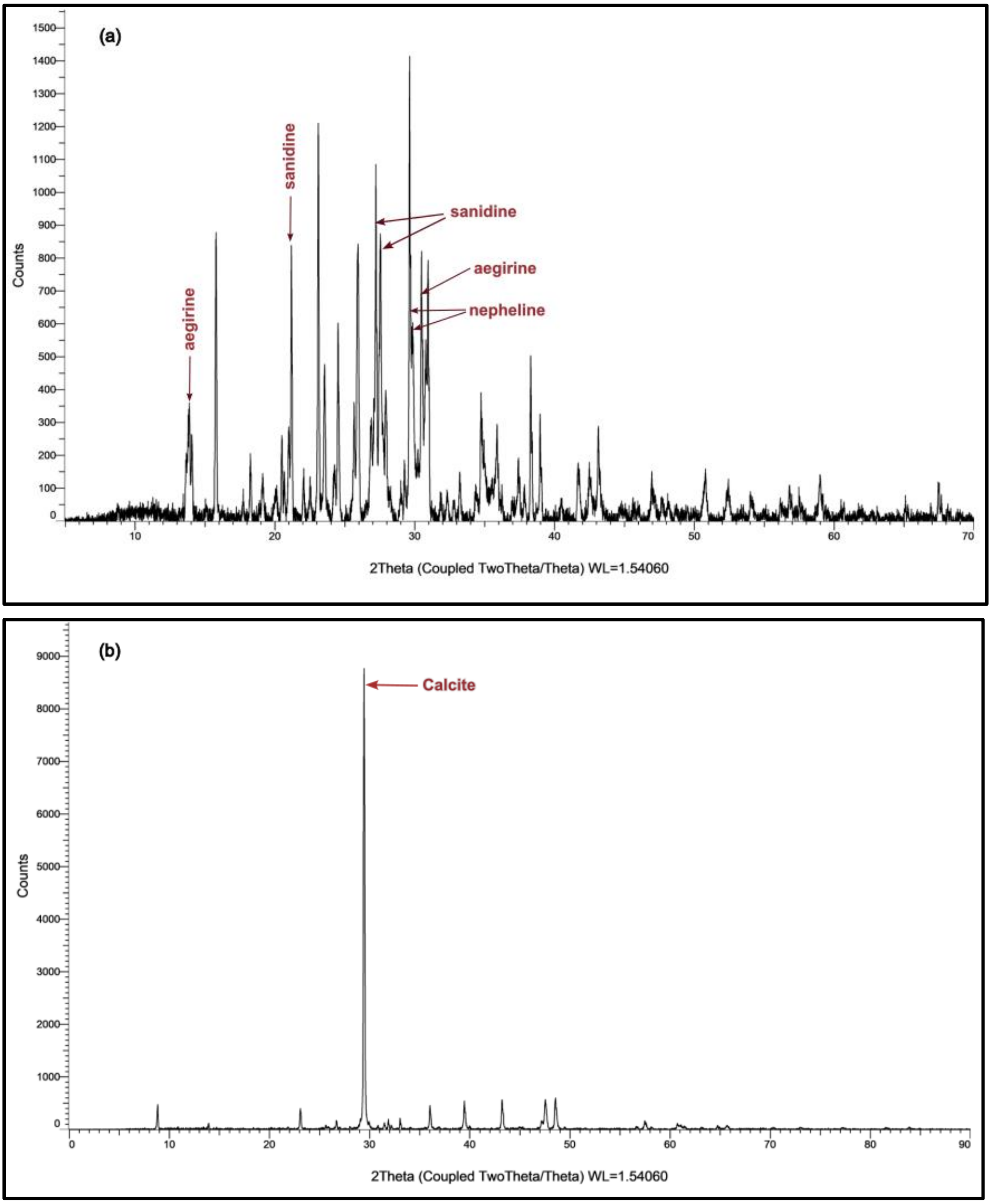

Fig. 4.3. Typical powder X-Ray diffraction spectra for phonolite (a) and carbonatite (b) from the SDK complex. Nepheline, sanidine, and aegirine are the major mineral phases in phonolite. The carbonates of carbonatite are primarily calcite.

B. EPMA Data

A few thin-sections of whole rock samples and minerals were analyzed in an EPMA for mineral chemistry. *Tables 4.3* to *4.5* present these data. Calcites in carbonatites of the complex (e.g., KT-18-1C) are Ca-rich (>90%) with minor substitutions of Mg, Mn, Fe, Sr, Ba, and REEs. As revealed from the BSE images, the calcite microphenocrysts/phenocrysts often show cumulate texture, enclosing interstitial carbonate phases (*Fig. 4.4a*).

Phenocrysts/microphenocrysts of feldspars of carbonatites occur as euhedral to subhedral grains and commonly share boundaries with calcites and apatites. Most are perthites ($An_{0-1}Ab_{08-12}Or_{89-90}$) with irregular exsolved patches of albite ($An_0Ab_{94-99}Or_{1-2}$; *Table 4.3; Figs. 4.4a, 4.4b*). In contrast, Na-feldspars are dominant in tephrites and melanephelinites, although phenocrysts of perthite also occur in melanephelinite (*Figs 4.4c, 4.4d)*. Apatite in carbonatites occurs in clusters and forms euhedral to subhedral microphenocrysts (<300µm) between calcite grains and as inclusions within carbonate phases *(Figs. 4.4b & 4.4e)*. Zoned apatites, exhibiting compositional variations in Ca, are common in BSE images *(Fig. 4.4e)*. Apatites in melanephelinites occur as subhedral to anhedral microphenocrysts. Clinopyroxene forms the most abundant silicate mineral in the carbonatite sample, KT-18-1C (*Fig. 4.4e*). Clinopyroxenes commonly share contact with apatites. Ilmenites are the most abundant oxide mineral in carbonatites (e.g., KT-18-1C; *Fig. 4.4f*) and occur mainly as anhedral microphenocrysts. Biotite and phlogopite are minor and present in the groundmass (*Fig. 4.4g*).

Carbonate melt inclusions in Alkaline Silicate Rocks and Carbonatites

The composition of carbonate inclusions observed in K-feldspar (perthites) phenocrysts in the melanephelinite, KT-21-4 (*Figs. 4.5d to 4.5f*), is also like that of the inclusions found in the carbonatite KT-18-1C, with low SiO_2 and TiO_2. Their alkali and CaO contents vary between 0.20-0.35 wt.%, and 52-55 wt.%, respectively, and are like those of calcites of carbonatites *(Table 4.4)*. Carbonate melt inclusions occur within phenocrysts/microphenocrysts of K-feldspar, magnetite, and apatite of some carbonatites (e.g., KT-18-1C; *Figs 4.5a* to *4.5c*). Results of *in situ* chemical analyses (by EMPA) of these inclusions are summarized in *Table 4.5*. CaO content of carbonate inclusions in K-feldspar grains (*Fig. 4.5a*) varies between 47 and 54 wt.%, which is higher than that of the carbonate inclusions found in magnetites (43-49 wt.%) (*Fig. 4.5b*) and like that of the carbonate inclusions in apatites (48-54 wt.%; *Fig. 4.5c*). All the studied carbonate melt inclusions are calcite rich. In contrast, the MnO + FeO content

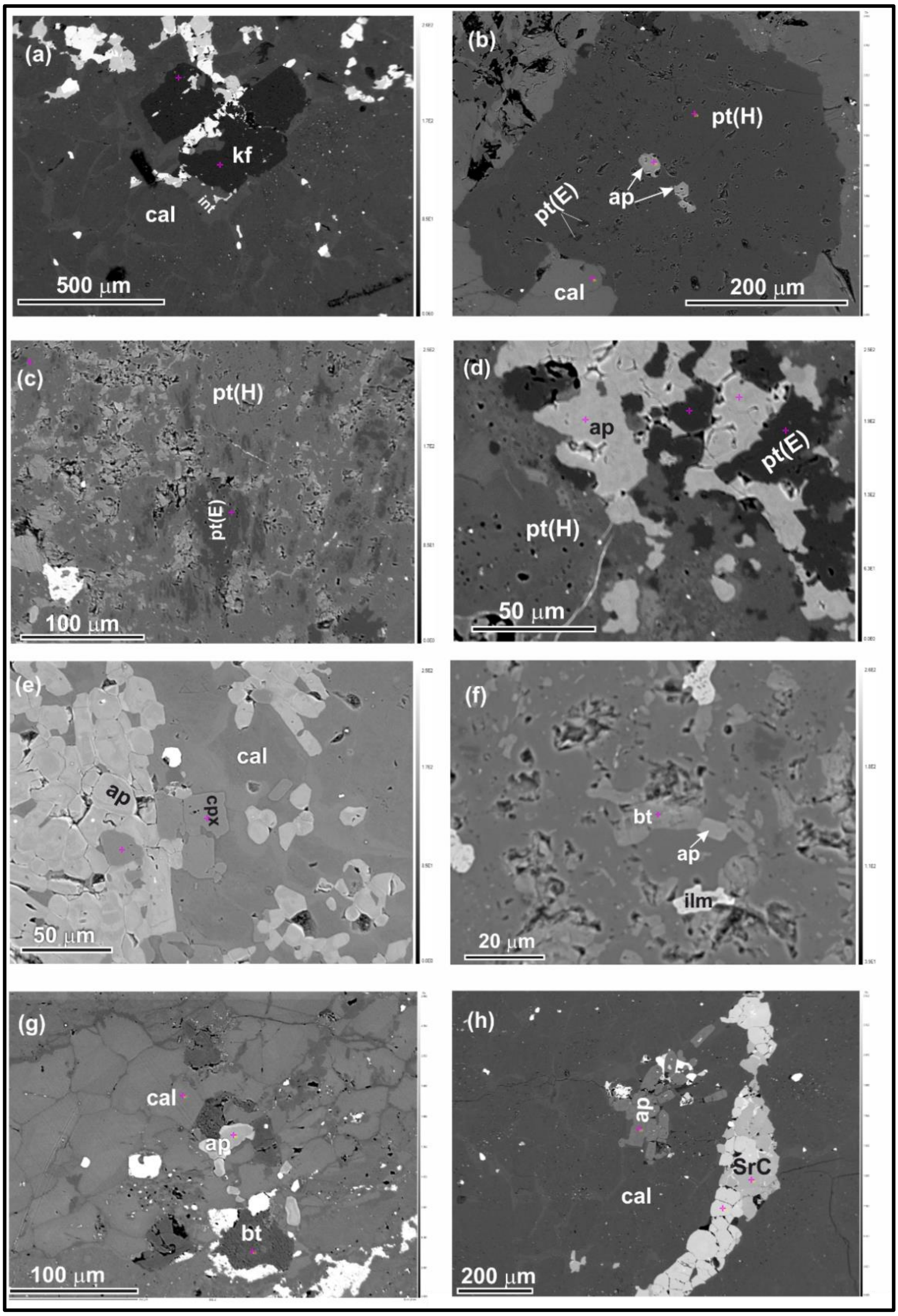

Fig. 4.4. Backscattered electron (BSE) images of the selected phases in carbonatites of the SDK complex: (a) Cumulates of calcite phenocrysts enclosing K-feldspar phenocrysts; (b) Exsolution patches of Na-rich feldspar (pt (E)) in a perthite host(pt(H)), which also contains inclusions of apatite; (c) A Phenocryst of perthite (pt(H)) with irregular exsolution patches (pt(E)) in a melanephelinite; (d) Anhedral apatite grains enclosed in a perthite (pt(H)) showing exsolution patches (dark, pt(E)); (e) Clusters of apatite (often zoned) with clinopyroxene phenocrysts surrounded by calcite phenocrysts and groundmass; (f) Inclusions of biotite, apatite, and ilmenite with K-feldspar host; (g) Phenocrysts of apatite and biotite surrounded by calcite grains; (h) Clusters of apatite and Sr-rich carbonate phases grow interstitially within calcite cumulates. Abbreviations: ap-apatite, cal-calcite, cpx-clinopyroxene, bt-biotite, and ilm -ilmenite

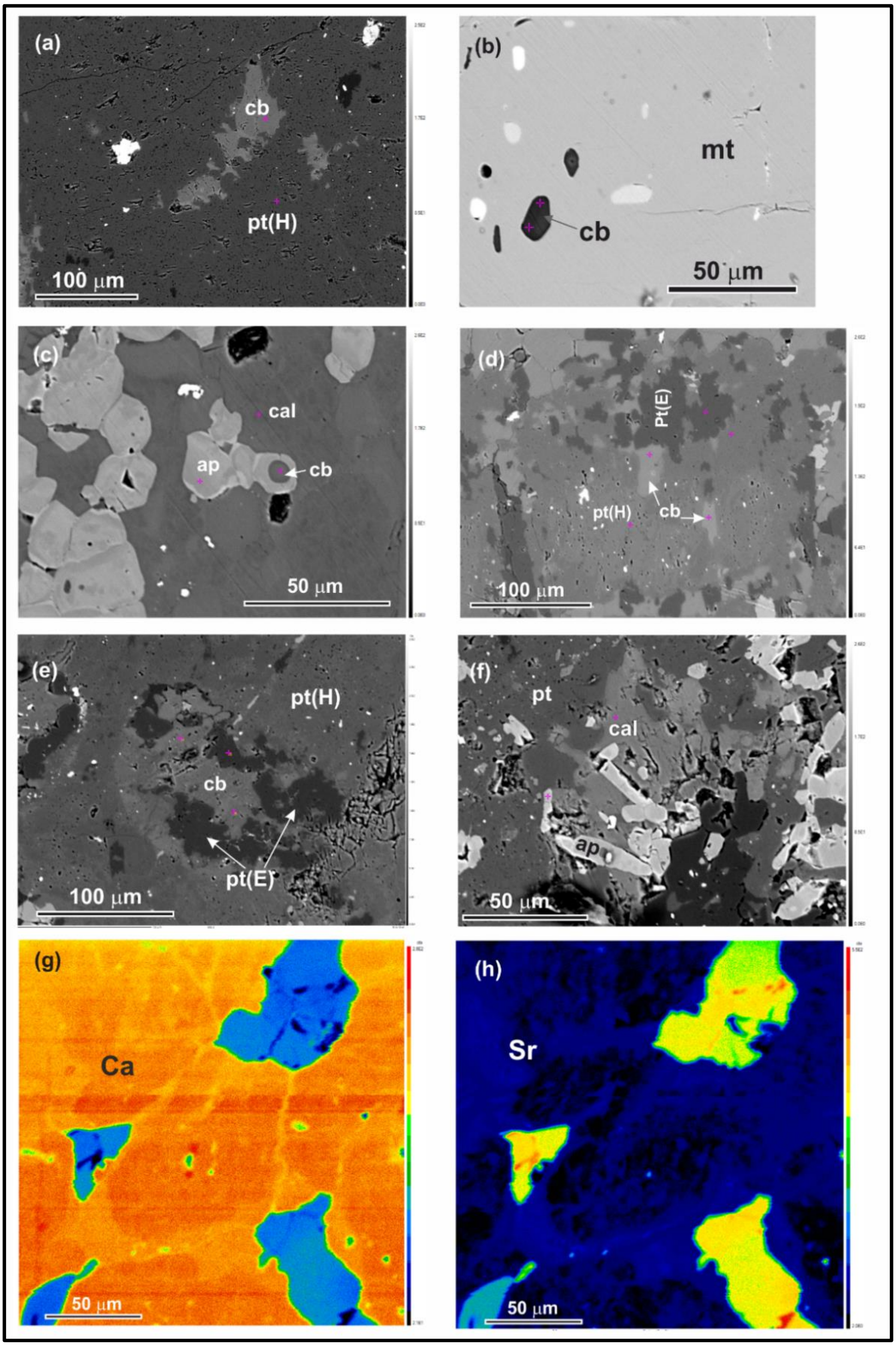

Fig. 4.5. Backscattered electron images of carbonate melt inclusions in various phases in a carbonatite (KT-18-1C; a-c) and a melanephelinite (KT-21-4; d-f): (a) A carbonate inclusion in a K-feldspar (perthite) grain; (b) Carbonate melt inclusions in magnetite; (c) Zoned apatite contains carbonate melt inclusions; (d) A perthite in melanephelinite (KT-21-4) containing numerous carbonate inclusions; (e) Globule-shaped carbonate inclusion in a perthite showing irregular exsolution patches; (f) Inclusions of apatite and carbonate in a perthite in the melanephelinite; (g) Cathodoluminescence (CL) image of the carbonatite (KT-18-1C) showing the distribution of Ca in calcites (orange) and Sr-Ba rich carbonates (blue). The pink marks are EPMA sampling spots. Abbreviations used are the same as those in Fig. 4.4

of the inclusions in magnetites (2.6-5.6 wt.%) is higher than that of inclusions in K-feldspar and apatite grains. All the inclusions contain low alkali ($Na_2O+K_2O < 0.2$ wt.%) and very low SiO_2, Al_2O_3, and TiO_2 contents, which is in contrast to the alkali contents of carbonatite melt inclusions reported from carbonatite complexes elsewhere in the world (Guzmics et al., 2015, 2012). SrO and BaO contents of these inclusions vary between 0.92 wt.% - 2.16 wt.% and 0.01 wt.% - 0.13 wt.%, respectively *(Table 4.5).*

<u>Carbonate xenolith in a Melanephelinite dyke (KT-21-4)</u>

A carbonate inclusion (xenolith) of ~3cm in diameter was found inside a melanephelinite dyke (KT-21-4; N25.631, E71.933). The xenolith is composed of euhedral calcite and apatite phenocrysts (*Figs. 4.6a;b*). Euhedral apatite grains (microphenocrysts) are present as inclusions inside the carbonate phases (*Fig. 4.6a;b).* SiO_2, Al_2O_3, TiO_2, and alkali contents of the carbonates are very low (<1wt.%).

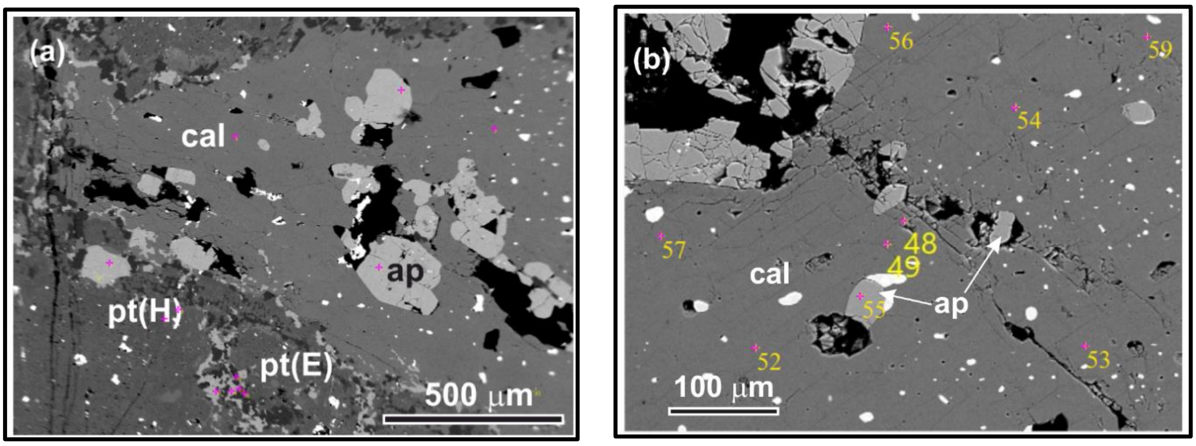

Fig. 4.6. Backscattered electron images of carbonate inclusion/xenolith in a melanephelinite dyke (KT-21-4): (a) Coarse calcite grains in the carbonate inclusion envelops euhedral grains of apatites. The host melanephelinite contains megacrysts of perthitic K-feldspars. Pt(H) and pt(E) represent the host and exsolved phases of the perthite, respectively. A reaction ream has developed at the contact between the carbonate inclusion and the melanephelinite; (b) Coarse-grained euhedral calcites with well-developed cleavages. Apatites present with the carbonate inclusion are marked. The dark spots are voids, and the pink marks are EPMA sampling spots.

4.2. Analytical Data

4.2.1. *^{40}Ar–^{39}Ar geochronology*

We carried out ^{40}Ar-^{39}Ar dating of five whole rock alkaline silicate rocks (dykes), three mineral separates from alkaline silicate rocks, and one biotite separate from a carbonatite dyke. The sample details and results of step heating ^{40}Ar-^{39}Ar dating are presented in *Tables 4.1* and *4.2.*

The age spectra, along with isochron and inverse isochron plots for each sample, are presented in *Fig. 4.7*. The mean values for the interference correction factors ($^{36}Ar/^{37}Ar)_{Ca}$, ($^{39}Ar/^{37}Ar)_{Ca}$, and ($^{40}Ar/^{39}Ar)_{K}$ are 0.003169, 0.005355 and 0.002805, respectively.

All samples yielded good plateaus (*Fig. 4.7*). We have defined a plateau age as the weighted average of ages of contiguous and concordant temperature steps comprising >50% of the total ^{39}Ar released. Ages were calculated using the decay constant of Steiger and Jäger (1977). The plateau and isochron ages were determined and plotted using ISOPLOT 2.49 (Ludwig 2012). The oldest age from the dated samples came from the phonolitic nephelinite dyke KT-20-39, which gave a plateau age of 78.7 $\underline{+}$ 0.4 (2σ) Ma (*Fig. 4.7a1*). Most of the phonolite and the carbonatite intrusions belonged to a younger magmatic phase at ~ 68.5 Ma. Three phonolite samples, KT-18-3, KT-18-9, and KT-18-12, yielded plateau ages of 68.3 $\underline{+}$ 0.4 Ma, 68.5 $\underline{+}$ 0.4 Ma, 68.5 $\underline{+}$ 0.4 Ma, which are identical within 2σ levels of uncertainty (*Figs. 4.7e1, 4.7f1, 4.7g1*). The plateau, normal, and inverse isochron ages of these samples are indistinguishable, and intercepts of isochrons have an atmospheric composition for $^{40}Ar/^{36}$ Ar (i.e., 295.5; *Table 4.2*); therefore, the weighted mean of these plateau ages, 68.5±0.2 (2σ) Ma, can be considered as their crystallization age. The age of the carbonatite, as determined from analysis of a biotite separate from a carbonatite dyke KT-18-7C, is 68.6±0.4 (2σ) Ma – the plateau age. This plateau age is identical to the isochron and inverse isochron ages of the sample within errors (*Table 4.2* and *Figs. 4.7h1 to 4.7h3*), and the same as the age of the alkaline magmatism in the complex (i.e., 68.5±0.2 Ma) of this time. The youngest magmatic phase of the complex is represented by the phonolite KT-20-17, the tephrite KT-20-31, and the tephriphonolite SAR-20-5, which yielded plateau ages of 66.7±0.4 Ma, 66.3±0.4 Ma, and 66.3±0.4 Ma, respectively, at 2σ levels of error (*Table 4.2* and *Figs. 4.7b1,4.7c1, 4.7d1*). The weighted mean age of these ages, 66.4±0.2 (2σ) Ma, therefore, is the time of the youngest intrusive alkaline activity in the SDK complex, which interestingly is synchronous with the first phase of the Deccan continental flood basalt volcanism in India that just predates the Cretaceous-Paleogene (KPg at 66.05±0.04 Ma) boundary (Renne et al., 2015; Sprain et al., 2019). The summary of the samples dated along with their *J* parameters is given in *Table 4.1*.

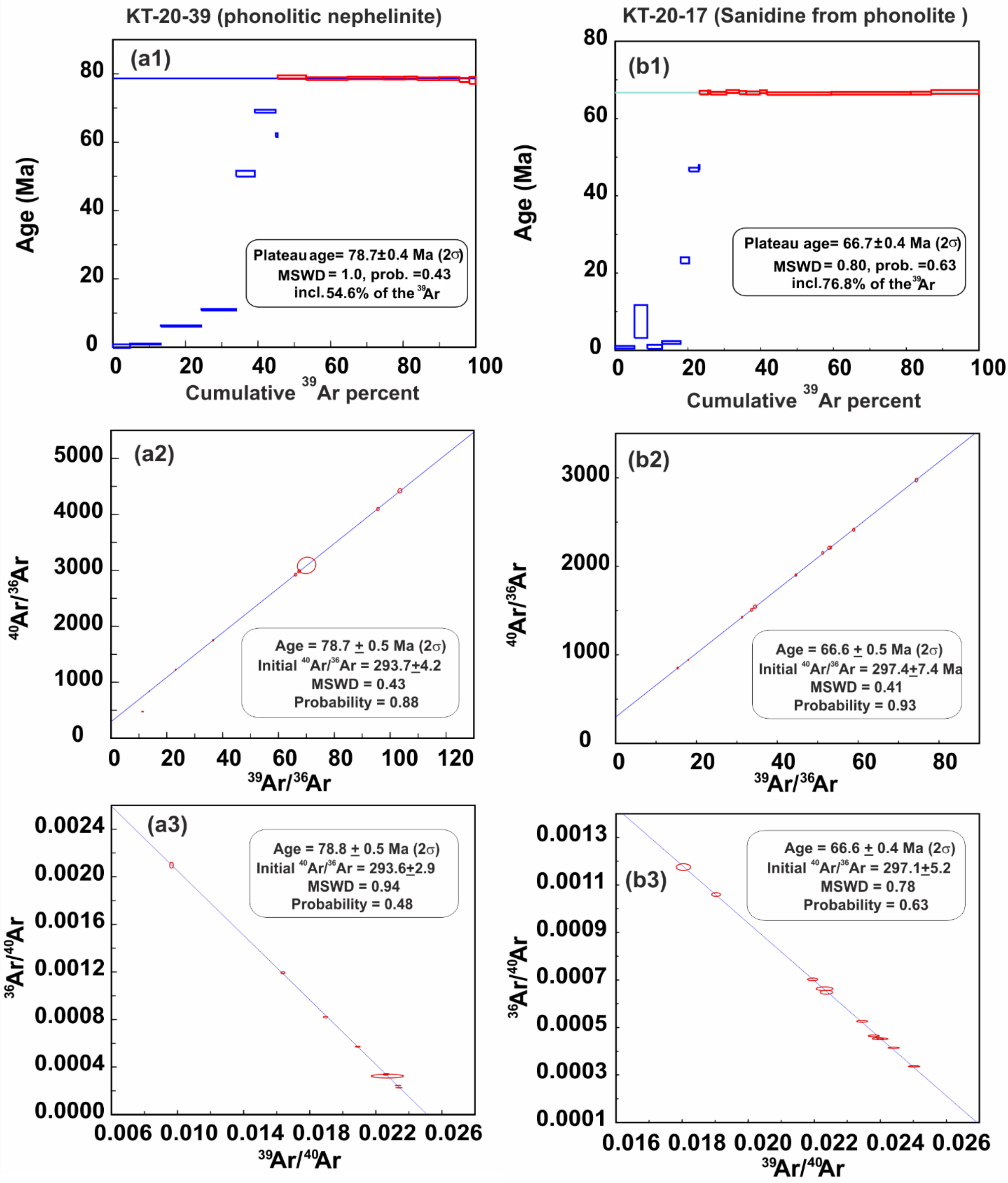

Fig. 4.7. (a1 to b3): Step heating ^{40}Ar/^{39}Ar apparent age spectra (a1 & b1), ^{40}Ar/^{36}Ar vs. ^{39}Ar/^{36}Ar correlation or isochron diagram (a2 & b2) and ^{36}Ar/^{40}Ar vs. ^{39}Ar/^{40}Ar correlation or inverse isochron diagram (a3 & b3) for the plateau steps of the samples KT-20-39 (phonolitic nephelinite) and KT-20-17 (sanidine from phonolite) from the SDK complex. Also shown are the MSWD (Mean Squared Weighted Deviate), initial ^{40}Ar/^{36}Ar, and regression probability values. Errors are at 2σ. A plateau age is defined as the weighted average of apparent ages of contiguous and concordant temperature steps comprising >50% of the total ^{39}Ar released (a1 & b1).

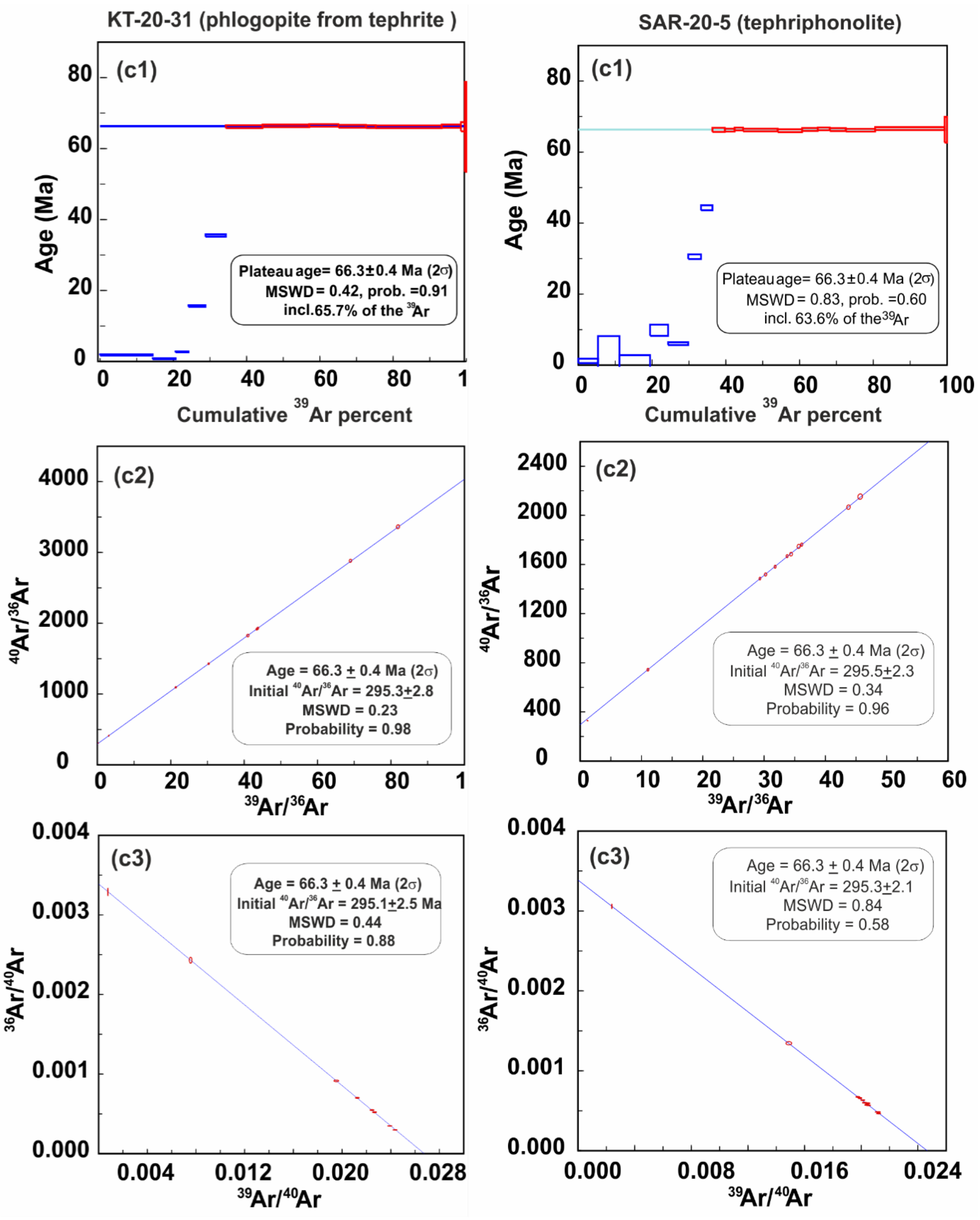

Fig. 4.7. (c1-d3): Step heating ^{40}Ar/^{39}Ar apparent age spectra (c1 & d1), ^{40}Ar/^{36}Ar vs. ^{39}Ar/^{36}Ar correlation or isochron diagram (c2 & d2) and ^{36}Ar/^{40}Ar vs. ^{39}Ar/^{40}Ar correlation or inverse isochron diagram (c3 & d3) for the plateau steps of the samples KT-20-31 (phlogopite from tephrite) and SAR-20-5 (tephriphonolite) from the SDK complex. Also shown are the MSWD, initial ^{40}Ar/^{36}Ar, and regression probability values. Errors are at 2σ. A plateau age is defined as the weighted average of apparent ages of contiguous and concordant temperature steps comprising >50% of the total ^{39}Ar released (c1 & d1).

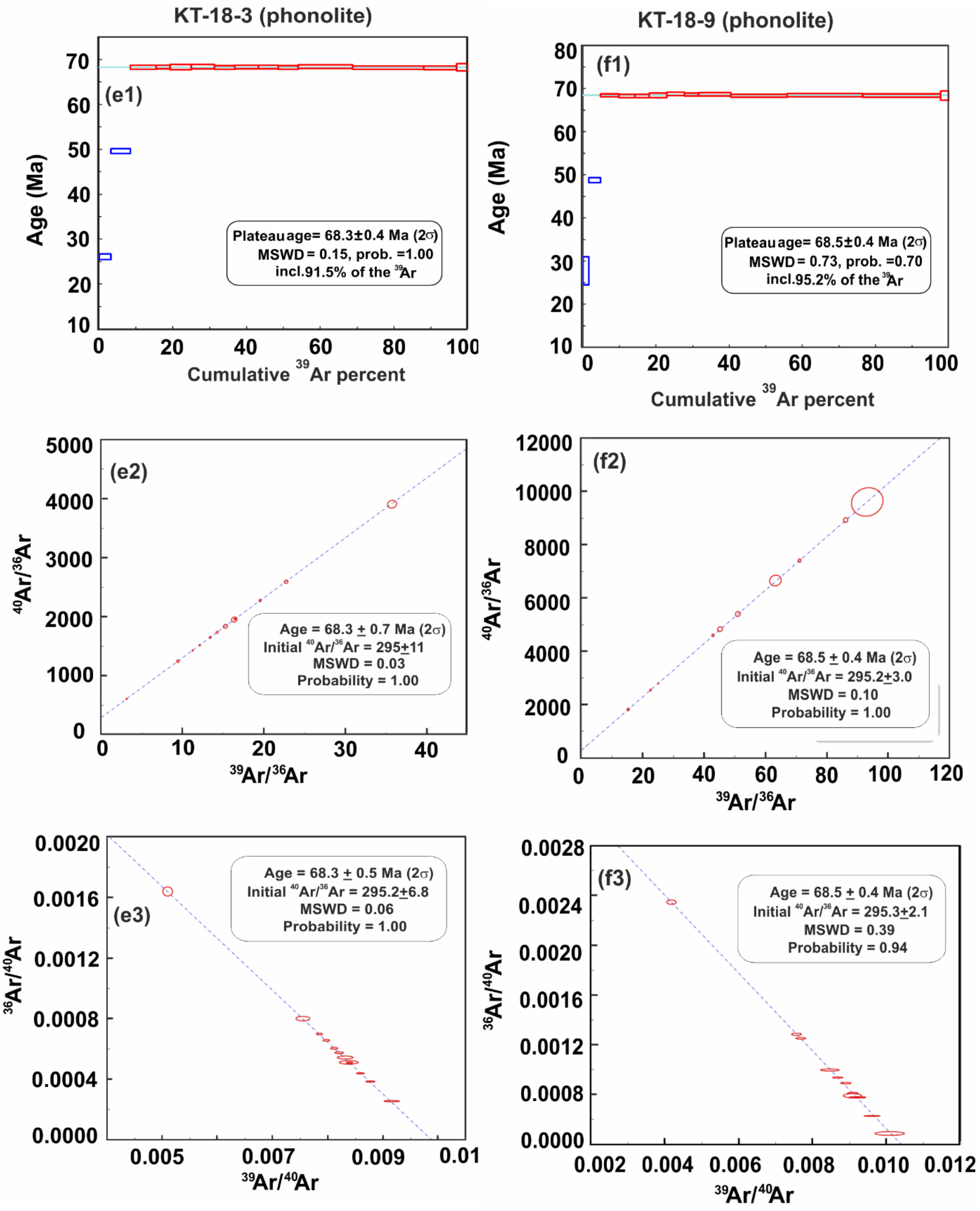

Fig. 4.7. (e1-f3): Step heating ^{40}Ar/^{39}Ar apparent age spectra (e1 & f1), ^{40}Ar/^{36}Ar vs. ^{39}Ar/^{36}Ar correlation or isochron diagram (e2 & f2) and ^{36}Ar/^{40}Ar vs. ^{39}Ar/^{40}Ar correlation or inverse isochron diagram (e3 & f3) for the plateau steps of the samples KT-18-3 (phonolite) and KT-18-9 (phonolite,) from the SDK complex. Other parameters/details are as in the previous figure.

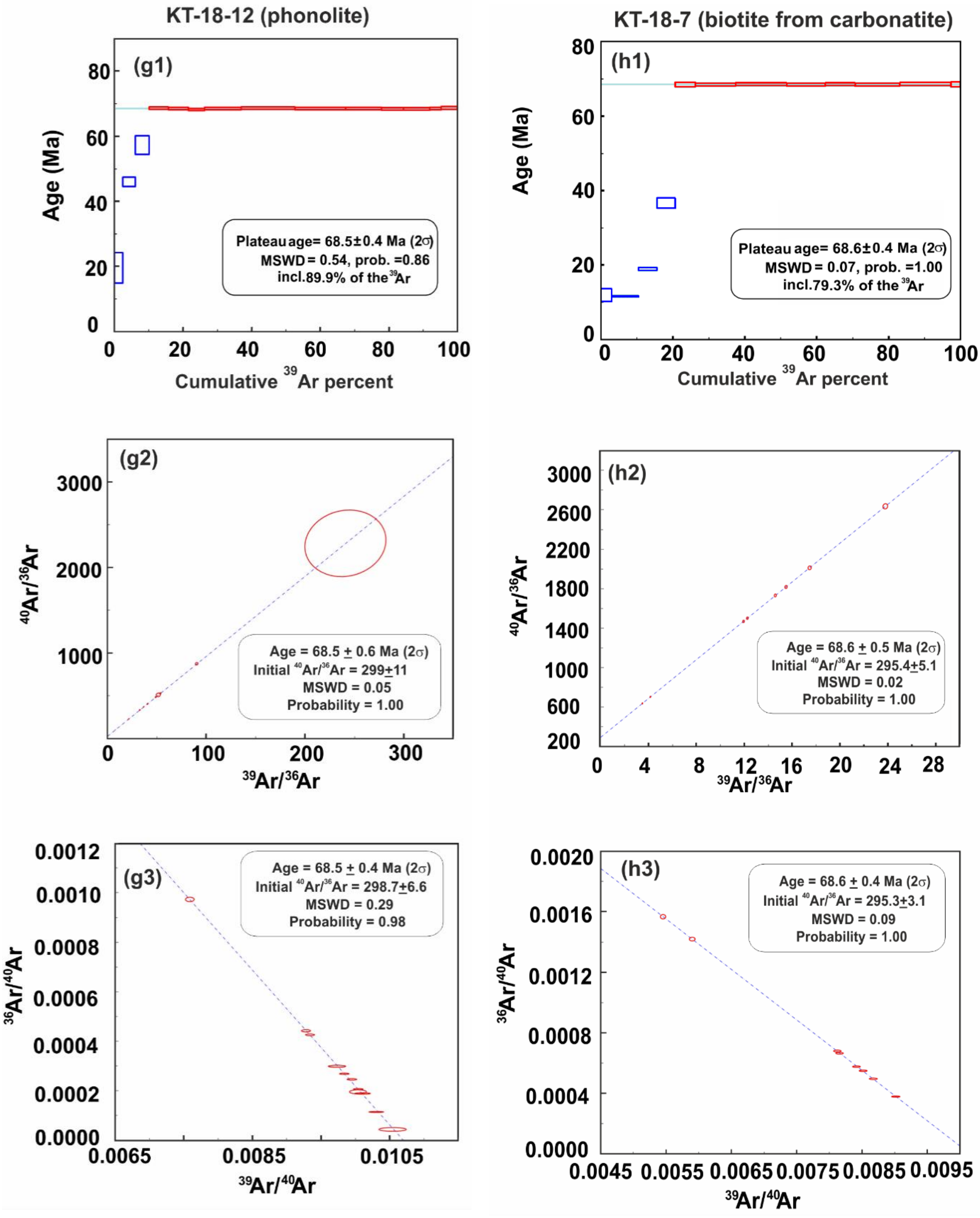

Fig. 4.7. (g1-h3): Step heating $^{40}Ar/^{39}Ar$ apparent age spectra (g1 & h1), $^{40}Ar/^{36}Ar$ vs. $^{39}Ar/^{36}Ar$ correlation or isochron diagram (g2 & h2) and $^{36}Ar/^{40}Ar$ vs. $^{39}Ar/^{40}Ar$ correlation or inverse isochron diagram (g3 & h3) for the plateau steps of the samples KT-18-12 (phonolite) and KT-18-7 (biotite from a carbonatite) from the SDK complex. Other parameters/details are as in the previous figure.

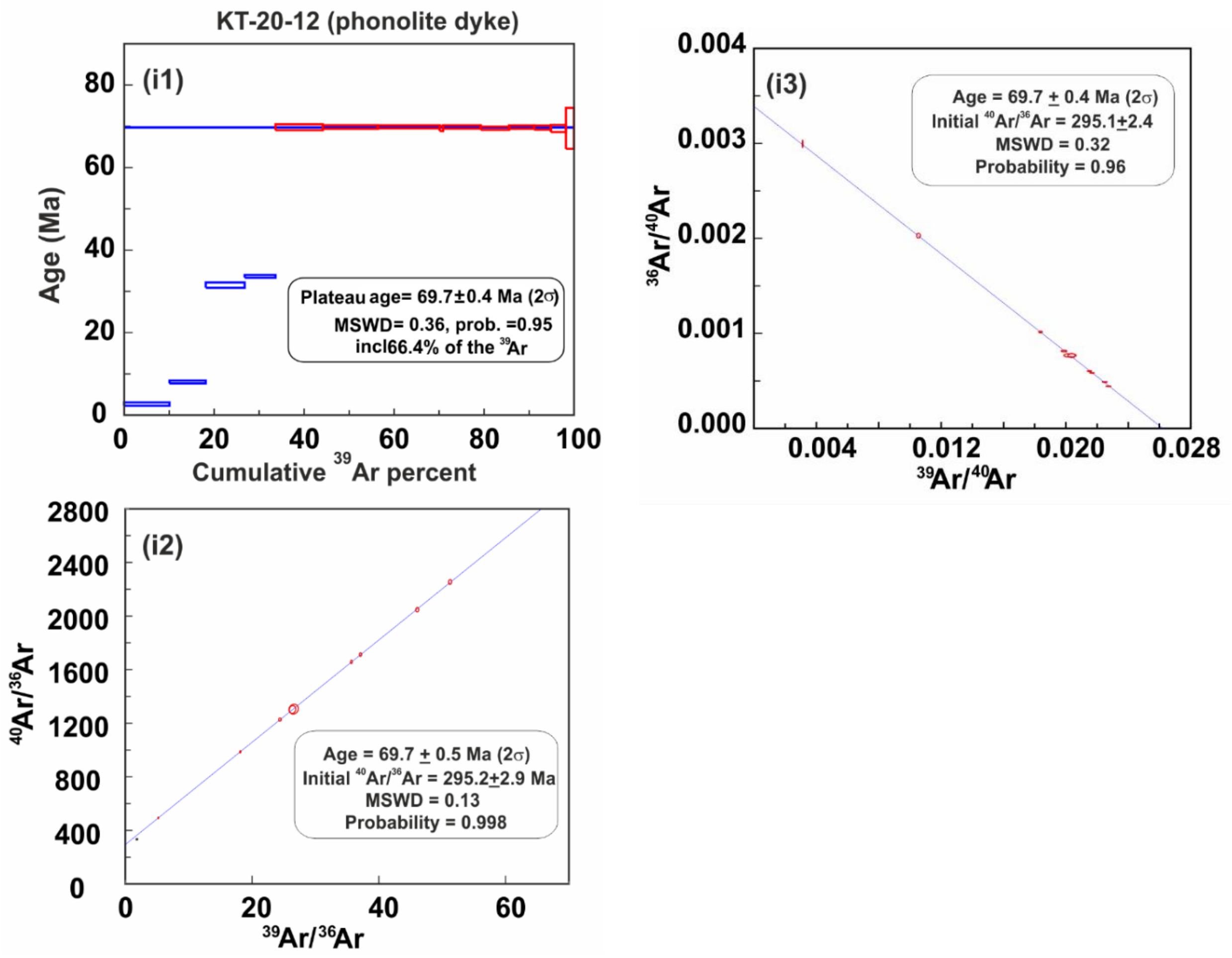

Fig. 4.7. (i1-i3): Step heating ^{40}Ar/^{39}Ar apparent age spectra (i1), ^{40}Ar/^{36}Ar vs. ^{39}Ar/^{36}Ar correlation or isochron diagram (i2) and ^{36}Ar/^{40}Ar vs. ^{39}Ar/^{40}Ar correlation or inverse isochron diagram (i3) for the plateau steps of the sample KT-20-12 (phonolite) from the SDK complex. Other parameters/details are as in the previous figure.

4.2.2. *Geochemical Data*

The data for major and trace element contents, radiogenic Sr-Nd-Pb isotopic ratios, and stable C-O isotopic ratios in samples of carbonatites and alkaline silicate rocks are presented in *Tables 4.6* to *4.17*. The following sections discuss the results of each geochemical dataset generated for this work.

A. Major elements

The major oxides data for alkaline silicate rocks and carbonatites from the SDK complex for this study are provided in *Tables 4.6* and *4.7*, respectively.

Alkaline silicate rocks

The intrusive members of the alkaline silicate rock series of the SDK complex fall mainly into the foidite–phonolite series according to the TAS classification scheme (*Fig. 4.8*; Le Bas &

Streckeisen, 1991). The foidites can be further classified as nephelinite, melanephelinite, and melilitite based on their petrography and CIPW normative mineralogy. Nephelinite and melanephelinite are the most abundant among the foidites. Phonolite dominates among highly differentiated rocks, and basanite, tephrite, and phonotephrite are minor among the alkaline intrusives. Syenite, alkali basalt, and melilitite occur in subordinate proportions.

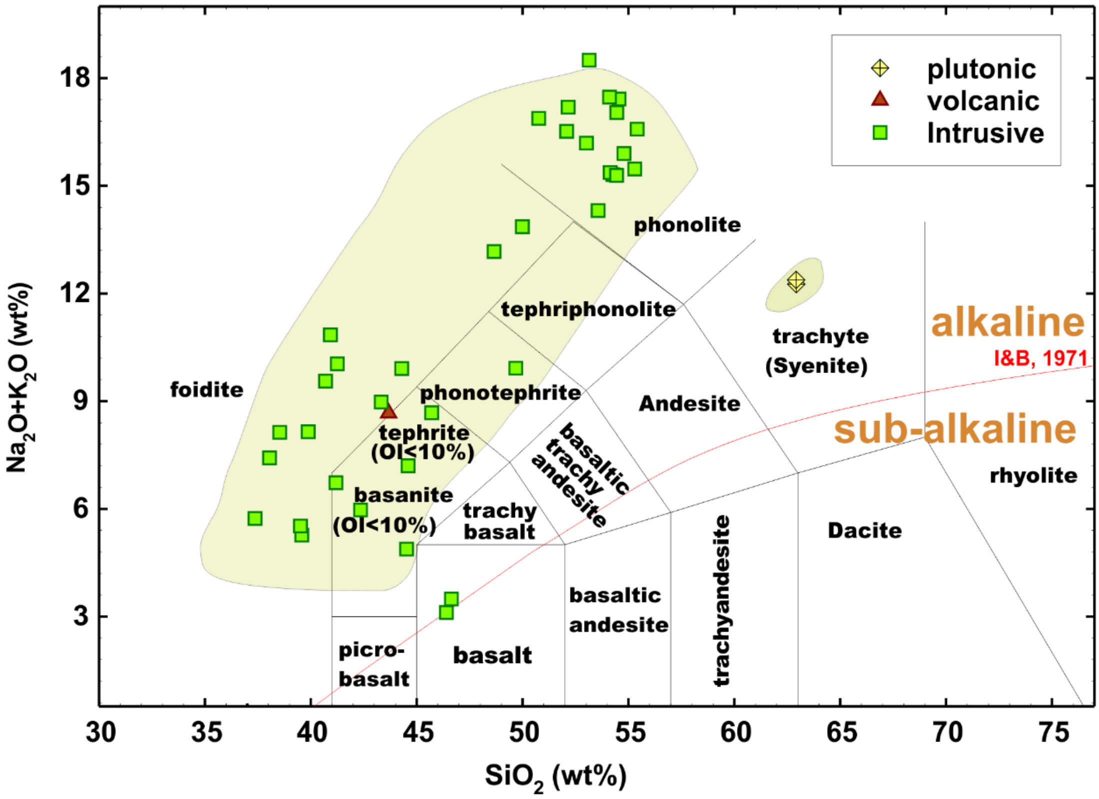

Fig. 4.8. Chemical classification for the alkaline silicate rocks of the SDK complex based on the TAS (Total Alkali Silica) classification scheme of Le Bas & Streckeisen (1991). For comparison, previously reported data for the highly alkaline rocks from the complex (Chandrasekaran et al., 1990; Vijayan et al., 2016) are plotted (shaded field). The dividing line (red) between alkaline (upper) and subalkaline series (lower) is after Irvine & Baragar (1971).

Nephelinites and most melanephelinites have peralkalinity indices (molar Na_2O+K_2O/Al_2O_3) greater than 1.0. Their atomic Mg# (Mg# = 100* [Mg/(Mg + Fe)] vary between 45 and 63. The melanephelinite, KT-18-15, and basanite, KT-20-23, have higher Mg# (55 and 65, respectively) and are part of the primitive alkaline members, besides the alkali basalt of the complex (Mg# = 56). However, the basanite sample contains abundant clinopyroxene phenocrysts (> 50%), so its Mg# is not likely representative of the magma composition. Mg# decreases from 65 to as low as 3 along the foidite-tephrite-phonotephrite-phonolite series. Phonolites that are coarse-grained have higher Mg# than fine-grained ones.

All phonolites are peralkaline with peralkalinity indices varying between 1.07 - 1.26 and Na_2O/K_2O >1.

Bivariate plots between the major oxides vs. SiO_2 are plotted separately for 68.5 million years old rocks *(Fig. 4.10)* and 66.4 million years old rocks *(Fig. 4.11)* of the complex. For the 68.5 Ma rocks, significant negative correlations ($R^2 > 0.6$) exist between SiO_2 and other oxides (MgO, CaO, Fe_2O_3, TiO_2, and P_2O_5). In contrast, alkalis (Na_2O+K_2O) and Al_2O_3 have significant positive correlations with SiO_2 ($R^2 > 0.7$). MgO values of some melanephelinites (e.g., KT-21-4, KT-20-10, KT-18-6) are lower than that of KT-18-4, KT-20-41, and KT-18-11 at similar SiO_2 levels. CaO/Al_2O_3 values show a systematic decline with SiO_2 towards the differentiated rocks. Major oxide data of 66.4 Ma alkaline silicate rocks are plotted together with the data of coeval melilitites from Simonetti et al. (1998) (*Fig.4.11*). No systematic trend is observed between the oxides and SiO_2 in these rocks.

Carbonatites

According to the chemical classification scheme of Woolley & Kempe (1989), most of the carbonatites from the SDK complex fall in the field of calciocarbonatites except for three samples, which are ferrocarbonatites *(Fig. 4.9).* The coarse-grained calciocarbonatites have higher CaO (40-47 wt.%) than the fine-grained calciocarbonatites (35-39 wt.%). SiO_2 contents of all but one calciocarbonatites are <5 wt.% (*Table 4.7*), which is lower than the range observed in ferrocarbonatites (2.39 wt % - 16.64 wt.%). The calciocarbonatites show a higher range of CaO content and a lower range of Al_2O_3, MnO, MgO, $(Fe_2O_3)_t$ contents compared to those in the ferrocarbonatites (*Table 4.7*). Alkali contents of both calciocarbonatites and ferrocarbonatites are low (≤2 wt.%), similar to that observed in the calciocarbonatites worldwide, and are lower than the primary carbonatite melt inclusions (e.g., Guzmics et al., 2012). Na_2O and K_2O contents of some carbonatites are below the detection limits. The TiO_2 content of all carbonatites of the SDK complex is also very low (<0.5 wt.%). The ferrocarbonatites are invariably altered, as noticed in both hand specimens and petrographic studies. The calciocarbonatites in carbonate veins have CaO <30 wt.% but are enriched in SrO and BaO. For example, the carbonatite vein sample KT-20-30C with 35 wt.% CaO contains 4.5 wt.% SrO and 1.7 wt.% of BaO. In bivariate plots of major oxides vs. SiO_2 (*Fig. 4.12*), significant correlations ($R^2 > 0.6$) exist in the plots of Al_2O_3, MgO, TiO_2, P_2O_5, and $(Fe_2O_3)_t$ vs. SiO_2 (*Figs. 4.12a to 4.12e*). On the other hand, the data in MnO and BaO vs. SiO_2 plots (*Figs. 4.12g, 4.12h*) are highly scattered ($R^2 \leq 0.05$). Fe_2O_{3t} (4-10 wt.%), MnO (3-11 wt.%),

SiO_2 (2-5 wt.%), TiO_2 (3-10 wt.%), and Al_2O_3 (2-5 wt.%) contents in ferrocarbonatites are higher than those in calciocarbonatites, whereas their CaO contents (31-38 wt.%) and P_2O_5 (0.09-0.29 wt.%) are lower than their average contents in calciocarbonatites (*Table 4.7*).

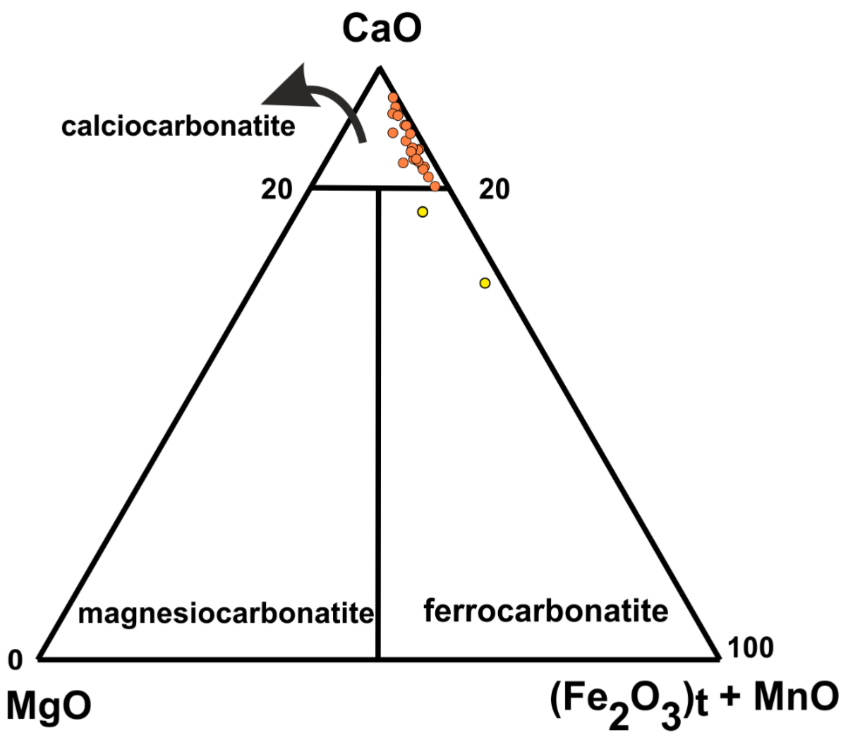

Fig. 4.9. Chemical classification of carbonatites of SDK complex based on the classification scheme of Woolley & Kempe (1989).

B. Trace elements

Alkaline Silicate Rocks

The trace element data for the alkaline silicate rocks from the SDK complex are summarized in *Table 4.8***.** Trace element results show that the most silica-undersaturated alkaline silicate rocks, nephelinites, and melanephelinites contain lower Ni (e.g., 7-42 ppm) and Cr (22-157 ppm) than those observed in the melilitites (95 ppm & 308 ppm, respectively) and are lower than the contents expected in mantle derived primary silicate magmas (e.g., Niu, 2005). Ni and Cr contents, respectively, of other alkaline rocks are as follows: Basanite:107 & 313 ppm; Tephrites: 5-53 ppm & 17-156 ppm; Alkali Basalt: 80 ppm & 152 ppm; Phonotephrite: 4.2-4.7 ppm & 8-29 ppm. The lowest abundances of Ni and Cr, respectively, are observed in phonolitic nephelinites (<3 ppm and <66ppm), phonolites (<4 ppm and <69ppm), syenites (<3 ppm and <73 ppm), and a rhyolite (3 ppm and 180 ppm).

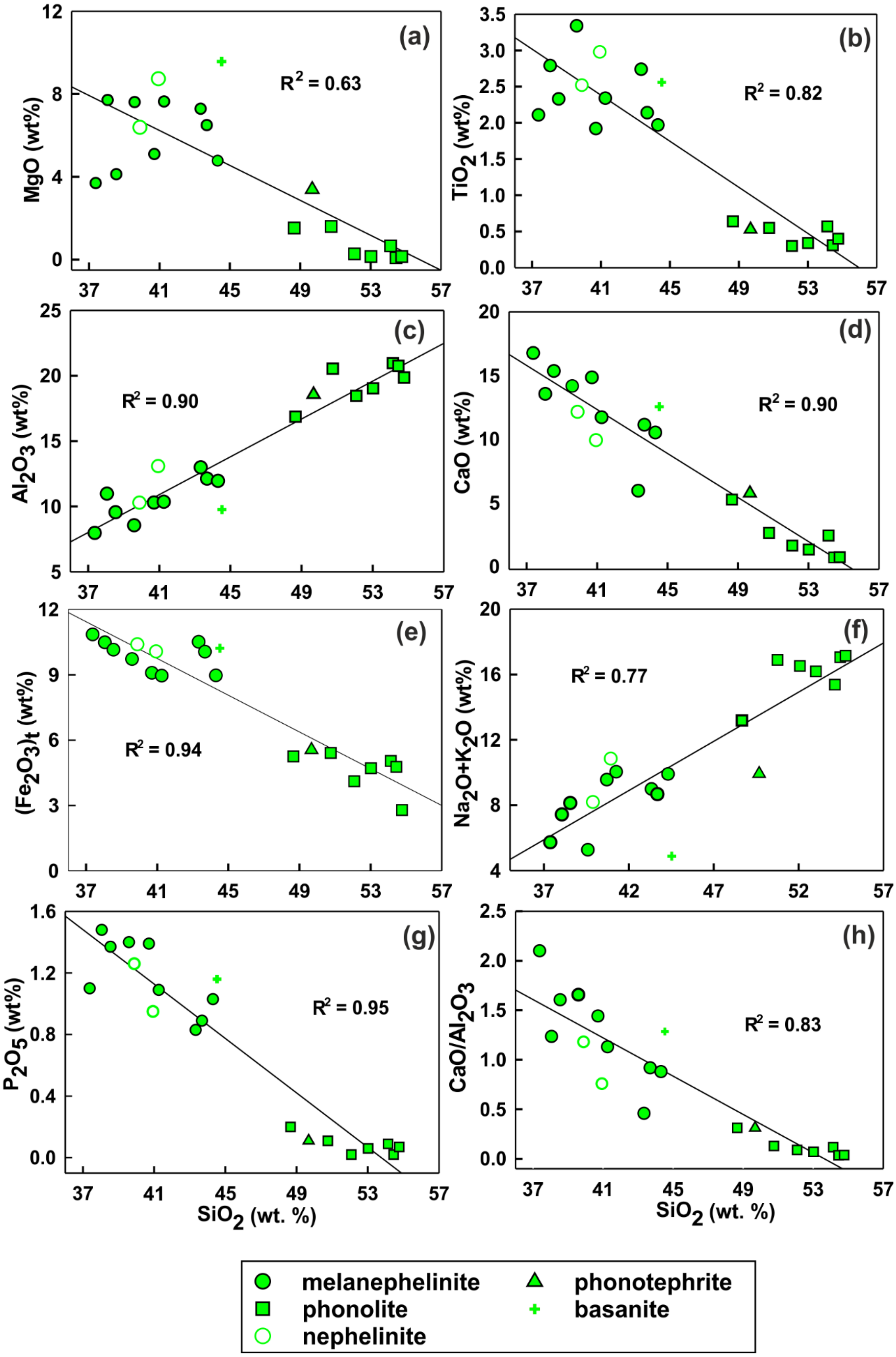

Fig. 4.10. Cross plots of major oxide contents/ratios versus SiO_2 content for 68.5 Ma alkaline silicate rocks from the SDK complex. The linear regressions with R^2 values are also shown.

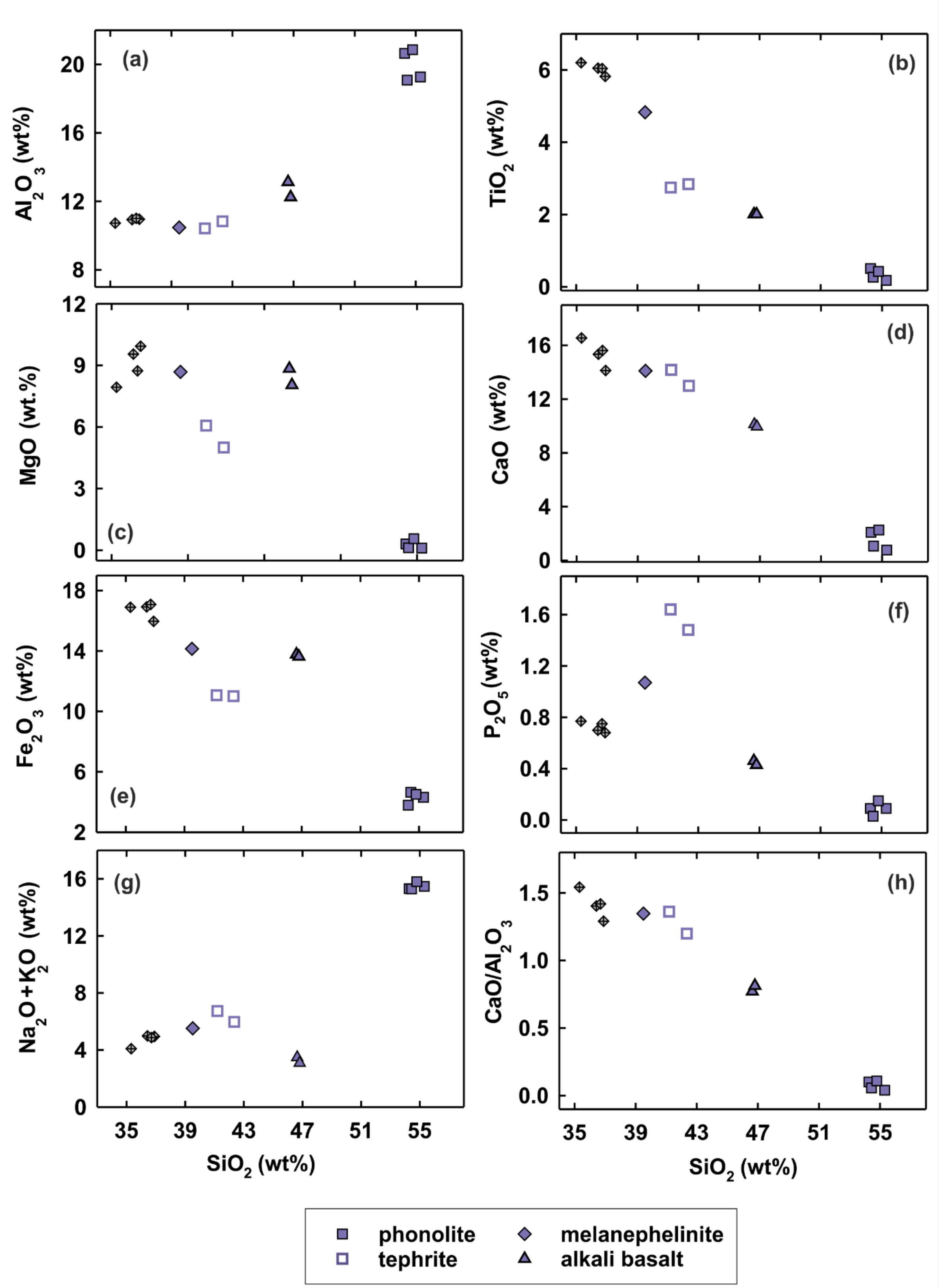

Fig. 4.11. Cross plots of major oxide contents/ratios versus SiO_2 content for 66.4 Ma alkaline silicate rocks from the SDK complex. For comparison, data for the melilitites from the complex (crossed diamonds; Simonetti *et al.*, 1998) are plotted along with our data.

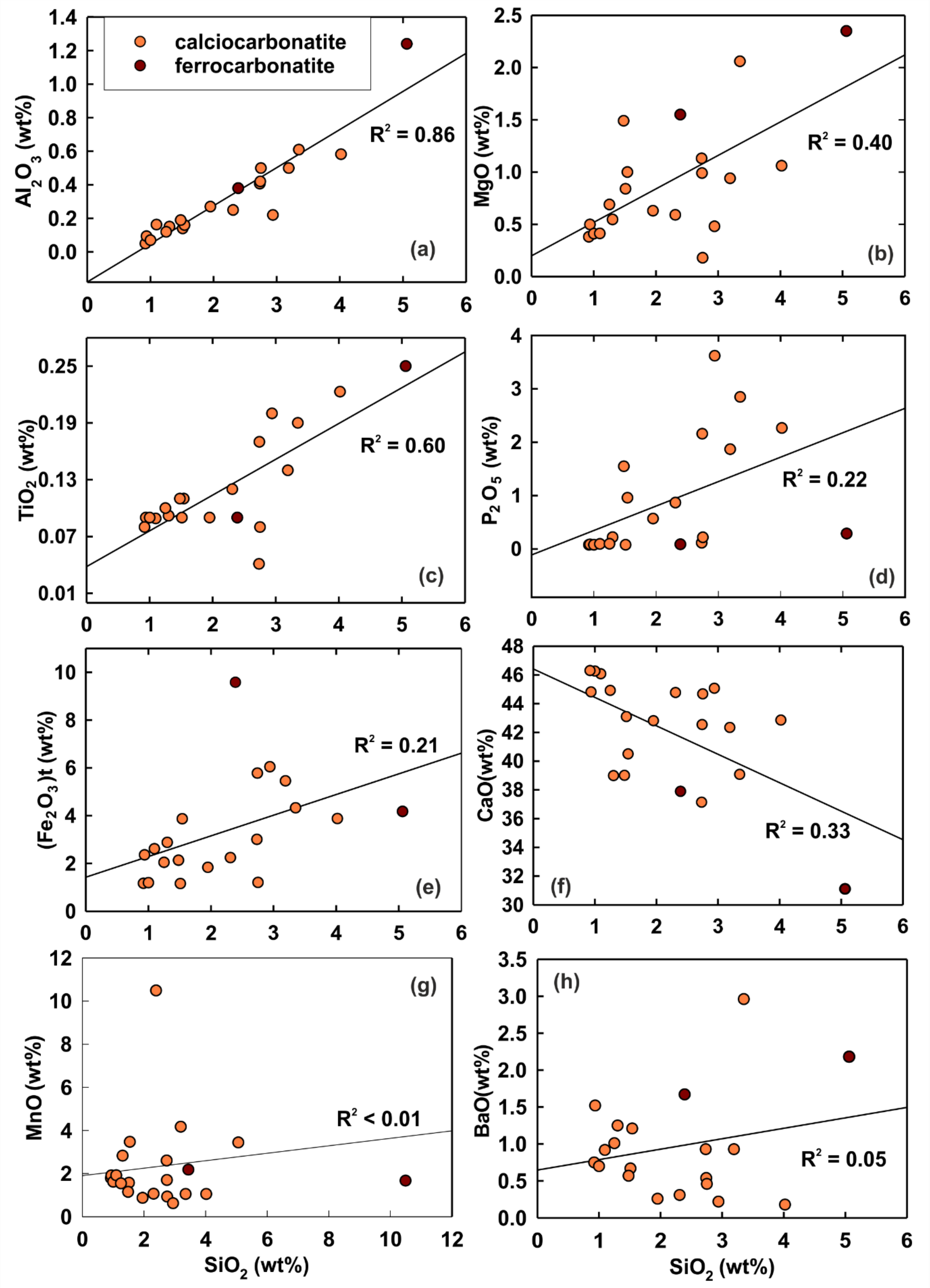

Fig. 4.12. Cross plots of major oxide contents versus SiO_2 content for carbonatites of SDK carbonatites. Also shown are the R^2 values of linear regression lines

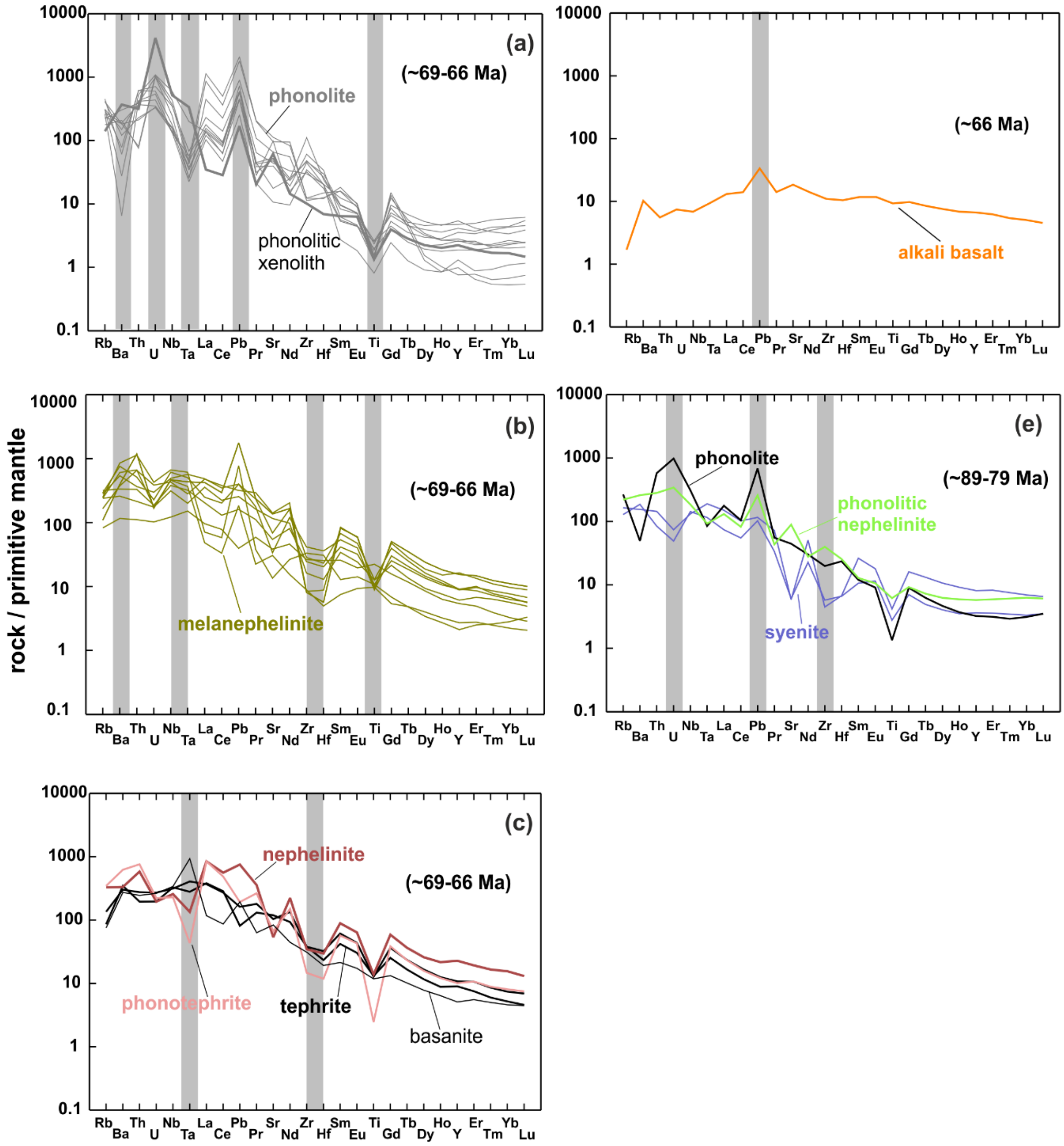

Fig. 4.13. Primitive-mantle normalized trace element patterns for alkaline silicate rock samples from the SDK complex: (a) phonolite and phonolitic xenolith; (b) melanephelinites; (c) nephelinite, phonotephrite, basanite, and tephrite; (d) alkali basalt (SAR-20-2); (e) syenite, phonolitic nephelinite, and phonolite. Some of the anomalous contents are highlighted (gray column). The ages for the samples were inferred from this study and from Sheth et al. (2017). The normalizing values are from Sun and McDonough (1989)

Primitive mantle normalized (Sun and McDonough, 1989) trace element patterns and chondrite normalized rare earth element (REE) patterns for alkaline silicate rocks of SDK complex are presented in *Fig. 4.13* and *Fig. 4.14*, respectively. The alkaline silicate rocks show enrichments in large ion lithophile elements (LILE), such as Rb, Ba, Th, U, and Nb, compared to the rest. The phonolites show pronounced positive anomalies of U, Pb, and Zr and negative anomalies of Ba, Ta, and Ti *(Fig. 4.13a).* These phonolites also have the highest $(La/Yb)_{CN}$, $(La/Sm)_{CN}$, and lowest $(Gd/Yb)_{CN}$, $(Sm/Ho)_{CN}$, Eu/Eu*, and Gd/Gd* among the alkaline series (*Table 4.14*). These rocks can be divided into two groups: (1) Group-A phonolites displaying lower slope or enrichment of LREEs with $(La/Yb)_{CN} < 94$, $(La/Sm)_{CN} < 28$, $(Gd/Yb)_{CN} < 3$, $(Sm/Ho)_{CN} < 4$, Eu/Eu* < 0.9, and Gd/Gd* < 0.2), and (2) Group-B phonolites with higher LREE slope and more pronounced MREE depletion with $(La/Yb)_{CN} > 220$, $(La/Sm)_{CN} > 47$, $(Gd/Yb)_{CN} > 6$, $(Sm/Ho)_{CN} > 6$, Eu/Eu* > 0.6, and Gd/Gd* > 0.1 (*Table 4.8*). Melanephelinites show enrichment in Ba, Th, Nb, and Ta and depletion in Zr, Hf, Sr, U, and Ti (*Fig. 4.13b*). The basanite shows LILE enriched pattern and possesses moderate enrichments in Ta and Pb, whereas tephrites and phonotephrites display depletion in Zr and Hf and enrichment in Ba (*Fig. 4.13c*). The nephelinite sample is marked by negative U, Ta, Sr, Zr, and Hf anomalies *(Fig. 4.13c).* The lone sample of alkali basalt (SAR-20-2) exhibits an OIB-like pattern showing enrichment in LILEs and in High Field Strength Elements (HFSE; such as La, Ce, Pb, Th, U, Nb, Ta; *Fig. 4.13d*). Most of them, except KT-18-15, show positive Pb anomalies. The syenites are less enriched in incompatible elements than other alkaline silicate rocks and are characterized by pronounced negative U and Sr anomalies (*Fig. 4.13e*).

In the chondrite normalized REE patterns, all the alkaline silicate rocks exhibit LREE enriched patterns (*Fig. 4.14a* to *Fig. 4.14e)* with variable $(La/Yb)_{CN}$, $(La/Sm)_{CN}$, $(Gd/Yb)_{CN}$, $(Sm/Ho)_{CN}$. Melanephelinites and the basanite show the lowest LREE fractionation *(Fig. 4.14b)* and negligible Eu anomaly, as indicated by their $(La/Sm)_{CN} <6$, Eu/Eu* <1.0 values (*Table 4.8*). The nephelinites show similar behavior as melanephelinites, whereas tephrites and phonotephrites show intermediate values between those observed in nephelinites/melanephelinites and phonolites *(Fig. 4.14c).* The alkali basalt has lower $(La/Sm)_{CN}$, $(La/Yb)_{CN}$, and higher $(Sm/Ho)_{CN}$ than those of tephrites and has a minor positive Eu anomaly (Eu/Eu*= 1.1, *Fig. 4.14d, Table 4.8*).

Carbonatites

The trace elements data for the carbonatites analyzed for this study are given in *Table 4.9*. Carbonatites show significant enrichment in Ba, Th, Sr, La, and Ce in primitive mantle normalized incompatible trace element patterns *(Fig. 4.15a)*, which is much higher than the carbonatites from other alkaline complexes of the Deccan Igneous Province (e.g., carbonatites of Chhota Udaipur). In addition, pronounced negative Ta, Pb, Zr, and Hf anomalies are observed for most carbonatites. In the chondrite normalized REE plot, carbonatites show LREE

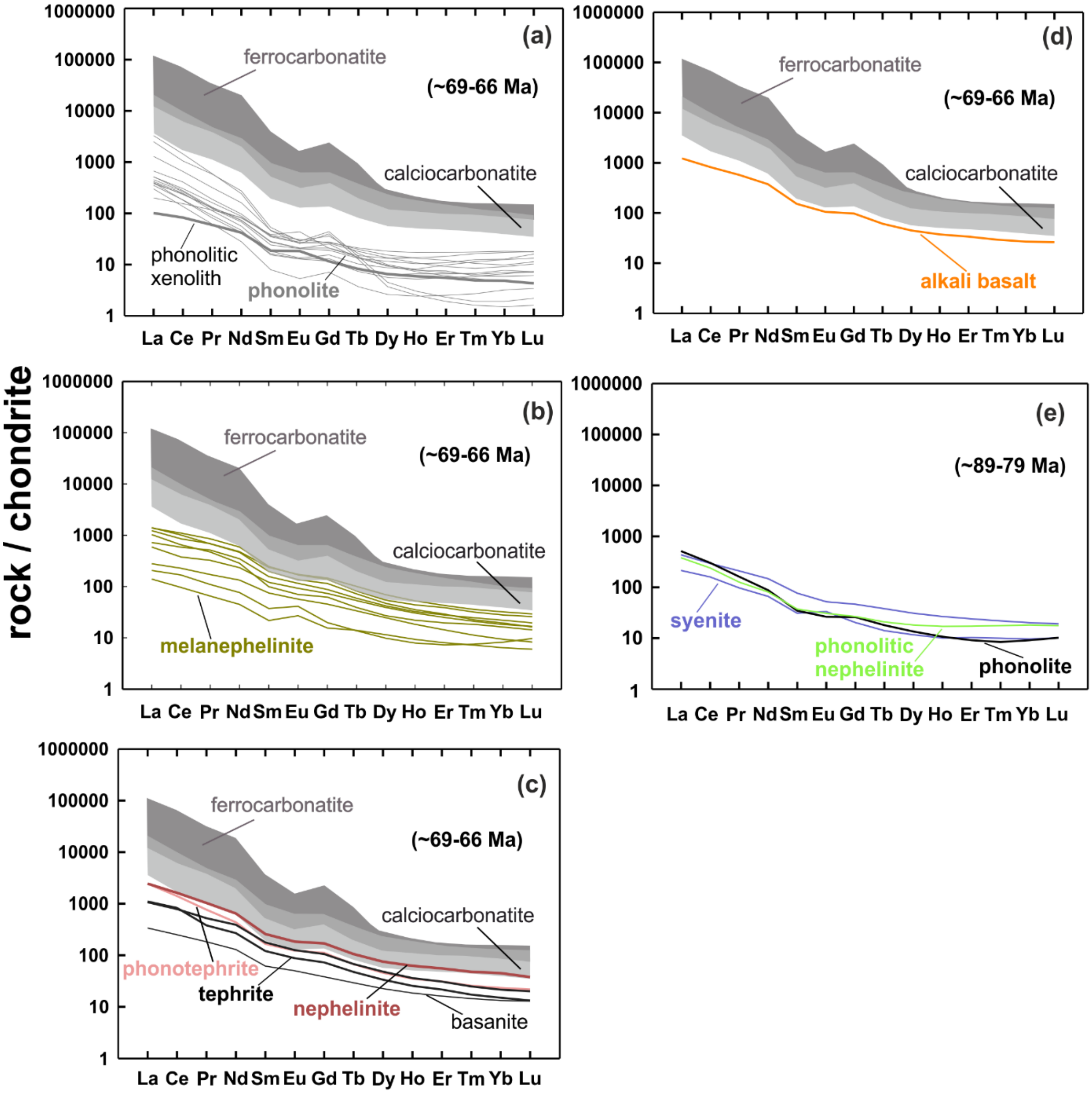

Fig. 4.14. Chondrite normalized rare earth elemental patterns for 69-66 Ma alkaline silicate rock samples (a-d) and 89-79 Ma silicate igneous rocks (e) from the SDK complex: (a) phonolites and phonolitic xenolith; (b) melanephelinites; (c) nephelinite, phonotephrite, basanite, and tephrite; (d) alkali basalt; (e) syenite, phonolitic nephelinite, and phonolite. For comparison, patterns for calciocarbonatites and ferrocarbonatites from the complex are also shown (grey fields). The ages of the samples were inferred from this study and from Sheth et al. (2017). The normalizing values are from Sun and McDonough (1989)

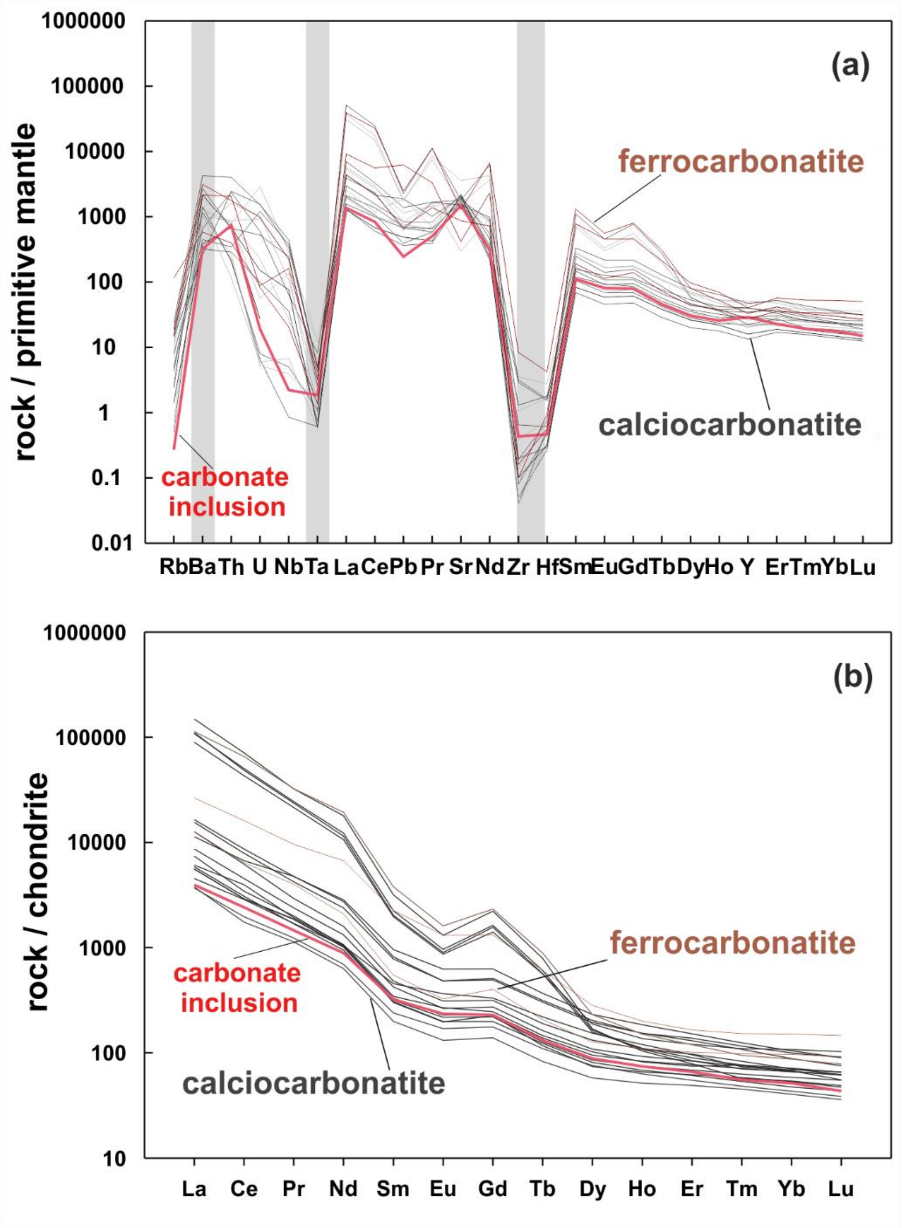

Fig. 4.15. Primitive-mantle normalized incompatible elemental patterns (a) and chondrite normalized REE patterns (b) for the calciocarbonatites (thin gray lines), ferrocarbonatites (light gray field), and carbonate inclusion/xenolith (red line) from the SDK complex. The normalizing values are from Sun and McDonough (1989).

enriched patterns *(Fig. 4.15b, Table 4.9)*. Their LREEs are more fractionated than HREEs, as indicated by higher values of $(La/Sm)_{CN}$ (20-54) than $(Gd/Yb)_{CN}$ (3.-25), except for KT-20-3C, which has $(Gd/Yb)_{CN}$ of 41. Ferrocarbonatites of the complex are more enriched in LREEs compared to the calciocarbonatites, whereas the HREE content of both overlaps. Interestingly, hydrothermal carbonatite veins ($\delta^{18}O > 15‰$) have the highest REE contents than most primary/unaltered massive carbonatites.

4.2.3. *Isotope Data*

A. Stable C-O isotopic compositions

The results of C-O isotopic compositions for the carbonate-bearing alkaline silicate rocks and carbonatites from the SDK complex have been summarized in *Tables 4.10* and *4.11*, respectively, and plotted in *Fig. 4.16*. The carbonate-bearing alkaline silicate rocks show a narrow range of $\delta^{13}C$ variations (-7‰ to -4.4‰), and their $\delta^{18}O$ varies for ~10 ‰ (6.3‰ - 16.3‰). These variations are more restricted compared to the compositions of calcites in the carbonatites of the complex (*Fig. 4.16*). The carbonatites and alkaline silicate rocks have similar $\delta^{13}C$, whereas the carbonatites show a spread towards more enriched $\delta^{13}C$ compositions *(Fig. 4.16b)*. The stacked histogram distribution of $\delta^{18}O$ (*Fig. 4.16c*) for carbonatites and alkaline silicate rocks shows a higher positive skewness compared to the uniformly distributed $\delta^{13}C$. The frequency of $\delta^{18}O$ of the carbonatites is highest between 5.5 to 10‰ and decreases progressively with higher $\delta^{18}O$. Moreover, ~60% of the carbonatites with lower $\delta^{18}O$ (<15‰) show unaltered carbonatite-like signatures, whereas those with higher $\delta^{18}O$ values (15.7 to 24.7‰) are likely altered by secondary processes. The $\delta^{13}C$ values of the altered carbonatites also increase with their $\delta^{18}O$ values, with a few reaching extreme values (-0.7‰).

Most calcite crystals from the carbonatite dykes/plugs/veins (except for 3 crystals) show much lower values and the spread in $\delta^{18}O$ (5.5‰ - 6.8‰) than the groundmass carbonates (8.7‰ - 24.7‰). However, $\delta^{13}C$ of the calcite crystals have higher variations (-6.1‰ to -3.8‰) than their $\delta^{18}O$ values. In addition, the calcite crystals also have the highest $\delta^{13}C$ at the lowest $\delta^{18}O$ values. On the other hand, $\delta^{13}C$ values of groundmass carbonates increase with their $\delta^{18}O$ values. The groundmass carbonates from carbonatite veins have higher $\delta^{13}C$ values at lower $\delta^{18}O$ values.

The lowest $\delta^{13}C$ (-7‰) and the lowest $\delta^{18}O$ (6.3‰) observed in alkaline silicate rocks fall well within the mantle field (*Fig. 4.16c*). Similarly, though the carbonatites display wide variations in $\delta^{13}C$ and $\delta^{18}O$ values, -6.5‰ to -0.7‰ and 5.5‰ to 24.7‰, respectively, the lower range of these values fall well within the variations expected in the mantle (*Fig. 4.16c*). Besides, much of the carbonatite data also falls well within the field defined for "Primary Carbonatites" by Ray and Ramesh (1999) in *Fig. 4.16a*. A carbonate inclusion found in a melanephelinite dyke has similar $\delta^{13}C$ and $\delta^{18}O$ values ($\delta^{13}C = -6.5 \pm 0.1$‰, $\delta^{18}O = 6.6 \pm 0.4$‰) to the unaltered SDK carbonatites.

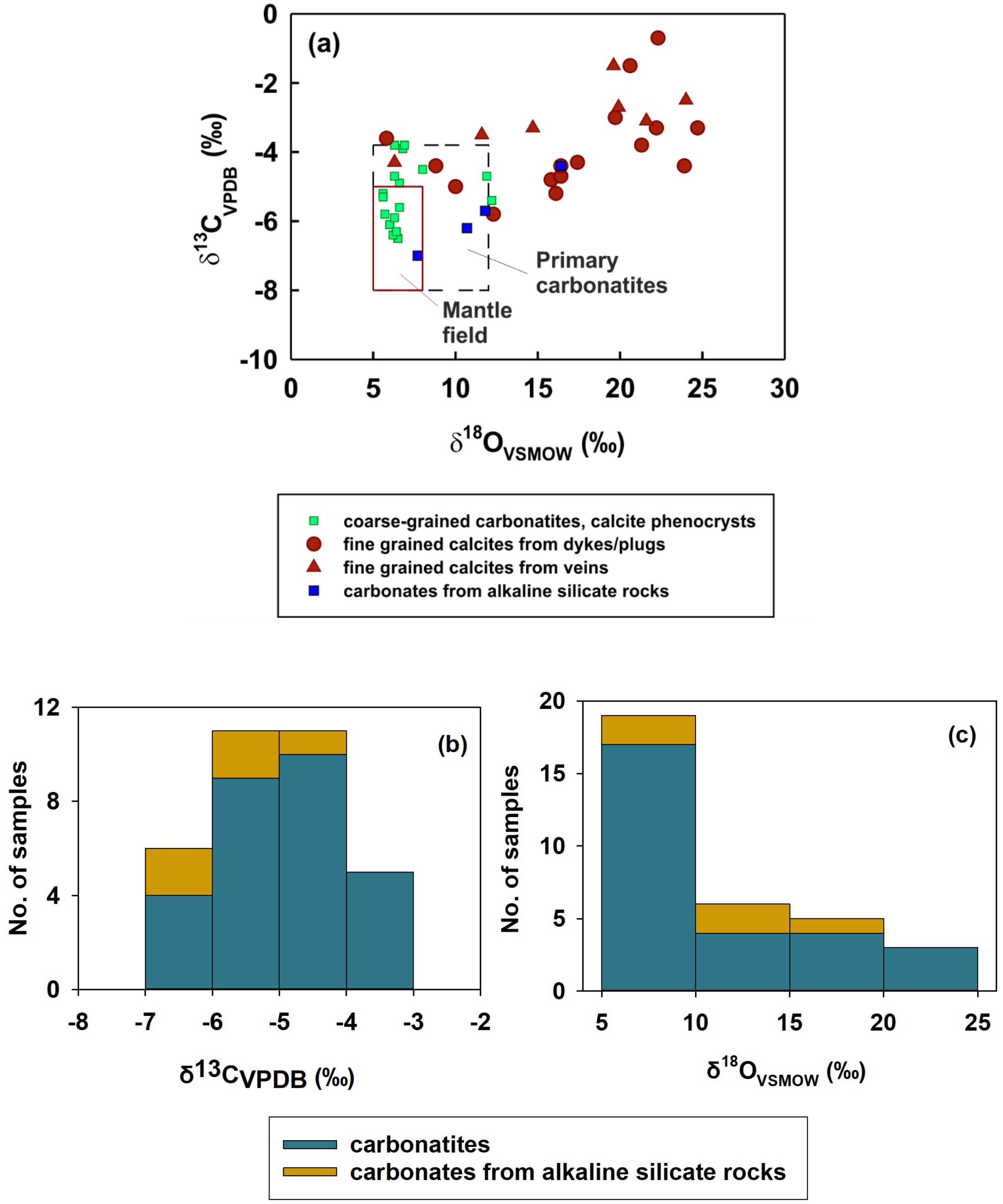

Fig. 4.16. (a) $\delta^{13}C_{VPDB}$ vs. $\delta^{18}O_{VSMOW}$ (in ‰) of calcites in various phases/rocks in the SDK complex. The rectangular field represents mantle compositions as defined in Ray and Ramesh (2006); The dashed box represents the field for primary unaltered carbonatites (after Ray and Ramesh, 1999) (b) and (c) Stacked histogram showing $\delta^{13}C$ and $\delta^{18}O$ distributions in the SDK carbonatites and carbonate-bearing alkaline silicate rocks

B. Radiogenic Sr-Nd-Pb isotopic compositions

The measured radiogenic Sr, Nd, and Pb isotopic ratios, age-corrected initial ratios for the samples analyzed in this study, along with their uncertainties, are summarized in *Tables 4.12-4.17* and plotted in *Fig. 4.17* through *Fig. 4.21*. Since the complex is known to have seen multiple phases of magmatic activities (e.g., Sheth et al., 2017; Bhunia et al., 2022), we have treated rocks of each phase separately to understand their origin and evolution. Therefore, the radiogenic isotopic data, which require age correction for the determination of primary compositions, are presented separately for each phase.

Isotopic compositions of 89 - 79 Ma Alkaline Silicate Rocks

Two syenites and one phonolite sample collected for this work were previously dated to be ~88.5 Ma (Sheth et al., 2017). Their initials Sr isotopic ratios, $(^{87}Sr/^{86}Sr)_i$ = 0.703648 and 0.704135, are the lowest observed ratios in the SDK complex, whereas their $(^{143}Nd/^{144}Nd)i$ values (0.512671-0.512719) overlap with that of the alkaline rocks of 66.5 Ma age group (*Table 4.12*). In terms of ε_{Nd} (t=88.5 Ma) these rocks show typical LREE-depleted mantle values in the range of +2.9 to +3.8. The phonolitic nephelinite sample, dated in this study to be 78.7 Ma, has $(^{87}Sr/^{86}Sr)_i$ and $(^{143}Nd/^{144}Nd)_i$ values of 0.704377 and 0.512694 *(Table 4.12)*, respectively. The Pb isotopic data for the lone sample analyzed for Pb isotopes from this age group, a syenite (KT-20-45; *Table 4.15*), are $(^{206}Pb/^{204}Pb)_i$ = 18.776, $(^{207}Pb/^{204}Pb)_i$ = 15.839 and $(^{208}Pb/^{204}Pb)_i$ = 39.312, fall in the same range of values observed in 68.5 and 66.4 Ma alkaline silicate rocks and carbonatites. In the $(^{87}Sr/^{86}Sr)_i$ vs. Sr *(Fig. 4.19a)* and $(^{143}Nd/^{144}Nd)_i$ vs. Nd plot *(Fig. 4.19b)*, the 89 - 79 Ma alkaline silicate rocks have higher variability in $(^{87}Sr/^{86}Sr)_i$ compared to their $(^{143}Nd/^{144}Nd)_i$, and no systematic mixing trend was observed among these rocks.

Isotopic compositions of 68.5 Ma Carbonatites and associated Alkaline Silicate Rocks

The initial isotopic ratios of Sr and Nd for the 68.5 Ma carbonatites, except four samples, show narrow ranges of variations: $(^{87}Sr/^{86}Sr)_i$ = 0.704225 - 0.704365 and $(^{143}Nd/^{144}Nd)i$ = 0.512663 - 0.512689 (*Figs. 4.17a,b; Table 4.13*). In terms of ε_{Nd} (t=68.5 Ma), these rocks show marginally LREE-depleted mantle values in the range of +2.2 to +2.8. The four samples (KT-18-2C, KT-18-4C, KT-18-5C & KT-21-15C; *Table 4.13*), which appear to be different from others, have relatively higher $(^{87}Sr/^{86}Sr)_i$ = 0.704439 - 0.704551, but similar $(^{143}Nd/^{144}Nd)_i$ = 0.512669 - 0.512678. Three of these samples also show very high $\delta^{18}O$ values (>17‰; *Table 4.11*), which suggests the altered nature of their Sr-O isotope systems. In general, carbonatites of SDK complex show similar or overlapping initial $^{87}Sr/^{86}Sr$ & $^{143}Nd/^{144}Nd$ for their widely

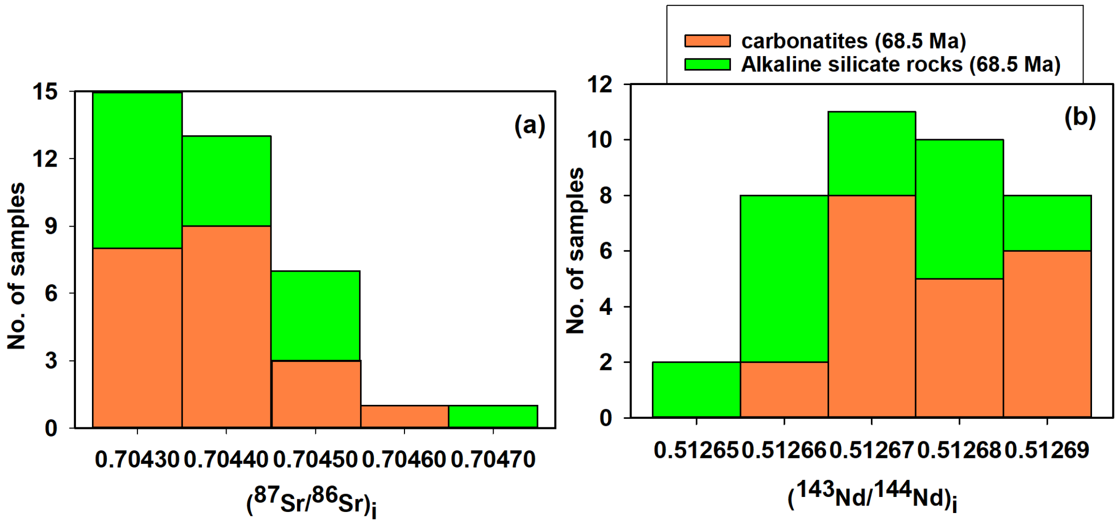

Fig. 4.17. Stacked histogram distributions of initial isotopic ratios of $(^{87}Sr/^{86}Sr)_i$ and $(^{143}Nd/^{144}Nd)_i$ for 68.5 Ma carbonatites and alkaline silicate rocks from the SDK comple

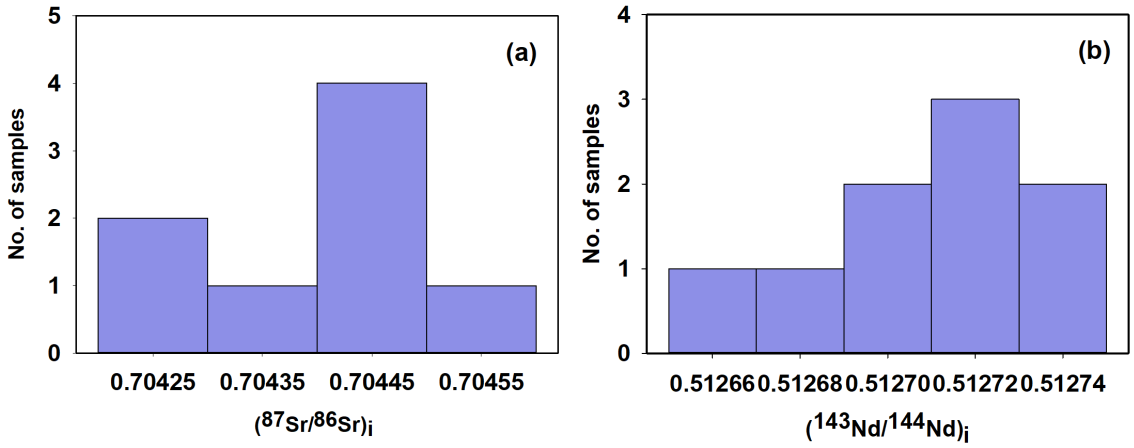

Fig. 4.18. Plots showing stacked histogram distributions of initial isotopic ratios of $(^{87}Sr/^{86}Sr)_i$ and $(^{143}Nd/^{144}Nd)_i$ for 66.4 Ma carbonatites and alkaline silicate rocks.

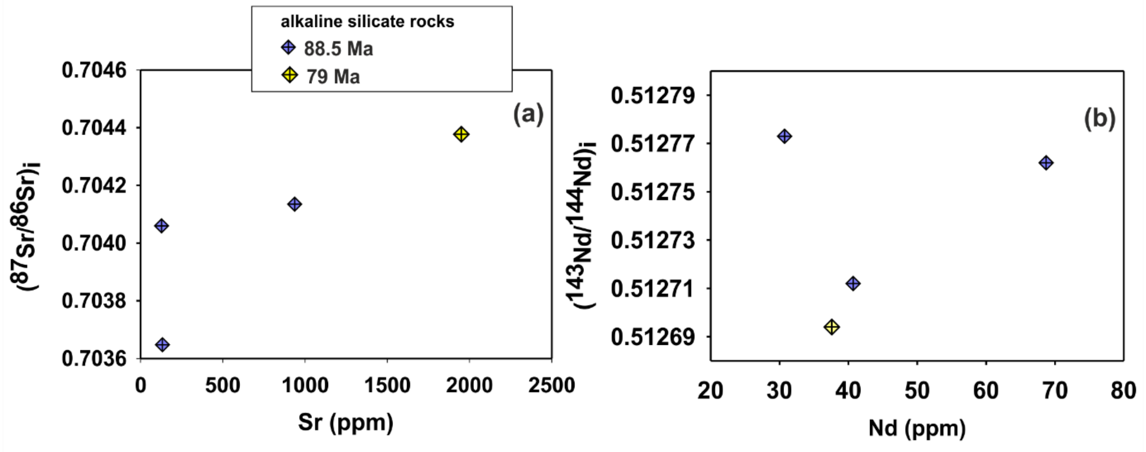

Fig. 4.19. Plots of initial radiogenic isotopic ratios versus concentrations of (a) Sr and (b) Nd for the 89-79 Ma alkaline silicate rock

varying Sr and Nd elemental concentrations (3600 ppm - 46000 ppm; *Fig. 4.20*). The average depleted mantle model age T_{DM} for the carbonatites is 0.38±0.06 (2σ) Ga, which essentially overlaps with that of the alkaline silicate rocks of the same age, i.e., 0.45±0.08 (2σ) Ga (*Table 4.13*).

Unlike the carbonatites, the associated ASRs of the 68.5 Ma age group show much wider variations in their initial Sr-Nd isotopic ratios [$(^{87}Sr/^{86}Sr)_i$ = 0.704251-0.704737; $(^{143}Nd/^{144}Nd)_i$ = 0.512648-0.512687], particularly in the $^{87}Sr/^{86}Sr$ variation (*Figs. 4.17a,b; Table 4.13*). However, there is a clear overlap of lower and higher ranges of $(^{87}Sr/^{86}Sr)_i$ and $(^{143}Nd/^{144}Nd)_i$ for both rock types. Also, these variations are much smaller when compared with similar data from other Indian alkaline igneous complexes (e.g., Amba Dongar, Mundwara, Sung Valley). Among ASRs, some phonolites and tephriphonolites exhibit higher radiogenic Sr and lower radiogenic Nd isotopic compositions compared to the rest *(Table 4.13)*, a typical signature of crustal contamination by the parental magma. The melanephelinite sample KT-20-20, which possesses a relatively higher $(^{87}Sr/^{86}Sr)_i$ than the rest (0.704513) at similar $(^{143}Nd/^{144}Nd)_i$ is appears to be altered. In the $(^{87}Sr/^{86}Sr)_i$ vs. Sr plot *(Fig. 4.20a)*, ASRs show progressively higher $(^{87}Sr/^{86}Sr)_i$ with decreasing Sr concentration, whereas their $(^{143}Nd/^{144}Nd)_i$ appears to decrease with a decrease in Nd concentration (*Fig. 4.20b)*. In terms of ε_{Nd} (t=68.5 Ma), the unaltered/uncontaminated rocks show marginally LREE-depleted mantle values as well as the carbonatites.

Unlike Sr-Nd isotopic ratios, Pb isotopic ratios of carbonatites and alkaline silicate rocks of the SDK overlap significantly, although the latter show larger spreads *(Table 4.16)*. The average values of the initial ratios of $(^{206}Pb/^{204}Pb)_i$, $(^{207}Pb/^{204}Pb)_i$, and $(^{208}Pb/^{204}Pb)_i$ of the 68.5 Ma carbonatites are 18.960±0.101, 15.571±0.047 and 39.152±0.179, respectively, whereas those of the associated alkaline silicate rocks are: 19.019±0.275, 15.611±0.016 and 39.099±0.344, respectively, at 1 sigma. Interestingly, the carbonate xenolith/inclusion has the same Pb isotopic compositions (18.966, 15.569, and 39.169), within errors, as the average compositions observed for the carbonatites *(Table 4.16)*. In the isotopic ratio versus Pb content plots (*Figs. 4.20 c, d, e)*, ASRs show larger variations in $^{206}Pb/^{204}Pb$ and $^{208}Pb/^{204}Pb$ at lower Pb concentrations, hinting at possible crustal contamination of the primary magma.

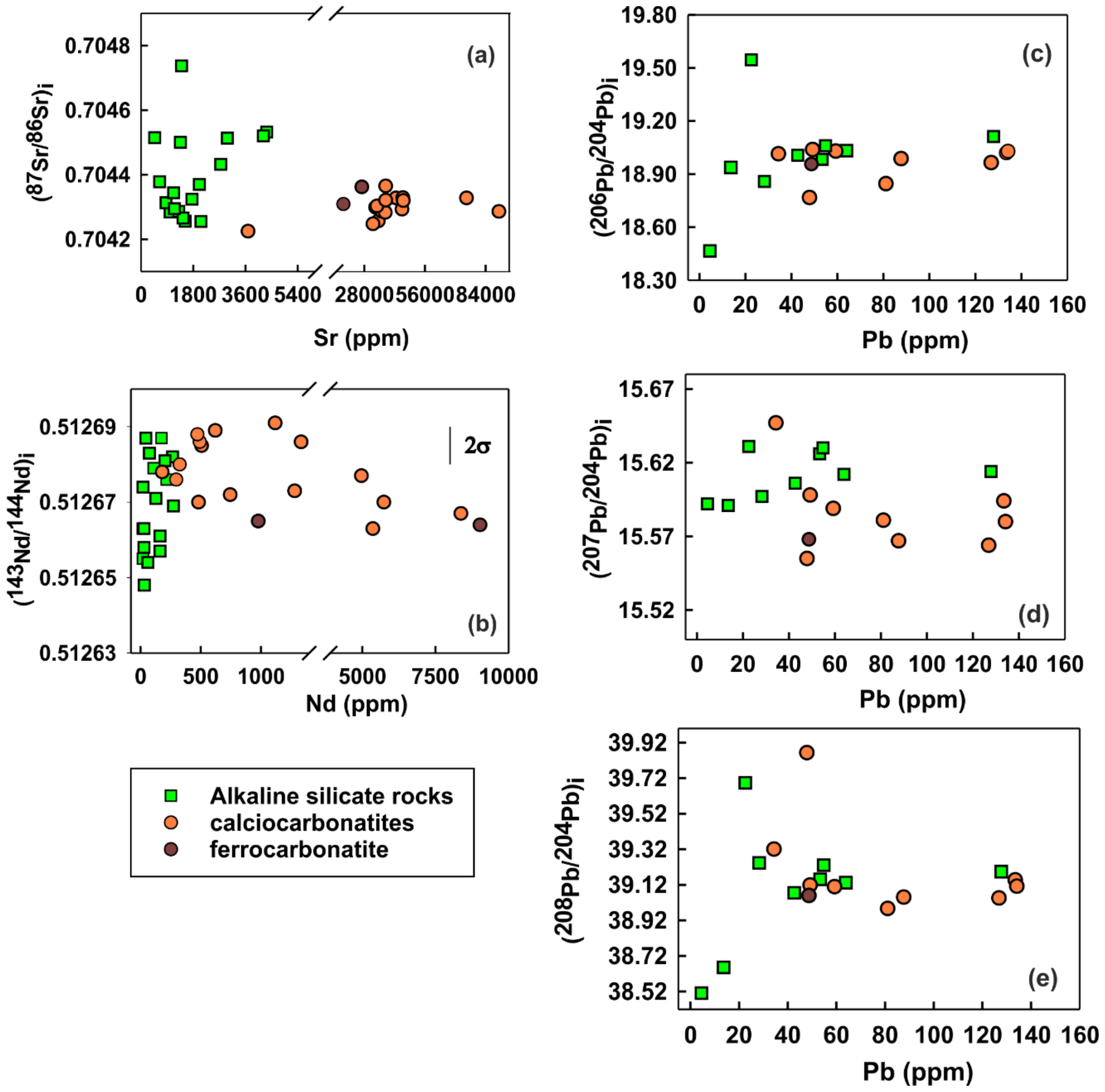

Fig. 4.20. Plots of initial radiogenic isotopic ratios versus concentrations of Sr, Nd and Pb for the 68.5 Ma calciocarbonatites, ferrocarbonatites, and alkaline silicate rocks of the SDK complex: (a) $(^{87}Sr/^{86}Sr)_i$ vs. Sr; (b) $(^{143}Nd/^{144}Nd)_i$ vs. Nd; (c) $(^{206}Pb/^{204}Pb)_i$ vs. Pb; (d) $(^{207}Pb/^{204}Pb)_i$ vs. Pb, (e) $(^{208}Pb/^{204}Pb)_i$ vs. Pb.

Isotopic compositions of 66.4 Ma Alkaline Silicate Rocks

The youngest magmatic rocks of the SDK complex are a few alkaline silicate and basaltic dykes. These rocks essentially show similar initial $(^{87}Sr/^{86}Sr)_i$ as that observed in older rocks *(Table 4.14)*. However, their $(^{143}Nd/^{144}Nd)_i$ values are somewhat higher, with ε_{Nd} (t=66.5 Ma) values going up to +3.4 *(Table 4.14)*, compared to the ε_{Nd}^t variation older magmatic rocks of

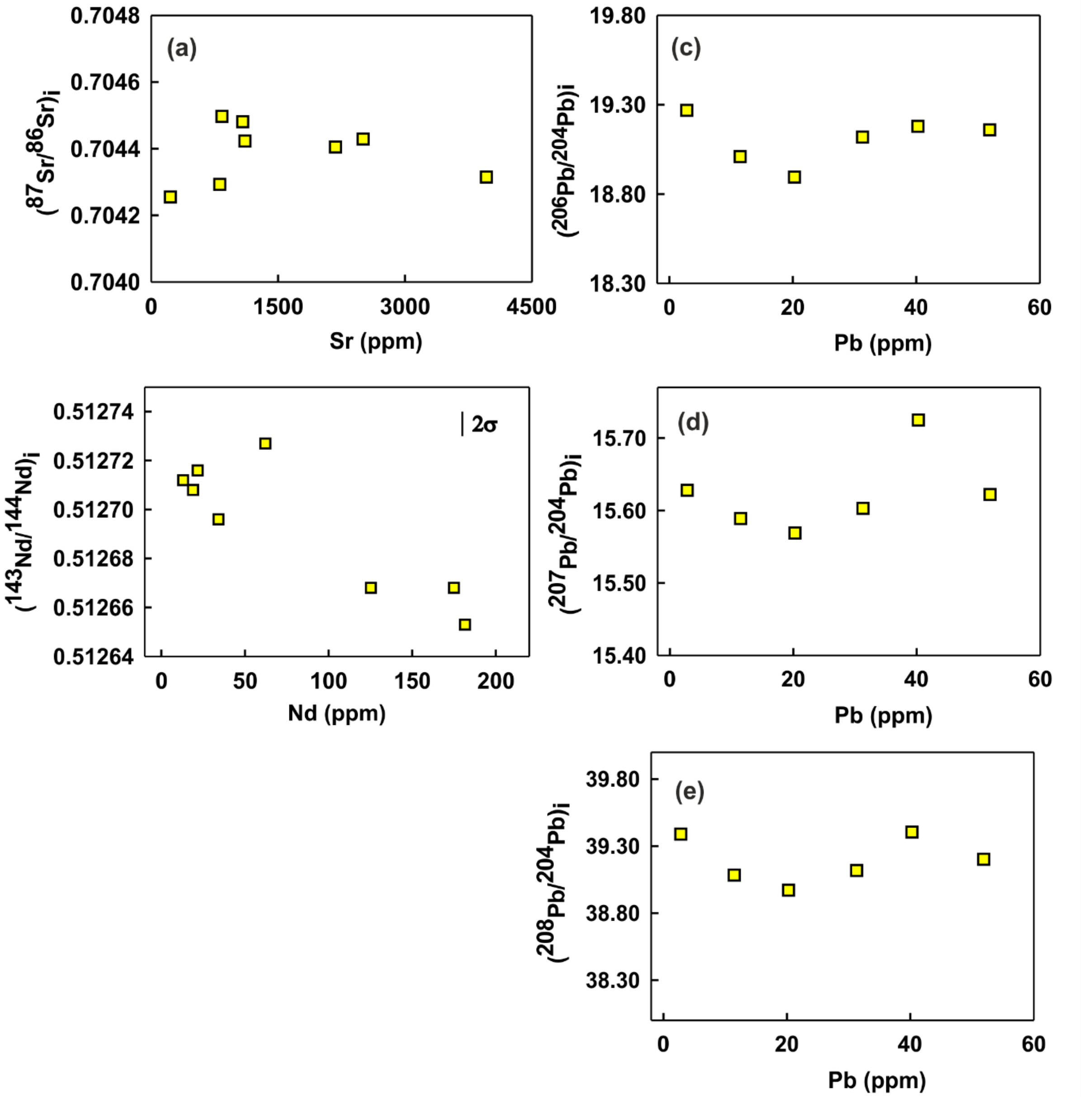

Fig. 4.21. Plots of initial radiogenic isotopic ratios versus concentrations of Sr, Nd and Pb for the 66.4 Ma alkaline silicate rocks of the SDK complex: (a) $(^{87}Sr/^{86}Sr)_i$ vs. Sr; (b) $(^{143}Nd/^{144}Nd)_i$ vs. Nd; (c) $(^{206}Pb/^{204}Pb)_i$ vs. Pb; (d) $(^{207}Pb/^{204}Pb)_i$ vs. Pb, (e) $(^{208}Pb/^{204}Pb)_i$ vs. Pb.

the complex (+1.9 to +2.8). Interestingly, the average T_{DM} value of the 66.4 Ma rocks (0.42±0.04 Ga) is the same as that of the 68.5 Ma (0.42±0.10) and 88.4 Ma rocks (0.43±0.04 Ga), within 2 sigma uncertainty. The alkali basalt sample (not shown), SAR-20-2, is unusually lower $(^{87}Sr/^{86}Sr)_i$ (=0.702817) than the rest, although it's $(^{143}Nd/^{144}Nd)_i$ falls in the observed range. Such a composition is atypical for Deccan Igneous Province and indicative of derivation from a LILE-depleted mantle source. A pyroxene phenocryst from a tephriphonolite (SAR-20-5) shows similar isotopic compositions ($^{87}Sr/^{86}Sr_i$ = 0.704380; $\varepsilon_{Nd}(t)$= +2.4) to those of the coeval rocks. As for the Pb isotopic compositions, barring the alkali basalt SAR-20-2 that possesses much lower radiogenic Pb isotopic ratios, the average (^{206}Pb/^{204}Pb)$_i$, (^{207}Pb/^{204}Pb)$_i$, and (^{208}Pb/^{204}Pb)$_i$ are 18.900±0.560, 15.599±0.075, and 38.957±0.719, respectively, which overlap with compositions of the older magmatic rocks of the complex. In the (^{87}Sr/^{86}Sr)$_i$ vs. Sr and (^{143}Nd/^{144}Nd)$_i$ vs. Nd plots *(Fig. 4.21a,b)*, the alkaline silicate rocks show a minor increase in (^{87}Sr/^{86}Sr)$_i$ and minor decrease in (^{143}Nd/^{144}Nd)$_i$ with a decrease in Sr and an increase in Nd concentration, respectively. In Pb isotopic ratio vs. concentration plots (*Fig. 4.21 c, d, e)*, the alkaline silicate rocks (except for one sample with the lowest Pb content) have similar initial Pb isotopic ratios.

Table 4.1. Samples for ^{40}Ar-^{39}Ar dating and J parameters obtained

Sample	Description	J value (± 2σ)
KT-18-3	Phonolite (whole rock)	0.000381243±0.0000019
KT-18-7	Biotite separates from a carbonatite	0.000393797±0.0000020
KT-18-9	Phonolite (whole rock)	0.00038567±0.0000019
KT-18-12	Phonolite (whole rock)	0.000413778±0.0000021
KT-20-12	Phonolite (whole rock)	0.001033127 ± 0.0000052
KT-20-17	Sanidine separates from a phonolite	0.001043741 ± 0.0000053
KT-20-31	Biotite separates from a tephrite	0.001001639 ± 0.0000050
KT-20-39	Phonolitic nephelinite (whole rock)	0.001120405 ± 0.0000057
SAR-20-5	tephriphonolite (whole rock)	0.000923929 ± 0.0000046

Note: Analytical details are presented in section 3.3.

Table 4.2. Summary of results of ^{40}Ar-^{39}Ar dating

Sample	Plateau					Isochron				Inverse Isochron			
	Steps	% ^{39}Ar released	Age (Ma) ±2σ	MSWD	Probability	Age (Ma) ±2σ	$(^{40}Ar/^{36}Ar)_{initial}$ ±2σ	MSWD	Probability	Age (Ma) ±2σ	$(^{40}Ar/^{36}Ar)_{initial}$ ±2σ	MSWD	Probability
KT-18-3 (ASR-wr)	12	91.5	68.3 ± 0.4	0.15	1.00	68.3 ± 0.7	295.0 ± 11	0.03	1.00	68.3 ± 0.5	295.2 ± 6.8	0.06	1.00
KT-18-7 (CAR-bio)	8	79.3	68.6 ± 0.4	0.07	1.00	68.6 ± 0.5	295.4 ±5.1	0.02	1.00	68.6 ± 0.4	295.3 ±3.1	0.09	1.00
KT-18-9 (ASR-wr)	11	95.2	68.5 ± 0.4	0.73	0.70	68.5 ± 0.4	295.2 ± 3.0	0.10	1.00	68.5 ± 0.4	295.3 ± 2.1	0.39	0.94
KT-18-12 (ASR-wr)	10	89.9	68.5 ± 0.4	0.54	0.86	68.5 ± 0.6	299 ± 11	0.05	1.00	68.5 ± 0.4	298.7 ± 6.6	0.29	0.98
KT-20-12 (ASR-wr)	10	66.4	69.7 ± 0.4	0.36	0.95	69.7 ± 0.5	295.2 ± 2.9	0.13	1.00	69.7 ± 0.4	295.1 ± 2.4	0.32	0.96
KT-20-17 (ASR-san)	11	76.8	66.7 ± 0.4	0.80	0.63	66.6 ± 0.5	297.4 ± 7.4	0.41	0.93	66.6 ± 0.4	297.1 ± 5.2	0.78	0.63
KT-20-31 (ASR-bio)	9	65.7	66.3 ± 0.4	0.42	0.91	66.3 ± 0.4	295.3 ± 2.8	0.23	0.98	66.3 ± 0.4	295.1 ± 2.5	0.44	0.88
KT-20-39 (ASR-wr)	9	54.6	78.7 ± 0.4	0.43	1.00	78.7 ± 0.5	293.7 ± 4.2	0.43	0.88	78.8 ± 0.5	293.6 ± 2.9	0.94	0.48
SAR-20-5 (ASR-wr)	11	63.6	66.3 ± 0.4	0.83	0.60	66.3 ±0.4	295.5 ± 2.3	0.34	0.96	66.3 ± 0.4	295.3 ±2.1	0.84	0.58

Note: ASR= alkaline silicate sock; CAR= carbonatite; wr= whole rock; bio = biotite; san=sanidine; MSWD = Mean Squared Weighted Deviate

Table. 4.3. EMPA data for feldspar in one carbonatite and two alkaline silicate rocks from the SDK complex.

	feldspars							
Sample#	KT-18-1C	KT-18-1C	KT-18-1C	KT-20-31	KT-20-31	KT-21-4A		
rock	CC	CC	CC	TP	TP	MN	MN	MN
description	pt(H) (7)	pt (E)	rim	p/core	p/rim	pt (E) (7)	pt (H) (7)	mp
SiO_2	65.71	70.17	66.00	69.08	70.82	68.99	64.41	63.98
TiO_2	b.d.	b.d.	b.d.	b.d.	b.d.	b.d	b.d.	0.09
Al_2O_3	18.44	20.05	18.21	20.10	19.74	18.91	18.35	17.48
FeO	0.65	0.09	0.11	0.19	0.49	0.56	0.10	1.24
MnO	0.03	b.d.	b.d.	b.d.	b.d.	0.02	0.01	0.04
MgO	0.14	0.01	0.01	b.d.	0.33	0.03	0.01	0.26
CaO	b.d.	0.72	b.d.	0.09	0.51	0.29	0.04	2.23
Na_2O	0.68	9.54	0.52	9.84	8.28	9.93	1.05	8.72
K_2O	14.18	0.59	14.67	0.14	0.31	0.45	13.61	1.26
P_2O_5	0.01	b.d.	0.01	b.d.	b.d.	0.08	0.01	0.57
F	-	-	-	-	-	-	-	0.03
SrO	0.01	0.05	0.01	0.01	0.09	b.d.	0.01	0.03
BaO	0.42	0.07	0.35	0.04	0.08	0.07	1.03	0.09
Nb_2O_5	0.03	b.d.	0.01	b.d.	b.d.	n.a.	n.a.	0.01
Rb_2O	b.d.	b.d.	b.d.	b.d.	b.d.	b.d.	b.d.	n.a.
La_2O_3	0.01	0.02	b.d.	b.d.	b.d.	0.01	0.01	n.a.
Ce_2O_3	0.04	0.01	0.07	0.01	0.01	0.01	0.17	n.a.
Pr_2O_3	0.07	0.12	0.18	b.d.	0.09	0.01	0.05	n.a.
Nd_2O_3	0.02	b.d.	0.04	0.02	0.06	0.03	0.01	n.a.
Sm_2O_3	0.04	0.14	0.01	b.d.	b.d.	0.03	0.04	n.a.
Eu_2O_3	0.10	0.02	0.01	0.20	0.07	0.06	0.06	n.a.
Gd_2O_3	b.d.	b.d.	0.01	b.d.	b.d.	0.03	0.04	n.a.
Tb_2O_3	0.07	0.06	0.02	0.06	0.13	0.05	0.03	n.a.
Dy_2O_3	0.09	0.16	0.04	0.08	0.19	0.05	0.06	n.a.
HOO_3	0.07	0.24	0.04	b.d.	0.08	0.05	0.11	n.a.
Er_2O_3	0.10	b.d.	0.11	b.d.	b.d.	0.04	0.06	n.a.
Tm_2O_3	0.03	0.18	0.12	0.12	b.d.	0.13	0.04	n.a.
Yb_2O_3	0.10	b.d.	b.d.	b.d.	0.14	0.07	0.13	n.a.
Lu_2O_3	0.12	b.d.	0.11	b.d.	b.d.	0.02	0.04	n.a.
sum	101.16	102.24	100.63	99.99	101.42	99.91	99.47	96.03
An	0	4	0	0	3	2	11	0
Ab	7	92	5	99	94	96	81	11
Or	93	4	95	1	2	3	8	89
number of ions calculated on the basis of 32 O atoms								
Si	12.220	12.320	12.290	12.304	12.701	12.330	12.156	12.001
Ti	0.000	0.000	0.000	0.000	0.000	0.000	0.000	0.013
Al	4.041	4.148	3.996	4.218	4.171	3.982	4.082	3.865
Fe(ii)	0.101	0.013	0.016	0.029	0.074	0.083	0.016	0.195
Ca	0.000	0.136	0.000	0.016	0.099	0.056	0.008	0.449
Na	0.244	3.246	0.187	3.398	2.879	3.441	0.386	3.170
K	3.363	0.132	3.485	0.032	0.070	0.103	3.276	0.300
Ba	0.031	0.005	0.026	0.003	0.006	0.005	0.076	0.006
TOTAL	20.000	20.000	20.000	20.000	20.000	20.000	20.000	20.000

Note: b.d. - below detection limit, n.a. – not analyzed, TP: tephrite, MN: melanephelinite, CC : calciocarbonatite, pt(H): perthite (host phase), pt (E): perthite (exsolution lamellae), mp : microphenocryst. Numbers in the brackets are the no. of analyses. EPMA detection limits for most of the major elements (oxides) are ≤ 0.01wt%.

Table 4.4. EMPA analyses of carbonate inclusions in the host K-feldspar in a melanephelinite dyke.

	Carbonate inclusions		
Sample#	KT-21-4A	KT-21-4A	KT-21-4A
rock	MN	MN	MN
Host mineral	Kfs	Kfs	Kfs
SiO_2	b.d.	b.d.	0.56
TiO_2	n.a.	n.a.	n.a.
Al_2O_3	0.02	0.03	0.07
FeO	0.92	0.55	1.13
MnO	0.71	0.54	0.68
MgO	0.17	0.10	0.11
CaO	55.55	52.59	52.25
Na_2O	0.02	0.08	0.20
K_2O	0.11	0.29	0.01
P_2O_5	b.d.	0.03	0.07
F	n.a	n.a	n.a
SrO	0.77	1.82	0.26
BaO	0.23	0.45	0.05
Nb_2O_5	n.a.	n.a.	n.a.
Rb_2O	b.d.	0.02	b.d.
La_2O_3	0.03	0.02	b.d.
Ce_2O_3	0.05	0.12	0.07
Pr_2O_3	b.d.	0.09	0.06
Nd_2O_3	0.04	b.d.	0.04
Sm_2O_3	0.06	b.d.	b.d.
Eu_2O_3	b.d.	b.d.	b.d.
Gd_2O_3	b.d.	b.d.	b.d.
Tb_2O_3	b.d.	b.d.	b.d.
Dy_2O_3	0.22	0.58	0.38
HOO_3	b.d.	0.03	b.d.
Er_2O_3	b.d.	b.d.	b.d.
Tm_2O_3	0.07	b.d.	0.05
Yb_2O_3	0.02	b.d.	b.d.
Lu_2O_3	b.d.	0.18	0.26
sum	59.99	57.53	56.33

Note: MN:melanephelinite; Kfs: K-feldspar; other abbreviations and detection limits are same as that in Table 4.3.

Table 4.5. EMPA data for carbonate inclusions in different host mineral phases of a carbonatite.

	carbonate inclusions							
Sample#	KT-18-1C							
rock	CC							
host mineral	Kfs	Kfs	Kfs	Kfs	mt	mt	ap	ap
SiO_2	b.d.	b.d.	b.d.	b.d.	b.d.	b.d.	b.d.	b.d.
TiO_2	b.d.	b.d.	b.d.	b.d.	b.d.	b.d.	b.d.	b.d.
Al_2O_3	0.72	0.01	b.d.	b.d.	b.d.	b.d.	b.d.	b.d.
FeO	0.90	1.09	0.98	1.22	2.60	3.21	0.47	0.45
MnO	1.76	2.43	1.68	2.74	2.04	2.32	1.46	0.92
MgO	0.22	b.d.	0.10	b.d.	0.07	0.23	0.02	0.08
CaO	47.74	53.10	48.17	54.11	43.55	49.07	54.40	48.08
Na_2O	0.15	b.d.	0.02	0.02	0.03	0.01	0.03	0.12
K_2O	0.06	0.16	0.11	0.01	b.d.	b.d.	b.d.	b.d.
P_2O_5	0.24	0.09	0.03	0.04	0.05	0.15	7.86	17.42
F	b.d.	b.d.	b.d.	b.d.	b.d.	b.d.	b.d.	b.d.
SrO	1.38	0.92	0.71	1.22	2.93	1.07	2.16	2.13
BaO	0.13	0.06	0.05	0.03	0.01	0.12	0.09	0.03
Nb_2O_5	0.03	b.d.	b.d.	0.04	b.d.	0.05	b.d.	b.d.
Rb_2O	b.d.	b.d.	b.d.	b.d.	b.d.	b.d.	b.d.	0.01
La_2O_3	0.01	0.03	0.01	0.02	0.07	0.03	0.09	0.11
Ce_2O_3	0.03	0.05	0.03	0.04	0.22	0.03	0.28	0.19
Pr_2O_3	b.d.	0.21	b.d.	b.d.	b.d.	0.12	b.d.	0.12
Nd_2O_3	0.03	b.d.	b.d.	0.08	0.04	0.09	0.12	0.11
Sm_2O_3	b.d.	0.25	0.02	0.13	b.d.	b.d.	b.d.	0.17
Eu_2O_3	b.d.	b.d.	b.d.	b.d.	b.d.	b.d.	b.d.	b.d.
Gd_2O_3	b.d.	b.d.	0.01	b.d.	0.06	b.d.	0.01	0.07
Tb_2O_3	0.14	b.d.	0.11	0.14	b.d.	b.d.	b.d.	0.11
Dy_2O_3	0.50	0.84	1.06	0.46	0.41	1.06	0.40	0.52
HOO_3	b.d.	b.d.	0.02	b.d.	0.08	b.d.	b.d.	b.d.
Er_2O_3	b.d.	b.d.	b.d.	b.d.	b.d.	0.11	0.21	b.d.
Tm_2O_3	0.10	0.18	0.07	0.17	b.d.	b.d.	b.d.	b.d.
Yb_2O_3	0.16	0.14	b.d.	b.d.	0.11	b.d.	0.13	b.d.
Lu_2O_3	0.45	b.d.	b.d.	0.04	0.11	0.65	b.d.	b.d.
sum	54.74	59.56	53.18	60.52	52.38	58.31	67.72	70.64

Note: abbreviations and detection limits are the same as that in Table 4.3

	no. of ions calculated on the basis of 6O atoms							
%$MgCO_3$	0.71	0.00	0.32	0.00	0.24	0.70	0.06	0.26
%$CaCO_3$	94.30	94.78	95.29	94.15	90.30	91.09	95.83	95.94
%$MnCO_3$	2.50	3.11	2.39	3.42	3.04	3.09	1.85	1.32
%$FeCO_3$	1.25	1.37	1.37	1.50	3.80	4.20	0.58	0.63
%$SrCO_3$	1.18	0.71	0.61	0.92	2.62	0.86	1.64	1.84
%$BaCO_3$	0.07	0.03	0.03	0.01	0.01	0.06	0.04	0.02

Table 4.6. Major oxide compositions of alkaline silicate rocks from the SDK complex determined by XRF analyses.

Sample# Rock type	kt-20-29 TP	KT-20-31 TP	KT-21-13 TP	KT-18-6 MN	KT-18-11 MN	KT-18-15 MN	KT-18-4 MN	KT-20-10 MN
SiO_2	41.19	42.35	45.71	40.70	38.05	39.51	39.58	38.54
TiO_2	2.75	2.84	2.69	1.92	2.79	4.83	3.34	2.33
Al_2O_3	10.42	10.83	10.27	10.30	10.98	10.47	8.56	9.56
$(Fe_2O_3)_t$	11.07	11.01	8.91	9.09	10.49	14.14	9.72	10.15
MnO	0.34	0.36	0.22	0.43	0.32	0.17	0.46	0.52
MgO	6.07	5.00	6.83	5.10	7.71	8.68	7.61	4.13
CaO	14.18	12.99	10.32	14.85	13.56	14.10	14.18	15.35
Na_2O	3.23	2.75	4.94	5.41	3.51	3.15	2.19	4.29
K_2O	3.50	3.22	3.74	4.15	3.92	2.37	3.08	3.84
P_2O_5	1.64	1.48	0.81	1.39	1.48	1.07	1.40	1.37
LOI	5.53	6.85	5.21	7.15	7.35	1.70	10.80	9.64
Sum	99.92	99.68	99.65	100.48	100.15	100.19	100.91	99.72
Mg#	52	47	60	53	59	55	61	45

Sample# Rock type	KT-21-16 MN	KT-21-4 MN	KT-21-8 MN	kt-20-41 MN	KT-20-2 MN	KT-20-4 MN	KT-20-36 NE
SiO_2	41.25	37.37	40.61	43.33	43.68	44.30	40.93
TiO_2	2.34	2.11	2.46	2.74	2.14	1.97	2.98
Al_2O_3	10.36	7.98	8.68	13.00	12.13	11.96	13.09
$(Fe_2O_3)_t$	8.96	10.85	11.26	10.51	10.06	8.97	10.07
MnO	0.55	0.44	0.32	0.49	0.39	0.33	0.58
MgO	7.64	3.70	5.52	7.29	6.50	4.78	8.74
CaO	11.72	16.76	14.90	5.96	11.14	10.53	9.93
Na_2O	6.15	3.28	4.39	3.21	6.51	4.32	6.00
K_2O	3.89	2.45	2.20	5.78	2.16	5.59	4.85
P_2O_5	1.09	1.10	1.44	0.83	0.89	1.03	0.95
LOI	5.50	13.61	8.70	5.50	5.17	6.30	2.81
Sum	99.45	99.65	100.48	98.64	100.77	100.07	100.93
Mg#	63	40	49	58	56	51	63

Sample# Rock type	KT-20-27 PT	KT-20-39 PN	KT-20-18 PH	KT-20-34 PH	KT-20-17 PH	KT-20-1 PH	KT-20-5 PH	KT-20-21 PH
SiO_2	49.68	49.99	55.30	53.57	54.27	54.44	48.66	53.02
TiO_2	0.53	1.34	0.18	0.23	0.51	0.27	0.64	0.34
Al_2O_3	18.57	19.42	19.27	17.60	20.64	19.08	16.87	19.04
$(Fe_2O_3)_t$	5.55	7.10	4.31	8.57	3.79	4.64	5.25	4.71
MnO	0.34	0.24	0.23	0.47	0.18	0.26	0.57	0.14
MgO	3.39	1.21	0.10	0.16	0.31	0.12	1.53	0.15
CaO	5.77	4.33	0.77	3.13	2.09	1.07	5.27	1.35
Na_2O	2.33	8.75	10.37	9.47	10.19	10.18	6.95	12.02
K_2O	7.59	5.11	5.10	4.84	5.12	5.11	6.23	4.17
P_2O_5	0.11	0.24	0.09	0.03	0.09	0.03	0.20	0.06
LOI	6.74	0.79	2.98	1.59	1.38	3.52	5.47	3.78
Sum	100.60	98.50	98.69	99.65	98.57	98.72	97.62	98.77
Mg#	55	25	4	4	14	5	37	6

Sample# Rock type	KT-18-3 PH	KT-18-9 PH	KT-18-12 PH	KT-18-13 PH	KT-20-44 SY	KT-20-32 PH	kt-20-35 PH	KT-21-2 PH
SiO_2	54.14	50.76	54.45	52.15	54.56	53.15	55.41	54.79
TiO_2	0.57	0.55	0.31	0.29	0.32	0.31	0.17	0.43
Al_2O_3	20.97	20.54	20.76	21.21	20.26	20.08	21.75	20.86
$(Fe_2O_3)_t$	5.04	5.41	4.77	4.43	4.08	4.17	3.39	4.52
MnO	0.19	0.22	0.34	0.30	0.33	0.24	0.14	0.10
MgO	0.67	1.60	0.09	0.13	0.25	0.43	0.13	0.56
CaO	2.45	2.65	0.73	0.97	0.81	0.97	0.87	2.27
Na_2O	10.54	11.73	10.99	12.19	11.18	11.64	9.47	6.99
K_2O	4.83	5.16	6.06	5.00	6.25	6.85	7.12	8.82
P_2O_5	0.09	0.11	0.02	0.03	0.03	0.03	0.02	0.15
LOI	1.53	1.69	2.42	3.60	2.41	2.30	1.80	0.30
Sum	101.01	100.41	100.93	100.30	100.48	100.18	100.26	99.79
Mg#	21	37	3	5	11	17	7	20

Sample#	KT-21-17	KT-20-12	KT-21-22	KT-20-23	KT-18-14	kt-20-45	SAR-20-2	SAR-20-5
Rock type	PH	PH	PH(Xenolith)	BS	SY	SY	AB	TP
SiO_2	52.08	54.77	54.11	44.53	62.93	62.92	46.64	46.81
TiO_2	0.30	0.40	0.29	2.56	0.89	0.59	2.01	2.01
Al_2O_3	18.46	19.87	20.31	9.77	17.32	17.83	13.13	12.24
$(Fe_2O_3)_t$	4.11	2.79	3.27	10.22	3.22	3.13	13.78	13.63
MnO	0.12	0.27	0.17	0.24	0.18	0.19	0.18	0.18
MgO	0.28	0.15	0.14	9.57	0.97	0.71	8.84	8.04
CaO	1.66	0.75	1.14	12.55	0.85	0.70	10.13	9.95
Na_2O	11.76	12.82	11.70	3.03	7.60	7.66	3.39	3.01
K_2O	4.76	4.32	5.77	1.85	4.66	4.72	0.10	0.10
P_2O_5	0.02	0.07	0.04	1.16	0.17	0.19	0.46	0.43
LOI	5.81	2.89	2.69	4.78	0.70	0.70	1.45	2.68
Sum	99.36	99.10	99.63	100.25	99.50	99.33	100.11	99.07
Mg#	12	10	8	65	37	31	56	54

Note: TP: Tephrite, MN: Melanephelinite; NE: Nephelinite; PT: Phonotephrite; PN: Phonolitic nephelinite; PH: Phonolite; BS: Basanite; SY: Syenite; AB: Alkali Basalt; TP: Tephriphonolite

Table 4.7. Major oxide compositions (wt.%) of carbonatites from the SDK complex determined by XRF analyses.

	KT-18-10C	KT-21-19C	KT-18-1C*	KT-18-2C	KT-18-4C	KT-18-5C	KT-18-7C	KT-18-8C	KT-20-9C	KT-20-30C
Rock Type	CC	CC	CC	CC	CC	CC	CC	CC	CC	CC
SiO_2	1.30	1.95	4.02	4.78	2.37	2.22	0.94	1.10	1.25	3.78
TiO_2	0.092	0.090	0.223	0.154	0.101	0.101	0.09	0.089	0.100	0.130
Al_2O_3	0.15	0.27	0.58	0.24	0.34	0.34	0.09	0.16	0.12	0.68
$(Fe_2O_3)t$	2.89	1.84	3.88	3.79	3.65	2.79	2.36	2.62	2.05	3.17
MnO	2.828	0.870	1.053	1.598	3.021	4.010	1.911	1.918	1.540	2.390
MgO	0.55	0.63	1.06	0.48	0.75	0.80	0.50	0.41	0.69	0.91
CaO	38.99	42.18	42.86	47.24	37.06	33.72	44.82	46.08	44.92	35.74
Na_2O	1.14	b.d	0.36	0.14	1.04	1.61	1.26	1.24	0.27	0.45
K_2O	b.d	b.d	0.36	0.07	b.d	0.25	b.d	b.d	b.d	0.58
P_2O5	0.22	0.57	2.27	2.33	0.47	0.13	0.09	0.10	0.10	0.28
BaO	1.40	0.30	0.46	0.99	1.43	1.33	1.70	0.92	1.04	2.11
SrO	10.65	5.36	0.44	0.75	3.00	3.39	8.00	4.07	4.57	4.47
LOI	37.95	35.76	35.76	35.86	36.92	36.80	35.82	40.76	42.00	36.23

Sum	98.15	93.32	93.32	98.42	90.14	87.49	97.57	99.46	98.65	90.92

Sample# Rock Type	KT-20-11C CC	KT-20-14C CC	KT-20-15C CC	KT-20-16C CC	KT-20-24C CC	KT-20-25C CC	KT-20-28C CC	KT-21-7C CC	KT-20-33C CC	KT-21-5C CC
SiO_2	1.51	2.73	2.74	1.54	3.60	2.62	2.59	1.48	2.03	1.00
TiO_2	0.090	0.041	0.170	0.110	0.190	0.190	0.100	0.110	0.110	0.090
Al_2O_3	0.14	0.41	0.42	0.16	0.46	0.40	0.46	0.19	0.31	0.07
$(Fe_2O_3)t$	1.16	3.01	5.78	3.87	5.36	5.26	2.09	2.14	1.86	1.20
MnO	1.570	2.601	1.700	3.470	1.080	1.640	2.480	1.150	1.770	1.620
MgO	0.84	1.13	0.99	1.00	1.27	1.08	0.71	1.49	0.70	0.41
CaO	44.83	37.14	42.54	40.50	46.96	42.72	34.05	39.01	26.47	46.27
Na_2O	0.31	0.98	0.09	0.32	b.d.	b.d.	0.57	0.47	0.64	1.24
K_2O	b.d.	0.18	0.26	0.04	0.50	0.23	0.14	b.d.	0.15	b.d.
P_2O_5	0.08	0.12	2.16	0.96	2.34	2.27	0.15	1.55	0.15	0.08
BaO	0.67	1.05	0.54	1.21	0.49	0.80	1.47	0.57	1.88	0.79
SrO	3.79	3.92	3.28	3.45	0.35	3.99	8.88	5.43	8.49	4.45
LOI	41.89	35.05	34.87	36.83	36.70	38.70	36.11	36.61	32.64	43.88
Sum	96.88	88.37	95.55	93.45	99.30	99.90	89.80	90.20	77.20	101.09

Sample# Rock Type	KT-20-3C CC	KT-20-6C CC	KT-20-7 CC	KT-21-11C CC	KT-21-14C CC	KT-21-18C CC	KT-21-1C CC	KT-21-15C FC	KT-21-10C FC	KT-20-37C FC
SiO_2	3.35	2.31	10.09	0.92	2.94	2.75	3.19	2.39	16.64	5.06
TiO_2	0.190	0.120	0.500	0.080	0.200	0.080	0.140	0.090	0.420	0.250
Al_2O_3	0.61	0.25	2.13	0.05	0.22	0.50	0.50	0.38	3.77	1.24
$(Fe_2O_3)t$	4.33	2.25	5.83	1.17	6.05	1.21	5.46	9.58	6.47	4.18
MnO	1.05	1.06	4.68	1.79	0.62	0.93	4.17	10.49	3.93	3.44
MgO	2.06	0.59	1.66	0.38	0.48	0.18	0.94	1.55	1.80	2.35
CaO	39.08	44.77	33.07	46.30	45.07	44.68	42.34	37.90	28.74	31.11
Na_2O	0.02	0.42	0.85	1.29	b.d.	1.03	0.15	1.16	0.77	b.d.
K_2O	0.52	0.26	1.35	b.d.	0.07	0.51	0.66	0.20	4.63	0.51
P_2O_5	2.85	0.87	0.46	0.08	3.62	0.22	1.87	0.09	0.72	0.29
BaO	3.31	0.35	1.44	0.83	0.25	0.51	0.93	1.67	0.45	2.44
SrO	5.03	4.87	1.71	4.26	2.50	3.78	0.33	1.04	2.17	3.17
LOI	34.60	38.72	30.19	41.93	35.95	40.35	33.86	33.91	24.75	30.97
Sum	97.00	96.84	93.96	99.09	97.97	96.73	94.54	100.45	95.26	85.01

Note: CC: Calciocarbonatite; FC: Ferrocarbonatite

Table 4.8. Trace element concentrations (in ppm)) of alkaline silicate rocks from the SDK complex determined by ICPMS.

Sample#	KT-20-29	KT-20-31	KT-21-13	KT-18-6	KT-18-11	KT-18-4	KT-20-18	KT-20-17	KT-20-1	KT-20-5T	KT-20-12
Rock type	TP	MN		MN	MN	MN	PH	PH	PH	PH	PH
Sc	10.6	11.3	19.4	18.1	13.4	11.9	0.4	1.4	0.3	2.3	2.5
V	212	218	255	292	286	185	22	69	49	91	39
Cr	18	26	156	55	22	16	48	61	57	69	40
Co	23	23	29	36	31	8	1	4	2	6	1
Ni	5.6	9.6	53	31	7.9	6.2	0.89	1.02	0.96	3.8	4.0
Cu	30	23	36	38	38	8	2	4	2	10	2
Rb	85.5	54.3	128.1	185.7	177.2	35.6	165.9	197.5	192.9	77.0	195.1
Cs	4.51	2.54	nd	nd	8.67	0.43	2.30	4.78	5.87	2.59	5.60
Sr	2179	2506	476	711	1449	48745	226	1107	837	793	372
Ba	2100	2412	1089	5292	3764	5219	45	1044	546	6162	194
Y	48.8	40.8	11.4	40.2	41.3	227	5.95	21.6	16.2	7.04	12.8
La	253	261	50.3	171	333	1513	70.94	122	99	47.28	93
Ce	481	506	87.6	359	617	2574	83.14	169	152	94.00	142
Nd	182	125	29.0	163	217	732	13.0	34.2	26.0	38.5	33.8
Sm	27.2	18.6	4.4	23.8	30.1	102	1.21	4.31	2.78	5.90	4.21
Nb	223	233	222	437	350	396	95.7	93.9	127	376	424
Ta	16.6	11.4	10.4	20.6	23.2	13.6	0.9	2.4	1.4	11.0	8.2
Pr	49.6	36.1	8.6	48.7	64.5	245	5.86	12.5	10.7	11.03	12.4
Zr	423	423	232	465	319	488	385	520	682	128	1238
Hf	9.97	7.20	3.87	11.1	7.15	10.3	6.20	9.17	10.5	2.02	7.42
Eu	7.31	5.09	1.26	6.72	7.91	27.1	0.31	1.22	0.78	2.52	1.20
Gd	21.7	15.0	3.68	18.0	23.5	90.0	1.47	4.32	3.16	4.25	5.13
Tb	2.53	1.78	0.47	2.21	2.69	10.1	0.14	0.56	0.38	0.52	0.50
Dy	12.2	8.55	2.49	10.6	11.9	51.8	0.67	3.36	2.20	2.41	2.36
Ho	2.05	1.44	0.49	1.84	2.00	8.02	0.14	0.77	0.47	0.41	0.44
Er	5.11	3.59	1.38	4.63	4.82	19.5	0.42	2.38	1.63	1.00	1.16
Tm	0.63	0.44	0.20	0.63	0.57	2.55	0.07	0.42	0.29	0.13	0.16
Yb	3.65	2.56	1.29	3.77	3.31	13.7	0.54	2.91	2.12	0.80	1.18
Lu	0.51	0.34	0.19	0.50	0.41	1.84	0.09	0.45	0.34	0.11	0.18
Pb	11.5	5.76	3.25	28.2	28.2	54.3	18.0	40.3	51.9	12.4	41.7
Th	23.4	16.6	27.7	43.7	31.1	260	36.0	35.4	52.3	45.1	44.8
U	5.67	4.12	3.00	4.77	6.27	16.0	11.4	9.13	12.6	7.45	22.7
(La/Sm)$_N$	6.0	9.1	7.4	4.6	7.2	9.5	37.8	18.3	23.0	5.2	14.3
(La/Yb)$_N$	49.7	73.2	28	32.5	72.1	79.0	94.4	30.1	33.4	42.4	56.4

$(Gd/Yb)_N$	4.9	4.8	2.4	3.9	5.9	5.4	2.2	1.2	1.2	4.4	3.6
$(La/Ce)_N$	1.40	1.3	1.5	1.2	1.4	1.5	2.2	1.9	1.7	1.3	1.7
Eu/Eu*	0.90	0.90	1.0	1.0	0.9	0.9	0.7	0.9	0.8	1.5	0.8
Gd/Gd*	0.30	0.20	0.20	0.3	0.2	0.2	0.1	0.1	0.1	0.3	0.2
Ce/Pb	41.9	87.8	26.9	12.7	21.8	47.3	4.6	4.2	2.9	7.6	3.4
Th/Nb	0.10	0.07	0.12	0.10	0.09	0.6	0.4	0.4	0.4	0.1	0.1
Sm/Hf	2.7	2.6	1.1	2.1	4.2	9.9	0.2	0.5	0.3	2.9	0.6
Nb/La	0.9	0.9	4.4	2.56	1.05	0.26	1.4	0.8	1.3	8.0	4.6
Pb/Nd	0.06	0.05	0.11	0.17	0.13	0.07	1.4	1.2	2.0	0.3	1.2
Th/Ta	1.4	1.4	2.7	2.1	1.3	19.1	39.2	14.9	37.3	4.1	5.5

Sample#	KT-20-21	KT-18-3	KT-18-9	KT-18-12	KT-18-13	KT-21-2	KT-21-17	KT-21-17R	KT-21-22	KT-20-23	KT-18-14
Rock type	PH	PH	PH	PH	PH	PH	PH	PH	PH	BS	SY
Sc	3.4	6.9	3.0	1.2	1.3	1.7	8.7	10.3	0.7	17.2	2.1
V	120	83	128	86	42	46	96	105	126	258	13
Cr	32	46	63	34	31	32	31	33	19.90	314	32
Co	1	4	5	1	1.6	2	2	2	2.19	34	0.53
Ni	0.06	2.9	1.6	0.78	0.46	0.53	0.50	0.55	0.53	107	0.41
Cu	2	12	4	2	4.99	4	10	11	3.26	38	1.27
Rb	128.5	262.9	259.6	286.2	169	175.1	112.9	148.7	88.85	47.6	104
Cs	4.69	4.00	3.12	4.63	6.78	nd	nd	4.36	18.29	nd	0.57
Sr	1385	1001	2063	931	937	1082	2011	2375	1301	1757	124
Ba	2120	842	1274	424	345	1323	1453	1289	2571	1902	1079
Y	11.8	18.8	11.9	24.5	14.7	8.60	3.45	4.50	10.14	23.2	37.0
La	306	107	93	158	121	83	590	779	23.9	80	103
Ce	400	162	110	249	186	112	641	883	50.5	153	181
Nd	74.9	31.6	19.7	45.0	40.7	21.7	128	112	19.5	60.2	68.7
Sm	7.10	3.69	2.48	5.50	5.32	2.36	8.11	7.01	2.85	9.47	11.7
Nb	175	99.6	115	248	221	110	261	308	368	242	93.8
Ta	1.0	1.9	1.5	2.8	3.5	1.08	1.7	2.02	13.8	38	7.8
Pr	30	11.8	7.7	17.8	15.3	8.66	55.1	56.4	5.61	17.3	19.9
Zr	127	539	498	335	222	357	138	138	113	348	50
Hf	3.87	8.14	6.25	6.30	7.26	5.42	3.76	4.63	2.13	5.91	2.08
Eu	1.71	1.18	0.75	1.58	1.53	0.74	1.66	1.48	1.06	2.89	3.02
Gd	7.39	3.91	2.66	5.70	5.35	2.38	9.01	8.15	2.36	7.88	9.55
Tb	0.61	0.49	0.30	0.74	0.67	0.27	0.54	0.47	0.31	1.09	1.42
Dy	2.53	2.92	1.61	3.89	3.43	1.43	1.14	0.95	1.65	5.74	7.86

Ho	0.44	0.59	0.37	0.75	0.61	0.29	0.17	0.14	0.33	1.05	1.51
Er	1.24	1.79	1.09	2.00	1.50	0.90	0.37	0.31	0.91	2.66	3.95
Tm	0.15	0.32	0.17	0.27	0.22	0.15	0.05	0.04	0.13	0.37	0.56
Yb	1.00	2.17	1.31	1.66	1.54	1.12	0.33	0.26	0.82	2.27	3.43
Lu	0.15	0.41	0.18	0.29	0.26	0.19	0.06	0.04	0.11	0.33	0.48
Pb	63.9	32.3	42.7	41.8	48.6	31.3	128	148	12.0	13.7	8.23
Th	32.9	19.4	17.9	52.3	49.0	31.3	6.41	6.88	26.8	20.8	12.2
U	20.9	6.92	7.05	14.9	20.6	7.36	21.4	22.6	87.0	5.5	1.55
$(La/Sm)_N$	27.8	18.7	24.3	18.6	14.7	23	47	72	5.4	5.5	5.7
$(La/Yb)_N$	220	35	51	68	56.5	53	1292	2149	20.8	25.4	21.5
$(Gd/Yb)_N$	6.1	1.5	1.7	2.8	2.9	1.7	22.7	25.9	2.4	2.9	2.3
$(La/Ce)_N$	2.0	1.7	2.2	1.6	1.7	1.9	2.4	2.3	1.2	1.4	1.5
Eu/Eu*	0.70	0.90	0.90	0.90	0.9	1.00	0.60	0.60	1.3	1.0	0.9
Gd/Gd*	0.10	0.10	0.10	0.10	0.2	0.10	0.10	0.10	0.3	0.3	0.3
Ce/Pb	6.3	5.0	2.6	6.0	3.8	3.6	5.0	6.0	4.2	11.2	21.9
Th/Nb	0.19	0.19	0.16	0.21	0.2	0.29	0.02	0.02	0.07	0.09	0.1
Sm/Hf	1.8	0.5	0.4	0.9	0.7	0.4	2	1.5	1.3	1.6	5.6
Nb/La	0.6	0.9	1.2	1.6	1.8	1.3	0.4	0.4	15.4	3.0	0.9
Pb/Nd	0.85	1.02	2.17	0.93	1.2	1.4	1.0	1.3	0.6	0.2	0.1
Th/Ta	32.2	10.2	11.7	18.9	14.1	28.9	3.7	3.4	2.0	0.6	1.6

Sample#	kt-20-45	SAR-20-2	SAR-20-5	KT-18-15	KT-20-10T	KT-21-16	KT-21-4	KT-21-8	kt-20-41	KT-20-27	KT-20-20
Rock type	SY	AB	TP	MN	MN	MN	MN	MN	MN	PT	MN
Sc	2.04	35.76	5.11	35.85	14.03	18.82	3.72	15.30	15.32	10.14	16.88
V	10.53	286.18	86.17	473.54	267.97	306.25	205.05	198.73	287.28	92.35	346.09
Cr	72.57	151.66	29.64	308.26	38.18	109.47	38.04	111.33	29.51	8.24	51.56
Co	0.74	47.02	7.38	56.95	30.25	30.06	18.46	27.51	26.11	7.37	33.02
Ni	2.17	80.77	4.73	94.86	18.40	42.24	13.29	42.15	12.74	4.18	24.57
Cu	3.52	60.98	11.20	84.44	34.87	43.79	24.47	41.42	80.27	10.18	25.78
Rb	81.32	1.07	86.18	52.32	158.45	201.07	152.27	46.73	151.99	219.33	104.77
Cs	0.54	0.11	1.78	0.59	nd	nd	nd	nd	nd	0.85	3.70
Sr	127.85	387.41	3962.70	811.10	285.39	1151.48	643.91	1295.53	2445.18	1398.78	2972.37
Ba	1300.80	71.50	2836.96	808.67	5942.93	2341.72	4227.84	2074.64	1803.82	4345.44	2611.55
Y	16.53	30.17	56.42	24.62	9.64	41.39	12.34	49.09	27.78	45.76	74.17
La	50.78	8.99	289.33	65.87	48.83	139.76	33.11	171.37	244.28	578.68	327.33
Ce	97.38	24.84	500.10	138.71	102.88	230.84	58.92	318.64	397.26	859.37	675.29
Nd	30.75	18.91	174.95	62.21	35.74	108.98	20.94	130.09	132.57	203.09	274.28
Sm	4.71	5.20	23.26	11.46	5.70	18.45	3.32	21.11	15.16	25.27	37.50

Nb	101.81	4.88	275.76	86.73	473.89	270.34	327.07	188.86	222.38	162.56	305.59
Ta	4.73	0.38	12.41	6.20	25.08	13.15	15.07	10.34	8.19	1.77	11.49
Pr	9.24	3.87	54.35	16.26	10.43	30.75	6.18	36.20	44.71	72.80	80.85
Zr	64.34	122.39	681.93	293.98	371.73	273.50	98.97	51.25	180.61	163.73	93.69
Hf	2.04	3.22	11.50	7.89	9.51	6.29	1.53	1.17	3.99	3.65	2.70
Eu	1.92	1.97	6.10	3.29	2.38	5.35	1.57	5.81	4.06	7.17	9.81
Gd	4.18	5.79	19.98	9.34	4.06	15.10	3.21	17.63	12.80	22.91	28.35
Tb	0.53	0.91	2.28	1.26	0.51	1.99	0.52	2.43	1.46	2.51	3.06
Dy	2.97	5.55	11.38	6.25	2.50	9.89	2.93	12.57	6.85	11.61	13.73
Ho	0.57	1.12	2.10	1.03	0.45	1.72	0.53	2.30	1.24	1.98	2.48
Er	1.71	2.97	5.56	2.37	1.21	4.13	1.33	5.73	3.25	5.13	6.42
Tm	0.26	0.40	0.75	0.29	0.19	0.54	0.18	0.75	0.47	0.66	0.81
Yb	1.63	2.50	4.55	1.60	1.39	3.09	1.09	4.28	2.77	3.97	4.75
Lu	0.26	0.34	0.66	0.21	0.25	0.42	0.15	0.57	0.36	0.55	0.66
Pb	7.26	2.37	20.26	2.80	54.77	11.40	13.06	10.68	18.08	13.63	22.54
Th	7.16	0.47	25.11	9.43	96.23	27.97	56.34	40.92	18.17	64.21	55.71
U	1.03	0.16	7.68	2.14	8.96	3.91	3.69	3.34	3.65	4.66	8.10
(La/Sm)$_N$	7.0	1.1	8.0	3.70	5.50	4.90	6.40	5.20	10.40	14.8	5.64
(La/Yb)$_N$	22.3	2.6	45.6	29.50	25.10	32.40	21.70	28.70	63.20	104.6	49.46
(Gd/Yb)$_N$	2.1	1.9	3.6	4.80	2.40	4.00	2.40	3.40	3.80	4.8	4.94
(La/Ce)$_N$	1.3	0.9	1.5	1.20	1.20	1.60	1.50	1.40	1.60	1.7	1.25
Eu/Eu*	1.3	1.1	0.9	1.00	1.50	1.00	1.50	0.90	0.90	0.9	0.92
Gd/Gd*	0.2	1.0	0.2	0.40	0.20	0.40	0.30	0.30	0.20	0.2	0.24
Ce/Pb	13.41	10.47	24.69	49.47	1.88	20.24	4.51	29.84	30.92	63.05	29.95
Th/Nb	0.07	0.10	0.09	0.11	0.20	0.10	0.17	0.22	0.10	0.40	0.18
Sm/Hf	2.31	1.62	2.02	1.45	0.60	2.93	2.17	18.01	4.40	6.92	13.89
Nb/La	2.01	0.54	0.95	1.32	9.71	1.93	9.88	1.10	0.53	0.28	0.93
Pb/Nd	0.24	0.13	0.12	0.05	1.53	0.10	0.62	0.08	0.11	0.07	0.08
Th/Ta	1.51	1.23	2.02	1.52	3.84	2.13	3.74	3.96	2.06	36.26	4.85

Sample#	KT-20-4	KT-20-39T	KT-20-36	KT-20-2	SAR-20-5R	Pyroxene	Biotite
Rock type	MN	PN	NE	NE	TP	mineral	mineral
Sc	12.0	5.0	21.6	1.8	55.0	18.8	0.6
V	284	166	456	117	83	233	526
Cr	48	67	33	158	29.64	108.96	104.88
Co	27	8.7	33	19	7.38	30.83	23.74
Ni	20	2.64	19	45.1	4.73	39.73	3.75
Cu	41	18.92	66	31.3	11.2	28.66	3.21

Rb	69.0	121	208.1	81.9	98.7	88.68	492.35
Cs	nd	nd	7.68	3.88	1.5	2.44	4.77
Sr	2868	1813	1128	4216	4695	1966	56
Ba	2761	1635	2316	5268	3344	2186	1362
Y	70.0	21.8	104	62.7	67.4	42.55	0.31
La	291	89.1	579	295.08	380	192	5.53
Ce	520	124	992	512	652	350	10.7
Nd	224	35.4	301	174	209	141	1.35
Sm	36.2	5.32	39.5	24.9	27.8	21.2	0.16
Nb	331	137	183	277	332	157	157
Ta	17.8	2.7	5.5	12.5	13.7	10.1	0.9
Pr	65.3	11.5	98.2	52.2	65.2	36.8	0.50
Zr	90	424	386	59	824	335	0.8
Hf	1.76	5.58	9.13	1.08	13.8	9.23	0.03
Eu	10.0	1.68	10.7	7.08	8.30	5.78	0.12
Gd	30.04	5.10	34.9	20.96	24.4	17.9	0.19
Tb	3.77	0.73	3.94	2.52	2.82	2.01	0.02
Dy	17.6	4.34	19.04	12.1	13.3	9.48	0.06
Ho	2.97	0.90	3.54	2.24	2.48	1.64	0.01
Er	7.07	2.67	9.23	5.70	6.42	4.11	0.03
Tm	0.91	0.42	1.22	0.75	0.84	0.50	0.00
Yb	5.44	2.82	7.65	4.25	5.46	2.88	0.02
Lu	0.74	0.41	0.96	0.56	0.74	0.38	0.00
Pb	125	16.5	53.3	25.9	25.8	4.55	14.7
Th	100	21.6	49.2	44.1	31.9	13.5	0.12
U	3.53	6.42	4.10	9.72	8.5	3.65	0.01
$(La/Sm)_N$	5.2	10.8	9.5	7.65	8.8		
$(La/Yb)_N$	38.3	22.7	54.3	49.82	49.9		
$(Gd/Yb)_N$	4.6	1.5	3.8	4.08	3.7		
$(La/Ce)_N$	1.4	1.8	1.5	1.49	1.5		
Eu/Eu*	0.93	0.99	0.9	0.95	0.97		
Gd/Gd*	0.33	0.23	0.2	0.24	0.22		
Ce/Pb	4.2	7.5	18.6	19.73	25.3		
Th/Nb	0.3	0.2	0.3	0.16	0.10		
Sm/Hf	20.6	0.95	4.3	23.11	2.02		
Nb/La	1.14	1.54	0.32	0.94	0.88		
Pb/Nd	0.56	0.47	0.18	0.15	0.12		
Th/Ta	5.63	8.00	8.95	3.53	2.32		

Note: TP: Tephrite; MN: Melanephelinite; PH: Phonolite, BS: Basanite; SY: Syenite; AB: Alkali basalt; PT: Phonotephrite; TP: Tephriphonolite; PN: Phonolitic nephelinite; NE: Nephelinite; nd- not determined

Table 4.9. Trace element concentrations (in ppm)) of calciocarbonatites and ferrocarbonatites from the SDK complex determined by ICPMS.

Sample#	KT-18-10C	KT-18-1C*	KT-18-2C	KT-18-4C	KT-18-5C	KT-18-7C	KT-18-8C	KT-20-9C	KT-20-14C	KT-20-25C	KT-20-28C	KT-21-4C
Rock Type	CC	CC	CC	CC	CC	CC	CC	CC	CC	CC	CC	xenolith
Sc	1.5	1.1	10.3	0.5	5.0	3.8	6.0	3.6	1.7	0.9	1.4	0.6
V	15	42	159	41	13	5.0	2.0	2.3	18	92	9	0.8
Cr	1	1	11	14	b.d.	4	b.d.	4	3	4	4	2.3
Co	3.93	5.68	9.40	13.98	3.357	4.30	0.66	1.29	5.69	5.66	3.62	0.76
Ni	3	5	4	7	5	5	4	4	4	3	3	6
Cu	7	2	14	13	2	5	0.2	1	4	3	11	0.4
Rb	5.6	9.1	9.5	3.5	7.2	1.6	9.5	0.3	7.6	4.4	6.3	0.2
Sr	90038	41592	6300	25351	32127	37616	34389	45724	33160	33770	75077	31195
Ba	12543	1778	8833	12777	11169	15195	8253	10141	9349	7134	13154	2251
Y	121	182	209	236	230	155	136	130	157	233	118	131
La	26178	1076	3907	27876	40280	4791	1446	2050	21214	3682	25601	937
Ce	29644	1756	5303	31758	51976	5824	2426	2779	26376	4825	30803	1480
Nd	5356	487	1279	4881	7141	1196	501	620	4964	1117	5734	416
Sm	311	69.6	125	324	458	109	52.6	64.6	302	119	342	49.1
Nb	118	241	207	90.1	24.9	0.0	0.6	3.5	97	159	18.9	1.6
Ta	0.09	0.21	0.49	0.08	0.04	0.04	0.03	0.05	0.04	0.14	0.07	0.08
Pr	2245	161	452	2074	3147	458	183	227	2041	401	2328	139
Zr	1.2	14.5	39.3	1.6	1.5	0.5	0.6	0.9	1.6	12	4.3	4.9
Hf	0.20	0.55	0.86	0.28	0.22	0.18	0.08	0.14	0.21	0.52	0.24	0.14
Eu	52.2	21.2	28.0	55.5	81.3	23.6	15.6	15.3	50.4	28.1	55.8	13.6
Gd	321	68.1	105	340	697	93.3	50.6	56.2	288	102	335	47.1
Tb	21.1	8.22	11.8	25.0	31.9	9.23	5.47	6.11	21.0	11.3	22.7	4.92
Dy	40.0	39.0	51.8	62.6	59.1	34.2	25.9	27.5	47.8	49.4	41.8	22.4
Ho	6.28	6.80	8.67	10.4	9.01	5.92	4.66	5.23	7.74	8.71	6.12	4.21
Er	14.8	15.9	25.1	13.1	22.9	18.2	12.3	14.7	19.9	23.0	13.9	10.9
Tm	1.95	1.88	2.96	3.53	3.07	2.28	1.95	1.92	2.80	2.76	1.79	1.41
Yb	12.2	11.4	17.0	21.7	19.5	13.0	11.3	11.7	18.3	15.0	11.3	8.8
Lu	1.66	1.41	2.30	3.10	2.80	1.85	1.56	1.67	2.61	1.91	1.56	1.10

Pb	87.7	47.8	58.1	149	187	97.9	49.2	59.2	126	81.0	127	17.3
Th	51.6	207	65.9	171	137	56.6	18.6	17.6	69.0	73.2	65.5	62.9
U	7.45	32.7	60.8	2.46	3.04	0.58	0.14	0.17	1.17	19.5	4.8	0.40
Zr/Hf	5.8	26.3	46.0	5.8	7.0	2.7	6.7	6.1	7.7	22.9	17.9	34.2
Nb/Ta	1391	1133	424	1098	664	0	24	79	2247	1112	266	21
(La/Sm)$_N$	54.4	10.0	20.2	55.6	51.5	28.4	17.7	20.5	45.4	19.9	48.3	12.3
(La/Yb)$_N$	1542	67	165	923	1287	264	92	126	831	176	1626	77
(Gd/Yb)$_N$	22	5	5	13	26	6	4	4	13	6	25	4
(La/Ce)$_N$	2.3	1.6	1.9	2.3	2.1	2.1	1.5	1.9	2.1	2.0	2.1	1.6
Eu/Eu*	0.51	0.94	0.75	0.51	0.47	0.72	0.92	0.78	0.52	0.78	0.50	0.87
Gd/Gd*	0.06	0.23	0.12	0.06	0.09	0.09	0.12	0.12	0.06	0.12	0.06	0.19

Sample#	KT-20-30C	KT-20-3C	KT-20-6C	KT-21-11C	KT-21-14C	KT-21-18C	KT-21-5C	KT-21-7C	KT-21-19C	KT-21-10C	KT-21-15C	KT-20-37C
Rock Type	CC	CC	CC	CC	CC	CC	CC	CC	CC	FC	FC	FC
Sc	0.7	2.9	1.3	3.1	0.6	0.9	2.5	0.9	0.7	2.1	4.8	3.3
V	15	145	65	2	3	101	5	63	4	14	26	65
Cr	5	4	3	0.5	0.4	1.0	0.6	0.5	0.3	0.5	7.2	3.8
Co	6.18	11.49	3.07	0.64	1.07	7.49	0.69	4.30	0.49	0.98	3.20	8.33
Ni	3	4	4	4	3	4	4	4	4	3	5	5
Cu	8	30	3	0.1	0.8	3	0.2	10	0.1	1.3	1.0	20
Rb	11.6	15.1	2.9	0.2	5.1	3.1	0.5	2.6	0.9	73.2	9.7	12.0
Sr	37788	42556	41154	36030	37788	31949	37614	45956	45324	18319	8762	26813
Ba	18939	29631	3125	7477	2231	4557	7045	5103	2649	4061	14997	21841
Y	102	180	101	92.0	60.8	215	91.5	102	72.2	125	183	150
La	35234	3003	1388	1328	894	2689	1319	1761	877	3009	6277	26901
Ce	43564	3804	1891	1782	1069	4113	1786	2106	1203	3937	9893	40175
Nd	8365	744	443	472	295	1332	481	492	324	977	3139	9020
Sm	486	73.3	46.8	48.3	30.5	147	50.5	46.0	36.7	84.1	345	580
Nb	175	314	273	4.8	25.7	45.5	2.8	76	54	115	14.5	158
Ta	0.11	0.20	0.20	0.02	0.03	0.34	0.06	0.09	0.02	0.17	0.06	0.13
Pr	3059	279	160	176	108	452	178	190	117	380	911	3085
Zr	2.1	7.3	32	0.5	2.2	35	0.5	1.0	1.2	1.8	1.2	93
Hf	0.23	0.19	0.47	0.11	0.09	0.50	0.10	0.09	0.10	0.18	0.29	1.30
Eu	75.8	18.1	11.5	12.6	7.6	36.3	13.2	11.4	9.84	18.9	76.3	93.3
Gd	456	64.7	40.8	45.2	28.5	129	47.6	46.3	36.3	82.7	271	477
Tb	29.5	7.09	4.60	4.77	3.10	13.8	5.18	4.38	4.10	7.75	22.8	33.2
Dy	43.0	33.5	20.6	21.7	14.7	58.9	24.2	18.8	19.3	32.2	71.6	58.7

Ho	5.90	6.14	3.87	4.23	2.91	10.5	4.71	3.73	3.57	6.21	11.3	8.51
Er	13.1	16.9	10.8	11.3	8.10	25.2	12.7	10.3	9.08	16.8	27.3	19.8
Tm	1.45	2.12	1.37	1.60	1.16	3.18	1.81	1.48	1.23	2.50	3.89	2.42
Yb	9.19	12.0	8.07	9.9	6.9	17.7	11.2	9.07	7.3	16.4	25.7	14.8
Lu	1.24	1.58	1.11	1.39	0.91	2.29	1.58	1.20	0.98	2.34	3.71	1.99
Pb	161	133	27.8	48.2	25.7	44.4	54.2	134	34.3	48.7	437	175
Th	56.2	339	29.3	9.96	24.3	202	22.5	134	57.8	33.6	174	149
U	11.0	32.1	25.3	0.12	2.08	12.5	0.11	21.7	3.15	1.84	1.72	20.4
Zr/Hf	9.2	38.2	69.2	5.1	24.0	71.0	4.4	11.1	11.7	10.2	4.0	71.5
Nb/Ta	1648	1577	1344	204	860	135	46	819	2208	664	257	1182
(La/Sm)$_N$	46.8	26.5	19.1	17.8	18.9	11.8	16.9	24.7	15.4	23.1	11.7	29.9
(La/Yb)$_N$	2750	180	123	96	93	109	84	139	86	131	175	1301
(Gd/Yb)$_N$	41	4	4	4	3	6	4	4	4	4	9	27
(La/Ce)$_N$	2.1	2.0	1.9	1.9	2.2	1.7	1.9	2.2	1.9	2.0	1.6	1.7
Eu/Eu*	0.49	0.80	0.81	0.83	0.79	0.81	0.83	0.76	0.82	0.69	0.76	0.54
Gd/Gd*	0.06	0.10	0.13	0.15	0.16	0.18	0.16	0.13	0.18	0.12	0.16	0.07

Note: CC: Calciocarbonatite; FC: Ferrocarbonatite; b.d.: below detection limit; detection limits for REEs is 0.0003 ppb and for other trace elements is 0.006 ppb.

Table 4.10. C and O isotopic compositions of carbonates from samples of alkaline silicate rocks from the SDK complex.

Sample#	description	$\delta^{13}C_{VPDB}$	$\delta^{18}O_{VSMOW}$
KT-20-13A	PH	-6.2	10.7
KT-20-13B	PH	-6.2	11.0
K-18-6	MN	-7.0	7.7
K-18-7(2)	MN	-5.7	11.8
K-18-4	MN	-4.4	16.4
K-18-11	MN	-5.0	6.3

Note- PH- phonolite, MN- melanephelinite

Table 4.11. C and O isotopic compositions of carbonates from samples of carbonatites.

Sample#	description	$\delta^{13}C_{VPDB}$ (‰)	$\delta^{18}O_{VSMOW}$ (‰)	Sample#	description	$\delta^{13}C_{VPDB}$ (‰)	$\delta^{18}O_{VSMOW}$ (‰)
KT-18-1C(A)	CG	-5.6	6.0	KT-20-33C	P	-4.5	8.0
KT-18-1C(B)	FG	-4.0	6.1	KT-20-28A	FG	-5.3	5.6

KT-18-1C(C)	CG	-5.9	6.3	KT-20-28B	FG	-3.6	5.8
KT-18-1C(D)	CG	-5.8	6.1	KT-20-30A	FG	-2.7	19.9
KT-18-1C(E)	CG	-6.1	6.1	KT-20-30B	P	-4.9	6.6
KT-18-10(A)	FG	-5.6	6.6	KT-20-7A	P	-5.8	8.8
KT-18-10(B)	FG	-5.3	5.8	KT-20-7B	FG	-4.6	15.3
KT-18-10(C)	FG	-4.4	8.8	KT-20-7C	FG	-5.6	12.1
KT-18-10(D)	FG	-5.6	6.2	KT-20-9A	P	-6.4	6.2
KT-18-2(A)	FG	-3.8	21.3	KT-20-9B	P	-6.4	6.2
KT-18-2(B)	FG	-3.3	24.7	KT-20-15A	P	-4.7	6.3
KT-18-2(C)	FG	-3.8	25.0	KT-20-15B	FG	-4.4	23.9
KT-18-2(D)	FG	-4.3	17.4	KT-20-14A	FG	-5.8	12.3
KT-18-2(E)	FG	-3.9	21.2	KT-20-14B	FG	-5.0	10.0
KT-18-4(A)	FG	-4.8	15.8	KT-20-11A	CG	-6.3	6.9
KT-18-4(B)	FG	-5.2	15.6	KT-20-11B	CG	-6.3	6.4
KT-18-4(C)	FG	-3.1	17.2	KT-20-16A	FG	-0.7	22.3
KT-18-4(D)	FG	-5.0	14.7	KT-20-16B	FG	-1.5	20.6
KT-18-4(E)	P	-5.4	12.2	KT-20-8A	P	-0.8	26.9
KT-18-5(A)	P	-3.0	19.7	KT-20-8B	P	-0.9	29.6
KT-18-5(B)	FG	-3.3	22.2	KT-20-3A	FG	-3.9	6.8
KT-18-5(C)	FG	-4.1	19.1	KT-20-3B	FG	-3.8	6.9
KT-18-5(D)	FG	-4.7	14.4	KT-20-38B	FG	-1.5	19.6
KT-18-5(E)	FG	-4.7	11.9	KT-20-25A	FG	-5.2	5.6
KT-18-7C	FG	-5.2	16.1	KT-20-25B	FG	-5.0	5.6
KT-18-8(A)	P	-6.5	7.0	KT-20-22A	FG	-2.5	24.0
KT-18-8(B)	P	-6.5	6.5	KT-20-22B	FG	-3.1	21.6
KT-18-8(C)	FG	-2.3	23.4	KT-20-6A	P	-4.9	11.0
KT-18-8(D)	P	-4.7	16.4	KT-20-6B	P	-5.8	5.7
KT-18-8(E)	P	-6.5	6.8	KT-20-6C	P	-5.6	6.0
KT-20-37A	FG	-4.3	6.3	KT-20-33A	FG	-3.5	11.6
KT-20-37B	FG	-4.3	6.5	KT-20-33B	FG	-3.3	14.7
KT-20-24A	FG	-3.2	18.4	KT-21-4C	xenolith	-6.4	7.0
KT-20-24B	FG	-3.8	6.3	KT-21-4C*	xenolith	-6.6	6.2
KT-20-38A	FG	-1.0	24.2				

Note. CG: coarse-grained; P-phenocryst, FG- fine-grained, Table. 4.12. Results of Sr-Nd isotopic composition of measurements for 89-79 Ma alkaline silicate rocks of the SDK complex.

Sample#	Rock	$(^{87}Sr/^{86}Sr)_m$	$(^{87}Rb/^{86}Sr)^*$	$(^{87}Sr/^{86}Sr)_i$	$(^{143}Nd/^{144}Nd)_m$	$(^{147}Sm/^{144}Nd)^*$	$^{(143}Nd/^{144}Nd)_i$	ε_{Nd} (t =88.5 Ma)	T_{DM}(Ga)
KT-18-14	Syenite	0.706503$\pm$5	2.2704	0.703648	0.512762$\pm$2	0.1028	0.512703	3.5	0.45
KT-20-45	Syenite	0.706374$\pm$12	1.8405	0.704060	0.512773$\pm$6	0.0925	0.512719	3.8	0.40
KT-18-13	Phonolite	0.704793$\pm$5	0.5231	0.704135	0.512712$\pm$4	0.0790	0.512694	2.9	0.43
KT-20-39	Ph. nephelinite	0.704642$\pm$5	0.2358	0.704377^a	0.512741$\pm$5	0.0915	0.512694^a	3.1^a	0.44

Note: *Determined from ICPMS concentration data. Subscripts m: measured; i: initial ratio corrected to 88.5 Ma. Superscript a: corrected for t=79 Ma. Analytical errors ($\pm 1\sigma$) are in the last decimal place(s).

ε_{Nd} (t=88.5 Ma) = $[(^{143}Nd/^{144}Nd)_i/(^{143}Nd/^{144}Nd)_{CHUR}^{88.5} -1]\times 10^4$, where CHUR stands for Chondritic Uniform Reservoir and whose present-day values of $^{143}Nd/^{144}Nd$ = 0.512638 and $^{147}Sm/^{144}Nd$ = 0.1967. T_{DM} is Depleted Mantle Model Age (age of derivation) = $(1/\lambda)$ ln $[\{(^{143}Nd/^{144}Nd)_{sample}-(^{143}Nd/^{144}Nd)_{DM}\}/\{(^{147}Sm/^{144}Nd)_{sample}-(^{147}Sm/^{144}Nd)_{DM}\}+1]$, where λ is decay constant ($=6.54\times 10^{-12}$ y^{-1}). $(^{143}Nd/^{144}Nd)_{DM}$ and $(^{147}Sm/^{144}Nd)_{DM}$ are taken to be 0.513114 and 0.222, respectively (Michard et al., 1985).

Table 4.13. Sr-Nd isotopic composition of measurements for 68.5 Ma Alkaline Silicate Rocks and Carbonatites.

Sample No.	Rock Type	$^{87}Sr/^{86}Sr_m$	$^{87}Rb/^{86}Sr^*$	$(^{87}Sr/^{86}Sr)_i$	$^{143}Nd/^{144}Nd_m$	$^{147}Sm/^{144}Nd^*$	$^{(143}Nd/^{144}Nd)_i$	ε_{Nd} (t=68.5 Ma)	T_{DM}(Ga)
Alkaline Silicate Rock									
KT-18-3	Phonolite	0.705023±4	0.7595	0.704284	0.512682±13	0.0763	0.512648	1.9	0.45
KT-18-12	Phonolite	0.705019±4	0.7259	0.704313	0.512720±3	0.0736	0.512687	2.7	0.41
KT-18-9	Phonolite	0.704609±5	0.3640	0.704255	0.512690±4	0.0775	0.512655	2.1	0.45
KT-20-5	Phonolite	0.704818±5	0.1001	0.704721	0.512668±5	0.0921	0.512627	1.5	0.52
KT-21-22	Phonolite	0.704478±5	0.1976	0.704286	0.512703±4	0.0882	0.512663	2.2	0.47
KT-20-21	Phonolite	0.705832±4	0.2939	0.705546	0.512721±2	0.0573	0.512695	2.8	0.36
KT-20-21(R)	Phonolite	0.704786±4	0.2939	0.704500	0.512709±2	0.0573	0.512683	2.6	0.38
KT-21-17	Phonolite	0.704528±7	0.1624	0.704370	0.512688±4	0.0383	0.512671	2.4	0.35
KT-20-12	Phonolite	0.705728±6	1.5177	0.704251	0.512720±4	0.0754	0.512686	2.7	0.41
KT-18-7	Melanephelinite	0.704703±9	0.1751	0.704533	0.512696±34	0.0916	0.512655	2.0	0.49
KT-18-4	Melanephelinite	0.705354±6	0.1646	0.705194	0.512725±4	0.0878	0.512686	2.6	0.44
KT-18-6	Melanephelinite	0.704538±9	0.2898	0.704256	0.512701±4	0.0886	0.512661	2.2	0.47
KT-18-11	Melanephelinite	0.704610±14	0.3538	0.704266	0.512714±3	0.0837	0.512676	2.5	0.44
KT-21-4	Melanephelinite	0.705044±5	0.6843	0.704378	0.512717±3	0.0959	0.512674	2.4	0.48
KT-20-10	Melanephelinite	0.704617±6	0.1059	0.704514	0.512723±3	0.0918	0.512682	2.6	0.46

KT-21-16	Melanephelinite	0.704787±5	0.5053	0.704295	0.512725±4	0.1023	0.512679	2.5	0.50
KT-20-20	Melanephelinite	0.704612±4	0.1020	0.704513	0.512706±11	0.0827	0.512669	2.3	0.45
KT-20-41	Melanephelinite	0.704626±8	0.1799	0.704451	0.512689±5	0.0720	0.512657	2.1	0.43
KT-21-13	Tephrite	0.705273±5	0.7791	0.704515	0.512699±2	0.0911	0.512658	2.1	0.48
KT-20-27	Phonotephrite	0.705179±5	0.4537	0.704737	0.512715±4	0.0752	0.512681	2.6	0.42
KT-20-36	Nephelinite	0.704622±4	0.5339	0.704102	0.512704±3	0.0911	0.512663	2.2	0.48
KT-20-36(R)	Nephelinite	0.704864±7	0.5339	0.704344	0.512712±3	0.0911	0.512671	2.4	0.47
KT-20-2	Nephelinite	0.704575±6	0.0562	0.704520	0.512726±7	0.0867	0.512687	2.7	0.44
KT-20-23	Basanite	0.704400±5	0.0785	0.704324	0.512697±4	0.0951	0.512654	2.0	0.50
Carbonatite									
KT-18-7-Bt	Biotite Separate	0.715674±18			0.512736±3				
KT-18-1C	Calciocarbonatite	0.704284±4	0.06018	0.704225	0.512719±4	0.0904	0.512678	2.5	0.46
KT-18-2C	Calciocarbonatite	0.704443±5	0.00438	0.704439	0.512700±4	0.0591	0.512673	2.4	0.39
KT-18-4C	Calciocarbonatite	0.704453±10	0.00041	0.704453	0.512687±4	0.0401	0.512669	2.3	0.36
KT-18-5C	Calciocarbonatite	0.704464±3	0.00065	0.704463	0.512687±1	0.0388	0.512670	2.3	0.36
KT-18-8C	Calciocarbonatite	0.704258±8	0.00080	0.704257	0.512714±5	0.0653	0.512685	2.6	0.39
KT-18-10C	Calciocarbonatite	0.704286±8	0.00018	0.704286	0.512679±5	0.0351	0.512663	2.2	0.36
KT-20-3C	Calciocarbonatite	0.704329±6	0.00103	0.704328	0.512699±3	0.0596	0.512672	2.4	0.39
KT-20-9C	Calciocarbonatite	0.704329±4	0.00002	0.704329	0.512717±3	0.0630	0.512689	2.7	0.38
KT-20-14C	Calciocarbonatite	0.704300±5	0.00067	0.704299	0.512693±3	0.0367	0.512677	2.5	0.35
KT-21-18C	Calciocarbonatite	0.704248±4	0.00028	0.704248	0.512716±2	0.0667	0.512686	2.7	0.39
KT-21-10C	Ferrocarbonatite	0.704320±5	0.01156	0.704309	0.512688±6	0.0520	0.512665	2.2	0.38
KT-21-4C	Calciocarbonatite	0.704282±5	0.00002	0.704282	0.512707±2	0.0714	0.512675	2.4	0.41
KT-21-15C	Ferrocarbonatite	0.704554±5	0.00320	0.704551	0.512708±4	0.0665	0.512678	2.5	0.40
KT-21-19C	Calciocarbonatite	0.704293±6	0.00006	0.704293	0.512711±3	0.0685	0.512680	2.5	0.40
KT-21-7C	Calciocarbonatite	0.704320±6	0.00016	0.704320	0.512709±2	0.0565	0.512684	2.6	0.37
KT-21-14C	Calciocarbonatite	0.704365±4	0.00039	0.704365	0.512704±2	0.0623	0.512676	2.5	0.39
KT-21-11C	Calciocarbonatite	0.704286±8	0.00001	0.704286	0.512716±2	0.0619	0.512688	2.7	0.38
KT-21-5C	Calciocarbonatite	0.704283±6	0.00004	0.704283	0.512698±14	0.0635	0.512670	2.3	0.40
KT-20-25C	Calciocarbonatite	0.704303±5	0.00038	0.704303	0.512720±5	0.0647	0.512691	2.8	0.38
KT-20-28C	Calciocarbonatite	0.704328±16	0.00024	0.704328	0.512686±2	0.0361	0.512670	2.3	0.35
KT-20-30C	Calciocarbonatite	0.704321±4	0.00089	0.704321	0.512683±2	0.0351	0.512667	2.3	0.35
KT-20-37C	Ferrocarbonatite	0.704362±4	0.00130	0.704362	0.512681±2	0.0389	0.512664	2.2	0.36

Note: see the footnote given in Table 4.18; i: initial ratio calculated relative to an age of 68.5 Ma; R: Replicate

Table. 4.14. Results of Sr-Nd isotopic composition of measurements for 66.4 Ma alkaline silicate rocks.

Sample#	Rock/mineral	$(^{87}Sr/^{86}Sr)_m$	$(^{87}Rb/^{86}Sr)$*	$(^{87}Sr/^{86}Sr)_i$	$(^{143}Nd/^{144}Nd)_m$	$^{147}Sm/^{144}Nd$*	$(^{143}Nd/^{144}Nd)_i$	ε_{Nd} (t=66.5 Ma)	T_{DM}(Ga)
KT-21-2	Phonolite	0.704920±9	0.4683	0.704478	0.512740±5	0.0658	0.512711	3.1	0.37
KT-20-17	Phonolite	0.704907±4	0.5161	0.704419	0.512741±3	0.0762	0.512708	3.0	0.39
KT-20-18	Phonolite	0.706571±6	2.3796	0.704323	0.512721±3	0.0564	0.512696	2.8	0.36
KT-20-1	Phonolite	0.705123±6	0.6672	0.704493	0.512744±4	0.0646	0.512716	3.2	0.36
KT-20-29	Tephrite	0.704515±5	0.1135	0.704408	0.512692±5	0.0904	0.512653	2.0	0.49
KT-20-31-	Tephrite	0.70449±5	0.0627	0.704431	0.512707±3	0.0896	0.512668	2.3	0.47
SAR-20-5	Tephriphonolite	0.704374±7	0.0629	0.704315	0.512703±3	0.0804	0.512668	2.3	0.44
KT-18-15	Melanephelinite	0.704468±4	0.1867	0.704292	0.512775±4	0.1114	0.512727	3.4	0.47
SAR-20-2	Alkali basalt	0.702825±7	0.0080	0.702817	0.512798±4	0.1662	0.512726	3.4	0.86
SAR-20-5-P	pyroxene	0.704503±5	0.1305	0.704380	0.512714±2	0.0909	0.512674	2.4	0.47

Note: see the footnote given in Table 4.18; i: initial ratio calculated relative to an age of 66.5 Ma.

Table. 4.15. Results of Pb isotopic measurements for an 88.5 Ma syenite of the SDK complex.

Sample#	Rock	U*	Th*	Pb*	$^{206}Pb/^{204}Pb$	$^{207}Pb/^{204}Pb$	$^{208}Pb/^{204}Pb$	$(^{206}Pb/^{204}Pb)_i$	$(^{207}Pb/^{204}Pb)_i$	$(^{208}Pb/^{204}Pb)_i$
KT-20-45	Sy	1.0	7.2	7.3	18.904	15.845	39.609	18.776	15.839	39.318

Note: *determined from ICPMS concentration data. Subscripts m: measured; i: initial, calculated relative to an age of 88.5 Ma. 2 SE uncertainties obtained by NBS-981 measurements (n=10) are 0.002, 0.003, 0.006 for $^{206}Pb/^{204}Pb$, $^{207}Pb/^{204}Pb$, $^{208}Pb/^{204}Pb$, respectively.

Table. 4.16. Results of Pb isotopic measurements for 68.5 Ma alkaline silicate rocks and carbonatites of the SDK complex.

Sample#	Rock	U*	Th*	Pb*	$(^{206}Pb/^{204}Pb)_m$	$(^{207}Pb/^{204}Pb)_m$	$(^{208}Pb/^{204}Pb)_m$	$(^{206}Pb/^{204}Pb)_i$	$(^{207}Pb/^{204}Pb)_i$	$(^{208}Pb/^{204}Pb)_i$
Alkaline silicate Rock										
KT-20-36	Nepheline	4.1	49.2	53.3	19.037	15.628	39.360	18.983	15.626	39.151
KT-18-9	Phonolite	7.1	17.9	42.7	19.121	15.611	39.170	19.006	15.606	39.075
KT-20-27	Tephriphonolite	4.7	64.2	13.6	19.175	15.602	39.735	18.937	15.591	38.656
KT-18-6	Melanephelinite	4.8	43.7	28.2	19.152	15.602	39.596	19.035	15.597	39.243
KT-21-17	Phonolite	21.4	6.4	127.8	19.228	15.619	39.206	19.112	15.614	39.194
KT-20-21	Phonolite	20.9	32.9	63.9	19.258	15.622	39.250	19.032	15.612	39.132
KT-20-23	Basanite	5.5	20.8	4.6	19.312	15.632	39.560	18.465	15.592	38.511

KT-20-10	Melanephelinite	9.0	96.2	54.8	19.174	15.636	39.633	19.060	15.630	39.231
KT-20-20	Melanephelinite	8.1	55.7	22.5	19.800	15.643	40.269	19.546	15.631	39.694
Carbonatite										
KT-21-7C	Calciocarbonatite	21.7	134.4	134.1	19.141	15.585	39.340	19.029	15.580	39.112
KT-21-19C	Calciocarbonatite	3.2	57.8	34.3	19.079	15.650	39.707	19.015	15.647	39.321
KT-18-8C	Calciocarbonatite	0.1	18.6	49.2	19.041	15.598	39.205	19.039	15.598	39.119
KT-18-10C	Calciocarbonatite	7.4	51.6	87.7	19.046	15.569	39.185	18.987	15.567	39.051
KT-20-9C	Calciocarbonatite	0.2	17.6	59.2	19.032	15.589	39.178	19.030	15.589	39.110
KT-18-1C	Calciocarbonatite	32.7	207.5	47.8	19.164	15.574	40.038	18.686	15.552	39.041
KT-20-3C	Calciocarbonatite	32.1	339.4	133.5	19.187	15.602	39.731	19.020	15.594	39.148
KT-21-14C	Calciocarbonatite	2.1	24.3	25.8	19.036	15.444	39.869	18.980	15.441	39.653
KT-20-25C	Calciocarbonatite	19.5	73.2	81.0	19.012	15.589	39.192	18.846	15.581	38.987
KT-20-28C	Calciocarbonatite	4.8	65.5	126.8	18.990	15.565	39.163	18.965	15.564	39.046
KT-21-10C	Ferrocarbonatite	1.8	33.6	48.7	18.982	15.569	39.217	18.956	15.568	39.060
KT-21-4C	xenolith	0.4	62.9	17.3	18.982	15.570	40.005	18.966	15.569	39.169

Note: *determined from ICPMS concentration data. Subscripts m: measured; i: initial, calculated for t= 68.5 Ma.

Table. 4.17. Results of Pb isotopic composition of measurements for 66.4 Ma alkaline silicate rocks of the SDK complex.

Sample#	Rock	U*	Th*	Pb*	$(^{206}\mathrm{Pb}/^{204}\mathrm{Pb})_\mathrm{m}$	$(^{207}\mathrm{Pb}/^{204}\mathrm{Pb})_\mathrm{m}$	$(^{208}\mathrm{Pb}/^{204}\mathrm{Pb})_\mathrm{m}$	$(^{206}\mathrm{Pb}/^{204}\mathrm{Pb})_\mathrm{i}$	$(^{207}\mathrm{Pb}/^{204}\mathrm{Pb})_\mathrm{i}$	$(^{208}\mathrm{Pb}/^{204}\mathrm{Pb})_\mathrm{i}$
KT-20-29	Tephrite	5.7	23.4	11.5	19.341	15.604	39.536	19.007	15.589	39.083
KT-20-17	Phonolite	9.1	35.4	40.3	19.331	15.732	39.600	19.178	15.725	39.405
KT-21-2	Phonolite	7.4	31.3	31.3	19.275	15.611	39.339	19.117	15.603	39.118
KT-20-1	Phonolite	12.6	52.3	51.9	19.322	15.630	39.425	19.158	15.622	39.201
KT-18-15	Melanephelinite	2.1	9.4	2.8	19.788	15.653	40.147	19.264	15.628	39.389
SAR-20-2	Alkali basalt	0.2	0.5	2.4	17.585	15.457	37.258	17.543	15.455	37.217
SAR-20-5	Tephriphonolite	7.7	25.1	20.3	19.148	15.581	39.245	18.894	15.569	38.971
KT-20-18	Phonolite	11.4	36.0	18.0	19.471	15.625	39.715	19.043	15.604	39.269

Note: *determined from ICPMS concentration data. Subscripts m: measured; i: initial, calculated for t= 66.5 Ma.

Chapter 5

Discussion

5.1. Nature of Emplacements

Not all crystalline carbonate rocks are magmatic; many of them form as a result of assimilation of (meta-)sedimentary carbonates by silicate magmas or by pneumatolytic melting of sedimentary carbonates in the presence of H_2O-rich volatiles/fluids under high metamorphic grade conditions in the upper crust (anatectic pseudo carbonatites), or by metasomatic reaction of the sedimentary carbonates with silicate magmas (e.g., skarns and antiskarns), or as crystallization products of carbothermal residual fluids derived as CO_2-rich late-stage differentiated fluids from silicate magmas (e.g., Stoppa, 2021; Mitchell, 2005; Yaxley et al., 2022; references therein). Therefore, there was a need to investigate the carbonate-rich rocks in the Sarnu-Dandali-Kamthai (SDK) complex, confirm their proposed magmatic origin, and understand their mode of origin and implications for the study of carbonatites in general.

The carbonate-rich rocks in the SDK complex occur in various forms (e.g., plugs, dykes, sills, and veins) and as independent bodies and intrude into earlier alkaline silicate rocks or Proterozoic country rocks. Apart from their modes of occurrence, the following properties of SDK carbonates clearly rule out their possible non-magmatic origin.

1. Carbonate-rich rocks derived from sedimentary rocks generally contain Sr not more than ~200 ppm and REE < 25 ppm. In contrast, the carbonate-rich rocks in the SDK complex have very high contents of Sr (> 3500 ppm) and REE (> 1000 ppm).
2. The texture and mineralogy of the carbonate-rich rocks derived from the melting of sedimentary limestones or marbles are generally similar to the sedimentary protolith. In contrast, the cumulate textures of the calcite grains, the presence of minerals showing crystallization from a melt (e.g., zoned apatite and calcite), and the presence of Nb-rich minerals (e.g., pyrochlore) in the carbonate-rich rocks of this complex do not support a sedimentary origin.
3. The range of lowest $\delta^{13}C$ and $\delta^{18}O$ of the carbonate-rich rocks (e.g., $\delta^{13}C$ = -6.5 to -4 ‰, $\delta^{18}O$ = 5.6 to 12 ‰; *Fig 4.16a*, *Chapter - 4*) from the SDK complex fall within the

$\delta^{13}C$, and $\delta^{18}O$ of the global carbonatites, and some plot well within the field of mantle ($\delta^{13}C$ = -5.0 to -8.0 ‰, $\delta^{18}O$ = 5.0 to 8.0 ‰; Deines, 1989). Similarly, their Sr-Nd isotopic compositions (e.g., $^{87}Sr/^{86}Sr$ = 0.7042-0.7045, $^{143}Nd/^{144}Nd$ = 0.512663-0.512689) overlap those of mantle-derived igneous rocks.

Therefore, carbonate-rich rocks of the SDK complex are clearly magmatic and can be classified as carbonatites. In the next sections, their age of emplacement, mode of origin, and genetic link with the associated alkaline silicate rocks are discussed in detail.

5.2. Temporal evolution of the complex

As revealed by our ^{40}Ar-^{39}Ar age data and published geochronological information for the SDK complex (e.g., Basu et al., 1993; Sheth et al., 2017; Dongre te al., 2022; Bhunia et al., 2022), the varying ages of emplacements of the alkaline silicate rocks and carbonatites suggest that the complex had seen multiple episodes of alkaline magmatism in Late Cretaceous period. We recognize that there were at least two episodes of such activities: an older 89-79 Ma intrusive event and a younger 70-66 Ma intrusive-extrusive event. Interestingly, carbonatite activity appears to have occurred during the latter phase because neither have we encountered these rocks along with the 89-79 Ma rock association, nor any of the earliest studies report so. As pointed out by Sheth et al. (2017), the timing of the older episode of alkaline activity in the SDK complex coincides with that of the continental breakup between India and Madagascar (92-84 Ma), as evidenced by same age magmatic activities in the western margin of India and eastern margin of Madagascar (e.g., Storey et al., 1995; Torsvik et al., 2000). Our age data confirm that the younger, widespread alkaline activity in the complex is clearly coeval with the emplacement of the Deccan Large Igneous Province (69-62 Ma; Kale and Pande, 2022). Thus, the current age data from the complex point to a possible hiatus of about 9 million years between the two episodes of magmatic activities.

The older alkaline activity in the complex (89-79 Ma) that lasted for about 11 million years saw emplacements of plutonic, sub-volcanic, and volcanic rocks. Syenite plutons, nephelinite plugs, phonolite dykes, and melanephelinite and rhyolite lava flows belong to this episode. The SDK complex is located on the eastern margin of the Barmer rift basin, whose evolution has remained uncertain. According to some, the basin is an ancient, failed continental rift that had been reactivated multiple times during the separation of various parts of the Gondwanaland (e.g., Bladon et al., 2015 a, b; Burley et al., 2022). However, except for the late Cretaceous magmatic activities, evidence for older tectonic events remains elusive. The continental breakup of Madagascar and India, which was believed to have taken place during 92-84 Ma (e.g., Storey et al., 1999; Torsvik et al., 2000), was the likely tectonic reason for the alkaline magmatic activity in the Barmer basin that continued at least until 79 Ma. The Mundwara alkaline complex, located 120 km southeast of the SDK complex – along the eastern margin of the Barmer rift, contains 84-80 Ma igneous activities, which have also been linked to the India-Madagascar breakup (Pande et al., 2017). Additional evidence for this event comes from southern India in the form of basic dyke intrusions (e.g., Radhakrishna et al., 1999; Kumar et al., 2001), and it is highly likely that many such intrusions could be present beneath the Deccan Traps.

The younger alkaline activity of the SDK complex appears to have lasted for a much shorter duration, about 3 million years, from 69.7 Ma to 66.4 Ma. This activity is contemporaneous with the Deccan continental flood basalt (CFB) eruptions, located more than 500 km south of the complex. The age data for various rocks emplaced suggest that there were three major phases of alkaline magmatism in the complex during this phase, one during the very early phase of Deccan volcanism (at ~70 Ma), one at 68.5±0.2 (2σ) Ma (weighted mean) when carbonatites got emplaced along with phonolites during the India-Seychelles break up (Sheth et al., 2017), and the third one, represented by phonolite, tephrite, and tephriphonolite, at 66.4±0.2 (2σ) Ma (weighted mean) which marginally predates the Cretaceous-Paleogene (KPg) boundary (66.05±0.08 Ma; Sprain et al., 2019) and is contemporaneous with the bottommost Deccan lava flows in the Western Ghats (see Rennet e al., 2015). Thus, it is apparent that the younger phase of alkaline magmatism of the SDK complex was contemporaneous with the tectonic and magmatic activities associated with the Deccan CFB eruptions. There exist numerous other alkaline (and carbonatite) volcanic/sub-volcanic centers in the Deccan CFB province, a large number of which either are contemporaneous with the main phase of Deccan basaltic eruptions or postdate it (Basu et al., 2020).

The carbonatites of the SDK complex were emplaced along with the alkaline silicate rocks at 68.6±0.4 Ma. This coeval emplacement age of both the rock types points towards a possible common origin for both the rock types. Since similarity in age and spatial proximity are not sufficient enough evidence to suggest a genetic relationship, we took the help of geochemical and isotopic investigations.

5.3. Fractional crystallization

5.3.1. *Fractional crystallization in the silicate magma*

Given the errors in the ^{40}Ar-^{39}Ar ages of the alkaline silicate rocks from the SDK complex obtained in this study, all alkaline silicate rocks with age in the range of 69.7 and 66.3 Ma are considered to represent a single episode of alkaline magmatism. Since primitive alkaline silicate rocks (SiO_2<46 wt%) of this alkaline suite, such as nephelinites, melanephelinites, basanite, and alkali basalt, have lower Ni (<120 ppm), and Cr (<310 ppm) contents than those expected in primary magmas, these rocks are likely to have been produced by fractional crystallization of their primary magmas. The decrease in MgO, TiO_2, CaO, and Fe_2O_3 with an increase in SiO_2 can be ascribed to the fractionation of primarily clinopyroxene, sphene, and oxide phases (magnetite, ilmenite) during the fractional crystallization of the magma, which also leads to the increase in Al_2O_3 and alkalis in the residual magma *(Fig. 4.10)*. The negative correlation observed between P_2O_5 and SiO_2 may be due to removal of apatites from the parental magma. Similar crystallization may be inferred for the 66.4 Ma alkaline silicate rocks *(Fig. 4.11)*, but the current interpretation is limited due to the limited data set, which is reflected in the lack of good correlation among the oxides. Rb, Zr, and Th are relatively more incompatible than Yb and Lu (i.e., $D_{Rb} < D_{Yb}$, $D_{Zr} < D_{Lu}$, and $D_{Th} < D_{Lu}$) in the early crystallizing silicate minerals (e.g., olivine, pyroxene, nepheline, magnetite, sphene, etc.) in alkaline silicate magmas. As a result, Rb, Zr and Th tend to get enriched in the residual melt compared to Yb and Lu, thus leading to higher Rb/Yb, Zr/Lu, and Th/Lu in more evolved rocks like phonolites compared to those in the early crystallizing rocks such as nephelinites, melanephelinites and basanites. Therefore, in primitive mantle normalized $(Rb/Yb)_{PM}$ vs. $(Zr/Lu)_{PM}$ and $(Rb/Yb)_{PM}$ vs. $(Th/Lu)_{PM}$ plots, positive trends are expected for a cogenetic suite of rocks produced by fractional crystallization. In primitive mantle normalized $(Rb/Yb)_{PM}$ vs. $(Zr/Lu)_{PM}$ and $(Rb/Yb)_{PM}$ vs. $(Th/Lu)_{PM}$ plots *(Figs. 5.1a, 5.1b)*, these alkaline silicate rocks form positively correlated linear trends ($R^2 = 0.7$), and phonolites have higher $(Rb/Yb)_{PM}$, $(Zr/Lu)_{PM}$, and $(Th/Lu)_{PM}$ than the other rocks, suggesting that the phonolites likely have been produced from the parental melanephelinites. Some phonolites plotting significantly outside the trend may be either due to their higher phenocrysts to groundmass ratios or due to their derivation from different batches of the parental magmas. In chondrite normalized $(La/Sm)_{CN}$

vs. Eu/Eu* plot (Fig. 5.1c), Eu/Eu* decreases with increasing LREE fractionation, as indicated by increasing (La/Sm)$_{CN}$ values, suggesting that feldspar (K and Na feldspars) as one of the fractionating phases. The feldspar fractionation is evident from decreasing Sr and Ba in phonolites, seen as negative Sr and Ba anomalies in normalized multi-element trace element patterns *(Fig. 4.13a, Chapter 4)*. Phonolite veins intruding older melanephelinites and having the lowest Sr, Ba, and Eu/Eu* confirm their late-stage crystallization from a highly fractionated alkaline silicate magma.

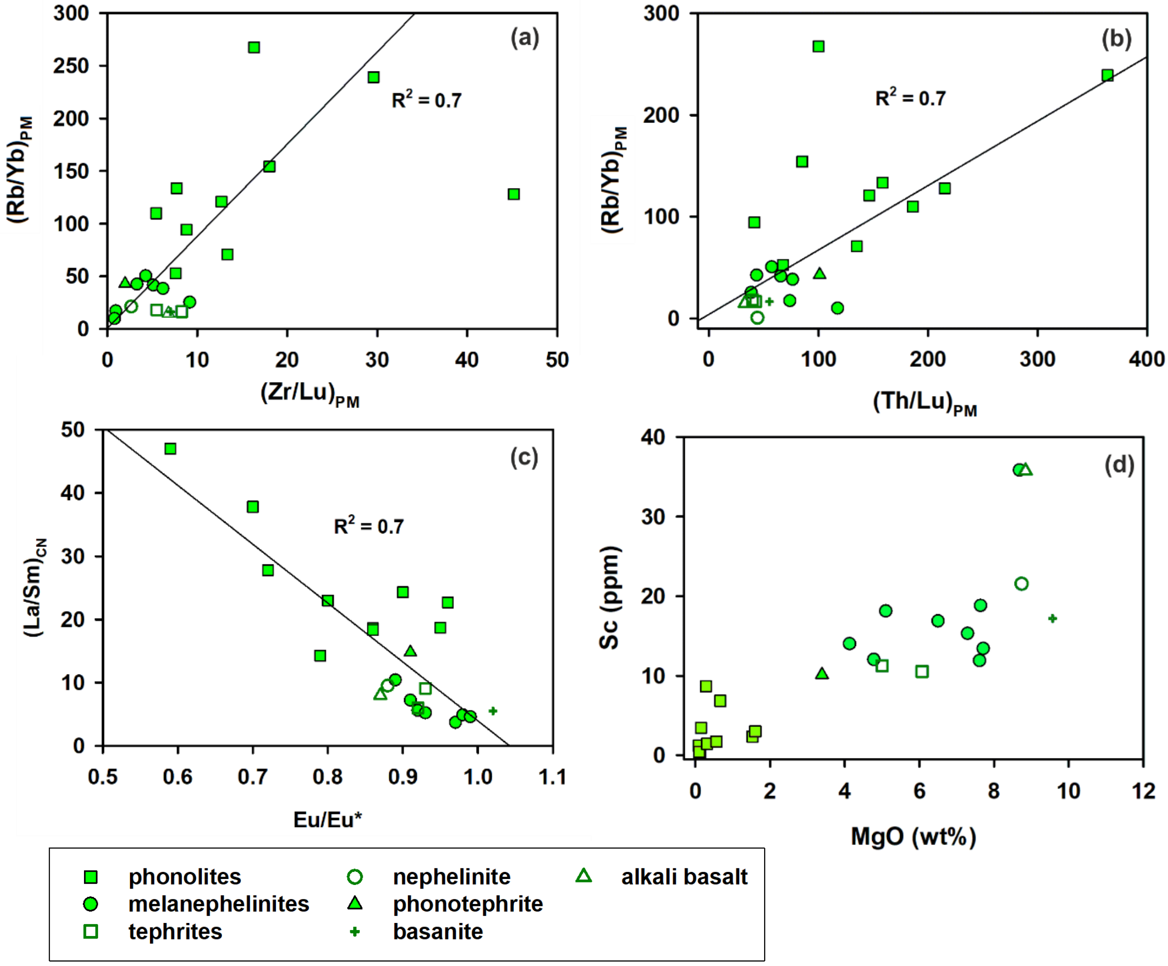

Fig. 5.1. Primitive mantle normalized (a) (Rb/Yb)$_{PM}$ vs. (Zr/Lu)$_{PM}$, (b) (Rb/Yb)$_{PM}$ vs. (Th/Lu)$_{PM}$ plots, (c) Chondrite normalized (La/Sm)$_{CN}$ vs. Eu/Eu* plot and (d) Sc vs. MgO plot for the 69-66 Ma SDK alkaline silicate rocks. Normalized values are after Sun and McDonough (1989).

Among other fractionating mineral phases, clinopyroxenes are the major phases accountable for the origin of the alkaline silicate rocks. Clinopyroxene fractionation is evident from the MgO vs. Sc plot *(Fig. 5.1d)*, where the melanephelinites, nephelinite, and basanite have much higher Sc content than that of the phonolites. The decrease of CaO/Al_2O_3 ratio with increasing

SiO_2 *(Fig. 4.10h, Chapter 4)* also supports the removal of clinopyroxene. Nepheline, magnetite, ilmenite, apatite, sphene, and monazite are other phenocryst phases observed in the alkaline silicate rocks, hence are likely the other fractionating phases.

5.3.2. Fractional crystallization in the carbonatite magma

A. Major oxide constraints

In major oxides vs. SiO_2 plots *(Fig. 4.12, Chapter 4)* for the carbonatites from the SDK complex, the correlated negative variation of CaO content and correlated positive variations of Al_2O_3, MgO, and TiO_2 contents with SiO_2 content in the carbonatites can be attributed to fractional crystallization, i.e., removal of calcite, which forms the dominant crystallizing phase in the carbonatites, from the parental carbonatite magma. The lack of any significant correlation for other oxide contents against SiO_2 could be due to the crystallization of apatite, silicates, magnetite, and other oxide phases at different points of time during the crystallization process.

To further understand the crystallization behavior of carbonatite magma as well as the variation in major oxide contents of the carbonatites, we carried out a Principal Component Analysis (PCA) of the data using the method of Abdi and Williams (2010). Samples having extreme values were considered outliers and were excluded from the PCA. Since most of our samples are calciocarbonatites, only calciocarbonatites were chosen to observe the variations within the calciocarbonatites. We performed PCA for carbonatites on a subset of variables (CaO, MnO, Fe_2O_3, SiO_2, Al_2O_3, TiO_2, and P_2O_5) and 21 samples to explain the observed compositional variations (multivariate data) in a reduced dimensional space. MgO, Na_2O, and K_2O were not taken into account, considering their low content and large spreads. The first three principal components (PC 1, PC 2, and PC 3) together can explain ~91% of the total variance in the data set, with PC 1, PC 2, and PC 3 each accounting for about 56%, 24%, and 13% of the total variance, respectively. The component loadings of the variables, which are the correlations between the variables and the principal components, are plotted in *Fig. 5.2a*. In the PC 2 vs. PC 1 plot (*Fig 5.2a*), PC 2 separates MnO from CaO, which can be explained by the early fractionation of calcite and apatite, causing depletion of CaO and enrichment of MnO in the residual carbonatite magma. The higher CaO and lower MnO contents in the coarse-grained calciocarbonatites support this observation, suggesting their early stage of crystallization during the evolution of the parental carbonatite magma. The high positive loadings of SiO_2, Al_2O_3, TiO_2, $(Fe_2O_3)_{T,}$ and P_2O_5 with PC 1 can be attributed to the presence of silicate and phosphate minerals (e.g., mica, K-feldspar, clinopyroxene, and apatite) in the calciocarbonatites. In the PC 2 vs. PC 1 component score plot (*Fig 5.2b*), the component scores of the calciocarbonatites are plotted. The calciocarbonatites can be divided into three groups considering their component scores. The first group is represented by the coarse-grained calciocarbonatites, which are the early crystallization products and contain the highest amount of calcite and apatite among other groups, thus containing the higher CaO (> 44 wt%) and lower MnO (< 2 wt%) content. The second group is represented by the calciocarbonatite veins, which contain lower CaO (< 39 wt%) and higher MnO content (> 2 wt %). The third group is represented by the calciocarbonatites intermediate between the above groups and have a higher modal fraction of silicate minerals than the first and second groups.

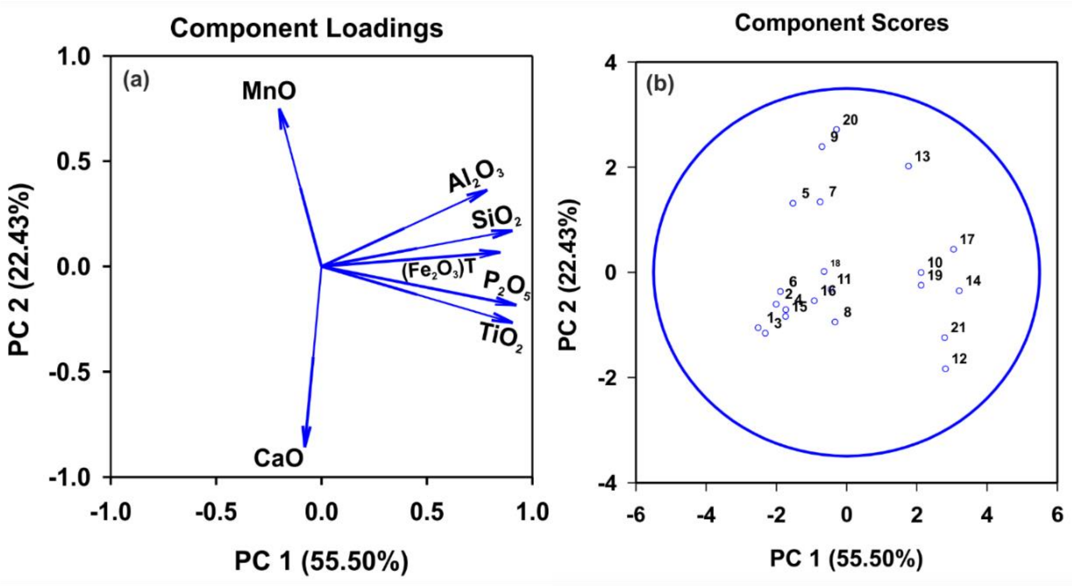

Fig 5.2 Principal component analysis of the major oxide data of the SDK carbonatites. The 2 principal components (PC1 and PC2) explain ~79% variance in the data set. (a) Component loadings plot for the variables; (b) Component score plot for each data point. The circle shows 2σ locus.

B. Trace element constraints

In chondrite normalized rare earth element (REE) plots *(Fig. 4.15b, Chapter 4)*, the ferrocarbonatites generally show higher contents of light REEs compared to the calciocarbonatites, which could be due to fractional crystallization of the parental carbonatite melt. In the chondrite normalized $(La/Yb)_N$ vs. La_N and $(Ba/Y)_N$ vs. Ba_N trace element ratio plots *(Fig. 5.3a, 5.3b)*, La/Yb and Ba/Y increase with the increase in La and Ba, respectively.

$(La/Yb)_N$ shows significant positive linear correlations with La_N, and similar positive correlations are also observed in the $(Ba/Y)_N$ vs. Ba_N plot. This behavior suggests that La and Ba are more incompatible in the carbonatite melt than Yb and Y. These observations can be explained by the fractional crystallization of a parental carbonatite melt, where the residual melt becomes more enriched in incompatible elements compared to compatible elements.

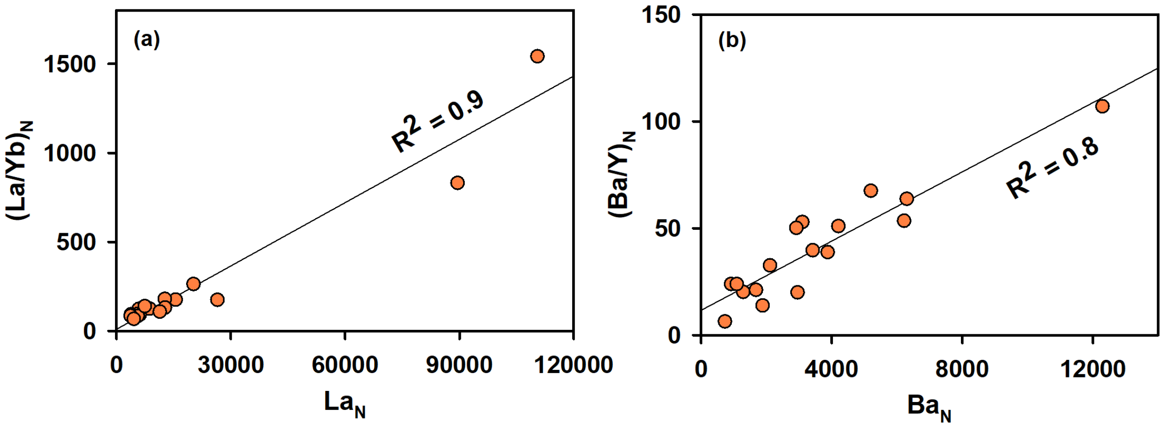

Fig 5.3. Chondrite normalized (Sun and McDonough, 1989) $(La/Yb)_N$ vs. La_N plot (a) and $(Ba/Yb)_N$ vs. Ba_N plot for the SDK carbonatites.

C. Stable C-O isotopic constraints

The $\delta^{13}C$ and $\delta^{18}O$ of most of the carbonates/calcite phenocryst samples from coarse-grained carbonatites of the SDK complex fall well within the field defined for mantle compositions *(Fig. 4.16a, Chapter 4)*, which suggests that they are least affected by secondary alteration processes and have preserved their magmatic signatures. The $\delta^{13}C$ and $\delta^{18}O$ data for fine-grained calcites (groundmass) from the carbonatites, on the other hand, fall outside the mantle field and have $\delta^{18}O$ values those fall beyond 12‰ *(Fig. 4.16a, Chapter 4)*, which is generally considered as the limit of variation for primary/magmatic carbonatites (e.g., Demény et al., 2004; Giuliani et al., 2014; Ray and Ramesh, 2006). Therefore, only the data for the unaltered/primary carbonatites ($\delta^{18}O \leq 12‰$), defined by the primary carbonatite field ($\delta^{13}C \leq -3.8‰$, $\delta^{18}O \leq 12‰$), have been utilized to understand the role of various magmatic processes, such as fractional crystallization, assimilation, degassing, exsolution, etc., in the evolution of the SDK carbonatites. We observe that most coarse-grained carbonatites and unaltered fine-grained carbonatites from the SDK complex show a positive correlation in their $\delta^{13}C$ and $\delta^{18}O$ compositions *(Fig.,4.16a, Chapter 4)*, which is likely due to the fractional crystallization of these rocks from an H_2O-CO_2 bearing parental melt (Deines, 1989; Ray and Ramesh, 2000). The presence of micas (e.g., biotite, phlogopite) in the carbonatites of the SDK complex clearly supports the fluid richness of the parental carbonate magma. To understand the effect of fractional crystallization, determine the range of crystallization temperature, and estimate the initial isotopic compositions of the magma and hence that of the mantle source from which the magma was derived, we employed the RIFMS (Rayleigh Isotopic Fractionation from a Multi-Component Source) model of Ray and Ramesh (2000) and Ray (2009) to the observed data for the primary carbonatites.

Since calcite is the dominant carbonate mineral in the carbonatites, the C isotopic fractionation behavior of carbonatite magma and CO_2 can be explained by the fractionation between calcite and CO_2, presuming the fractionation factor between carbonatite magma and calcite is unity. According to the RIFMS model, the C isotopic composition of calcite fractionating from an H_2O+CO_2 bearing source (i.e., carbonatite magma) is controlled by the CO_2 component, and O isotopic composition is controlled by both H_2O and CO_2 components of the source. We assumed that CO_2 is the largest component in the source. The model has the following parameters: (1) Temperature of crystallization, which controls the C and O isotopic fractionation factors between the source components (i.e., CO_2 and H_2O) and the product (i.e., calcite/carbonatite); (2) initial molar ratio of H_2O and CO_2 (i.e., $r_{H_2O-CO_2}$); (3) the initial $\delta^{13}C$ of the source (i.e., $\delta^{13}C^i_s$); (4) the initial $\delta^{18}O$ of the source (i.e., $\delta^{18}O^i_s$). Since the C isotope fractionation factor between calcite and CO_2 ($\alpha^c_{Cal-CO_2}$), oxygen isotope fractionation factor between calcite and CO_2 ($\alpha^o_{Cal-CO_2}$) and that between H_2O and CO_2($\alpha^o_{\mathrm{H2O}-CO_2}$) < 1 at high temperatures (>500^0C), the high-temperature fractional crystallization of calcite from an H_2O+CO_2 bearing carbonatite magma would cause a progressive increase in $\delta^{13}C$ and $\delta^{18}O$ of the residual magma. The RIFMS model curves, which represent the isotopic evolution of the product (i.e., carbonatite), along with the observed analytical data, are presented in *Fig. 5.4.* Model curves were generated using C and O isotopic fractionation factors between calcite and CO_2, calcite and H_2O, and H_2O and CO_2 from Chacko et al. (1991) and Richet et al. (1977). It is observed that the model can best explain the observed trends in the carbonatite data at a temperature of crystallization of 850°C, an initial molar H_2O/CO_2 ratio of 0.8, and the initial compositions of $\delta^{13}C^i_s$ = -4.6±0.4‰ and $\delta^{18}O^i_s$ = 7.6±1.2‰ for the carbonatite magma (*Fig. 5.4*). The crystallization temperature of 850°C lies well within the proposed range of 880°-550°C for carbonatites (e.g., Barker, 1989; and references therein).

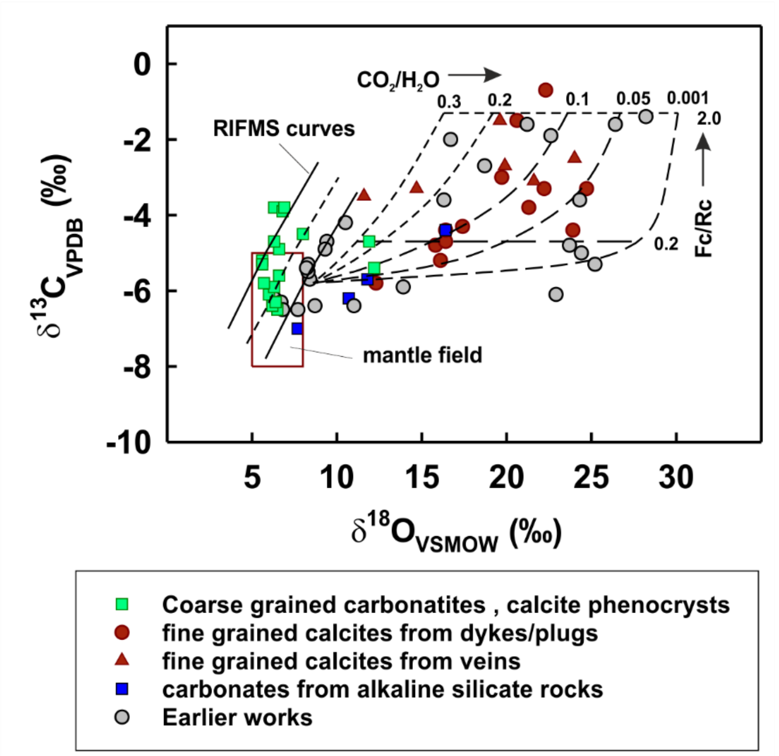

Fig. 5.4. Plot of δ^{13}C vs. δ^{18}O of calcites from carbonatites and alkaline silicate rocks of the SDK complex. The red box represents the mantle field (after Ray and Ramesh, 2006). The dashed line represents the mean RIFMS model curve (Ray and Ramesh, 2000) applied to the data for a starting primary magma, and the solid lines represent the variation in δ^{13}C and δ^{18}O of the primary magma. The following model parameters: δ^{13}C = -4.6±0.4‰, δ^{18}O = 7.6±1.2‰, molar H_2O/CO_2 = 0.8, and temperature of crystallization = 850°C. Also plotted are the fluid-rock interaction model curves (dash-dot-dash lines) for 100°C for the altered samples (after Ray and Ramesh, 1999; 2006). The starting compositions for the rock: δ^{13}C = -5.8 and δ^{18}O = 8.6‰ and for the fluid: δ^{13}C = –3 and δ^{18}O = 9.5‰.

The data for two calcite phenocrysts, one fine-grained carbonatite dyke, and one fine-grained carbonatite vein, which fall off the model curves, have relatively higher δ^{18}O values and may have been affected by post-magmatic fluid alteration. The larger uncertainty in the initial O isotope composition of the magma may be attributed to different batches of carbonatite magma derived at different depths. Assuming that there are negligible C and O isotopic fractionations between the mantle minerals and the primary carbonate magma or the carbonated silicate magma because of their very high temperature of derivation (melting), the mantle source compositions for the SDK rocks can be considered to be the same/similar as those of the parental magma (i.e., δ^{13}C = -4.6±0.4‰ and δ^{18}O = 7.6±1.2‰). From the above modeling results, we infer that a Rayleigh-style fractional crystallization of a fluid-rich mantle-derived carbonatite magma was the cause of the observed variations in C and O isotopic compositions of the unaltered carbonatites of the SDK complex.

5.4. Post-magmatic processes

5.4.1. Effects of post-magmatic fluid alteration

As noted above, many of the SDK complex carbonatites (fine-grained carbonatite dykes, plugs, veins) have higher δ^{18}O than what is expected for the primary/magmatic carbonatites, at a similar range of δ^{13}C *(Fig.4.16a, Chapter 4),* and some of these also have much higher δ^{13}C (> -2‰) and δ^{18}O (>20‰) than magmatic carbonates. These uncorrelated C and O isotopic variations cannot be attributed to any magmatic processes and are likely the results of post-magmatic fluid alteration processes, which can easily affect primary signals of carbonatites because carbonate minerals are highly susceptible to alteration, isotopic exchange, and re-equilibration (e.g., Cheng et al., 2018; Fosu et al., 2020; Ray and Ramesh, 2006; Santos and Clayton, 1995). These uncorrelated/random variations δ^{13}C and δ^{18}O depend on the nature of the fluids (e.g., meteoric, hydrothermal, sea-water), CO_2/H_2O ratio in the fluids, the temperature of alteration (e.g., Ray and Ramesh, 2006; Santos and Clayton, 1995).

Several fluid-rock interaction models have been proposed to understand the nature of the change in C and O isotopic compositions of the carbonatites caused fluids and constrain the nature of the fluids involved and the temperature of alteration (e.g., Demény et al., 1998; Giuliani et al., 2014; Ray and Ramesh, 2006; Santos and Clayton, 1995). A closed-system fluid-Rock interaction modeling (after Ray and Ramesh, 1999; Ray and Ramesh, 2006) was used by us to understand the nature of post-magmatic alteration that affected the carbonatites of the SDK complex. According to this model, the final δ^{13}C and δ^{18}O of a rock $\left(\delta^{13}C_R^f, \delta^{18}O_R^f\right)$ after the isotopic exchange with a fluid is given by:

$$\delta^{13}C_R^f = \frac{(Fc/Rc)\left(\delta^{13}C^i_{fluid}+\Delta^C_{Rock-fluid}\right)+\delta^{13}C^i_{Rock}}{1+(Fc/Rc)} \tag{5.1}$$

$$\delta^{18}O_R^f = \frac{(Fo/Ro)\left(\delta^{18}O^i_{fluid}+\Delta^O_{Rock-fluid}\right)+\delta^{18}O^i_{Rock}}{1+(Fo/Ro)} \tag{5.2}$$

$$\Delta^O_{Rock-fluid} = 10^3 ln\alpha^O_{Cal-CO_2} + 10^3 ln(1+2x) - 10^3 ln\left(2x + \alpha^O_{H_2O-CO_2}\right) \tag{5.3}$$

$$\mathrm{Fo/Ro} = \{(2x+1)/3x\}(\mathrm{Fc/Rc}) \tag{5.4}$$

where $\delta^{13}C_R^i$ and $\delta^{13}C_f^i$ denote the initial δ^{13}C of the rock and fluid, respectively, $\delta^{18}O_R^i$ and $\delta^{18}O_f^i$ denote the initial δ^{18}O of the rock and fluid, respectively. $\Delta^C_{Rock-fluid}$ and $\Delta^O_{Rock-fluid}$ denote C and O isotope fractionation, respectively, between rock and fluid. Fc & Fo and Rc & Ro represent the amount (in moles) of carbon and oxygen in the fluid and rock, respectively. The *x* is the initial molar CO_2/H_2O ratio in the fluid.

Model curves were generated for the final isotopic compositions for the rock after alteration using equations 5.1 to 5.3 and compared with the δ^{13}C and δ^{18}O data from SDK complex that were deemed secondary (*Fig. 5.4*). We assumed $\delta^{13}C_R^i$ = -4.9‰ and $\delta^{18}O_R^i$ = 6.5‰ for the unaltered/primary carbonatite. The fractionation factors were taken from Chacko et al. (1991) and Richet et al. (1977). We observed that the family of curves generated for calcite-fluid interaction at 100°C best explains the data when the fluid compositions are $\delta^{13}C_{fluid}^i$= -3‰, $\delta^{18}O_{fluid}^i$= 9.5‰ at varying CO_2/H_2O ratios between 0.01 to 0.2 (water-rich fluid), with F_c/R_c and F_o/R_o varying between 0 to 2 and 0 to 5, respectively. The presence of the secondary carbonate and oxide-filled veins in the SDK carbonatites is a testimony to large-scale fluid infiltration and secondary alteration in the complex.

5.4.2. REE enrichment in carbonatites

The Sarnu-Dandali-Kamthai carbonatite complex is the only known carbonatite-hosted REE deposit of India (Bhushan and Kumar, 2013). The REE content of these rocks, at places, reaches wt% (> 10^4 ppm; this study). We find that the late-stage veins/dykes are the hosts of these high amounts of REEs. The unaltered and altered carbonatites of the SDK complex also have a significant difference in their REE budget. The carbonatites, which are deemed as near primary and do not show any evidence of alteration, based on petrographic and isotopic evidence, have lower total REE (TREE < 2.3 wt.%), higher CaO and lower MnO contents compared to the altered carbonatites *(Fig. 5.5 a & b)*. Among the altered carbonatites, the calciocarbonatites have much lower CaO (< 39 wt.%) and higher MnO (>2 wt.%) contents than the observed ranges of the calciocarbonatites of the world (CaO > 39.2 wt%, MnO < 2.6 wt%; e.g., Woolley and Kempe, 1989), but are extremely rich in REE content, at time reaching 5 wt%.

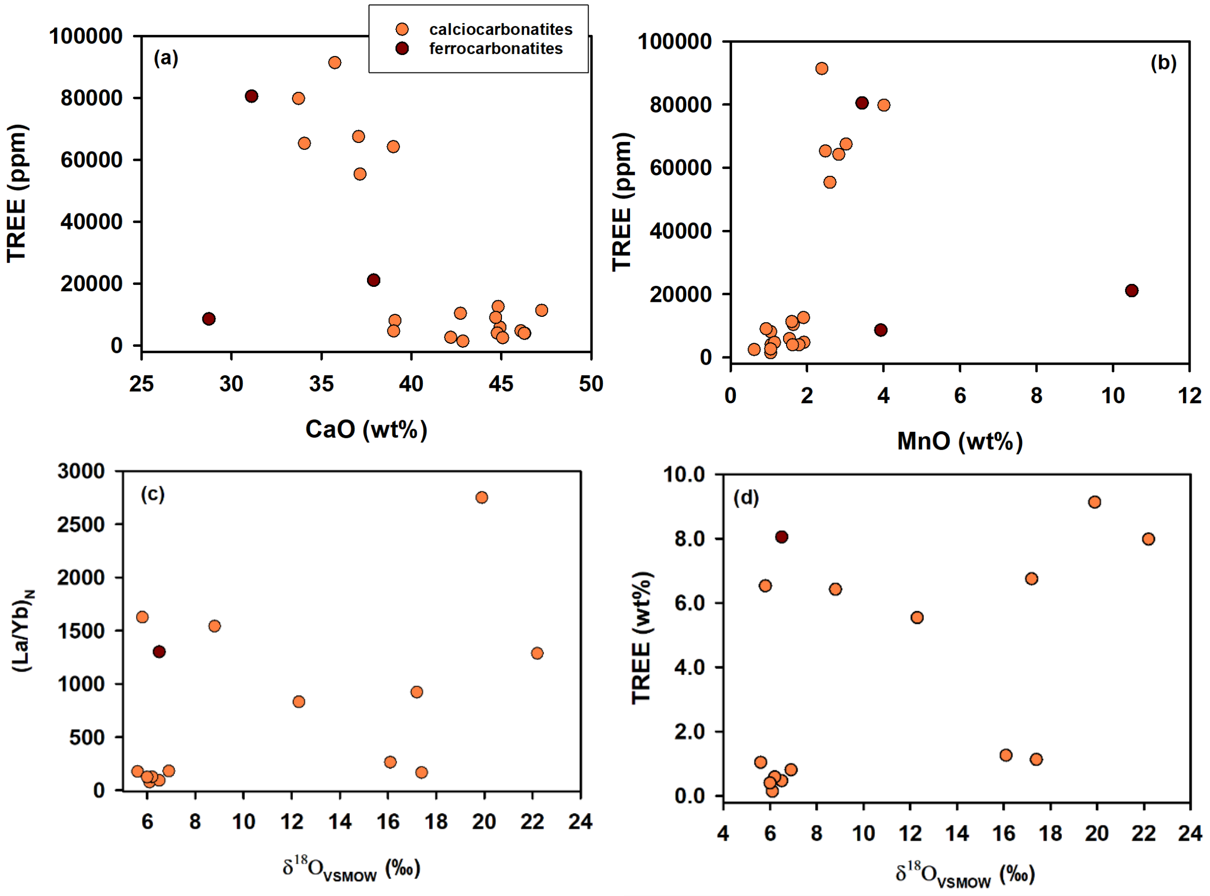

Fig. 5.5. (a) TREE (Total REE) vs. CaO content; (b) TREE vs. MnO content of the SDK carbonatites, (c) chondrite normalized $(La/Yb)_N$ vs. $\delta^{18}O$ ($R^2 = 0.2$); (d) TREE vs. $\delta^{18}O$ ($R^2 = 0.2$) plots for the SDK carbonatites. Normalized values are from Sun & McDonough (1989).

In a chondrite normalized $(La/Yb)_N$ vs. $\delta^{18}O$ plot, carbonatites formed from the residual melt of a continuously fractionating carbonatite melt are expected to show a positive correlation because fractionation of early crystallizing minerals (e.g., clinopyroxene, apatite, calcite), in which LREE are relatively more incompatible than HREE (e.g., Chebotarev et al., 2018; Klemme and Dalpe, 2003; Klemme et al., 1995) and ^{16}O is preferred over ^{18}O (e.g., Deines 1989, Ray and Ramesh, 2000). This results in an increase in LREE/HREE ratio and also $\delta^{18}O$ of the residual melt. As can been seen in *Fig. 5.5(c)*, no correlation is seen in magmatic/unaltered carbonatites ($\delta^{18}O$ < 10‰) of the SDK complex, whereas carbonatite having higher $\delta^{18}O$ show a scatter with some samples showing very high La/Yb fractionation.

Similarly, the total REE (TREE) content of the carbonatites, progressively precipitating from a fractionating melt, ideally should increase and show a positive correlation with their

$\delta^{18}O$ (e.g., Beard et al., 2023). In a TREE (Total REE) vs. $\delta^{18}O$ plot *(Fig. 5.5d)*, though the SDK carbonatites show higher TREE content for samples having higher $\delta^{18}O$; no good positive correlation is observed (R^2 =0.2). The lack of correlations between $(La/Yb)_N$ and $\delta^{18}O$, and TREE vs. $\delta^{18}O$ suggest that the extreme REE enrichment in the REE-rich carbonatites is not likely the result of fractional crystallization. The samples having very high contents of REEs (1.13-9.13 wt%) are deemed altered because of their high $\delta^{18}O$ (> 10‰). As predicted by the fluid-rock interaction model (discussed in the previous section), the observed $\delta^{18}O$ scatter is likely due to the superimposed effect of their interaction with multiple secondary hydrothermal fluids with varying H_2O/CO_2. Thus, the REE mineralization in the SDK carbonatites may be attributed to hydrothermal processes. The presence of hydrothermal minerals (e.g., synchisite, parisite, bastnasite, ancylite, carbocernaite) in the altered carbonatites of the SDK complex, as reported by previous workers (Bhushan, 2015; Upadhyay et al., 2021), support such a hypothesis. Furthermore, the low CaO and high MnO contents of the carbonatites, coupled with extreme REE enrichment, can be attributed to the replacement of primary calcite in the calciocarbonatites by secondary REE-bearing carbonates (e.g., Bastnasite, parisite, synchisite, ancylite) by hydrothermal fluids (e.g., Chakhmouradian et al., 2017; Anenburg et al., 2021). The hydrothermal fluids containing chloride and sulfate complexes are efficient REE transporting agents at pH between 3.2 and 7.4 (e.g., Migdisov and Williams-zones, 2014), whereas those containing fluoride, phosphate, and hydroxyl ligands (or complexes) are effective REE precipitating agents (e.g., Smith et al., 2018; Migdisov et al., 2016). The hydrothermal fluids responsible for the secondary REE enrichment were likely enriched in LREEs. The REE enrichment in the hydrothermal fluids might have occurred through the scavenging of REEs from earlier magmatic carbonatites through fluid-rock interaction. The LREEs in the altered carbonatites of the SDK complex account for more than 95% of the total REE budget.

Many of the altered SDK carbonatites show dissolution and reprecipitation texture, giving the rock a panther skin-like appearance (e.g., Bhushan 2015), suggesting local scale remobilization and redistribution of REEs from primary carbonatites by low-temperature acidic fluids (e.g., Broom Fendley et al., 2016). These low-temperature acidic fluids can leach REEs from primary minerals (e.g., calcite, fluorapatite, burbankite, monazite) and reprecipitate secondary REE-rich minerals close to the original host at a higher pH (e.g., Anenburg et al., 2021; and references therein; Chakhmouradian et al., 2017). In addition, the intergrowth of

REE minerals in calcite and precipitation of REE-rich carbonate minerals in the boxwork hematites (Upadhyay et al., 2021) support the secondary REE enrichment of the SDK carbonatites. As stated before, stable isotope data indicate that no single stage/event of alteration can explain the observed $\delta^{13}C$ and $\delta^{18}O$ data and requires the fluid-rock interactions by multiple fluids of varying isotopic compositions.

5.5. Relationship between Carbonatites and Alkaline Silicate Rocks

As discussed in section 5.2, carbonatites of the SDK complex got emplaced at ~68.5 Ma, along with alkaline silicate rocks, particularly phonolites. We, however, cannot rule out the possible presence of as yet undiscovered carbonatites in the 89-79 Ma or the 66.4 Ma magmatic activities in the complex. Considering their spatial and temporal association, it is highly likely that carbonatites and alkaline silicate rocks of the 68.5 Ma episode are genetically related, similar to what has been observed worldwide. In the following subsections, we test the two known models of carbonatite generation from parental carbonated silicate magma in order to establish the most likely mechanism for the cogenesis of carbonatites and alkaline silicate rocks of the SDK complex.

5.5.1. Carbonatite from a residual melt

As can be seen in the chondrite normalized $(Ba/Y)_N$ vs. Ba_N plot *(Fig. 5.6a)* for the 68.5 million-year-old carbonatites and alkaline silicate rocks, two different fractional crystallization trends are observed. Ba is more incompatible than Y in both carbonatite and alkaline silicate melts, and therefore, fractional crystallization would cause the enrichment in the Ba/Y ratio in the residual melt. If the carbonatites were derived as the residual melt after the fractional crystallization of alkaline silicate rocks from the parental carbonated silicate magma, then they should have plotted on the same trend as the alkaline silicate rocks; however, we do not observe the same *(Fig. 5.6a)*. The different crystallization trends are also observed for both rock types in the $(Nd/Sr)_N$ vs. Nd_N plot *(Fig. 5.6b),* clearly suggesting independent crystallization trends. Therefore, the generation of carbonatites from a residual melt after the crystallization of the silicate rocks is ruled out. However, the observation that both trends originate from a single point (in both plots) suggests a common parentage of both rock types, i.e., derivation from a single parental magma.

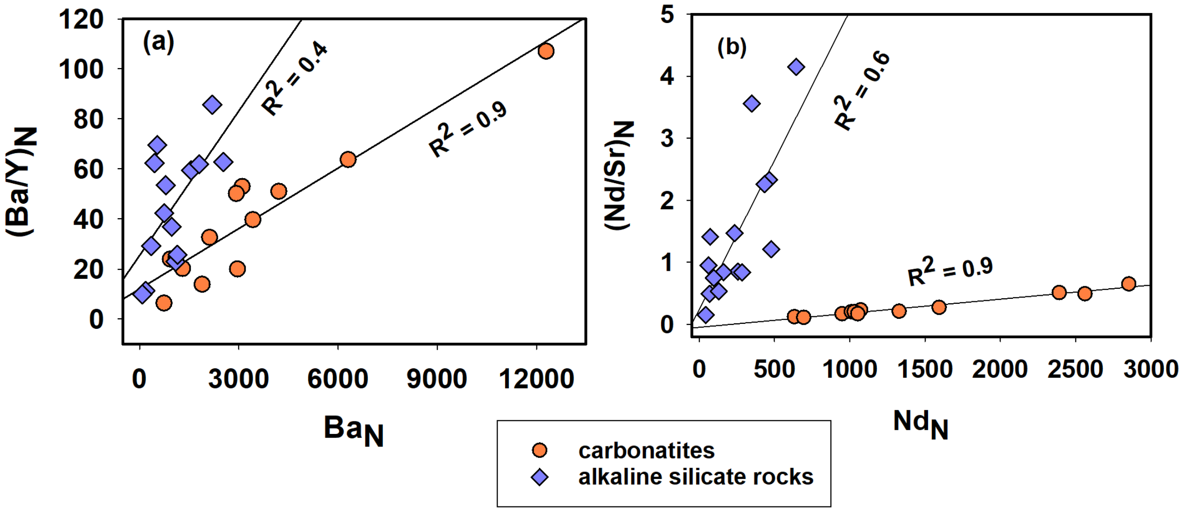

Fig. 5.6. Chondrite normalized $(Ba/Y)_N$ vs. Ba_N plot (a) and $(Nd/Sr)_N$ vs. Nd_N plot (b) for the 68.5 Ma SDK alkaline silicate rocks and carbonatites. The normalized values are from Sun and McDonough (1989)

The coexistence of carbonatites and alkaline silicate rocks in a complex does not necessarily imply that the parental magmas for both rocks are cogenetic because genetically unrelated carbonatite and silica undersaturated alkaline magmas can use the same crustal conduit for their emplacement (e.g., Gittins and Harmer, 2003). However, in addition to the trace element data above, there exist multiple lines of evidence suggesting common parentage for both types of rocks in the SDK complex. One of the most compelling pieces of evidence is that the uncontaminated or pristine initial $^{87}Sr/^{86}Sr$ and $^{143}Nd/^{144}Nd$ isotopic ratios of both rocks overlap *(Fig. 4.17, Chapter 4)*, in spite of the fact that crustal contamination had affected the isotopic ratios. Had the carbonatite crystallized from a residual melt, from a contaminated parental melt, at the end of crystallization of the silicate rocks, then their initial $^{87}Sr/^{86}Sr$ and $^{143}Nd/^{144}Nd$ could not have been the same as the most pristine ratios observed in silicate rocks. Thus, we rule out the simple fractional crystallization model for the generation of carbonatite in the SDK complex.

5.5.2. Carbonate-Silicate Melt Immiscibility

Liquid immiscibility between carbonate and silicate melts at crustal depths is one of the recognized processes for carbonatite magma generation (e.g., Brooker and Kjarsgaard, 2011; and references therein). Several experimental studies on synthetic (silicate + carbonate) and natural rock powders by early workers (e.g., Brooker and Kjarsgaard, 2011; Martin et al., 2013;

Veksler et al., 2012; Weidendorfer and Asimow, 2022) have proven the existence of the silicate-carbonatite miscibility gap, which is also corroborated by the presence of carbonate and silicate melt inclusions in different minerals (e.g., nepheline, perovskite, magnetite, apatite) in alkaline silicate rocks (e.g., Guzmics et al., 2019, 2015, and references therein). However, considering that such a differentiation process happens at crustal depths, it is highly likely that it is accompanied by fractional crystallization of high-temperature minerals (silicate) and assimilation of crustal rocks within a magma chamber. Such a process has been modeled mathematically using trace elements like Sr, Nd, and Pb and their isotopic ratios to understand the entire evolutionary process of a given complex having carbonatite and alkaline silicate rock association (Ray 1998; 2009).

Ray (1998) proposed the AFCLI (Assimilation - Fractional Crystallization - Liquid Immiscibility) model to evaluate the effect of concurrent assimilation of crustal rock, fractional crystallization of alkaline silicate rocks, and immiscible separation of a carbonate melt from a parental carbonated silicate magma on the Sr-Nd-Pb isotopic ratios of the alkaline silicate rocks and carbonatites. The AFCLI model assumes that the exsolved carbonate melt packets remain in equilibrium with the parental magma until the complete crystallization of silicate minerals and, subsequently, the exsolved carbonate melt packets are squeezed out and pool together to form a separate carbonatite magma which is then emplaced. The concentration and isotopic ratio of an element in the parental silicate magma during the AFCLI process are determined by the following equations (Ray, 1998):

$$C_m = C_m^0 F^{-Z} + \left(\frac{a}{a - b - 1}\right)\left(\frac{C_a}{Z}\right)(1 - F^{-Z}) \tag{5.5}$$

$$\frac{E_m - E_m^0}{E_a - E_a^0} = 1 - \left(\frac{C_m^0}{C_m}\right) F^{-Z} \tag{5.6}$$

where C and E represent the concentration and isotopic ratio of an element, F stands for the fraction of remaining melt, and m, a, and o stand for magma, assimilant or contaminant, and initial value, respectively. Model parameters are a = rate of assimilation/rate of crystallization, b = rate of carbonate immiscibility/rate of crystallization, $z = (a - b + bD_l + D_c - 1) / (a - b - 1)$, D_l = bulk carbonate melt-silicate melt partition coefficient and D_c = silicate rock-melt distribution coefficient and. Using D_c, the concentration of an element in the alkaline silicate rock formed from the parental magma, $C_c = D_c * C_m$. The concentration and isotopic ratio of the element in the exsolved/separated carbonatite magma after the completion of the AFCLI process are given by:

$$\overline{C}_l = D_l \left[\frac{aC_a + (1+b-a)C_m^0}{D_c + b\,D_l}\right] \tag{5.7}$$

$$\overline{E}_l = E_m \left[\frac{E_m^0\,C_m^0 + E_a C_a\left(\frac{a}{a-b-1}\right)}{C_a\left(\frac{a}{1+b-a}\right) + C_m^0}\right] \tag{5.8}$$

We employed this model for the SDK rocks to understand their coevolution. As can be seen in *Fig. 4.19 (Chapter - 4)* in the Results chapter, the Sr, Nd, and Pb isotopic ratios of the alkaline silicate rocks display wider variations compared to those for the carbonatites and tend to show values moving towards crustal ratios at lower elemental contents, which are definite signs of crustal contamination. On the other hand, carbonatites show almost flat patterns on these isotopic ratios versus concentration plots *(Fig. 4.20, Chapter 4)*. These observations make the observed data from the SDK complex best suited for the application of the AFCLI model. For the model, the concentration and isotopic compositions of the assimilant and parental carbonated silicate magma were chosen considering the following observations: Banded Gneissic Complex (BGC), constituting the Archean basement of the Aravalli craton, is the preferred assimilant under the SDK complex (e.g., Gopalan et al., 1990; Tobisch et al., 1994). Therefore, a BGC-like composition ((^{87}Sr/^{86}Sr)$_i$ = 0.72500, Sr = 376 ppm, (^{143}Nd/^{144}Nd)$_i$ = 0.511044, Nd = 55 ppm) was chosen for the assimilant for the model calculations. The details of the parameters and initial assumptions used in the model are given in Table 5.1. Considering a trachytic to phonolitic melt composition (clinopyroxene - 40%, K-feldspar - 16%, plagioclase - 7%, nepheline - 7%, and groundmass - 30%), the alkaline silicate rock–melt distribution coefficients (D_c) for Sr and Nd were calculated to be 1.25 and 0.73, respectively. Mineral-melt partition coefficients for clinopyroxene (K_d^{Sr} = 0.659, K_d^{Nd} = 1.04; Baudouin et al., 2020; Mollo et al., 2016), K-feldspar (K_d^{Sr} = 2.3, K_d^{Nd} = 0.026; Larsen, 1979), nepheline (K_d^{Sr} = 0.24, K_d^{Nd} = 0.013; Larsen, 1979), plagioclase (K_d^{Sr} = 4.15, K_d^{Nd} = 0.219; Nagasawa, 1973). The calcite, though, appears as a crystallizing phase in some alkaline silicate rock; their small modal proportions (< 2%) may not affect the bulk distribution coefficients of Sr and Nd, and therefore, its effect on crystallization was not considered in the model. D_l taken for Sr and Nd is 3.15 and 2.83, respectively (Martin et al., 2013).

The AFCLI model curves are compared with the data in isotopic ratio versus concentration plots in *Fig. 5.7*. The $^{87}Sr/^{86}Sr$ variations observed in the alkaline silicate rocks are best explained when a parental carbonated silicate magma ($^{87}Sr/^{86}Sr$ = 0.70422, Sr = 2500 ppm) assimilates a BGC-like lower crustal material ($^{87}Sr/^{86}Sr$ = 0.72500, Sr = 376 ppm; Tobisch et al., 1994), and amount of assimilation is $\leq$ 5% *(Fig. 5.7a)*. Each of the AFCLI model curves in *Fig. 5.6a* represents a pair of assumed values of *a* and *b*. The compositions of exsolved carbonatite magma are determined to be: Sr = 5323±963 ppm and $^{87}Sr/^{86}Sr$ = 0.704306±0.000053; the uncertainties are due to the range of variations used for parameters *a* and *b (Table 5.1)*. The spread in Sr concentrations at similar $(^{87}Sr/^{86}Sr)_i$ observed for the SDK carbonatites can be explained by fractional crystallization of the parental carbonatite magma after immiscible separation. The evidence of fractional crystallization of the parental SDK carbonatite magma has been discussed earlier (see section 5.3.2, this chapter). To model the fractional crystallization of the carbonatite magma, a rock-melt bulk distribution coefficient for Sr (D^{Sr}) of 0.846 was taken considering the crystallization of calcite (90%), apatite (8%), and clinopyroxene (2%). The concentration of fractionated carbonatite at different values of *f* (fraction of remaining melt) is shown as dashed values marked. Similarly, each of the AFCLI modeled Nd curves *(Fig. 5.7b)* was generated for alkaline silicate rocks using different values of a (0.02-0.06) and b (0.14-1.0). The model curves can explain the trends shown by the SDK alkaline rocks when a parental carbonated silicate magma ($^{143}Nd/^{144}Nd$ = 0.512692±0.000004, Nd = 280 ppm) assimilates a BGC-like lower crustal material ($^{143}Nd/^{144}Nd$ = 0.511044, Nd = 55 ppm; Tobisch et al., 1994) with $\leq$ 5%. The $^{143}Nd/^{144}Nd$ (0.512668-0.512693) of the exsolved carbonatite melt predicted by the model covers the entire $(^{143}Nd/^{144}Nd)_i$ spread observed in the SDK carbonatites. The linear spread of carbonatite data along the x-axis *(Fig. 5.7b)* is a result of fractional crystallization of the carbonatite magma (dashed line). The model-predicted Sr (5323±963 ppm) and Nd concentration (699±258 ppm) of the exsolved carbonatite magma are

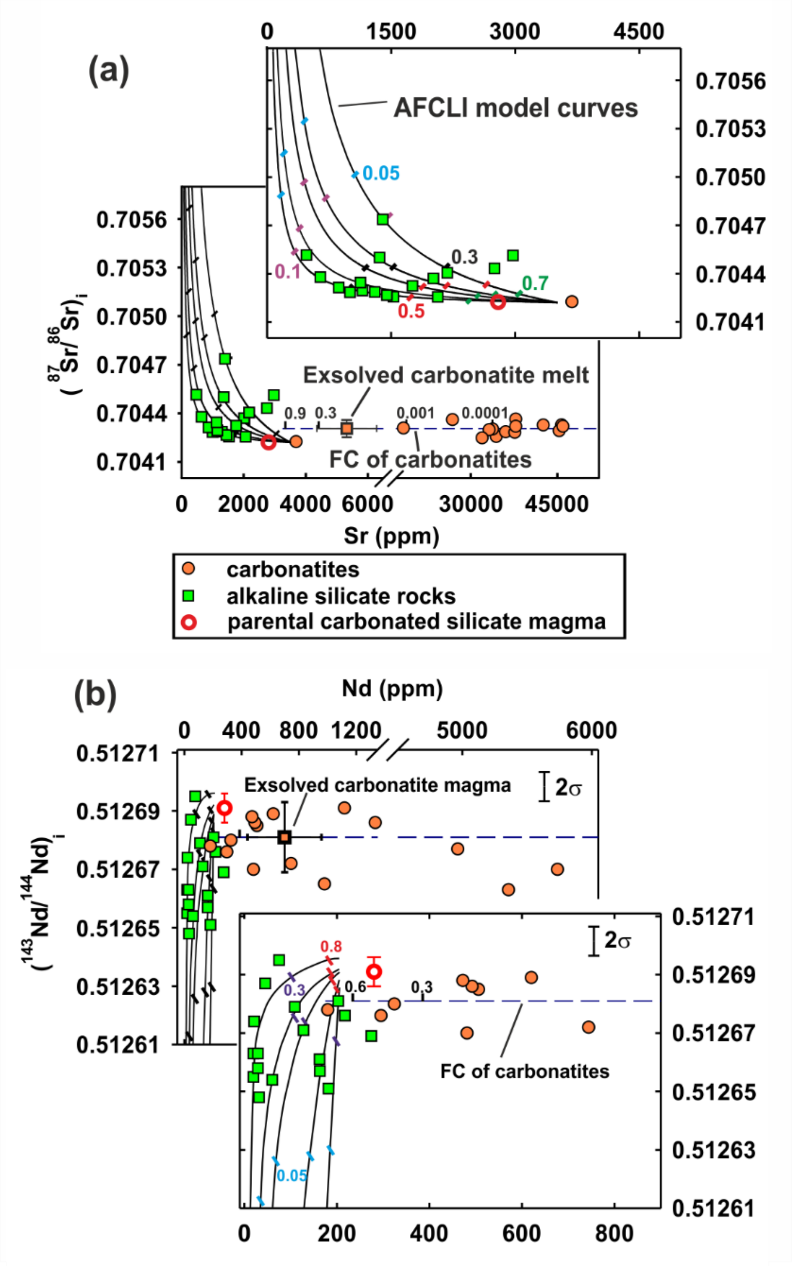

Fig. 5.7. (a) Plots of initial $^{87}Sr/^{86}Sr$ vs. Sr content and (b) initial $^{143}N/^{144}Nd$ vs. Nd content for the 68.5 Ma alkaline silicate rocks and carbonatites of the SDK complex. The continuous curves represent AFCLI model curves for the alkaline silicate rocks derived from the parental carbonated silicate magmas, and the dashed lines are Rayleigh fractional crystallization curves for carbonatites derived from the exsolved carbonate magmas (marked as squares). Multiple AFCLI curves are for different values of the rate of assimilation. Ticks on the curves are F (fraction of remaining magma) values. The compositions of the parental magma (marked) and the contaminant, respectively, are $^{87}Sr/^{86}Sr=0.70422$ ($^{143}Nd/^{144}Nd=0.512692\pm0.000004$) and Sr=2500 ppm (Nd=280 ppm), and $^{87}Sr/^{86}Sr=0.7205$ ($^{143}Nd/^{144}Nd=0.511044$) and Sr=376 ppm (Nd=55 ppm).

higher than the alkaline silicate rocks, which can explain the higher Sr and Nd contents of the carbonatites than that in the alkaline silicate rocks of the SDK complex.

Table 5.1: Summary of parameters used in the AFCLI model

	a	**b**	**Dc**	**D1**
Sr	0.02-0.03	0.05-0.65	1.255	3.15
Nd	0.02-0.06	0.14-1	0.734	2.83

The above AFCLI modeling of the Sr-Nd isotopic data for carbonatites and associated alkaline silicate rocks of the SDK complex established the following facts about the evolution of the complex: (1) extraction of a parental carbonated alkaline silicate magma from the mantle, (2) differentiation of the parental magma in a crustal magma chamber, with concurrent activities of fractional crystallization of silicate rocks, assimilation of wall rocks and immiscible separation of a carbonate melt, and (3) complete removal of a carbonatite magma from the silicate rocks and emplacement. Thus, we prove that carbonatite and associated alkaline silicate rocks of the SFK complex are cogenetic through an immiscible process.

5.5.3. Other evidence for liquid immiscibility

A carbonate inclusion/xenolith found in a melanephelinite dyke (KT-21-4) has mantle-like C and O isotopic compositions ($\delta^{13}C$ = -6.5±0.1‰, $\delta^{18}O$ = 6.6±0.4‰) similar to the unaltered SDK carbonatites. This inclusion also has a similar trace element pattern to the SDK carbonatites *(Fig. 4.15 a,b)*. Overlapping initial Sr, Nd, and Pb isotopic compositions of the carbonate inclusion *(Tables 4.13, 4.16)* with the associated carbonatites and alkaline silicate rocks suggest a common parentage (mantle source and parental magma). The inclusion consists of euhedral calcite megacrysts and euhedral apatite microphenocrysts, hinting at its origin from a carbonate melt that got separated from the parental carbonated-silicate magma as an immiscible melt but got trapped in the crystallizing silicate rock *(Fig 4.6 a,b; Chapter 4)*. Furthermore, carbonate inclusions in perthite phases *(Fig. 4.5 d,e,f; Chapter 4)* in the melanephelinite (KT-21-4) also favor a liquid immiscibility origin for the SDK carbonatites. The immiscible separation of the carbonatite magma from the primary carbonated silicate magma (likely to be a nephelinite melt) could have been facilitated at lower crustal pressure owing to the chemical disequilibrium between the two magmas. The presence of albitic exsolution patches in perthites containing carbonate inclusions may have recorded such disequilibrium conditions at lower pressure conditions.

5.6. Nature of mantle source for 89-79 Ma magmatism

The 89-79 Ma alkaline silicate rocks of the SDK complex (syenite, phonolite, phonolitic nephelinite) are petrologically very diverse and evolved compared to their younger counterparts. The Sr and Nd isotopic ratio (initial) versus concentration plots for four analyzed samples from this magmatic episode *(Fig. 4.19, Chapter 4)* do not show any noteworthy correlations that would suggest significant crustal contamination. However, the large variability of the isotopic ratios *(Fig. 4.19, Chapter 4)* hints at a derivation from chemically heterogeneous mantle source domains. In the ε_{Nd}(t) vs. (^{87}Sr/^{86}Sr)$_i$ plot *(Fig. 5.8)*, the 89-79 Ma SDK alkaline silicate rocks are compared with the 92-84 Ma basalts of Madagascar (e.g., Cucciniello et al., 2013; Mahoney et al., 1991; Melluso et al., 2003). The ε_{Nd}(t) > 0 and lower (^{87}Sr/^{86}Sr)$_i$ than that of the BSE suggest their derivation from LREE-depleted mantle sources. The Madagascar basalts, which are believed to have an origin related to the Marion plume activity (e.g., Storey et al., 1995), show spread from an LREE-depleted mantle field to an enriched field in the ε_{Nd}(t) versus (^{87}Sr/^{86}Sr)$_i$ plot which may be attributed to crustal contamination *(Fig. 5.8)*. Eastern Madagascar basalts show more contaminated signatures than the corresponding basalts on the southwestern and western sides of the island. However, none of the initial Sr and Nd isotopic compositions of the Madagascar basalts and the SDK alkaline rocks have compositions similar to the Marion plume basalts *(Fig. 5.8)*.

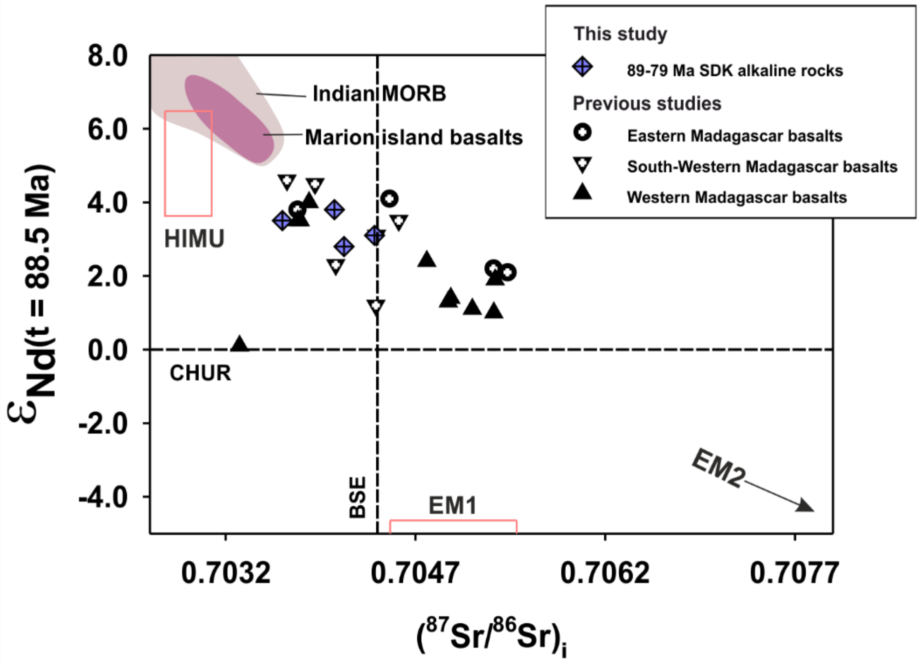

Fig. 5.8. ε_{Nd}(t) vs. (^{87}Sr/^{86}Sr)$_i$ plot for the 89-79 Ma SDK alkaline silicate rocks. See Table 4.18 for the data. Reported data of Cretaceous basalts from Eastern, Southwestern, and Western Madagascar are

plotted for comparison. The data are taken from Cucciniello et al. (2013), Mahoney et al. (1991), and Melluso et al. (2003). Marion (Mahoney et al.,1991) and Indian MORB (Mahoney et al., 1989) fields are also shown. Mantle fields HIMU, EM1, and EM2 are after Zindler and Hart (1986).

Geochemical, isotopic, and other evidence in support of a non-Marion plume origin for the late Cretaceous Madagascar basalts has been presented by some authors (e.g., Bardintzeff et al., 2010; Cucciniello et al., 2013; Melluso et al., 2003). According to Bardintzeff et al. (2010), Cenozoic Ambre and Nosy Be volcanic formations in the northern part of Madagascar have similar geochemical and isotopic signatures to those of the Marion Island basalts, but the location of the Marion plume at that time was far away from Madagascar, was located far to the south of Madagascar. The geochemical and isotopic signatures of the Cretaceous basalts in the southern part of Madagascar, where the advocated plume was in the vicinity, constrained by plate reconstructions, are inconsistent with the Marion plume signatures. Cucciniello et al. (2013) showed that the geochemical and isotopic characteristics of the late Cretaceous basalts from northwestern Madagascar could not be reconciled by contamination of plume-derived magma with the Archean crust, instead requires two different mantle sources – a MORB type LREE depleted source, another an LREE-enriched source.

Since a plume model is untenable, the most plausible reason for the 89-79 Ma alkaline magmatism in the SDK complex was the lithospheric extension-related magmatism during the breakup of India and Madagascar. Because the LREE-depleted character of these rocks suggests derivation from a sub-lithospheric source, we hypothesize that the asthenospheric-derived melts emplaced during the breakup of India were the source magmas, with small contributions from the Indian subcontinental lithospheric mantle, which marginally modified the Sr-Nd isotopic compositions towards enriched sources *(Fig. 5.8)*.

5.7. Nature of mantle source for 69-66 Ma magmatism

The uncontaminated 69-66 Ma alkaline silicate rocks, having the lowest range of $(^{87}Sr/^{86}Sr)_i$ and highest $(^{143}Nd/^{144}Nd)_i$ and carbonatites of the SDK complex have sub-BSE $(^{87}Sr/^{86}Sr)_{68.5}$ and superchondritic $\varepsilon_{Nd}(68.5)$, suggesting their derivation from a LREE-depleted mantle source. Besides, the least differentiated alkaline silicate rocks of SDK show both Nb and Ba enrichments in PM-normalized plots *(Fig. 4.13, Chapter 4)*. These signatures rule out any direct derivation of SDK magmas from an SCLM source because it is usually LREE enriched and has negative ε_{Nd} (e.g., Elkins et al., 2020, Rasoazanamparany et al., 2022). Thus, in every likelihood, these magmas were extracted from an asthenospheric source.

Simonetti et al. (1998) advocated for the involvement of three mantle sources to explain the origin of the SDK complex, the Deccan-Reunion plume, SCLM, and Indian MORB-type asthenospheric mantle. As established earlier, the 68.5 Ma alkaline silicate rocks and some carbonatites show signs of crustal contamination in their (initial) Sr-Nd isotopic compositions; however, the 66.4 Ma alkaline rocks appear more primitive *(Figs. 4.17, 4.18; Chapter 4)*. In ε_{Nd}(t) vs. $(^{87}Sr/^{86}Sr)_i$ plot *(Fig. 5.9)*, the least contaminated alkaline silicate rocks and carbonatites have $(^{87}Sr/^{86}Sr)_i$ extending from modern Reunion basalts-like compositions towards higher $(^{87}Sr/^{86}Sr)_i$, and have lower ε_{Nd}(t) values than that of the modern Reunion basalts ($(^{87}Sr/^{86}Sr)_i$ = 0.70405-0.70429; ε_{Nd}(0) = 4.0±0.4). Similarly, in $(^{87}Sr/^{86}Sr)_i$ vs. $(^{206}Pb/^{204}Pb)_i$ *(Fig. 5.10a)* and ε_{Nd}(t) vs. $(^{206}Pb/^{204}Pb)_i$ *(Fig. 5.10b)* plots, most SDK carbonatites, and the primitive alkaline silicate rocks fall between the fields of the Reunion basalts and EM 2 mantle component, suggesting that the primary magma was not derived entirely from a (Reunion) plume like source. More evolved rocks deviating towards higher or lower $(^{206}Pb/^{204}Pb)_i$ may have resulted from crustal contamination. The lower $(^{206}Pb/^{204}Pb)_i$ and $(^{207}Pb/^{204}Pb)_i$ (18.465,15.592) observed in a basanite (KT-20-23) is probably due to the contamination of magma with the lower crust. However, the contribution of the Reunion plume-like mantle in the source of these rocks is evident in the $(^{207}Pb/^{204}Pb)_i$ vs. $(^{206}Pb/^{204}Pb)_i$ plot *(Fig. 5.11a)*, where most of the SDK carbonatites and the least contaminated alkaline silicate rocks show overlapping Pb isotope compositions with the Reunion basalts. Barring a few carbonatites and one alkaline silicate rock (tephriphonolite: SAR-20-5), most of these rocks show a trend toward more radiogenic Pb isotopic compositions than the modern Reunion basalts in the $(^{208}Pb/^{204}Pb)_i$ vs. $(^{206}Pb/^{204}Pb)_i$ plot *(Fig. 5.11b)*, suggesting the involvement a more enriched source component, along with the Reunion plume component.

From combined Sr-Nd-Pb isotopic studies, the involvement of a Reunion plume mantle source component is inferred in the source of 69-66 Ma SDK alkaline silicate rocks and carbonatites, though only the plume component cannot explain the Sr-Nd isotope data of these rocks. As the initial Sr, Nd, and Pb isotopic ratios of the least contaminated alkaline silicate rocks and most carbonatites plot between the plume and EM2 component, an EM2-type enriched mantle component in the source of these rocks can explain their isotopic data. EM2-

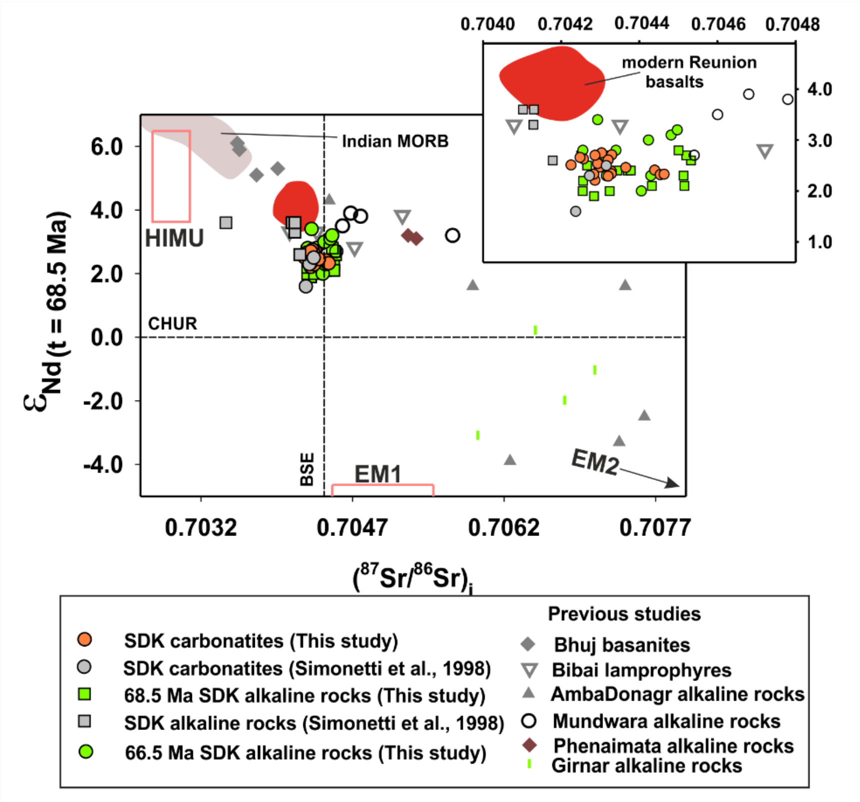

Fig. 5.9. ε_{Nd}(t) vs. (^{87}Sr/^{86}Sr)$_i$ plot for the 69-66 Ma SDK alkaline silicate rocks and carbonatites. Earlier work of Simonetti et al. (1998) for the SDK complex (Barmer) is shown. Also plotted for comparison are previously reported data from other Deccan alkaline complexes - Mundwara, Bhuj, Phenaimata, Girnar, Bibai, and Amba Dongar. Data sources: Simonetti et al. (1998), Banerjee and Chakravarti. (2019), Sahoo et al. (2020), Chandra et al. (2019), Kerr et al. (2010). Reunion data are taken from Albarède et al. (1977), Bosch et al. (2008), Di Muro et al. (2014), Vlastelic et al. (2009), and Fisk et al. (1988). Data sources from Indian MORB and other Mantle fields are the same as in Fig. 5.8

type mantle sources, as inferred from the geochemical studies of global OIBs, commonly have different incompatible trace element ratios such as lower Ce/Pb (< 22), higher Th/U (>4.5) and Ba/La (>11) than that of modern Reunion lavas (Ce/Pb =27.0±1.45; Th/U = 4.07±0.10; Ba/La = 6.89 ±0.08) which have relatively homogeneous compositions (e.g., Di Muro et al., 2014; Vlastelic et al., 2005; Willbold and Stracke, 2006; and references therein). Isotopic studies of Reunion basalts and EM2 type OIB (Samoa, Society, Marquesas) basalts (e.g., Di Muro et al., 2014; Vlastelic et al., 2005; Willbold and Stracke, 2006; and references therein) also support the distinction between Reunion and EM2 mantle sources. Therefore, the most plausible explanation for the enriched mantle component in the SDK magmas would be the Indian SCLM, which was possibly metasomatized by sublithospheric mantle-derived melts and fluid during its breakup from the Gondwana supercontinent. To quantitatively estimate the proportion of lithospheric mantle in the source of the SDK rocks, binary mixing calculations

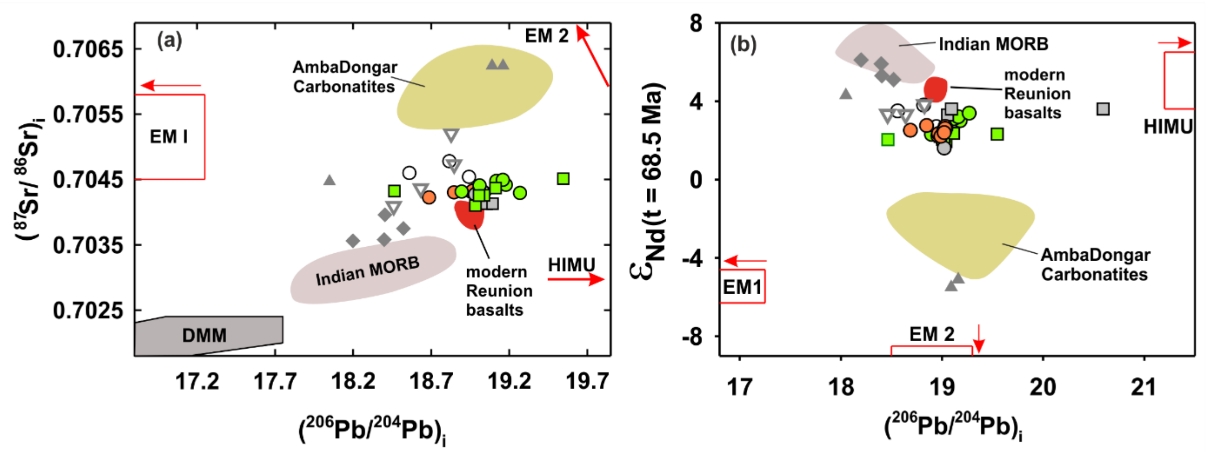

Fig. 5.10. $(^{87}Sr/^{86}Sr)_i$ vs. $(^{206}Pb/^{204}Pb)_i$ plot (a), $\varepsilon_{Nd}(t)$ vs. $(^{206}Pb/^{204}Pb)_i$ plot for the 69-66 Ma SDK alkaline silicate rocks and carbonatites. Earlier work of Simonetti et al. (1998) for the SDK complex (Barmer) is shown. Previously reported data (data sources same as in Fig. 5.7) from other Deccan alkaline complexes are also plotted for comparison. Data sources for Indian MORB, Reunion, and mantle fields are the same as in Fig. 5.8.

between a Reunion mantle-like source and assumed SCLM was done *(Fig. 5.12 a, b, c)*. The following compositions for plume component were chosen for the Reunion plume source: $(^{87}Sr/^{86}Sr)_i = 0.70405$, Sr =371 ppm, $(^{143}Nd/^{144}Nd)_i = 0.512845$, Nd = 25.0 ppm, $(^{206}Pb/^{204}Pb)_i = 18.902$, Pb = 1.7 ppm (Albarède et al., 1997; Bosch et al., 2008; Vlatselic et al., 2005). Following SCLM compositions were taken for calculations: $(^{87}Sr/^{86}Sr)_i = 0.7100$, Sr =49 ppm, $(^{143}Nd/^{144}Nd)_i = 0.51000$, Nd = 8.4 ppm, $(^{206}Pb/^{204}Pb)_i = 19.300$, Pb = 0.86 ppm. These values are taken from data for South African mantle xenoliths (e.g., Cohen et al., 1984; Walker et al., 1989), because there are no such data available from the Indian subcontinent, and we assume

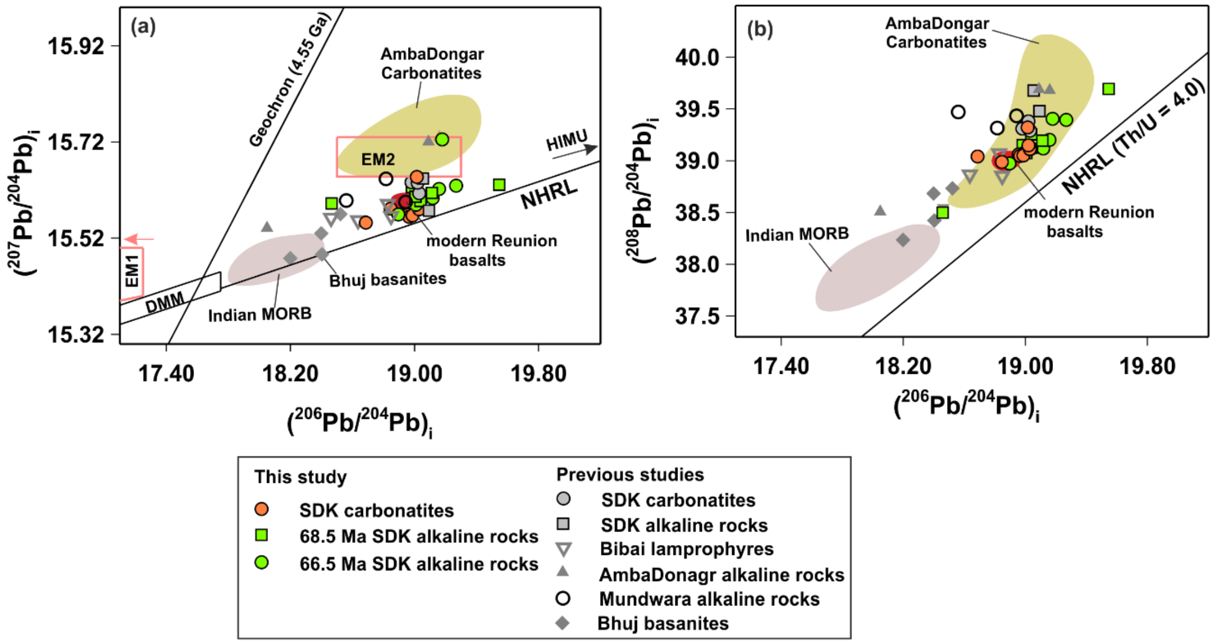

Fig. 5.11. (^{207}Pb/^{204}Pb)$_i$ vs. (^{206}Pb/^{204}Pb$_i$ (a) and (^{208}Pb/^{204}Pb)$_i$ vs. (^{206}Pb/^{204}Pb)$_i$ (b) plots for the 69-66 Ma SDK alkaline silicate rocks and carbonatites of the SDK complex. Data sources: Previously reported SDK data (Simonetti et al., 1997), Deccan alkaline complexes (Chandra et al., 2019; Kerr et al., 2010; Simonetti et al., 1998)), Modern Reunion basalts (Albarède et al., 1997; Bosch et al., 2008; Di Muroet al., 2014; Fisk et al., 1988); Indian MORB (Mahoney et al., 1989; Janney et al., 2005). Fields of DMM, EM1, and EM2 (Hart and Zindler, 1989), NHRL (Hart, 1984). µ values (= ^{238}U/^{204}Pb) of 8.3, 8.4, and 8.5 are also shown.

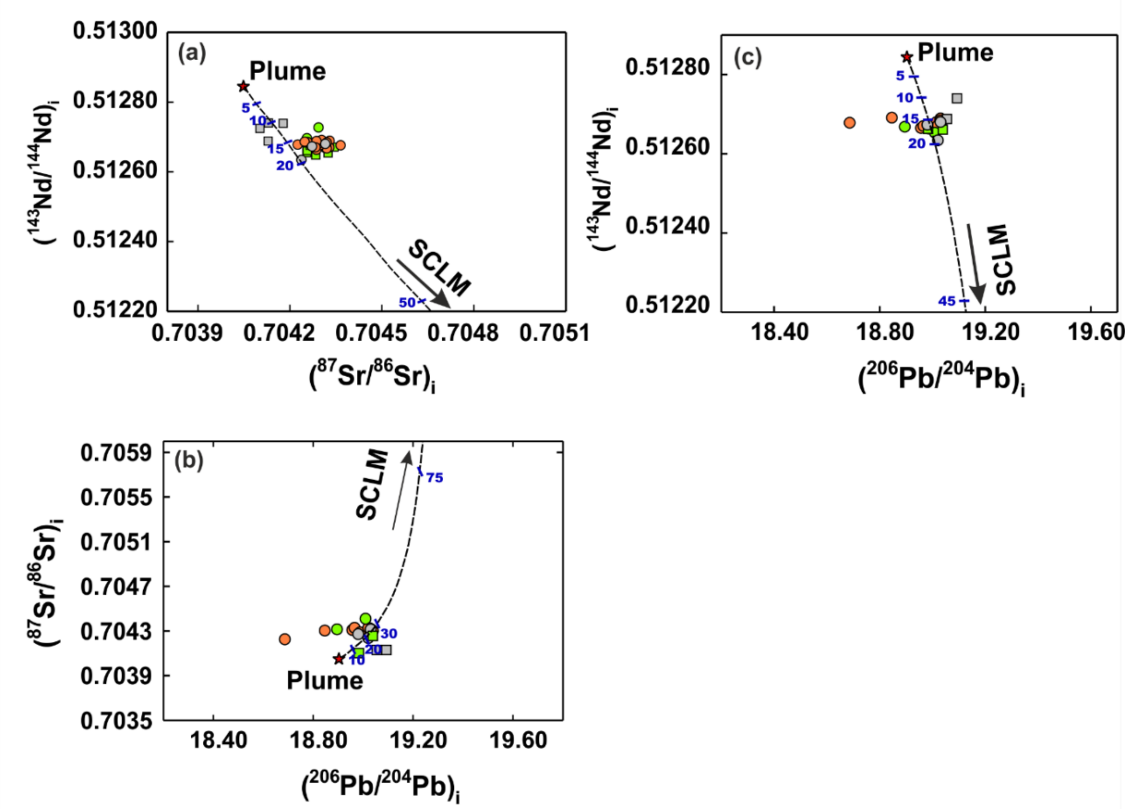

Fig. 5.12. (^{143}Nd/^{144}Nd)$_i$ vs. (^{87}Sr/^{86}Sr)$_i$ (a), (^{87}Sr/^{86}Sr)$_i$ vs. (^{206}Pb/^{204}Pb$_i$ (b), and (^{143}Nd/^{144}Nd)$_i$ vs. (^{206}Pb/^{204}Pb$_i$ diagrams showing binary mixing of two mantle source components: Reunion Plume and Indian subcontinental lithospheric mantle. Symbols are the same as in Fig. 5.10. See text for discussion.

that during late Cretaceous, the Indian and South African SCLMs could have been similar in compositions. The calculations predict that the presence of ~10-15% SCLM component is required to explain the initial Sr, Nd, and Pb isotopic compositions of the least contaminated alkaline silicate rocks of the SDK complex *(Fig. 5.12 a,b,c)*.

5.8. Evolution of Sarnu-Dandali-Kamthai complex

The extensional event that led to the separation of India and Madagascar from the East Gondwana continents (Africa, Antarctica, Australia) at ~120 Ma perhaps also created the Cambay-Barmer rift basin and related fracture zones, which later facilitated the crustal migration of the mantle-derived magmas at different point of time during Late Cretaceous (100-

66 Ma). The commencement of rifting of India from Madagascar at ~88 Ma associated heat and melt from the asthenosphere could have caused a low degree of partial melting in the metasomatized Indian sub-continental lithospheric mantle to produce rift-related alkaline magmatism that continued for at least ~10 Ma.

Based on our data, we propose a petrogenetic model *(Fig. 5.13)* for the origin of the second phase of magmatic activities in the Barmer basin during 69-66 Ma, while the Deccan volcanism was shaping the geology of western India. The arrival of the Reunion-Deccan mantle plume at the Indian lithosphere-asthenosphere boundary reactivated the Barmer rift system and emplacement of alkaline and carbonate magmas in the SDK complex.

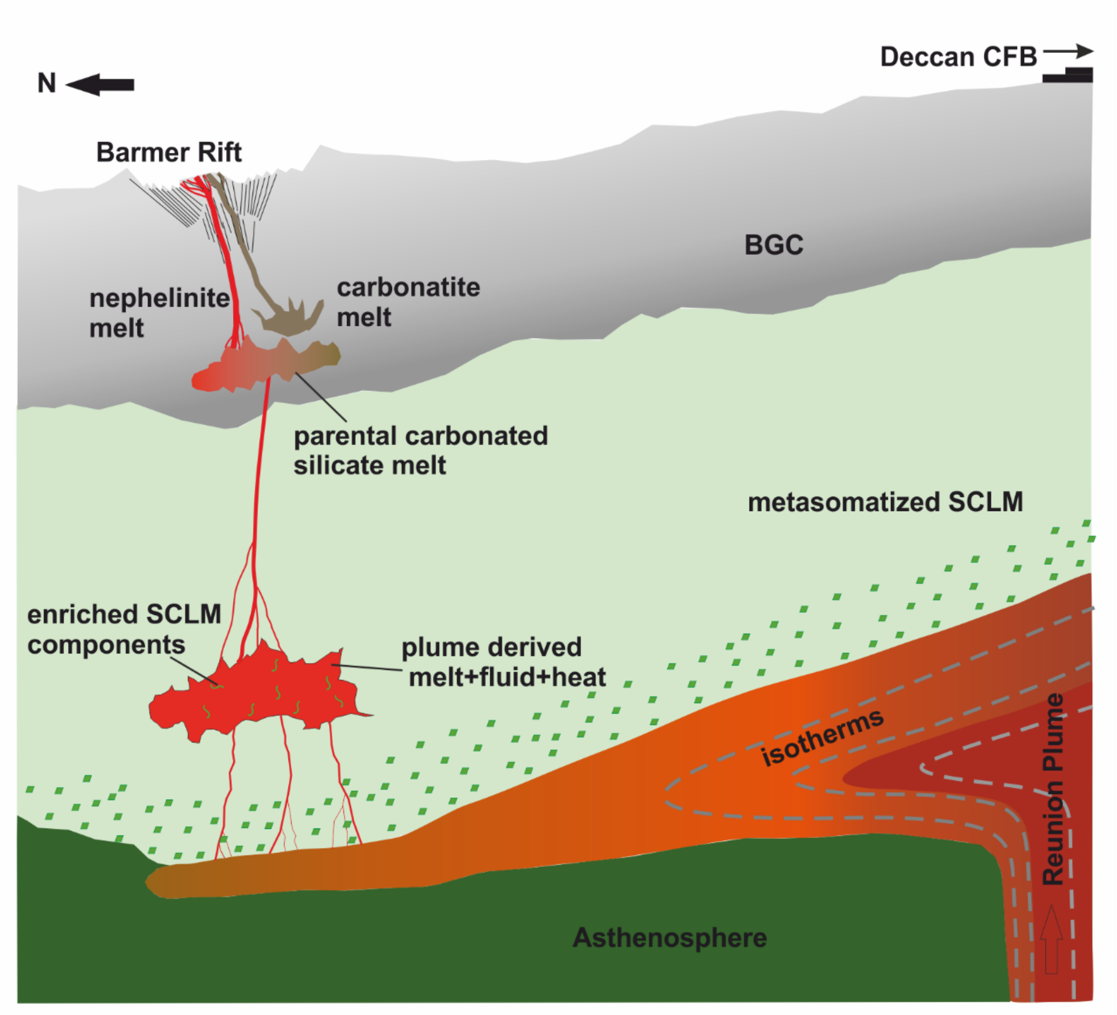

Fig. 5.13. Proposed petrogenetic model (not to scale) showing the origin of pre-Deccan Sarnu-Dandali-Kamthai carbonatite-alkaline complex during the northward drift of the Indian plate at 69-66 Ma. Deccan continental flood basalts (CFB), which is the result of melting of the Reunion plume head, lie ~500 km south of the SDK complex. See the discussion (5.5.6) for details.

The key to this plume association model is the large volume of fluids needed for the generation of carbonatites that otherwise would not be possible with the involvement of the SCLM alone. As shown in our proposed petrogenetic model in *Fig. 5.13*, at the edge of the Reunion plume, the plume-derived melts, along with the fluids and heat, caused low-degree melting in the metasomatized Indian SCLM incorporating enriched components. Subsequently, this mantle mixture (re)melted to form a primary carbonated alkaline silicate magma which ascended through the lithosphere to a magma chamber in the lower crust. At this lower crustal magma chamber, concurrent crustal assimilation, fractional crystallization of silicate minerals, and liquid immiscibility of carbonate melt modified the magma before two different melts (i.e., silicate and carbonate melt) got separated and emplaced.

5.9. Geodynamic Implications

The Sarnu-Dandali-Kamthai complex records a polychronous history of late Cretaceous alkaline magmatism in the Northwestern part of the Indian subcontinent. The presence of the complex in the Barmer rift basin elucidates the importance of extensional tectonics for the generation and migration of mantle-derived melts and fluids. The lithospheric extension owing to the amalgamation and breakup of the Indian subcontinent with other Gondwana continents must have facilitated the metasomatism of the Indian subcontinental lithospheric mantle prior to the late Cretaceous alkaline magmatism in the complex and elsewhere in the Deccan Igneous Province. The oldest alkaline event (89-79 Ma) in the complex is the result of magmatism without any plume association in an extensional environment. However, the absence of carbonatites of this generation in the complex may highlight the different metasomatic history of the Indian SCLM and the absence of enough fluids necessary to produce carbonatite magma during this period. The huge volume of fluids carried by the Reunion plume could have triggered the generation of carbonated silicate magma in the Indian SCLM during the youngest phase of alkaline magmatism in the complex. Compared to the Deccan continental flood basalts, where the direct melting of the reunion mantle directly produced the picritic-basaltic lavas during 66.5-65.5 Ma, the pre-Deccan alkaline magmatism in a region lying far away to the north of the main Deccan activity probably occurred in the lithospheric mantle, triggered by the plume derived heat and fluids. The presence of crustal-scale layered mafic intrusions and a low-velocity anomalous zone in the upper mantle structure beneath the thinned crust of the Barmer rift, as constrained by geophysical studies (Bandalamudi et al., 2022; Kilaru et al., 2013), also supports the fact that huge volume of asthenospheric melts and fluids had penetrated and metasomatized the Indian lithosphere, probably during Reunion plume activity in the late Cretaceous period.

5.10. Nature and source of carbon in SDK carbonatites

Our carbon isotopic data for the unaltered SDK carbonatites ($\delta^{13}C$ = -6.5 to -4.0‰) bear the signature of primordial mantle carbon, which still remains as the primary source of carbon in mantle xenoliths and volcanic CO_2 (e.g., Deines 2002). Based on Ca, S, and B isotopic studies in global carbonatites, many believe that the apparent increase in the carbonatite activity in the globe could be due to increased recycling of sedimentary carbonate into the convecting mantle after ca 1 Ga, perhaps due to the transition from hot subduction to cold subduction tectonics (e.g., Thomson et al., 2016; Hulett et al., 2016; Amsellem et al., 2020). Direct evidence for the incorporation of recycled inorganic carbon in carbonatites was first reported by Ray et al. (1999) in Sung Valley carbonatites of India which were believed to have been produced by Kerguelen-Rajmahal-Sylhet plume activity. Unfortunately, the nature of carbonatite intrusion in the SDK (veins/dykes) appears to have caused extensive isotopic fractionation during the crystallization process obliterating the presence/signature (if any) of the recycled carbon in these rocks.

Chapter 6

Summary and Conclusions

In this work, I made an attempt to provide answers to some outstanding questions related to the origin and evolution of carbonatites, one of the most enigmatic mantle-derived rocks on Earth. For this purpose, I chose an interesting Cretaceous carbonatite-alkaline complex of India that had recurrent alkaline magmatism linked to a couple of major continental rifting events and one to a continental flood basalt eruption caused by a deep mantle plume. This complex, known as the Sarnu-Dandali-Kamthai (SDK) complex, is spread over ~300km^2, is located in northwestern India – in the state of Rajasthan, about 500 km to the north of Deccan basaltic province, along the Cambay-Barmer rift system. Although there existed some limited geochronological information, mostly on one of the earliest alkaline activities, a detailed chronology of various activities in the complex was lacking, and geochemical and isotopic data were almost nonexistent. With the specific objectives of finding ages of emplacements of various magmatic events, understanding differentiation processes and the evolution of carbonatites and their relationship with the associated alkaline silicate rocks, establishing the role of crustal assimilation (if any) in the origin and diversification of carbonatites and associated silicate rocks, understanding the nature of the mantle source(s) for different episodes of magmatism and their link to the regional tectonic activities, and finding the nature of carbon (primordial vs. recycled) in these carbonatites, I carried out a detailed field, petrographic, geochronological (^{40}Ar-^{39}Ar dating), geochemical (major and trace elements) and isotopic (C-O-Sr-Nd-Pb) investigation in the SDK complex.

For my work, I carried out three field studies in the complex to establish field relationships between different episodes of magmatic activities and collected samples for various studies. Nine samples (seven alkaline silicate rocks, one sanidine separate from a phonolite and one biotite separate from a carbonatite) were dated using ^{40}Ar-^{39}Ar method. Petrological microscopy and XRD technique were employed to study the mineralogy and texture. EMPA technique was used for mineral chemistry. More than sixty samples were analyzed for major oxide and trace element contents using XRF and Q-ICPMS techniques. Seventy-one samples were analyzed for C-O isotopic compositions, fifty-one samples were analyzed for Sr-Nd isotopic ratios, and twenty-one for Pb isotopic compositions using mass spectrometric techniques. The data were modeled using various known mathematical models for magmatic and secondary alteration processes. Based on the results from data and models, I make the following inferences about the origin and evolution of the SDK complex and discuss their implications for the evolution of carbonatites in general.

1. From the results of our ^{40}Ar-^{39}Ar dating, it is evident that at least two episodes of alkaline magmatism had occurred in the SDK complex during the late Cretaceous period. The older event happened during 89-79 Ma and the younger during 69.7-66.4 Ma. We did not find any evidence for carbonatite activity during the older episode; however, the younger episode did see an intrusion of carbonatites along with alkaline silicate rocks. Our age data also establish the coeval emplacements of carbonatites and alkaline silicate rocks in the SDK complex at ~68.5 Ma.

2. The alkaline magmatic episode that occurred during 89-79 Ma, which lasted for about 11 million years, was contemporaneous with the continental breakup of Madagascar and India (92-80 Ma), whereas the younger episode of 69.7-66.4 Ma, lasting for only about 3 million years, was contemporaneous with the India-Seychelles break up and eruption of the Deccan CFB in western India (69-62 Ma).

3. The initial Sr-Nd isotopic ratios of the 89-79 Ma alkaline silicate rocks of the SDK overlap with those of the same/similar age basalts of Madagascar, which hints at a common origin. These data, however, do not support the derivation of these magmas from the Marion plume which has been linked by some to the India-Madagascar separation and contemporaneous magmatism on both the continents.

4. Field, petrography, geochemical and isotopic data confirm a magmatic origin for the SDK carbonatites. They occur as veins and dykes, show magmatic texture, contain typical carbonatitic minerals, show LREE-enriched trace element patterns, their unaltered and unfractionated $\delta^{13}C_{V\text{-}PDB}$ (~ -6.0‰) and $\delta^{18}O_{V\text{-}SMOW}$ (~ +7‰) are mantle like, and have $(^{87}Sr/^{86}Sr)_i < 0.7046$; $\varepsilon_{Nd(t=68.5)} \geq +2.2$ and $(^{206}Pb/^{204}Pb)_i < 19.03$, which overlap with the compositions of the mantle.

5. The presence of carbonatite veins/dykes and carbonate melt inclusions in alkaline silicate rocks rules out the possibility of a primary carbonatite magma in the SDK complex. The same is also indicated by the trace element geochemistry of these rocks that suggest a coevolution of carbonatites with the coeval alkaline silicate rocks. The carbonatitic melt inclusions and/or xenolith found in alkaline silicate rocks possess the same initial C-O-Sr-Nd-Pb isotopic ratios as those of the host rock, which clearly suggests cogenesis for both rock types.

6. Major and trace element data for carbonatites and alkaline silicate rocks of 68.5 Ma show evidence of fractional crystallizations. The existence of two separate crystallization trends for carbonatites and alkaline silicate rocks suggests that carbonatites have unlikely been formed from a residual melt of a fractionating alkaline silicate magma. However, their overlapping least fractionated trace elemental ratios suggest a common parentage. Since the formation of SDK carbonatites from a primary carbonate magma or from a residual melt of a parental silicate magma are ruled out, the only possible scenario that can explain the overlapping unfractionated trace elemental ratios is the immiscible separation of carbonate and silicate melts from a single parental magma.

7. The $\delta^{13}C$ and $\delta^{18}O$ compositions of unaltered carbonatites show evidence of fractional crystallization. Using a multicomponent Rayleigh fractionation model called RIFMS, it was established that the SDK carbonatites had fractionally crystallized from a CO_2+H_2O-rich carbonate melt at a temperature of ~ 850^{o}C. This melt possibly had differentiated from a parental carbonated silicate magma. Mathematical treatment of data for altered carbonatites using fluid-rock interaction models suggests secondary alteration by CO_2-bearing hydrothermal fluids at low temperatures (≤100^{o}C). Therefore, we hypothesize that the extremely high concentration of REEs observed in the altered carbonatites is likely the result of the dissolution and reprecipitation of REE-rich minerals from the hydrothermal fluids as a result of low-temperature interaction of the hydrothermal fluids with the primary carbonatites.

8. The initial Sr-Nd-Pb isotopic ratios for 68.5 Ma SDK carbonatites and alkaline silicate rocks largely overlap and suggest cogenesis for both rocks. These isotopic ratios, particularly those of the evolved silicate rocks, hint at possible crustal contamination.

Application of a mathematical model that treats elemental and isotopic effects of concurrent crustal assimilation, fractional crystallization of silicate rocks, and immiscibility separation of a carbonate melt from a parental carbonated silicate magma (AFCLI model) reveals that Sr and Nd contents and their variable isotopic ratios observed in the alkaline silicate rocks can be explained by the AFCLI process with < 6% lower crustal assimilation. Results of this model not only establish that the liquid immiscibility process as the responsible magmatic process for the generation of SDK carbonatites but also points to the possibility that carbonatites, too, can preserve the effects of crustal contamination. It also establishes that crustal contamination plays a key role in the liquid immiscibility process and subsequent diversification of carbonatites and alkaline silicate rocks.

9. The carbon in the ~68.5 Ma SDK carbonatites ($\delta^{13}C \sim -6 \pm 1$ ‰) is primordial. No signature of recycled inorganic carbon was found. The absence of a HIMU (high-$^{238}U/^{204}Pb$) component in the SDK carbonatites also rules out the incorporation of any recycled crustal components in the mantle source of these young carbonatites, contrary to that observed elsewhere in carbonatites younger than 200 Ma, especially in oceanic carbonatites.

10. Based on initial Sr-Nd-Pb isotopic ratios, the SDK carbonatites and associated alkaline silicate rocks of 69-66 Ma age group can be genetically linked to the Deccan-Reunion mantle plume. However, an EM2-type enriched mantle component is required to explain the entire variations observed. Indian sub-continental lithospheric mantle, which is likely to have been metasomatized during its amalgamation with and breakup from the Gondwana continents earlier, was likely the source of this enriched mantle component. Thus, it is apparent that the metasomatized lithosphere plays a vital role in the chemical and isotopic variability observed in carbonatites in continental settings.

Recommendations for Future Research

From the findings of this work for the late Cretaceous Sarnu-Dandali-Kamthai carbonatite alkaline complex, I recommend the following aspects to be taken care of in future studies of the Indian carbonatite-alkaline complexes.

1. A detailed geochemical and isotopic investigation of the older generation of alkaline silicate rocks is required to understand their origin, which will help the tectonic framework and nature of mantle sources involved in the late Cretaceous period much before the initiation of the Deccan-Reunion plume activity. Since this complex has not been fully explored, therefore, detailed investigations of rock types in this complex and in regions north to this complex are required.

2. Recently, mantle xenoliths (phlogopite-spinel-wehrlite) from lamprophyre dykes in the SDK complex have been reported. Geochemical and isotopic studies of those xenoliths will add important contributions to the nature and metasomatic history of the Indian subcontinental lithospheric mantle.

3. Many new carbonatites have been discovered in India. However, there have not been thorough petrological and/or geochemical investigations in these to prove their true identity. If found to be carbonatites, they are likely to provide important information about the evolution of the Indian subcontinental mantle during the interim period between the Proterozoic and the Cretaceous.

References

Abdi, H., Williams, L.J., 2010. Principal component analysis. Wiley Interdiscip. Rev. Comput. Stat. 2, 433–459. https://doi.org/10.1002/WICS.101

Ackerman, L., Magna, T., Rapprich, V., Upadhyay, D., Krátký, O., Čejková, B., Erban, V., Kochergina, Y. V., Hrstka, T., 2017. Contrasting petrogenesis of spatially related carbonatites from Samalpatti and Sevattur, Tamil Nadu, India. Lithos 284–285, 257–275. https://doi.org/10.1016/j.lithos.2017.03.029

Albarède, F., Luais, B., Fitton, G., Semet, M., Kaminski, E., Upton, B.G.J., Bachèlery, P., Cheminée, J.L., 1997. The Geochemical Regimes of Piton de la Fournaise Volcano (Réunion) During the Last 530 000 Years. J. Petrol. 38, 171–201. https://doi.org/10.1093/PETROJ/38.2.171

Amsellem, E., Moynier, F., Bertrand, H., Bouyon, A., Mata, J., Tappe, S., Day, J.M.D., 2020. Calcium isotopic evidence for the mantle sources of carbonatites. Sci. Adv. 6, 1–7. https://doi.org/10.1126/sciadv.aba3269

Anantharamu, T.R., Rao, K.N.N., Ahmed, S., Prasad, T.K.G., Reddy, T.G., Dasu, S.P.V., Sugavanam, E.B., others, 1995. Carbonatite around Ajjipuram, Kollegal Taluk, Karnataka. Geol. Soc. India 46, 663–668.

Anenburg, M., Broom-Fendley, S., Chen, W., 2021. Formation of Rare Earth Deposits in Carbonatites. Elements 17, 327–332. https://doi.org/10.2138/GSELEMENTS.17.5.327

Banerjee, A., Chakrabarti, R., 2019. Lithos A geochemical and Nd , Sr and stable Ca isotopic study of carbonatites and associated silicate rocks from the ~ 65 Ma old Ambadongar carbonatite complex and the Phenai Mata igneous complex , Gujarat , India : Implications for crustal contamination . LITHOS 326–327, 572–585. https://doi.org/10.1016/j.lithos.2019.01.007

Bardintzeff, J.M., Liégeois, J.P., Bonin, B., Bellon, H., Rasamimanana, G., 2010. Madagascar volcanic provinces linked to the Gondwana break-up: Geochemical and isotopic evidences for contrasting mantle sources. Gondwana Res. 18, 295–314. https://doi.org/10.1016/J.GR.2009.11.010

Barker, D., 1989. Field relations of carbonatites, in: Bell. K (Ed.), Carbonatites, Genesis and Evolution. Unwin-Hynman.

Basu, A.R., Chakrabarty, P., Szymanowski, D., Ibañez-Mejia, M., Schoene, B., Ghosh, N., Bastian Georg, R., 2020. Widespread silicic and alkaline magmatism synchronous with the Deccan Traps flood basalts, India. Earth Planet. Sci. Lett. 552, 116616. https://doi.org/10.1016/J.EPSL.2020.116616

Basu, A.R., Renne, P.R., DasGupta, D.K., Teichmann, F., Poreda, R.J., 1993. Early and late alkali igneous pulses and a high-3He plume origin for the Deccan flood basalts. Science (80-.). 261, 902–906. https://doi.org/10.1126/science.261.5123.902

Basu, S., Murty, S.V.S., 2006. Noble gases in carbonatites of Sung Valley and Ambadongar: Implications for trapped components. Chem. Geol. 234, 236–250. https://doi.org/10.1016/J.CHEMGEO.2006.05.004

Basu, S.K., Bhattacharyya, T., 2014. Petrography and mineral chemistry of alkaline-carbonatite complex in Singhbhum crustal province, Purulia region, eastern India. J. Geol. Soc. India 83, 54–70.

Beard, C.D., Goodenough, K.M., Borst, A.M., Wall, F., Siegfried, P.R., Deady, E.A., Pohl, C., Hutchison, W., Finch, A.A., Walter, B.F., Elliott, H.A.L., Brauch, K., 2023. Alkaline-Silicate REE-HFSE Systems. Econ. Geol. 118, 177–208. https://doi.org/10.5382/ECONGEO.4956

Bell, K., Simonetti, A., 2010. Source of parental melts to carbonatites-critical isotopic constraints. Mineral. Petrol. 98, 77–89. https://doi.org/10.1007/s00710-009-0059-0

Bhunia, S., Chalapathi Rao, N.V., Belyatsky, B., Talukdar, D., Pandey, R., Lehmann, B., 2022. SHRIMP U-Pb zircon geochronology of the carbonatite-hosted REE deposit of Kamthai, Late Cretaceous polychronous Sarnu Dandali alkaline complex, NW India: Links to plume-related metallogeny and CO2 outgassing at the K-Pg boundary. Gondwana Res. 112, 116–125. https://doi.org/10.1016/J.GR.2022.09.012

Bhushan, S.K., 2015. Geology of the Kamthai Rare Earth Deposit. J. Geol. Soc. India 85, 537–546. https://doi.org/10.1007/s12594-015-0247-y

Bhushan, S.K., Kumar, A., 2013. First carbonatite hosted REE deposit from India. J. Geol. Soc. India 81, 41–60. https://doi.org/10.1007/s12594-013-0005-y

Bizimis, M., Salters, V.J.M., Dawson, J.B., 2003. The brevity of carbonatite sources in the mantle: Evidence from Hf isotopes. Contrib. to Mineral. Petrol. 145, 281–300. https://doi.org/10.1007/s00410-003-0452-3

Bladon, Andrew J., Clarke, S.M., Burley, S.D., 2015a. Complex rift geometries resulting from inheritance of pre-existing structures: Insights and regional implications from the Barmer Basin rift. J. Struct. Geol. 71, 136–154. https://doi.org/10.1016/j.jsg.2014.09.017

Bladon, A.J., Burley, S.D., Clarke, S.M., Beaumont, H., 2015b. Geology and regional significance of the Sarnoo Hills, eastern rift margin of the Barmer Basin, NW India. Basin Res. 27, 636–655.

Borodin, L.S., Gopal, V., Moralev, V.M., Subramanian, V., Ponikarov, V., 1971. Precambrian carbonatites of Tamil Nadu, South India. Geol. Soc. India 12, 101–112.

Bosch, D., Blichert-Toft, J., Moynier, F., Nelson, B.K., Telouk, P., Gillot, P.Y., Albarède, F., 2008. Pb, Hf and Nd isotope compositions of the two Réunion volcanoes (Indian Ocean): A tale of two small-scale mantle “blobs”? Earth Planet. Sci. Lett. 265, 748–765. https://doi.org/10.1016/J.EPSL.2007.11.018

Brahma, S., Sahoo, S., Durai, P.R., 2022. First Report of Carbonatite from Gundlupet Area, Western Dharwar Craton, Karnataka, Southern India. J. Geol. Soc. India 98, 35–40. https://doi.org/10.1007/S12594-022-1924-2/METRICS

Brent Dalrymple, G., Lanphere, M.A., 1971. 40Ar/39Ar technique of KAr dating: a comparison with the conventional technique. Earth Planet. Sci. Lett. 12, 300–308. https://doi.org/10.1016/0012-821X(71)90214-7

Brooker, R.A., Kjarsgaard, B.A., 2011. Silicate-carbonate liquid immiscibility and phase relations in the system SiO2-Na2O-Al2O3-Cao-Co2 at 0·1-2·5 GPa with applications to carbonatite genesis. J. Petrol. 52, 1281–1305. https://doi.org/10.1093/petrology/egq081

Broom-Fendley, S., Styles, M.T., Appleton, J.D., Gunn, G., Wall, F., 2016. Evidence for dissolution-reprecipitation of apatite and preferential LREE mobility in carbonatite-derived late-stage hydrothermal processes. Am. Mineral. 101, 596–611. https://doi.org/10.2138/AM-2016-5502CCBY/ASSET/GRAPHIC/J_AM-2016-5502CCBY_FIG_009.JPG

Burley, S.D., Gould, T., Taylor, A., Mishra, P., 2022. Syn-rift volcanism in the Barmer Basin: An intra-basin extrusive complex at the northern limit of the Deccan volcanic province in India. Geol. J. https://doi.org/10.1002/GJ.4659

Chacko, T., Mayeda, T.K., Clayton, R.N., Goldsmith, J.R., 1991. Oxygen and carbon isotope fractionations between CO2 and calcite. Geochim. Cosmochim. Acta 55, 2867–2882. https://doi.org/10.1016/0016-7037(91)90452-B

Chakhmouradian, A.R., Reguir, E.P., Zaitsev, A.N., Couëslan, C., Xu, C., Mumin, A.H., Yang, P., 2017. Lithos Apatite in carbonatitic rocks : Compositional variation , zoning , element partitioning and petrogenetic significance 275, 188–213. https://doi.org/10.1016/j.lithos.2016.12.037

Chakraborti, M.K., Bose, M.K., 1978. Theralite-melteigite-carbonatite association in Mer ring of Mundwara suite, Sirohi district, Rajasthan. Geol. Soc. India 19, 454–463.

Chakrabarty, A., Sen, A.K., 2010. Enigmatic association of the carbonatite and alkali-pyroxenite along the Northern Shear Zone, Purulia, West Bengal: A saga of primary magmatic carbonatite. J. Geol. Soc. India 76, 403–413. https://doi.org/10.1007/s12594-010-0113-x

Chandra, J., Paul, D., Stracke, A., Chabaux, F., Granet, M., 2019. The Origin of Carbonatites from Amba Dongar within the Deccan Large Igneous Province. J. Petrol. 60, 1119–1134. https://doi.org/10.1093/petrology/egz026

Chandra, J., Paul, D., Viladkar, S.G., Sensarma, S., 2018. Origin of the Amba Dongar carbonatite complex , India and its possible linkage with the Deccan Large Igneous Province 137–169.

Chandrasekaran, V., Srivastava, R.K., Chawade, M.P., 1990. Geochemistry of the alkaline rocks of Sarnu-Dandali area, district Barmer, Rajasthan, India. Geol. Soc. India 36, 365–382.

Chebotarev, D.A., Veksler, I. V., Wohlgemuth-Ueberwasser, C., Doroshkevich, A.G., Koch-Müller, M., 2019. Experimental study of trace element distribution between calcite, fluorite and carbonatitic melt in the system CaCO3 + CaF2 + Na2CO3 ± Ca3(PO4)2 at 100 MPa. Contrib. to Mineral. Petrol. 174, 1–13. https://doi.org/10.1007/s00410-018-1530-x

Cheng, Z., Zhang, Z., Aibai, A., Kong, W., Holtz, F., 2018. The role of magmatic and post-magmatic hydrothermal processes on rare-earth element mineralization: A study of the Bachu carbonatites from the Tarim Large Igneous Province, NW China. Lithos 314–315, 71–87. https://doi.org/10.1016/J.LITHOS.2018.05.023

Choudhary, S., Sen, K., Kumar, S., Rana, S., Ghosh, S., 2021. Forsterite reprecipitation and carbon dioxide entrapment in the lithospheric mantle during its interaction with carbonatitic melt: a case study from the Sung Valley ultramafic–alkaline–carbonatite complex, Meghalaya, NE India. Geol. Mag. 158, 475–486. https://doi.org/10.1017/S0016756820000631

Cohen, R.S., O'Nions, R.K., Dawson, J.B., 1984. Isotope geochemistry of xenoliths from East Africa: Implications for development of mantle reservoirs and their interaction. Earth Planet. Sci. Lett. 68, 209–220. https://doi.org/10.1016/0012-821X(84)90153-5

Craig, H., 1957. Isotopic standards for carbon and oxygen and correction factors for mass-spectrometric analysis of carbon dioxide. Geochim. Cosmochim. Acta 12, 133–149. https://doi.org/10.1016/0016-7037(57)90024-8

Cucciniello, C., Melluso, L., Jourdan, F., Mahoney, J.J., Meisel, T., Morra, V., 2013. 40Ar–39Ar ages and isotope geochemistry of Cretaceous basalts in northern Madagascar: refining eruption ages, extent of crustal contamination and parental magmas in a flood basalt province. Geol. Mag. 150, 1–17. https://doi.org/10.1017/S0016756812000088

Dalton, J.A., Wood, B.J., 1993. The compositions of primary carbonate melts and their evolution through wallrock reaction in the mantle. Earth Planet. Sci. Lett. 119, 511–525. https://doi.org/10.1016/0012-821X(93)90059-I

Dalrymple, G.B., 1991. The age of the Earth. Stanford University Press.

Dasgupta, R., Hirschmann, M.M., 2006. Melting in the Earth's deep upper mantle caused by carbon dioxide. Nature 440, 659–662. https://doi.org/10.1038/nature04612

Deines, P., 1989. Stable isotpe variations in carbonatites, in: Bell, K. (Ed.), Carbonatites, Genesis and Evolution. Unwin-Hynman, pp. 301–357.

Deines, P., 2002. The carbon isotope geochemistry of mantle xenoliths. Earth-Science Rev. 58, 247–278. https://doi.org/10.1016/S0012-8252(02)00064-8

Demény, A., Ahijado, A., Casillas, R., Vennemann, T.W., 1998. Crustal contamination and fluid/rock interaction in the carbonatites of Fuerteventura (Canary Islands, Spain): A C, O, H isotope study. Lithos 44, 101–115. https://doi.org/10.1016/S0024-4937(98)00050-4

Demény, A., Sitnikova, M.A., Karchevsky, P.I., 2004. Stable C and O isotope compositions of carbonatite complexes of the Kola Alkaline Province: phoscorite-carbonatite relationships and source compositions. Phoscorites carbonatites from mantle to mine 407–431. https://doi.org/10.1180/MSS.10.12

Dessai, A.G., Viegas, A., 2010. Petrogenesis of alkaline rocks from Murud-Janjira, in the Deccan Traps, Western India. Mineral. Petrol. 98, 297–311. https://doi.org/10.1007/S00710-009-0105-Y

Dhote, P., Zamarkar, P., Meshram, D.C., Dongre, A., 2022. Evidence and timing of metasomatism of the lithospheric mantle before large-scale Deccan magmatism: Insights from the phlogopite–spinel–wehrlite xenoliths from Sarnu–Dandali alkaline igneous complex, Rajasthan, northwestern India. J. Earth Syst. Sci. 131, 1–11. https://doi.org/10.1007/S12040-022-01895-0

Di Muro, A., Métrich, N., Vergani, D., Rosi, M., Armienti, P., Fougeroux, T., Deloule, E., Arienzo, I., Civetta, L., 2014. The shallow plumbing system of Piton de la Fournaise Volcano (La Réunion Island, Indian Ocean) revealed by the major 2007 caldera-forming eruption. J. Petrol. 55, 1287–1315. https://doi.org/10.1093/petrology/egu025

Dongre, A., Dhote, P.S., Zamarkar, P., Sangode, S.J., Belyanin, G., Meshram, D.C., Patil, S.K., Karmakar, A., Jain, L., 2022. Short-lived alkaline magmatism related to the Réunion plume in the Deccan Large Igneous Province: inferences from petrology,40Ar/39Ar geochronology and palaeomagnetism of lamprophyre from the Sarnu-Dandali Alkaline Igneous Complex, Geological Society Special Publication. The Geological Society Special Publications. https://doi.org/10.1144/SP513-2021-34

Doroshkevich, A.G., Viladkar, S.G., Ripp, G.S., Burtseva, M. V., 2009. hydrothermal ree mineralization in the amba dongar carbonatite complex, gujarat, india. Can. Mineral. 47, 1105–1116. https://doi.org/10.3749/CANMIN.47.5.1105

Doroshkevich, A.G., Ripp, G., Viladkar, S., 2010. Newania carbonatites, Western India: Example of mantle derived magnesium carbonatites. Mineral. Petrol. 98, 283–295. https://doi.org/10.1007/s00710-009-0076-z

Doroshkevich, A.G., Veksler, I. V., Klemd, R., Khromova, E.A., Izbrodin, I.A., 2017. Trace-element composition of minerals and rocks in the Belaya Zima carbonatite complex (Russia): Implications for the mechanisms of magma evolution and carbonatite formation. Lithos 284–285, 91–108. https://doi.org/10.1016/j.lithos.2017.04.003

Doucelance, R., Bellot, N., Boyet, M., Hammouda, T., Bosq, C., 2014. What coupled cerium and neodymium isotopes tell us about the deep source of oceanic carbonatites. Earth Planet. Sci. Lett. 407, 175–186. https://doi.org/10.1016/j.epsl.2014.09.042

Elkins, L.J., Meyzen, C.M., Callegaro, S., Marzoli, A., Bizimis, M., 2020. Assessing Origins of End-Triassic Tholeiites From Eastern North America Using Hafnium Isotopes. Geochemistry, Geophys. Geosystems 21, e2020GC008999. https://doi.org/10.1029/2020GC008999

Feng, M., Song, W., Kynicky, J., Feng, B., Fang, G., 2021. Geochronology and C-O-Sr-Nd isotopic study of the Ulgii Khiid carbonatite from the Southern Mongolian alkaline Province and its implications for the mantle sources. Ore Geol. Rev. 139, 104495. https://doi.org/10.1016/J.OREGEOREV.2021.104495

Foley, S.F., Fischer, T.P., 2017. An essential role for continental rifts and lithosphere in the deep carbon cycle. Nat. Geosci. 2017 1012 10, 897–902. https://doi.org/10.1038/s41561-017-0002-7

Fosu, B.R., Ghosh, P., Chew, D.M., Viladkar, S.G., 2019. Composition and U—Pb ages of apatite in the Amba Dongar carbonatite–alkaline complex, India. Geol. J. 54, 3438–3454. https://doi.org/10.1002/GJ.3350

Fosu, B.R., Ghosh, P., Viladkar, S.G., 2020. Clumped isotope geochemistry of carbonatites in the north-western Deccan igneous province: Aspects of evolution, post-depositional alteration and mineralisation. Geochim. Cosmochim. Acta 274, 118–135. https://doi.org/10.1016/J.GCA.2020.01.020

Freestone, I.C., Hamilton, D.L., 1980. The role of liquid immiscibility in the genesis of carbonatites - An experimental study. Contrib. to Mineral. Petrol. 73, 105–117. https://doi.org/10.1007/BF00371385

Ghatak, A., Basu, A.R., 2013. Isotopic and trace element geochemistry of alkalic – mafic – ultramafic – carbonatitic complexes and flood basalts in NE India : Origin in a heterogeneous Kerguelen plume. Geochim. Cosmochim. Acta 115, 46–72.

https://doi.org/10.1016/j.gca.2013.04.004

Gittins, J., Harmer, R.E., 2003. Myth and reality in the carbonatite--silicate rock “association.” Period. di Mineral. 72, 19–26.

Giuliani, A., Phillips, D., Kamenetsky, V.S., Fiorentini, M.L., Farquhar, J., Kendrick, M.A., 2014. Stable isotope (C, O, S) compositions of volatile-rich minerals in kimberlites: A review. Chem. Geol. 374–375, 61–83. https://doi.org/10.1016/j.chemgeo.2014.03.003

Goldstein, S.L., O’Nions, R.K., Hamilton, P.J., 1984. A Sm-Nd isotopic study of atmospheric dusts and particulates from major river systems. Earth Planet. Sci. Lett. 70, 221–236. https://doi.org/10.1016/0012-821X(84)90007-4

Gopalan, K., Macdougall, J.D., Roy, A.B., Murali, A. V., 1990. Sm-Nd evidence for 3.3 Ga old rocks in Rajasthan, northwestern India. Precambrian Res. 48, 287–297. https://doi.org/10.1016/0301-9268(90)90013-G

Grady, J.C., 1971. Deep main faults in South India. Geol. Soc. India 12, 56–62.

Green, D.H., 2015. Experimental petrology of peridotites, including effects of water and carbon on melting in the Earth’s upper mantle. Phys. Chem. Miner. 42, 95–122. https://doi.org/10.1007/S00269-014-0729-2

Guo, P., Ionov, D.A., Xu, W.L., Wang, C.G., Luan, J.P., 2020. Mantle and Recycled Oceanic Crustal Components in Mantle Xenoliths From Northeastern China and their Mantle Sources. J. Geophys. Res. Solid Earth 125. https://doi.org/10.1029/2019JB018232

Guzmics, T., Berkesi, M., Bodnar, R.J., Fall, A., Bali, E., Milke, R., Vetlényi, E., 2019. Natrocarbonatites : A hidden product of three-phase immiscibility 47, 527–530.

Guzmics, T., Mitchell, R.H., Ratter, K., 2012. Liquid immiscibility between silicate , carbonate and sulfide melts in melt inclusions hosted in co-precipitated minerals from Kerimasi volcano (Tanzania): evolution of carbonated nephelinitic magma 101–122. https://doi.org/10.1007/s00410-012-0728-6

Guzmics, T., Zajacz, Z., Mitchell, R.H., Szabó, C., Wälle, M., 2015. The role of liquid – liquid immiscibility and crystal fractionation in the genesis of carbonatite magmas : insights from Kerimasi melt inclusions. https://doi.org/10.1007/s00410-014-1093-4

Gwalani, L.G., Rock, N.M.S., Chang, W.J., Fernandez, S., Allégre, C.J., Prinzhofer, A., 1993. Alkaline rocks and carbonatites of Amba Dongar and adjacent areas, Deccan Igneous Province, Gujarat, India: 1. Geology, petrography and petrochemistry. Mineral. Petrol. 47, 219–253. https://doi.org/10.1007/BF01161569

Halama, R., Vennemann, T., Siebel, W., Markl, G., 2005. The Grønnedal-Ika carbonatite--syenite complex, South Greenland: carbonatite formation by liquid immiscibility. J. Petrol. 46, 191–217.

Hari, K.R., Kumar, M.S., Santosh, M., Rai, S.K., 1998. Petrology, geochemistry and stable isotope studies of carbonate-rich dyke-like bodies, Chhaktalao area, Madhya Pradesh. Geol. Soc. India 52, 591–595.

Heaman, L.M., Srivastava, R.K., Sinha, A.K., 2002. A precise U–Pb zircon/baddeleyite age for the Jasra igneous complex, Karbi–Analong District, Assam, NE India on JSTOR. Curr. Sci. 744–748.

Hegner, E., Rajesh, S., Willbold, M., Müller, D., Joachimski, M., Hofmann, M., Linnemann, U., Zieger, J., Pradeepkumar, A.P., 2020. Sediment-derived origin of the putative Munnar carbonatite, South India. J. Asian Earth Sci. 200, 104432. https://doi.org/10.1016/J.JSEAES.2020.104432

Hoernle, K., Tilton, G., Le Bas, M.J., Duggen, S., Garbe-Schönberg, D., 2002. Geochemistry of oceanic carbonatites compared with continental carbonatites: Mantle recycling of oceanic crustal carbonate. Contrib. to Mineral. Petrol. 142, 520–542. https://doi.org/10.1007/s004100100308

Hou, Z., Tian, S., Yuan, Z., Xie, Y., Yin, S., Yi, L., Fei, H., Yang, Z., 2006. The Himalayan collision zone carbonatites in western Sichuan, SW China: Petrogenesis, mantle source and tectonic implication. Earth Planet. Sci. Lett. 244, 234–250. https://doi.org/10.1016/J.EPSL.2006.01.052

Hulett, S.R.W., Simonetti, A., Rasbury, E.T., Hemming, N.G., 2016. Recycling of subducted crustal components into carbonatite melts revealed by boron isotopes. Nat. Geosci. 2016 912 9, 904–908. https://doi.org/10.1038/ngeo2831

Irvine, T.N., Baragar, W.R.A., 2011. A Guide to the Chemical Classification of the Common Volcanic Rocks. https://doi.org/10.1139/e71-055 8, 523–548. https://doi.org/10.1139/E71-055

Khandelwal, M.K., Maithani, P.B., Pant, P.C., Hansda, P.K., Ramachandran, S., 1997. Geological and geochemical studies on carbonatites and rocks of carbonatitic (?) affinity from areas north of the Narmada Lineament in Madhya Pradesh and Gujarat. Geol. Soc. India 50, 307–313.

Jacobsen, S.B., Wasserburg, G.J., 1980. Sm-Nd isotopic evolution of chondrites. Earth Planet. Sci. Lett. 50, 139–155. https://doi.org/10.1016/0012-821X(80)90125-9

Kale, V.S., Pande, K., 2022. Reappraisal of Duration and Eruptive Rates in Deccan Volcanic Province, India. J. Geol. Soc. India 98, 7–17. https://doi.org/10.1007/S12594-022-1921-5

Kent, R.W., Pringle, M.S., Müller, R.D., Saunders, A.D., Ghose, N.C., 2002. 40Ar/39Ar Geochronology of the Rajmahal Basalts, India, and their Relationship to the Kerguelen Plateau. J. Petrol. 43, 1141–1153. https://doi.org/10.1093/PETROLOGY/43.7.1141

Kjarsgaard, B., Peterson, T., 1991. Nephelinite-carbonatite liquid immiscibility at Shombole volcano, East Africa: Petrographic and experimental evidence. Mineral. Petrol. 43, 293–314. https://doi.org/10.1007/BF01164532

Kjarsgaardl, B.A., Hamilton, D.L., Peterson, T.D., 1995. Peralkaline Nephelinite / Carbonatite Liquid Immiscibility : Comparison of Phase Compositions in Experiments and Natural Lavas from Oldoinyo Lengai. In Carbonatite Volcanism: Oldoinyo Lengai and the Petrogenesis of Natrocarbonatites'., ed. K Bell, J Keller, pp. 163–90. Berlin: Springer-Verlag.

Klemme, S., Dalpé, C., 2003. Trace-element partitioning between apatite and carbonatite melt. Am. Mineral. 88, 639–646. https://doi.org/10.2138/am-2003-0417

Klemme, S., van der Laan, S.R., Foley, S.F., Günther, D., 1995. Experimentally determined trace and minor element partitioning between clinopyroxene and carbonatite melt under upper mantle conditions. Earth Planet. Sci. Lett. 133, 439–448.

https://doi.org/10.1016/0012-821X(95)00098-W

Krishnamurthy, P., 1977. On some geochemical aspects of the Sevattur carbonatite complex, North Arcot District, Tamil Nadu. Geol. Soc. India 18, 265–274.

Krishnamurthy, P., 1985. Petrology of the carbonatites and associated rocks of Sung Valley, Jaintia Hills district, Meghalaya, India. Geol. Soc. India 26, 361–379.

Krishnamurthy, P., 2019. Carbonatites of India. J. Geol. Soc. India 94, 117–138. https://doi.org/10.1007/s12594-019-1281-y

Krishnamurthy, P., Cox, K.G., 1980. A potassium-rich Alkalic Suite from the Deccan Traps, Rajpipla, India. Contrib. to Mineral. Petrol. 73, 179–189. https://doi.org/10.1007/BF00371393

Kumar, A., Gopalan, K., 1991. Precise Rb-Sr age and enriched mantle source of the Sevattur carbanatites, Tamil Nadu, South India. Curr. Sci. 60, 653–655.

Kumar, A., Charan, S.N., Gopalan, K., Macdougall, J.D., 1998. A Long-Lived Enriched Mantle Source for Two Proterozoic Carbonatite Complexes from Tamil Nadu, Southern India. Geochim. Cosmochim. Acta 62, 515–523. https://doi.org/10.1016/S0016-7037(97)00341-4

Kumar, P.S., Parthasarathy, G., Sharma, S. Das, Srinivasan, R., Krishnamurthy, P., 2001. Mineralogical and geochemical study on carbonate veins of the Salem-Attur fault zone, Southern India: Evidence for carbonatitic affinity. Journal-Geological Soc. India 58, 15–26.

Le Bas, M.J., Streckeisen, A.L., 1991. The IUGS systematics of igneous rocks. J. Geol. Soc. London. 148, 825–833. https://doi.org/10.1144/GSJGS.148.5.0825

Lee, W.J., Wyllie, P.J., 1994. Experimental Data Bearing on Liquid Immiscibility, Crystal Fractionation, and the Origin of Calciocarbonatites and Natrocarbonatites. http://dx.doi.org/10.1080/00206819409465489 36, 797–819.

Lee, W., Wyllie, P.J., 1997a. Liquid immiscibility between nephelinite and carbonatite from 1 . 0 to 2 . 5 GPa compared with mantle melt compositions 1–16.

Lee, W.J., Wyllie, P.J., 1998. Petrogenesis of Carbonatite Magmas from Mantle to Crust, Constrained by the System CaO–(MgO + FeO*)–(Na2O + K2O)–(SiO2 + Al2O3 + TiO2)-CO2. J. Petrol. 39, 495–517. https://doi.org/10.1093/PETROJ/39.3.495

Le Maitre, R.W., Streckeisen, A., Zanettin, B., Le Bas, M.J., Bonin, B., Bateman, P. (Eds.), 2002. Igneous rocks: a classification and glossary of terms: recommendations of the International Union of Geological Sciences Subcommission on the Systematics of Igneous Rocks, 2nd ed. Cambridge University Press.

Ludwig, K.R., 2012. Using Isoplot/Ex, version 3.75: a geochronological toolkit for Microsoft Excel. Berkeley Geochronol. Cent. Spec. Pubublication 6.

Mahoney, J., Nicollet, C., Dupuy, C., 1991. Madagascar basalts: tracking oceanic and continental sources. Earth Planet. Sci. Lett. 104, 350–363. https://doi.org/10.1016/0012-821X(91)90215-4

Martin, L.H.J., Schmidt, M.W., Mattsson, H.B., Guenther, D., 2013. Element Partitioning between Immiscible Carbonatite and Silicate Melts for Dry and H2O-bearing Systems at

1-3gpa. J. Petrol. 54, 2301–2338. https://doi.org/10.1093/petrology/egt048

McCulloch, M.T., Black, L.P., 1984. SmNd isotopic systematics of Enderby Land granulites and evidence for the redistribution of Sm and Nd during metamorphism. Earth Planet. Sci. Lett. 71, 46–58. https://doi.org/10.1016/0012-821X(84)90051-7

Melluso, L., Morra, V., Brotzu, P., Franciosi, L., Lieberknecht, A.M.P., Bennio, L., 2003. Geochemical provinciality in the Cretaceous basaltic magmatism of Northern Madagascar: mantle source implications. J. Geol. Soc. London. 160, 477–488. https://doi.org/10.1144/0016-764902-060

Melluso, L., Sethna, S.F., D'Antonio, M., Javeri, P., Bennio, L., 2002. Geochemistry and petrogenesis of sodic and potassic mafic alkaline rocks in the Deccan Volcanic Province, Mumbai area (India). Mineral. Petrol. 74, 323–342. https://doi.org/10.1007/S007100200009/METRICS

Melluso, L., Srivastava, R.K., Guarino, V., Zanetti, A., Sinha, A.K., 2010. mineral compositions and petrogenetic evolution of the ultramafic-alkaline – carbonatitic complex of sung valley, northeastern india. Can. Mineral. 48, 205–229. https://doi.org/10.3749/CANMIN.48.1.205

Michard, A., Gurriet, P., Soudant, M., Albarède, F., 1985. Nd isotopes in French Phanerozoic shales: external vs. internal aspects of crustal evolution. Geochim. Cosmochim. Acta 49, 601–610. https://doi.org/10.1016/0016-7037(85)90051-1

Mitchell, R.H., 2005. Carbonatites and carbonatites and carbonatites. Can. Mineral. 43, 2049–2068. https://doi.org/10.2113/gscanmin.43.6.2049

McDougall, I., Harrison, T.M., others, 1999. Geochronology and Thermochronology by the 40Ar/39Ar Method. Oxford University Press on Demand.

Migdisov, A., Williams-Jones, A.E., Brugger, J., Caporuscio, F.A., 2016. Hydrothermal transport, deposition, and fractionation of the REE: Experimental data and thermodynamic calculations. Chem. Geol. 439, 13–42. https://doi.org/10.1016/J.CHEMGEO.2016.06.005

Migdisov, A.A., Williams-Jones, A.E., 2014. Hydrothermal transport and deposition of the rare earth elements by fluorine-bearing aqueous liquids. Miner. Depos. 49, 987–997. https://doi.org/10.1007/S00126-014-0554-Z

Moralev, V.M., Voronovski, S.N., Borodin, L.S., 1975. New findings about the age of carbonatites and syenites from southern India, in: USSR Acad. Sci. pp. 46–48.

Nag, S., Sengupta, S.K., Gaur, R.K., Absar, A., 1999. Alkaline rocks of Samchampi-Samteran, District Karbi-Anglong, Assam, India. J. Earth Syst. Sci. 108, 33.

Nambiar, A.R., Golani, P.R., 1985. A new find of carbonatite from Meghalaya. Curr. Sci. 54, 281–282.

Natarajana, M., Bhaskar Rao, B., Parthasarathy, R., Kumar, A., Gopalan, K., 1994. 2.0 Ga old pyroxenite-carbonatite complex of Hogenakal, Tamil Nadu, South India. Precambrian Res. 65, 167–181. https://doi.org/10.1016/0301-9268(94)90104-X

Pande, K., Cucciniello, C., Sheth, H., Vijayan, A., Sharma, K.K., Purohit, R., Jagadeesan, K.C., Shinde, S., 2017. Polychronous (Early Cretaceous to Palaeogene) emplacement of the Mundwara alkaline complex, Rajasthan, India: 40Ar/39Ar geochronology, petrochemistry and geodynamics. Int. J. Earth Sci. 106, 1487–1504. https://doi.org/10.1007/s00531-016-1362-8

Pandit, M.K., Kumar, M., Sial, A.N., Sukumaran, G.B., Piementle, M., Ferreira, V.P., 2016. Geochemistry and C–O and Nd–Sr isotope characteristics of the 2.4 Ga Hogenakkal carbonatites from the South Indian Granulite Terrane: evidence for an end-Archaean depleted component and mantle heterogeneity. 58, 1461–1480. https://doi.org/10.1080/00206814.2016.1163646

Pandit, M.K., Sial, A.N., Sukumaran, G.B., Pimentel, M.M., Ramasamy, A.K., Ferreira, V.P., 2002. Depleted and enriched mantle sources for Paleo- and Neoproterozoic carbonatites of southern India: Sr, Nd, C-O isotopic and geochemical constraints. Chem. Geol. 189, 69–89. https://doi.org/10.1016/S0009-2541(02)00136-5

Panina, L.I., Motorina, I. V., 2008. Liquid immiscibility in deep-seated magmas and the generation of carbonatite melts. Geochemistry Int. 46, 448–464. https://doi.org/10.1134/S0016702908050029

Paul, D., Chandra, J., Halder, M., 2020. Proterozoic Alkaline rocks and Carbonatites of Peninsular India: A review. Int. Union Geol. Sci. 43, 249–277. https://doi.org/10.18814/epiiugs/2020/020015

Pintér, Z., Foley, S.F., Yaxley, G.M., Rosenthal, A., Rapp, R.P., Lanati, A.W., Rushmer, T., 2021. Experimental investigation of the composition of incipient melts in upper mantle peridotites in the presence of CO2 and H2O. Lithos 396–397, 106224. https://doi.org/10.1016/J.LITHOS.2021.106224

Potts, P.J., 1987. X-ray fluorescence analysis: principles and practice of wavelength dispersive spectrometry, in: A Handbook of Silicate Rock Analysis. Springer, pp. 226–285.

Randive, K., Meshram, T., 2020. An Overview of the Carbonatites from the Indian Subcontinent 85–116.

Rao, C.S., Das, G.R.N., Setty, B.K., Perumal, N., 1978. Radioactive carbonatites of Pakkanadu and Mulakkadu, Salem district, Tamil Nadu. Geol. Soc. India 19, 53–63.

Rasoazanamparany, C., Widom, E., Kuentz, D., Raharimahefa, T., Rakotondrazafy, A.M.F., Rakotondravelo, K.M., 2022. Origin and sources of recent continental alkaline volcanism in the Southwest Ankaratra volcanic field, Central Madagascar: Insights from major and trace element and Sr, Nd, Pb, Hf, Os isotopes. Chem. Geol. 606, 120949. https://doi.org/10.1016/J.CHEMGEO.2022.120949

Rathore, S.S., Venkatesan, T.R., Srivastava, R.K., 1996. Mundwara alkali igneous complex, Rajasthan, India: chronology and Sr isotope systematics. Geol. Soc. India 48, 517–528.

Ratnakar, J., Leelanandam, C., 1989. Petrology of the alkaline plutons from the eastern and southern Peninsular India. Mem. Geol. Soc. India 15, 145–176.

Ray, J.S., 2009. Radiogenic isotopic ratio variations in carbonatites and associated alkaline silicate rocks: Role of crustal assimilation. J. Petrol. 50, 1955–1971. https://doi.org/10.1093/petrology/egp063

Ray, J.S., 1998. Trace element and isotope evolution during concurrent assimilation, fractional crystallization, and liquid immiscibility of a carbonated silicate magma. Geochim. Cosmochim. Acta 62, 3301–3306. https://doi.org/10.1016/S0016-7037(98)00237-3

Ray, J.S., Pande, K., 2001. 40Ar-39Ar age of carbonatite-alkaline magmatism in Sung Valley, Meghalaya, India. Proc. Indian Acad. Sci. Earth Planet. Sci. 110, 185–190. https://doi.org/10.1007/BF02702233

Ray, J.S., Pande, K., 1999. Carbonatite alkaline magmatism associated with continental flood basalts at stratigraphic boundaries: Cause for mass extinctions. Geophys. Res. Lett. 26, 1917–1920. https://doi.org/10.1029/1999GL900390

Ray, J.S., Pande, K., Bhutani, R., Shukla, A.D., Rai, V.K., Kumar, A., Awasthi, N., Smitha, R.S., Panda, D.K., 2013. Age and geochemistry of the Newania dolomite carbonatites, India: implications for the source of primary carbonatite magma. Contrib. to Mineral. Petrol. 166, 1613–1632. https://doi.org/10.1007/s00410-013-0945-7

Ray, A., Paul, D.K., Sen, G., Biswas, S.K., 2014. Carbonatite-silicate immiscible melt inclusion in lamprophyre from Kutch, western India: Implication for plume-lithosphere interaction and initiation of Deccan Trap magmatism, in: EGU General Assembly Conference Abstracts. p. 1503.

Ray, J.S., Ramesh, R., 2006. Stable carbon and oxygen isotopic compositions of Indian carbonatites. Int. Geol. Rev. 48, 17–45. https://doi.org/10.2747/0020-6814.48.1.17

Ray, J.S., Ramesh, R., 2000. Rayleigh fractionation of stable isotopes from a multicomponent source. Geochim. Cosmochim. Acta 64, 299–306. https://doi.org/10.1016/S0016-7037(99)00181-7

Ray, J.S., Ramesh, R., 1999. Evolution of carbonatite complexes of the Deccan flood basalt province: Stable carbon and oxygen isotopic constraints. J. Geophys. Res. Solid Earth 104, 29471–29483. https://doi.org/10.1029/1999jb900262

Ray, J.S., Shukla, P.N., 2004. Trace element geochemistry of Amba Dongar carbonatite complex, India: Evidence for fractional crystallization and silicate-carbonate melt immiscibility. Proc. Indian Acad. Sci. Earth Planet. Sci. 113, 519–531. https://doi.org/10.1007/BF02704020

Ray, J.S., Trivedi, J.R., Dayal, A.M., 2000. Strontium isotope systematics of Amba Dongar and Sung Valley carbonatite-alkaline complexes, India: evidence for liquid immiscibility, crustal contamination and long-lived Rb/Sr enriched mantle sources. J. Asian Earth Sci. 18, 585–594. https://doi.org/https://doi.org/10.1016/S1367-9120(99)00072-3

Renjith, M.L., Santosh, M., Satyanarayanan, M., Rao, D.V.S., Tang, L., 2016. Multiple rifting and alkaline magmatism in southern India during Paleoproterozoic and Neoproterozoic. Tectonophysics 680, 233–253. https://doi.org/10.1016/J.TECTO.2016.04.041

Renne, P.R., Sprain, C.J., Richards, M.A., Self, S., Vanderkluysen, L., Pande, K., 2015. State shift in Deccan volcanism at the Cretaceous-Paleogene boundary, possibly induced by impact. Science (80-.). 350, 76–78. https://doi.org/10.1126/science.aac7549

Renne, P.R., Swisher, C.C., Deino, A.L., Karner, D.B., Owens, T.L., DePaolo, D.J., 1998. Intercalibration of standards, absolute ages and uncertainties in 40Ar/39Ar dating.

Chem. Geol. 145, 117–152. https://doi.org/10.1016/S0009-2541(97)00159-9

Richet, P., Bottinga, Y., Javoy, M., 1977. St Able Isotope Sulphur , and Chlorine Fractionation Among. Annu. Rev. Earth Planet. Sci. 5, 65–110.

Ryabchikov, I.D., Kogarko, L.N., 2016. Deep differentiation of alkali ultramafic magmas: Formation of carbonatite melts. Geochemistry Int. 54, 739–747. https://doi.org/10.1134/S001670291609007X

Saha, A., Ganguly, S., Ray, J., Koeberl, C., Thöni, M., Sarbajna, C., Sawant, S.S., 2017. Petrogenetic evolution of Cretaceous Samchampi-Samteran Alkaline Complex, Mikir Hills, Northeastern India: Implications on multiple melting events of heterogeneous plume and metasomatized sub-continental lithospheric mantle. Gondwana Res. 48, 237–256. https://doi.org/10.1016/J.GR.2017.04.022

Salters, V.J.M., Stracke, A., 2004. Composition of the depleted mantle. Geochemistry, Geophys. Geosystems 5. https://doi.org/10.1029/2003GC000597

Sant, D.A., Karanth, R. V, Jadhav, P.C., 1991. A note on the occurrence of carbonatite dykes in the lower Narmada valley. Geol. Soc. India 37, 119–127.

Santos, R. V, clayton, R.N., 1995. Variations of oxygen and carbon isotopes in carbonatites: A study of Brazilian alkaline complexes. Geochim. Cosmochim. Acta 59, 1339–1352. https://doi.org/https://doi.org/10.1016/0016-7037(95)00048-5

Sarkar, A., Datta, A.K., Poddar, B.C., Bhattacharyya, B.K., Kollapuri, V.K., Sanwal, R., 1996. Geochronological studies of Mesozoic igneous rocks from eastern India. J. Southeast Asian Earth Sci. 13, 77–81. https://doi.org/10.1016/0743-9547(96)00009-8

Schleicher, H., Kramm, U., Pernicka, E., Schidlowski, M., Schmidt, F., Subramanian, V., Todt, W., Viladkar, S.G., 1998. Enriched subcontinental upper mantle beneath southern India: Evidence from Pb, Nd, Sr, and C-O isotopic studies on Tamil Nadu carbonatites. J. Petrol. 39, 1765–1785. https://doi.org/10.1093/petroj/39.10.1765

Schleicher, H., Todt, W., Viladkar, S.G., Schmidt, F., 1997. Pb/Pb age determinations on the Newania and Sevattur carbonatites of India: evidence for multi-stage histories. Chem. Geol. 140, 261–273. https://doi.org/10.1016/S0009-2541(97)00022-3

Schmidt, M.W., Weidendorfer, D., 2018. Carbonatites in oceanic hotspots. Geology 46, 435–438. https://doi.org/10.1130/G39621.1

Sharma, S.R., T, D., Jayaram, M.S., 1971. carbonatites from nepheline syenite band near kunavaram, khammam district, andhra pradesh. Journal of Geol. Soc. India.

Sharma, A., Sahoo, S., Chalapathi Rao, N. V., Belyatsky, B., Dhote, P., Lehmann, B., 2022. Petrology and Nd–Sr isotopic composition of alkaline lamprophyres from the Early to Late Cretaceous Mundwara Alkaline Complex, NW India: evidence of crystal fractionation, accumulation and corrosion in a complex magma chamber plumbing system. Geol. Soc. Spec. Publ. 513, 413–442. https://doi.org/10.1144/SP513-2020-175

Sheth, H., Pande, K., Vijayan, A., Sharma, K.K., Cucciniello, C., 2017. Recurrent Early Cretaceous, Indo-Madagascar (89–86 Ma) and Deccan (66 Ma) alkaline magmatism in the Sarnu-Dandali complex, Rajasthan: 40Ar/39Ar age evidence and geodynamic significance. Lithos 284–285, 512–524. https://doi.org/10.1016/j.lithos.2017.05.005

Simonetti, A., Bell, K., Viladkar, S.G., 1995. Isotopic data from the Amba Dongar Carbonatite Complex, west-central India: Evidence for an enriched mantle source. Chem. Geol. 122, 185–198. https://doi.org/10.1016/0009-2541(95)00004-6

Simonetti, A., Goldstein, S.L., Schmidberger, S.S., Viladkar, S.G., 1998. Geochemical and Nd, Pb, and Sr Isotope Data from Deccan Alkaline Complexes - Inferences for Mantle Sources and Plume-Lithosphere Interaction. J. Petrol. 39, 1847–1864. https://doi.org/10.1093/petroj/39.11-12.1847

Smith, C.B., Haggerty, S.E., Chatterjee, B., Beard, A., Townend, R., 2013. Kimberlite, lamproite, ultramafic lamprophyre, and carbonatite relationships on the Dharwar Craton, India; an example from the Khaderpet pipe, a diamondiferous ultramafic with associated carbonatite intrusion. Lithos 182–183, 102–113. https://doi.org/10.1016/J.LITHOS.2013.10.006

Smith, M., Kynicky, J., Xu, C., Song, W., Spratt, J., Jeffries, T., Brtnicky, M., Kopriva, A., Cangelosi, D., 2018. The origin of secondary heavy rare earth element enrichment in carbonatites: Constraints from the evolution of the Huanglongpu district, China. Lithos 308–309, 65–82. https://doi.org/https://doi.org/10.1016/j.lithos.2018.02.027

Solovova, I.P., Girnis, A. V., Kogarko, L.N., Kononkova, N.N., Stoppa, F., Rosatelli, G., 2005. Compositions of magmas and carbonate-silicate liquid immiscibility in the Vulture alkaline igneous complex, Italy. Lithos 85, 113–128. https://doi.org/10.1016/j.lithos.2005.03.022

Sorcar, N., Mukherjee, S., Pant, N.C., Dev, J.A., Nishanth, N., 2021. Chemical dating of monazite: Testing of analytical protocol for U–Th–total Pb using CAMECA SXFive tactis EPMA at the National Centre for Earth Science Studies, Thiruvananthapuram, India. J. Earth Syst. Sci. 130, 1–11. https://doi.org/10.1007/S12040-021-01738-4

Sorokhtina, N. V., Belyatsky, B. V., Zaitsev, V.A., Viladkar, S.G., Kononkova, N.N., Ghatak, A., 2022. New Data on the Age and Genesis of the Newania Carbonatite Complex, Rajasthan, India. Geochemistry Int. 60, 1237–1261. https://doi.org/10.1134/S0016702922120072

Sprain, C.J., Renne, P.R., Vanderkluysen, L., Pande, K., Self, S., Mittal, T., 2019. The eruptive tempo of Deccan volcanism in relation to the Cretaceous-Paleogene boundary. Science (80-.). 363, 866–870. https://doi.org/10.1126/science.aav1446

Srivastava, R.K., 1997. Petrology, geochemistry and genesis of rift-related carbonatites of Ambadungar, India. Mineral. Petrol. 61, 47.

Srivastava, R.K., 2013. Petrological and geochemical characteristics of Paleoproterozoic ultramafic lamprophyres and carbonatites from the Chitrangi region, Mahakoshal supracrustal belt, central India. J. Earth Syst. Sci. 122, 759–776. https://doi.org/10.1007/S12040-013-0311-1

Srivastava, R.K., Heaman, L.M., Sinha, A.K., Shihua, S., 2005. Emplacement age and isotope geochemistry of Sung Valley alkaline–carbonatite complex, Shillong Plateau, northeastern India: implications for primary carbonate melt and genesis of the associated silicate rocks. Lithos 81, 33–54. https://doi.org/10.1016/J.LITHOS.2004.09.017

Srivastava, R.K., Guarino, V., Wu, F.Y., Melluso, L., Sinha, A.K., 2019. Evidence of sub-continental lithospheric mantle sources and open-system crystallization processes from in-situ U–Pb ages and Nd–Sr–Hf isotope geochemistry of the Cretaceous ultramafic-alkaline-(carbonatite) intrusions from the Shillong Plateau, north-eastern India. Lithos 330–331, 108–119. https://doi.org/10.1016/J.LITHOS.2019.02.009

Srivastava, R.K., Melluso, L., Sinha, A.K., 2016. Petrogenesis of an early Cretaceous potassic lamprophyre dyke from Rongjeng, East Garo Hills, Shillong plateau, north-eastern India. Curr. Sci. 649–658.

Srivastava, R.K., Wall, F., LeBas, M.J., 1993. Sr-REE rich carbonatite dyke from Sarnu-Dandali, Barmer, Rajasthan. Curr. Sci. 65, 170–171.

Steiger, R.H., Jäger, E., 1977. Subcommission on geochronology: Convention on the use of decay constants in geo- and cosmochronology. Earth Planet. Sci. Lett. 36, 359–362. https://doi.org/10.1016/0012-821X(77)90060-7

Storey, M., Mahoney, J.J., Saunders, A.D., Duncan, R.A., Kelley, S.P., Coffin, M.F., 1995. Timing of hot spot-related volcanism and the breakup of Madagascar and India. Science (80-.). 267, 852–855. https://doi.org/10.1126/SCIENCE.267.5199.852

Streckeisen, A., 1980. Classification and nomenclature of volcanic rocks, lamprophyres, carbonatites and melilitic rocks IUGS Subcommission on the Systematics of Igneous Rocks - Recommendations and suggestions. Geol. Rundschau 69, 194–207. https://doi.org/10.1007/BF01869032

Stoppa, F., 2021. Evolution and Involution of Carbonatite Thoughts. Elements 17, 303–304. https://doi.org/10.2138/GSELEMENTS.17.5.303

Stoppa, F., Rosatelli, G., Wall, F., Jeffries, T., 2005. Geochemistry of carbonatite-silicate pairs in nature: A case history from Central Italy. Lithos 85, 26–47. https://doi.org/10.1016/j.lithos.2005.03.026

Subrahmanyam, N.P., 1989. Differentiation due to probable initial immiscibility in the Musala pluton of the Mundwara alkaline igneous complex, Rajasthan, India. Mem. Geol. Soc. India 15, 25–46.

Subrahmanyam, N.P., Leelanandam, C., 1991. Geochemistry and petrology of the cumulophyric layered suite of rocks from the Toa pluton of the Mundwara alkali igneous complex, Rajasthan. Geol. Soc. India 38, 397–411.

Subrahmanyam, N.P., Rao, G.V.D., 1977. Petrography, geochemistry and origin of the carbonatite veins of Mer pluton, Mundwara igneous complex, Rajasthan. Geol. Soc. India 18, 306–322.

Subrahmanyam, N.P., Rao, G.V.U., 1972. Carbonatite veins of Mundwara Igneous Complex, Rajasthan. Geol. Soc. India 13, 388–391.

Sukheswala, R.N., Udas, G.R., 1967. Fluorspar mineralization related to carbonatite-alkalic complex at Amba Dongar, Gujarat State. Curr. Sci. 36, 14–16.

Sun, S.S., McDonough, W.F., 1989. Chemical and isotopic systematics of oceanic basalts: Implications for mantle composition and processes. Geol. Soc. Spec. Publ. 42, 313–345. https://doi.org/10.1144/GSL.SP.1989.042.01.19

Thirlwall, M.F., 1991. Long-term reproducibility of multicollector Sr and Nd isotope ratio analysis. Chem. Geol. Isot. Geosci. Sect. 94, 85–104. https://doi.org/10.1016/0168-

9622(91)90002-E

Thomson, A.R., Walter, M.J., Kohn, S.C., Brooker, R.A., 2016. Slab melting as a barrier to deep carbon subduction. Nat. 2016 5297584 529, 76–79. https://doi.org/10.1038/nature16174

TobischP, O.T., Collerson, K.D., Bhattacharyya, T., Mukhopadhyay, D., 1994. Structural relationships and Sr□Nd isotope systematics of polymetamorphic granitic gneisses and granitic rocks from central Rajasthan, India: implications for the evolution of the Aravalli craton. Precambrian Res. 65, 319–339. https://doi.org/10.1016/0301-9268(94)90111-2

Torsvik, T.H., Tucker, R.D., Ashwal, L.D., Carter, L.M., Jamtveit, B., Vidyadharan, K.T., Venkataramana, P., 2000. Late Cretaceous India–Madagascar fit and timing of break-up related magmatism. Terra Nov. 12, 220–224. https://doi.org/10.1046/J.1365-3121.2000.00300.X

Todt, W., Cliff, R.A., Hanser, A., Hofmann, A.W., 1996. Evaluation of a 202pb _ 205pb Double Spike for High-Precision Lead Isotope Analysis, in: Earth Processes: Reading the Isotopic Code. American Geophysical Union (AGU), pp. 429–437.

Udas, G.R., Krishnamurthy, P., 1968. an account of a rich fluorite deposit at hingoria, broach dt., gujarat state. Curr. Sci. 37, 77–78.

Upadhyay, D., Mondal, S., Patel, A.K., Mishra, B., Pruseth, K.L., Bhushan, S.K., 2021. Rare earth element precipitation induced by non-redox transformation of magnetite to hematite: Microtextural and geochemical evidence from the Kamthai carbonatite complex, western India. Lithos 400–401, 106381. https://doi.org/10.1016/J.LITHOS.2021.106381

Veena, K., Pandey, B.K., Krishnamurthy, P., Gupta, J.N., 1998. Pb, Sr and Nd Isotopic Systematics of the Carbonatites of Sung Valley, Meghalaya, Northeast India: Implications for Contemporary Plume-Related Mantle Source Characteristics. J. Petrol. 39, 1875–1884. https://doi.org/10.1093/PETROJ/39.11-12.1875

Veksler, I. V., Dorfman, A.M., Dulski, P., Kamenetsky, V.S., Danyushevsky, L. V., Jeffries, T., Dingwell, D.B., 2012. Partitioning of elements between silicate melt and immiscible fluoride, chloride, carbonate, phosphate and sulfate melts, with implications to the origin of natrocarbonatite. Geochim. Cosmochim. Acta 79, 20–40. https://doi.org/10.1016/j.gca.2011.11.035

Vijayan, A., Sheth, H., Sharma, K.K., 2016. Tectonic significance of dykes in the Sarnu-Dandali alkaline complex, Rajasthan, northwestern Deccan Traps. Geosci. Front. 7, 783–791. https://doi.org/10.1016/j.gsf.2015.09.004

Viladkar, S.G., 2018. Ferrocarbonatites in the Amba Dongar Diatreme, Gujarat, India. J. Geol. Soc. India 92, 141–144.

Viladkar, S.G., 2012. Evolution of calciocarbonatite magma: Evidence from the sovite and alvikite association in the Amba Dongar Complex, India. INTECH Open Access Publisher.

Viladkar, S.G., 1998. Carbonatite occurrences in Rajasthan, India. Petrology 6, 272–283.

Viladkar, S.G., Bismayer, U., Zietlow, P., 2017. Metamict U-rich pyrochlore of Newania carbonatite, Udaipur, Rajasthan. J. Geol. Soc. India 89, 133–138.

Viladkar, S.G., Subramanian, V., 1995. Mineralogy and geochemistry of the carbonatites of the Sevathur and Samalpatti complexes, Tamil Nadu. Geol. Soc. India 45, 505–517.

Viladkar, S.G., Wimmenauer, W., 1986. Mineralogy and geochemistry of the Newania carbonatite-fenite complex, Rajasthan, India. Neues Jahrb. Miner. Abh 156, 1–21.

Vladykin, N. V, Viladkar, S.G., Miyazaki, T., Mohan, V.R., 2008. Geochemistry of benstonite and associated carbonatites of Sevathur, Jogipatti and Samalpatti, Tamil Nadu, south India and Murun massif, Siberia. J. Geol. Soc. India 72, 312–324.

Vlastélic, I., Staudacher, T., Semet, M., 2005. Rapid Change of Lava Composition from 1998 to 2002 at Piton de la Fournaise (Réunion) Inferred from Pb Isotopes and Trace Elements: Evidence for Variable Crustal Contamination. J. Petrol. 46, 79–107. https://doi.org/10.1093/PETROLOGY/EGH062

Wall, F., Le Bas, M.J., Srivastava, R.K., 1993. Calcite and carbocernaite exsolution and cotectic textures in a Sr, REE -rich carbonatite dyke from Rajasthan, India . Mineral. Mag. 57, 495–513. https://doi.org/10.1180/minmag.1993.057.388.11

Walker, R.J., Carlson, R.W., Shirey, S.B., F.R, B., 1989. Os, Sr, Nd, and Pb isotope systematics of southern African peridotite xenoliths: Implications for the chemical evolution of subcontinental mantle. Geochim. Cosmochim. Acta 53, 1583–1595. https://doi.org/10.1016/0016-7037(89)90240-8

Wallace, M.E., Green, D.H., 1988. An experimental determination of primary carbonatite magma composition. Nature 335, 343–346. https://doi.org/10.1038/335343a0

Wasserburg, G.J., Jacousen, S.B., DePaolo, D.J., McCulloch, M.T., Wen, T., 1981. Precise determination of SmNd ratios, Sm and Nd isotopic abundances in standard solutions. Geochim. Cosmochim. Acta 45, 2311–2323. https://doi.org/10.1016/0016-7037(81)90085-5

Watkinson, D.H., Wyllie, P.J., 1971. Experimental Study of the Composition Join NaAlSiO4-CaCO3-H2O and the Genesis of Alkalic Rock—Carbonatite Complexes. J. Petrol. 12, 357–378. https://doi.org/10.1093/petrology/12.2.357

Weidendorfer, D., Asimow, P.D., 2022. Experimental constraints on truly conjugate alkaline silicate – carbonatite melt pairs. Earth Planet. Sci. Lett. 584, 117500. https://doi.org/10.1016/j.epsl.2022.117500

Weis, D., Kieffer, B., Maerschalk, C., Barling, J., De Jong, J., Williams, G.A., Hanano, D., Pretorius, W., Mattielli, N., Scoates, J.S., Goolaerts, A., Friedman, R.M., Mahoney, J.B., 2006. High-precision isotopic characterization of USGS reference materials by TIMS and MC-ICP-MS. Geochemistry, Geophys. Geosystems 7. https://doi.org/10.1029/2006GC001283

Willbold, M., Stracke, A., 2006. Trace element composition of mantle end-members: Implications for recycling of oceanic and upper and lower continental crust. Geochemistry, Geophys. Geosystems 7. https://doi.org/10.1029/2005GC001005

Woolley, A.R., Kempe, D.R.C., 1989. Carbonatites: nomenclature, average chemical composition in Carbonatites: genesis and evolution (ed. Bell, K.) 1--14.

Wolley, A.R and Kjarsgaard, B.., 2008. Geological Survey of Canada, Woolley, A.R. and Kjarsgaard, B.A., 2008. Carbonatite occurrences of the world. Geological Survey of

Canada.

Wörner, G., Zindler, A., Staudigel, H., Schmincke, H.U., 1986. Sr, Nd, and Pb isotope geochemistry of Tertiary and Quaternary alkaline volcanics from West Germany. Earth Planet. Sci. Lett. 79, 107–119. https://doi.org/10.1016/0012-821X(86)90044-0

Wyllie, P.J., Lee, W.J., 1998. Model system controls on conditions for formation of magnesiocarbonatite and calciocarbonatite magmas from the mantle. J. Petrol. 39, 1885–1893. https://doi.org/10.1093/petroj/39.11-12.1885

Wyllie, P.J., Huang, W.-L., 1975. Influence of mantle CO 2 in the generation of carbonatites and kimberlites. Nat. 1975 2575524 257, 297–299. https://doi.org/10.1038/257297a0

Xu, C., Chakhmouradian, A.R., Taylor, R.N., Kynicky, J., Li, W., Song, W., Fletcher, I.R., 2014. Origin of carbonatites in the South Qinling orogen: Implications for crustal recycling and timing of collision between the South and North China Blocks. Geochim. Cosmochim. Acta 143, 189–206. https://doi.org/10.1016/J.GCA.2014.03.041

Yaxley, G.M., Anenburg, M., Tappe, S., Decree, S., Guzmics, T., 2022. Carbonatites: Classification, Sources, Evolution, and Emplacement. Annu. Rev. Earth Planet. Sci. 50, 261–293. https://doi.org/10.1146/annurev-earth-032320-104243

Zindler, A., Hart, S., 1986. Chemical geodynamics. Annu. Rev. Earth Planet. Sci. Vol. 14 493–571. https://doi.org/10.1146/annurev.ea.14.050186.002425

List of Publications

Publications in Journals

1. S. Dey, N. Chauhan, **M.K. Mahala**, P. Chakravarti, A. Vasishtha, V. Jain, J.S. Ray: *Dominant role of deglaciation in Late Pleistocene-Early Holocene sediment aggradation in the Upper Chenab Valley, NW Himalaya, Quaternary Research.* https://doi.org/10.1017/qua.2022.57

2. A. Singh, J.S. Ray, V. Jain, **M.K. Mahala**: Evaluating the connectivity of the Yamuna and the Sarasvati during the Holocene: *Evidence from geochemical provenance of sediment in the Markanda River valley, India; 2022, Geomorphology 402, 108124, 2022.* https://doi.org/10.1016/j.geomorph.2022.108124

3. S. Tripati, J.S. Ray, R.P. Behera, P. Babu, **M.K. Mahala**, M. Kocherla, V. Khedekar: *Geochemical Provenance of an Indo-Arabian Stone Anchor from Manikapatna, East Coast of India: Implications for Medieval Maritime Trade of India, Scientific Reports 12 (1), 1-14 2022.* https://doi.org/10.1038/s41598-022-17910-9

4. B. G. George, J.S. Ray, S.P. Pillai, **M.K. Mahala**, S. Kumar, V.S. Kale: *C-Sr-Pb isotope systematics of the carbonate sequences of Kaladgi Supergroup, India: Implication for basin evolution and correlation with Proterozoic global events.* https://doi.org/10.1016/j.precamres.2023.107014

5. B. G. George, **M.K. Mahala**, J.S. Ray: *Pb-Pb age of the Gotan Limestone, Marwar Supergroup: Implications for Ediacaran-Cambrian transition events in peninsular India.* **(Under Review)**

Manuscripts (from Thesis) Under Preparation

1. **M.K. Mahala**, J.S. Ray, K. Pande. *Age and origin of the Sarnu-Dandali-Kamthai carbonatite-alkaline complex, India: Implications for genetic linkage with Deccan continental flood basalt province.*

2. **M.K. Mahala**, J.S. Ray. *On the association of carbonatite and alkaline silicate rocks: a case study from the Sarnu-Dandali-Kamthai carbonatite-alkaline complex, India.*

Presentations at Conferences

1. **Milan Kumar Mahala** and Jyotiranjan S. Ray. *Evolution of Kamthai carbonatites, Rajasthan: Evidence from geochemistry*. *Frontiers in Geoscience Research Conference 2021* (Oral). 27th to 28th Sep 2021

2. **Milan Kumar Mahala** and Jyotiranjan S. Ray. *Age and geochemistry of the Kamthai carbonatites, Rajasthan, western India*. *EGU General Assembly 2022* (Oral). 23rd to 27th May 2022

3. **Milan Kumar Mahala** and Jyotiranjan S. Ray. *On the association of Carbonatites and Alkaline silicate rocks: A case study from Sarnu-Dandali complex, India. Goldschmidt 2022* (Oral). 10th to 15th July 2022

4. **Milan Kumar Mahala** and Jyotiranjan S. Ray. *Carbonatite generation through carbonate-silicate immiscibility: An example from Sarnu-Dandali-Kamthai alkaline complex, India: Frontiers in Geoscience Research Conference 2021* (Oral). 1st to 3rd Feb 2023